UNIVERSITÀ
DEGLI STUDI
FIRENZE

DOTTORATO DI RICERCA IN
Fisica e Astronomia

CICLO XXIX

COORDINATORE Prof. Massimo Gurioli

Measurement of the energy spectra relative to neutrons produced at very small angle in $\sqrt{s}=13$ TeV proton-proton collisions using the LHCf Arm2 detector

Settore Scientifico Disciplinare FIS/04

Dottorando
Dott. Eugenio Berti

Tutore
Prof. Oscar Adriani

Coordinatore
Prof. Massimo Gurioli

Anni 2013/2016

Abstract

In the last years, several ground-based experiments have measured flux and composition of ultra high energy cosmic rays - *i.e.* cosmic rays having energies above 10^{18} eV - up to the GZK cutoff region. Nevertheless, these analyses suffer of large uncertainties due to the fact that they must rely on hadronic interaction models, that exhibit very different behavior in the forward region due to the lack of high energy calibration data. To provide measurements that can be useful to tune these models is exactly the main aim of the LHC-*forward* (LHCf) experiment. Thanks to two small sampling calorimeter, Arm1 and Arm2, installed at ± 140 m from LHC IP1, LHCf can detect neutral particles produced in the very forward region ($\eta > 8.4$) by proton-proton and proton-ion high energy collisions (proton-proton interaction at $\sqrt{s} = 14$ TeV is equivalent to the collision of a 10^{17} eV proton with a proton at rest, hence it is possible to perform measurements at an energy close to the typical one of UHECRs). Detectors are optimized for the reconstruction of π^0 from its 2γ decay, but they offer the possibility to study other secondary hadrons as well, despite with more limited performances. Neutrons, the most abundant hadrons reaching LHCf, have particular interest because it has been noted that a small change in the number of baryons produced very near to the first interaction point of a cosmic ray with the atmosphere can explain the *muon excess problem*, observed by Pierre Auger Observatory and Telescope Array.

In this work we present the results relative to energy spectra of forward neutrons produced in $\sqrt{s} = 13$ TeV proton-proton collisions measured using the LHCf Arm2 detector. It is ideally divided into two parts: the first one is dedicated to detector calibration, the second one to analysis itself.

Calibration of the energy scale for the reconstruction of hadronic showers was performed making use of both beam test data and MC simulations. This involved the estimation of scintillators absolute gains, position dependent correction factors and deposited energy to primary energy conversion coefficients. At the end, we obtained an uncertainty on the energy scale of about 3.5%, energy and position resolution above 350 GeV respectively better than 40% and 1 mm, 70% detection efficiency above 2 TeV.

Analysis of data relative to proton-proton collisions at $\sqrt{s} = 13$ TeV with the Arm2 detector was divided in three different pseudorapidity regions: $8.81 < \eta < 8.99$, $8.99 < \eta < 9.22$, $\eta > 10.76$. After some studies on simulations to set event selection criteria, we reconstructed energy spectra, applied necessary correction factors and estimated related systematic uncertainties. Being $\sigma_E/E \sim 40\%$, folded spectra are enough to test interaction models, but, in order to provide useful information for their tuning, deconvolution is needed. After applying iterative bayesian unfolding, unfolded spectra were finally compared to the most common models employed in cosmic rays physics. No one perfectly reproduces experimental data: in the most forward region a very large discrepancy was found, qualitatively explained only by QGSJet II-04; in the other two regions the agreement is generally better, especially in the case of EPOS-LHC. Finally, a test of Feynman scaling using Arm2 results relative to p-p collisions at $\sqrt{s} = 13$ TeV and Arm1-Arm2 combined ones in the case of $\sqrt{s} = 7$ TeV confirmed the validity of our analysis, that in the future will be extended to Arm1 as well.

Contents

Chapter 1

Cosmic Rays Physics

Even if LHCf measurements can be useful to understand different aspects of forward physics, their main application is to provide experimental results that can be used for the tuning of hadronic interaction models employed by ground-based cosmic rays experiments. In order to better understand this point, it is necessary to introduce the physics background of LHCf before describing the experiment itself. In this chapter we will give an outlook about cosmic rays (concerning in particular experimental observations, acceleration and propagation theories, open problems) and detection techniques employed in this field (in particular ground-based experiments, properties of extensive air showers, impact of models on experimental measurements).

1.1 Phenomenology of cosmic rays

Cosmic rays [1] are particles coming from the outer space. They are commonly divided into primaries and secondaries: the former are accelerated by astrophysical sources; the latter are produced by the interaction of primaries with the interstellar medium. Even particles generated by the interaction of primaries with terrestrial atmosphere are called secondaries.

About 99% of primary cosmic rays is formed by protons, α particles and other nuclei, whereas the remaining 1% includes electrons, γ and antimatter. Considering the first group, protons represent about 79% of the primary nucleons, α 15% and nuclei 6%. The latter can be produced directly by stellar nucleosynthesis (mainly C, N and O) or by spallation of these nuclei with the interstellar medium (mainly Li, Be and B from C and O; Sc, Ti, V, Cr and Mn from Fe). Thus, composition is an important quantity to obtain information about propagation of cosmic rays through the universe. In particular, it has been observed that the ratio of nuclei obtained by spallation to the ones generated by nucleosynthesis get smaller as energy rises up, indicating that life time of cosmic rays in our galaxy decreases with energy.

The quantity that give us important information on propagation and, furthermore, on acceleration mechanisms is the *differential flux* F, defined as the number of particles crossing a surface normal to the direction of propagation per unit of time, area, solid angle and energy. As shown in Fig.1.1, where F is multiplied by $E^{2.6}$ in order to highlight slope changes, differential flux follows a power law

$$F(E) \propto E^{-\alpha} \tag{1.1}$$

where *differential spectral index* α assumes different values depending on the considered energy range. As we can see, it is possible to identify three main discontinuity regions: the *knee* between 10^{15} and 10^{16} eV, the *ankle* around $10^{18.5}$ eV and the rapid steepening around 5×10^{19} eV called *Greisen–Zatsepin–Kuzmin (GZK) cutoff*. In addition, another slope change, called *second knee*, has been reported around 8×10^{16} eV by the Kascade-Grande experiment [2]. This change in the value of α indicates that cosmic rays belonging to the same energy region have the same acceleration and/or propagation mechanism and, conversely, that this mechanism is different from the one responsible for acceleration and/or propagation in the other regions. It is thus possible to develop models that, assuming some acceleration and propagation mechanisms in each energy range, are able to reproduce the observed differential flux.

So far, three main astrophysical sources have been identified as candidates for the acceleration of high energy cosmic rays (E $> 10^{12}$ eV): plasma clouds in interstellar medium, shock waves in supernovae remnants and active galactic nuclei. In the first two cases acceleration is performed through the so called *Fermi mechanism* [3]. This model employs statistical acceleration, *i.e.* energy gain by a particle through several consecutive interactions, being electromagnetic field intensity not enough to generate direct acceleration up to the observed energies. Fermi mechanism is of the 2nd order (Type I) in the case of plasma clouds and of the 1st order (Type II) in the case of shock waves. The reason of the success of this model is that it is able to reproduce the power law observed in the energy flux, but, on the other side, it can not explains the presence of ultra high energy cosmic rays (E $> 10^{18}$ eV). Because there are no astrophysical sources inside our galaxy able to accelerate ultra high energy cosmic rays (UHECRs), the latter must acquire their energy through some exotic extra-galactic sources like active galactic nuclei (AGN).

As we can see from Fig.1.1, differential flux dramatically decreases as energy rises up. For example, we expect an integral flux of 1 $particle/m^2\,s$ at 10^{11} eV, 1 $particle/m^2\,y$ at 10^{15} eV and 1 $particle/km^2\,y$ at 10^{18} eV. It is therefore natural to interpret this feature as a progressive power off of low energy acceleration mechanisms. Two main models have been proposed: *mixed composition model* and *proton composition model*. In the first one, the ankle is the transition region between galactic and extra-galactic sources, while the knee corresponds to the energy where most of cosmic accelerators present in our galaxy have reached an upper limit. In the second one, the knee separates galactic from extra-galactic

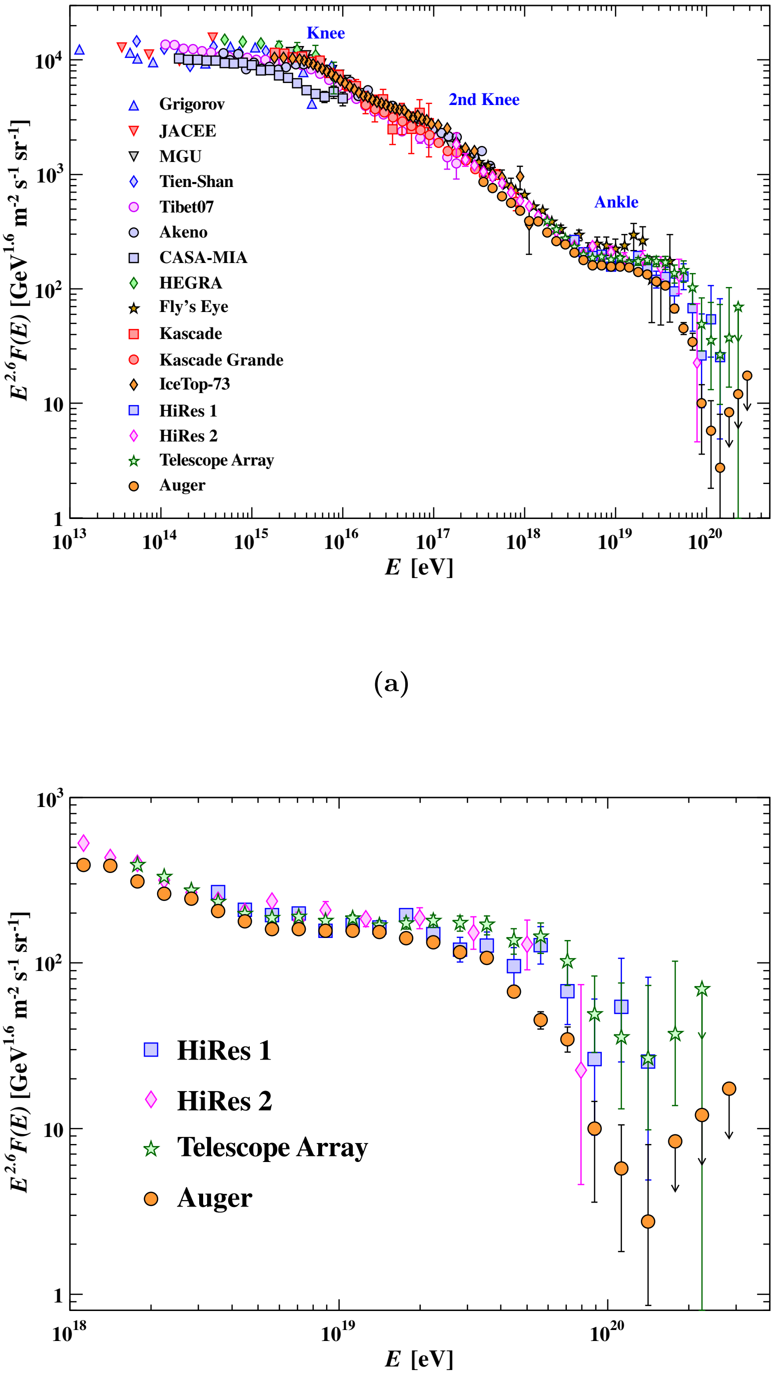

(a)

(b)

Figure 1.1: Cosmic rays differential flux as measured by several experiments [1]. The vertical scale is multiplied by $E^{2.6}$ in order to highlight slope changes. (a) shows the flux of high energy cosmic rays and (b) a zoom in the energy region where GZK cutoff is expected.

cosmic rays and the ankle corresponds to the threshold energy for the following interaction of protons with cosmic microwave background radiation (CMBR)

$$\gamma + p \longrightarrow e^- + e^+ + p$$

This dip structure in the ankle region has been cited as a robust indication that UHECRs are mainly formed by extra-galactic protons, whereas the contribution of other nuclei is negligible. This is a very important point, because it indicates that composition measurements of UHECRs can help us to understand which of the two models works better. Unfortunately, different experimental observations are not consistent each other on UHECRs composition: HiRes [4] indicating only protons and α above 10^{19} eV and Auger [5] [6] leading to a composition getting lighter up to 2×10^{18} eV and heavier above 3×10^{19}.

Another point for which composition measurements are helpful is the expected GZK cutoff around 5×10^{19} eV. This is the threshold energy of another proton-CMBR interaction

$$\gamma + p \longrightarrow \pi^0 + p$$

Because proton mean free path due to this interaction (~ 3 Mpc) is much smaller than intergalactic distances ($\sim 10 - 100$ Mpc), most of ultra high energy protons should interact before reaching Earth. If we assume that most of UHECRs are formed by extra-galactic protons we expect a cutoff at this energy. Anyway this cutoff can be reproduced also by the mixed composition model as a consequence of photo-dissociation. Carrying out measurements in this region is not easy because expected flux is 1 $particle/km^2\,century$. After the first results by the AGASA experiment were not able to see it, GZK cutoff has been confirmed by HiRes [7], Auger [8] and TA [9].

1.2 Detection of cosmic rays

When a primary cosmic ray reaches the Earth, it interacts with the atmosphere producing a so called extensive air shower (EAS). This shower is composed of a very high number of secondary cosmic rays, a part of which finally gets to the sea level. Because of this feature, two main detection technique are possible: *direct detection*, performed by the use of stratospheric balloons or space satellites in orbit around Earth, or *indirect detection*, realized employing large detector arrays on terrestrial surface.

Direct detection is characterized by high accuracy due to the possibility of direct measurements, but it is not useful for UHECRs because differential flux is too small at their typical energy. A large acceptance and/or long data taking campaigns will therefore be needed, but this is not achievable due to strong limitations on mass, volume and lifetime of payload. So far, stratospheric balloons (ATIC [10], CREAM [11]) and space satellite (PAMELA [12], AMS-02 [13], CALET [14], DAMPE [15]) experiments have been designed in order to perform measurements of cosmic rays below approximately 10^{12} eV for electrons and positrons and 10^{14} eV for protons and nuclei. Regarding satellite experiments, the main detector of the experimental apparatus was a *magnetic spectrometer* in the case of the former experiments (PAMELA, AMS-02) and an *electromagnetic calorimeter* in the latest ones (CALET, DAMPE). The main reason for this evolution is an improved resolution at high energy, because in the case of spectrometers $\sigma_E/E \propto E$, whereas in the case of calorimeters $\sigma_E/E \propto 1/\sqrt{E}$. In addition, differently from spectrometers, calorimeters do not have strong constraints on the geometry, that can be therefore optimized to maximize acceptance: new solutions are currently under study by several projects (CALOCUBE [16], HERD [17]). Even considering possible improvements in energy resolutions and geometric acceptance, at present it seems not feasible to extend direct detection of cosmic rays to energies above 10^{15} eV. In order to study UHECRs indirect detection is thus mandatory.

Indirect detection is performed collecting information coming from different components of the EAS initiated by the primary cosmic ray. After the first hadronic collision, the shower develops in the atmosphere through successive interactions. In particular, aside of the original hadronic component, γ originating mainly from π^0 decay gives rise to an electromagnetic one. When maximum development is reached, about 90% of the energy of the primary particle goes into the electromagnetic part, which deposits almost all its energy in the atmosphere, whereas the remaining 10% belongs to the hadronic part, that is indirectly detectable at the sea level through muons resulting from hadrons decays (mainly πs and Ks) [18]. Among particles reaching the sea level, muons are by far the most abundant with a vertical integrated flux of about 70 $m^{-2}s^{-1}sr^{-1}$ above 1 GeV/c, whereas the one of $e^+ + e^-$ is 30, 6, and 0.2 $m^{-2}s^{-1}sr^{-1}$ above 10, 100, and 1000 MeV respectively [1].

Three main detection techniques are commonly used to retrieve information on the EAS: *surface detection*, *Cherenkov light detection* and *fluorescence light detection*. Surface detectors are sensitive to particles reaching the sea level, mainly muons and, rarely, electrons, positrons and γ, even if the relative abundances of detected secondaries depends on the azimuthal angle of the shower, on the altitude where the maximum development is reached and on the experimental design of the detector. Cherenkov light detectors exploit photons emitted by charged particles traveling in the atmosphere with a velocity greater than the speed of light in it, so that, in principle, they give us information on both the electromagnetic and the hadronic component, but, because the number of electrons/positrons is much higher than the one of charged hadrons, the contribution of the electromagnetic component to the emission of Cherenkov photons is dominant. Fluorescence light detectors are sensitive to both electromagnetic and hadronic component, being fluorescence photons emitted by the disexcitation of atmospheric N_2 molecules previously excited by charged particles. Multiplicity in the electromagnetic component of the EAS is intense enough to give a high photon signal for both techniques.

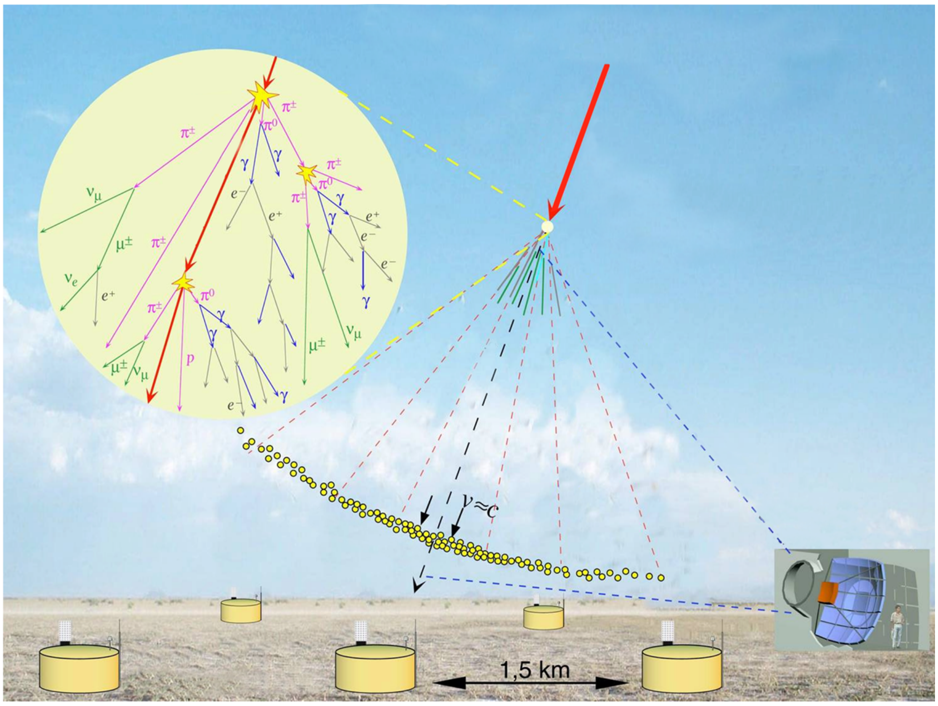

Figure 1.2: Schematic view of the Pierre Auger Observatory. On the right, one of the fluorescence detector, made up by a mirror that collects the incoming photons on a photomultipliers array. On the left, 5 surface detectors, formed by water tanks in which Cherenkov light is generated by incoming muons.

However, Cherenkov effect gives rise to a narrow light cone along the direction of the particle, whereas fluorescence effect generates an isotropic emission. This last detection technique is therefore more suitable for the reconstruction of the EAS evolution in the atmosphere, that can be performed with big photomultipliers apparatus, each of them facing a different region of the sky, together with proper time correlation between detected signals. On the other side, the Cherenkov technique is more able to reject the background due to cosmic γ from the signal of photons actually originated in the EAS. Apart from this difference, a common drawback of both methods is that they are very sensitive to light background, so that they require operation only in cloudless moonless nights. Ground-based experiments combine at least two of these three different techniques through a very large number of detectors on a very wide area.

Fig.1.2 shows a schematic view of the Pierre Auger Observatory [19] that is the largest ground-based experiment currently operating. Fluorescence detectors (FD) are divided in 27 telescopes made up by photomultipliers arrays for a total of 5 fluorescence station. Water-Cherenkov surface detectors (SD) arranged in hexagonal grids are divided into two groups: 1600 water tanks, 1.5 km spacing, on a $\sim$ 3000 km^2 and, nested within it, 71 water tanks, 750 m spacing, on a

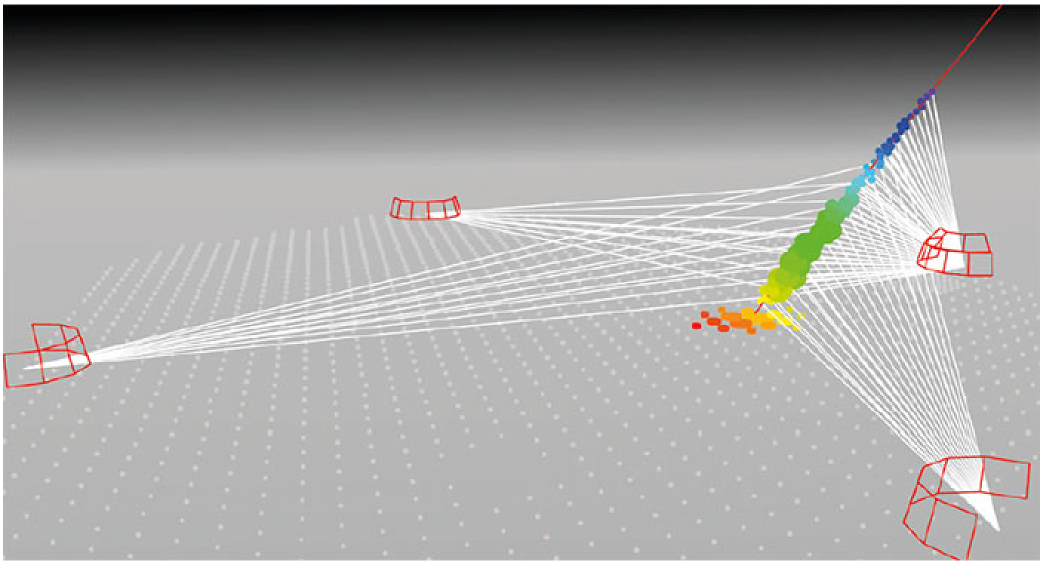

Figure 1.3: Illustration of the principle of stereoscopic reconstruction of the longitudinal profile making use of four fluorescence light detectors.

$\sim 27\ km^2$ area. Telescope array [20] experiment has a similar apparatus. The very wide area covered by these observatories ($\sim 3000\ km^2$ for Auger and $\sim 762\ km^2$ for TA) makes it possible to face the very small differential flux of the UHECRs, considering in addition that, differently from satellite experiments, ground-based experiments do not have limitation on operation lifetime. The main drawback of indirect detection is the large uncertainty coming from two different contribution: strong statistical fluctuation in the EASs and, most of all, systematic effects present in the hadronic interaction models used for data analysis. In order to understand better this last point, we must consider how important information related to the primary cosmic ray are extracted from the corresponding EAS. These information are basically two: energy and composition.

Energy can be measured in several ways, combining measurements from different detectors and using different kinds of parametrization: in order to obtain such relations between EASs observable parameters and energy of the primary particle, hadronic interaction models are necessary. For example, in the case of Auger experiment, both FD and SD can be used for energy reconstruction. As illustrated in Fig.1.3, in the case of fluorescence detectors the energy of the primary cosmic ray is obtained considering the release in each region of the sky seen by the FD, weighting it for the expected fluorescence efficiency at that depth, reconstructing the longitudinal profile, fitting it using the Gaisser-Hillas function and finally using this function to estimate the total deposit in the atmosphere [21]. However, being duty cycle $\sim 13\%$ and almost 100% for FD and SD respectively, in most events the energy is reconstructed using surface detectors. Two main analysis techniques are used for this purpose depending on the EAS zenith angle θ of the EAS [22].

For vertical events ($\theta < 60°$), the lateral distribution observed at ground at an optimal distance from the shower maximum is correlated to the energy of the primary particle. For inclined events ($62° < \theta < 80°$), energy is inferred from the relative muon content at ground compared to the one predicted by the simulations for a 10^{19} eV proton primary. The calibration of the energy scale of the SD is performed exploiting the one reconstructed by the FD for the events that independently triggered both telescopes.

Even if energy reconstruction requires hadronic interaction models, their effect on the final uncertainty is not as large as in the case of composition measurements. Among several methods proposed for this purpose, two of them are considered here, both employed by Auger. The first method [23] is based on the information given by the FD on the depth X_{max}, representing the distance between the point where the cosmic ray enters the atmosphere and the one where the EAS reaches its maximum development. Comparing the measured mean value and RMS of X_{max} as a function of energy with hadronic interaction models predictions in the case of proton and iron primaries, it is possible to estimate how much heavy the composition is. The second method [24] exploits the study of the evolution of the hadronic component of the EAS, whose longitudinal profile depends on the nature of the primary particle. Such kind of information can be obtained using the muon signal detected by the SD that, with proper time correlation, can be associated to different points of the evolution of the shower measured by the FD. Fig.1.4 shows Auger data compared to predictions by QGSJET II-04, EPOS-LHC and SIBYLL 2.1 models. Using the first method, the mean value and the RMS of X_{max}, expressed as a length per unit of atmosphere density, were obtained. These results are compared with the mean value of X^{μ}_{max}, the depth where the muon component reaches its maximum development, obtained using the second method. Is is evident that, despite the two models lead to similar conclusions in the former case, they provide very different predictions in the latter one: in particular EPOS-LHC is predicting a composition higher than iron, that is clearly unlikely. This discrepancy is originating from a limited understanding of the baryonic component in the EAS and, being this point very important in cosmic rays physics, we would like to discuss it in a separate paragraph.

1.3 The baryon component in EAS

Several ground-based experiments observed an issue in hadronic interaction models related to an inconsistency between the longitudinal profile measured by FD and muon signal at ground obtained by SD. This is shown in Fig.1.5, which depicts an event detected by Auger together with another one simulated making use of QGSJet II-03[1] [25] . Among different events present in the simulation sample, it was chosen the one that resulted to have the longitudinal profile more similar to

---

[1] Conclusions are similar for other hadronic interaction models

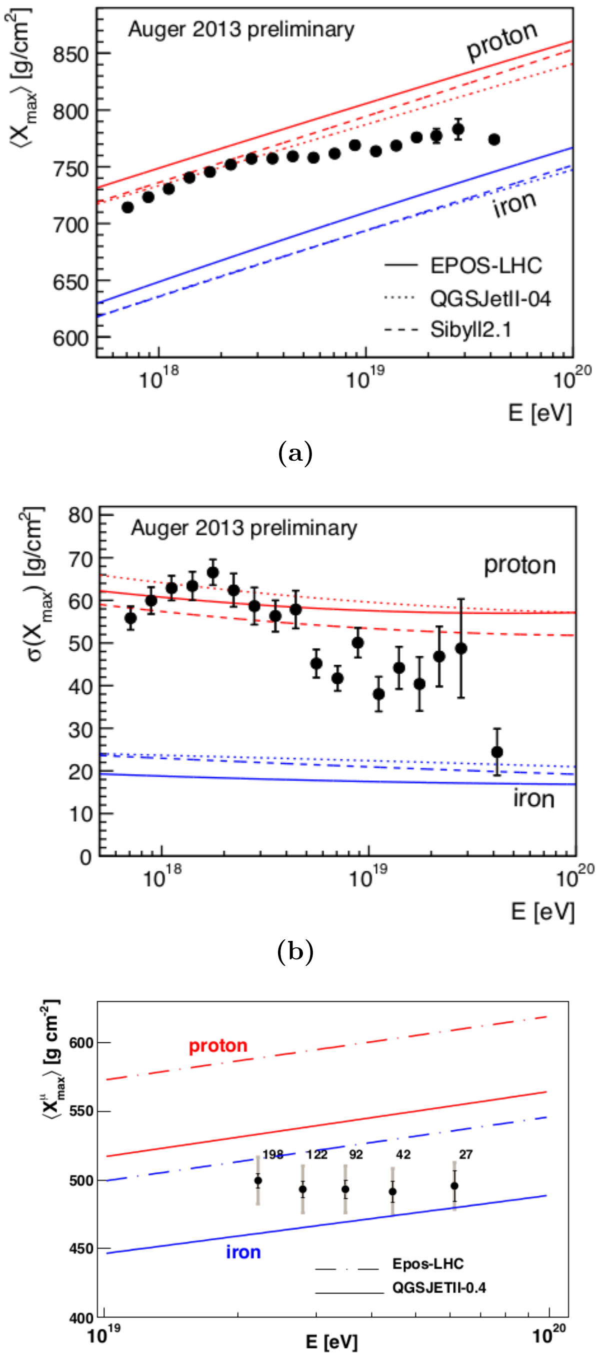

(a)

(b)

(c)

Figure 1.4: Auger longitudinal profile compared to QGSJET II-04, EPOS-LHC and SIBYLL 2.1 models. The mean value (a) and RMS (b) of X_{max} [23]. (c) The mean value of X^{μ}_{max} [24]. The longitudinal depth is reported as a length per unit of atmospheric density.

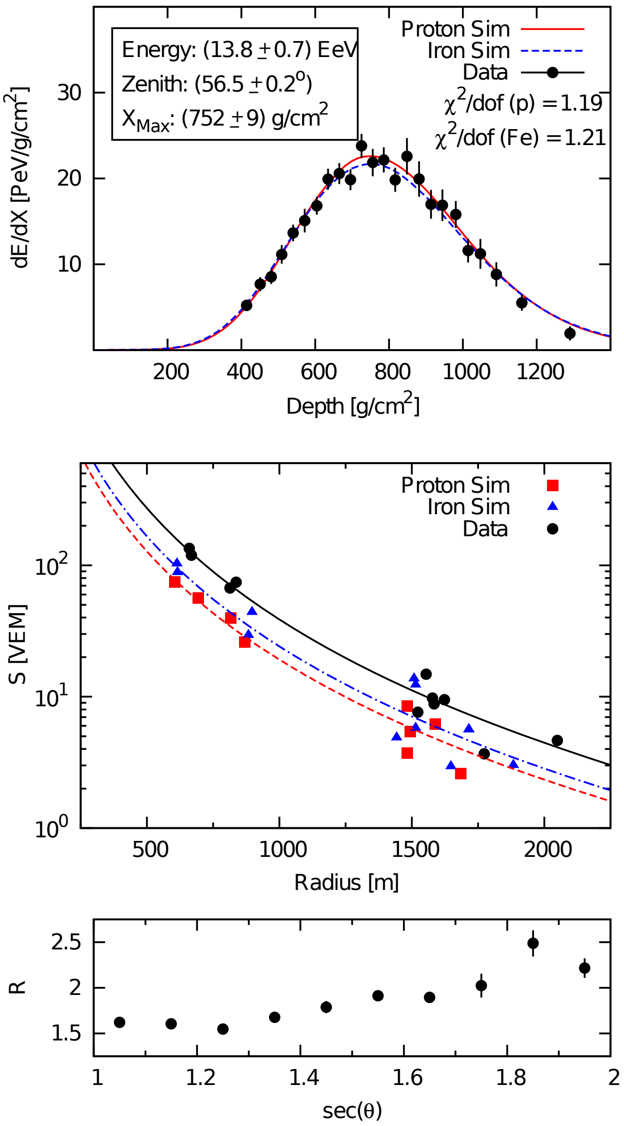

Figure 1.5: An EAS event observed by Auger [24]. (a) The longitudinal profile observed by FD compared to the event simulated using GQSJet II-03 for which we have the best agreement. (b) The observed signal in the SD at the ground level as a function of the radius from the core for the same event. Unit of ground signal is vertical equivalent muon (VEM). (c) The ratio of experimental data over model prediction for the signal in SD, as a function of the secant of the zenith angle.

the event detected, according to $\chi^2/ndof$. Having matched the two events using the longitudinal profile, the lateral distribution at the ground level is different in the two cases and, moreover, the signal expected by simulations is systematically smaller than the observed one. Because this discrepancy increases with zenith angle, where the muon signal at the ground level increases, this mean that simulations do not properly reproduce the hadronic component from which muons come. In addition, a large variation of this component is found when comparing different models.

An important point that we should keep in mind when dealing with hadronic interaction models is that among them there is a large difference in the expected number of muons at the ground level N_μ (up to a factor 2), whereas there is only a 10% change in the expected depth X_{max} where EAS reaches its maximum development [18]. This situation is due to the fact that X_{max} depends basically on the electromagnetic component, whose properties are well known, whereas N_μ is directly related to the hadron component, on which we lack of experimental measurements at high energy. It was suggested that the dependence of N_μ from the hadronic component is very strong and actually does not involves all hadrons but mainly baryons (and antibaryons) [18]. In order to understand this point, we need to extend the simplified model that describes the evolution of an electromagnetic shower (Heitler model) to the EAS case [26]. In this extension, each charged hadron having energy E will produce N_{tot} particles of energy E/N_{tot} at each interaction. Among these N_{tot} particles, N_{em} will give rise to an electromagnetic shower, whereas the other ones will undergo hadronic interactions. This evolution will then continue according to this scheme until charged particles reach a characteristic energy E_{dec} where they decay into muons. In a very simple version that consider only pions, N_{em} is the number of π^0 and $N_{tot} - N_{em}$ the number of $\pi^+ + \pi^-$. If we consider a primary energy E_0 the number of muons after n generations is

$$N_\mu = (N_{tot} - N_{em})^n = \left(\frac{E_0}{E_{dec}}\right)^{1+\frac{lnR}{lnN_{tot}}} \tag{1.2}$$

where $R = (N_{tot} - N_{em})/N_{tot}$ is generally chosen as 2/3 in the pion case. If we now extend this model to all hadrons, R will depend on the the individual hadrons yields and, because $R < 1$ and $N_{tot} \gg 1$, a small change in R will strongly affect N_μ. It has been observed that the number of baryons at a given generation has a large impact on the value of R and therefore on the hadronic component fraction in the next generation. In order to understand this point we need to consider how much different is R in the case of p-Air and π-Air interactions. This is shown in Fig.1.6, where we can see the dependence of this quantity on the energy fraction x_E of the hadron. Where produced particles contribute most to the shower development (high x_E), R is quite different between protons and pions because of the leading baryon effect. Thus, if a model predicts a higher multiplicity of baryons at the very beginning of EAS development, it will lead to a larger value of R in the next generation. This means that more energy goes into the

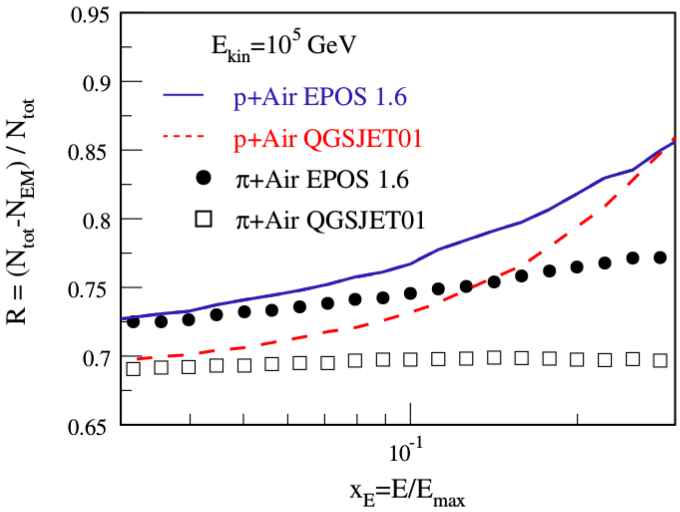

Figure 1.6: The factor R versus the energy fraction for p-Air and π-Air interaction at 10^{15} GeV: data were obtained using EPOS 1.6 and QGSJET01 models [18].

hadronic, and especially baryonic, component. In addition, this increased number of baryons at a given generation will enhance p-Air respect to π-Air interactions in the next one, leading to an even higher value of R. A very small change in the number of baryons produced in the early stages of EAS evolution can therefore lead to a strong change in the amount of its hadronic component and, finally, in the number of muons reaching the sea level. In order to tune models for this effect, experimental measurements related to baryons produced in the very forward region in p-nuclei collisions are necessary.

1.4 Hadronic interaction models

The main contribution to the development of EASs is coming from particles emitted in the very forward region after the first inelastic interaction. These particles are produced in soft QCD processes, *i.e.* interactions where momentum transfer Q^2 is very small ($Q^2 \lesssim 1$ GeV). In this case the coupling constant diverges, therefore it is not possible to develop a perturbative theory as in the case of hard QCD processes. Soft QCD interactions are indeed described by phenomenological models based on *Gribov-Regge theory* (GRT) [27, 28]. In this theory, multiple particles scattering occurs via parallel elementary interactions, treated as the exchange of phenomenological objects called Pomerons. A drawback of GRT is that cross sections and particles production are not calculated consistently, because energy sharing between the individual Pomerons is considered in the computation for particles production, but not for cross sections. This problem is overcome in *Parton Model*, used to describe hard interactions, where the inclusive cross section

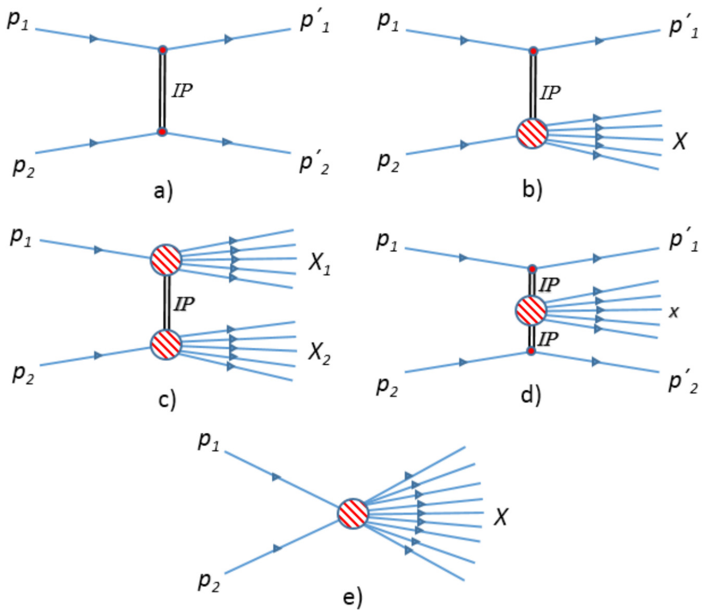

Figure 1.7: Schematic diagram of different event categories: a) elastic scattering; b-d) diffractive processes, respectively single, double and central diffractive; e) non diffractive scattering.

is calculated from the convolution of an elementary cross section with the parton distribution functions. However, the parton model is not able to compute exclusive parton level cross sections without arbitrary assumptions. In order to solve both problems, *Parton-based GRT* [29] has been proposed. In this last model, Pomerons are exchanged at a parton level (instead of at a hadron level like in GRT), cross sections and particles productions are treated consistently, hard processes are introduced in a natural way and it is possible to deal with exclusive cross sections.

Hadronic interaction models must be able to explain a large number of different interactions, that are generally treated separately inside the model formalism. The different event categories are summarized in Fig.1.7, where they are classified according to the final state. An event is called *elastic* if the particles in the final state are the same present in the initial state and *inelastic* otherwise. An inelastic event is *diffractive* if no exchange of color charge occurs: as a result we can have the dissociation of only one of the initial particles (single diffraction), of both of them (double diffraction) or no dissociation in the case of double Pomeron exchange (central diffraction). In both elastic and diffractive events the final states are well spatially separated, forming the so call *rapidity gaps* originated by Pomeron exchanges. Inelastic *non-diffractive* events are characterized by the exchange of color charge that leads to higher energy transfer, larger number of products and absence of rapidity gaps. It is important to note that in hadronic interaction models the implementation of inelastic processes is generally performed separately for diffractive and non-diffractive events.

The most common hadronic interaction models used in ground-based cosmic rays experiments are: EPOS-LHC [30,31] built on Parton-based GRT; QGSJET II-04 [32,33], developed in a standard GRT framework with a complex resummation scheme to take into account non-linear effect at high energies; SIBYLL 2.1 [34] and DPMJET 3-0.4 [35,36], based on Dual Parton Model, in which soft interactions are treated using GRT and hard ones using perturbative QCD; PYTHIA 8.2 [37,38], built on Parton Model. We should remark here that, even if two models are based on the same theory, their prediction can be very different. This happens because each model has a different approach for the computation of cross sections and particles spectra and, in addition, for the treatment of experimental calibration data. Another point we have to consider is that we lack of experimental measurements at high energy (comparable with UHECRs). Thus, models can not be tuned directly in this region, but some scaling hypothesis must be applied to low energy calibration data in order to extrapolate cross sections and particles spectra to high energy, possibly resulting in a large systematic uncertainty.

In order to tune hadronic interaction models for being used by ground-based cosmic rays experiments, high energy measurements are necessary. These measurements must focus on those parameters able to explain what can be considered the main feature of a EAS, *i.e.* the mechanisms that allows energy transfer from the hadronic channel to the electromagnetic and muonic components. Because of this reason, understanding the production rate and the energy fraction of each kind of particle along the shower core has a particular importance for the solution of the problem. Aside of secondary production spectra in the very forward region, we can identify three other key parameters in the evolution of EASs [26]: *inelastic cross section* σ_{inel}, *multiplicity* m and *inelasticity* k. The inelasticity is defined in such a way that $1 - k$, or elasticity, is the fraction of primary energy carried by the forward leading baryon, so that k is the one spent to generate all remaining secondaries. The importance of these parameters can be understood if we think that small values of σ_{inel}, m and k will result in deep penetrating showers, whereas large values in rapid development ones. This is highlighted in Fig.1.8, showing the mean value and RMS of X_{max} for EASs simulated using SIBYLL 2.1 and corresponding to $10^{19.5}$ eV proton and iron primaries. In order to understand the meaning of the quantity f_{19} we have to consider that, in the case of UHECRs, all values of σ_{inel}, m and k[2] must be extrapolated to high energy from measurements below 10^{15} eV obtained at accelerator facilities. Assuming that the relative extrapolation uncertainty is f_{19} at 10^{19} eV, we can extend it to other energy above 10^{15} eV using a logarithmic relation. Saying it simply, if in the evolution of the shower we consider a particle of energy E:

- if $E < 10^{15}$ eV we use experimental values at the energy E

---

[2] In Fig.1.8 it is also shown the *charge ratio* c, defined as the fraction of π^0 relative to the total number of pions produced in the interaction, but, as we can see, the results are almost independent from this parameter.

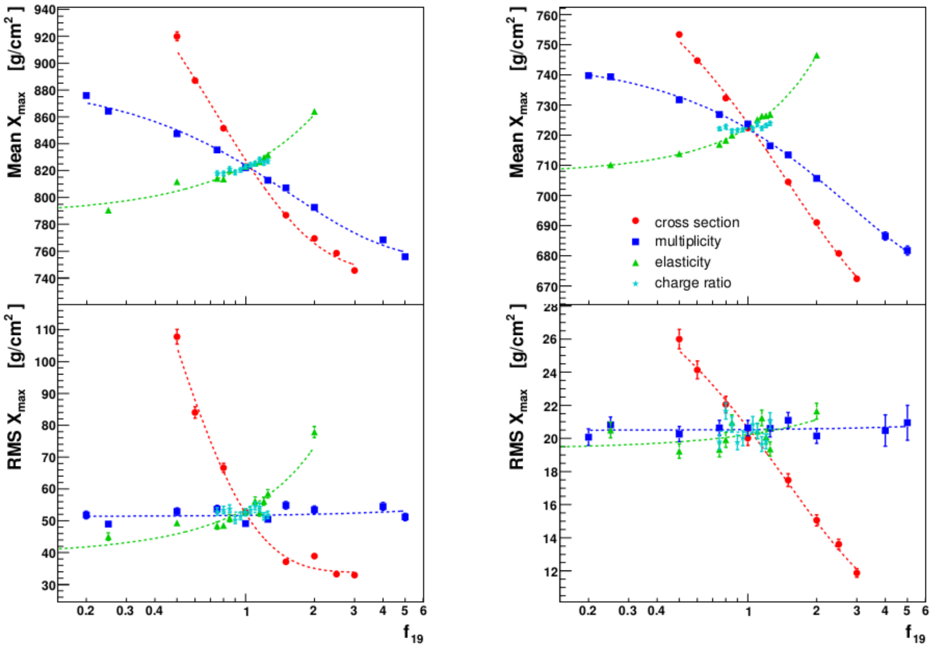

Figure 1.8: The mean value (top) and RMS (bottom) of X_{max} for EASs simulated using SIBYLL 2.1 and corresponding to $10^{19.5}$ eV proton (left) and iron (right) primaries [26]. The figures show the change in these quantities generated by an artificial shift in one of the four parameters considered.

- if $E > 10^{15}$ eV extrapolated value are modified according to the level of uncertainty expected at 10^{19} eV:
  - $f_{19} = 1$ means that we use extrapolated values at the energy E
  - $f_{19} \neq 1$ means that we artificially shift that extrapolated value by a factor $1 + (f_{19} - 1)(log(E[10^{15}eV])/4)$.

As we can see. an increase of the extrapolated value by a positive uncertainty ($f_{19} > 1$) in any of the three parameters considered results in a decrease of mean value and RMS of X_{max}, except for m that exhibits this behavior for the first quantity, but not for the second one that is apparently independent from it. The parameter having the largest impact on X_{max} is σ_{inel}, changing the mean value (and the RMS) up to ~ 100 g/cm^2 (~ 60 g/cm^2) for proton and ~ 40 g/cm^2 (~ 10 g/cm^2) for iron primaries. High energy measurements of σ_{inel}, m and k are therefore very important to reduce the extrapolation error at the typical energy of UHECRs, that, in turn, helps to distinguish in a more reliable way between proton and iron primaries.

Chapter 2

The LHCf experiment

After a brief introduction about the physics motivation of the LHCf experiment, we can now discuss the details of the experiment itself. In this chapter we describe the Large Hadron Collider, forward physics measurements at LHC and the LHCf experiment.

2.1 The Large Hadron Collider

The Large Hadron Collider (LHC) [39], the highest energy collider in the world, was designed as a proton-proton or ion-ion collider able to reach $\sqrt{s} = 14\ TeV$. It is part of the CERN (*Conseil européen pour la recherche nucléaire*) accelerators system, located near the border between Switzerland and France. The collider is a 26.7 km circular ring placed inside a tunnel located $50 - 175\ m$ underground that was formerly used to house the Large Electron Positron Collider (LEP) [40]. LEP operated between 1989 and 2000 when it was dismantled to make room for the construction of LHC. The maximum achievable energy in LEP ($\sqrt{s} = 209$ GeV) was strongly limited by the energy loss due to synchrotron radiation, whose power is proportional to γ^4 where γ is the Lorentz factor. This effect is much smaller for a p-p than for a e^+-e^- collider because, being $m_p \sim 2000\ m_e$, protons are much less relativistic than electrons at the same energy. The highest energy achievable at the LHC is instead limited by the most intense magnetic fields nowadays available, necessary to maintain high energy particles in the same circular ring. Making use of the latest technology in superconducting magnets, LHC has 1232 dipole magnets working up to 8.3 T, corresponding to a maximum beam energy of $\sqrt{s} = 14\ TeV$. They are designed using a 2-in-1 structure that bends at the same time the two beams circulating in opposite directions. Each beam, made by a certain number of protons or ions bunches, travels in a separate beam pipe, whereas collisions between two bunches can happen in each of the four interaction points (IPs) where they cross each other. In order to increase the probability of an interaction it is important that the transverse size of the beam at the IP is enough small. This is achieved making use of 392 quadrupoles magnets that keep beams focused, not only at the interaction point. Among quantities involved in the description of a collider two are particularly important: center of mass energy and instantaneous luminosity.

Center of mass energy settles the energy scale at which we are testing the standard model or looking for new physics. As said, the maximum energy achievable depends on the radius of the ring and on the most intense magnetic field available. In the case of the LHC, the machine is able to collide protons up to $\sqrt{s} = 14\ TeV$, $7\ TeV$ per beam. As shown in Fig.2.1, four pre-acceleration stages are present before beam injection in the Large Hadron Collider: Linac2, Proton Synchrotron Booster, Proton Synchrotron (PS), and Super Proton Synchrotron (SPS). After this last stage, $450\ GeV$ protons are injected in the LHC and then accelerated up to $7\ TeV$ making use of 16 radiofrequency cavities. Apart from protons, lead ions can also be injected in the collider, following exactly the same acceleration stages but starting from Linac3 instead of Linac2. In this case, if the machine is set to accelerate protons at an energy E_p, each nucleon in the Pb nucleus will be accelerated to an energy $E_n = E_p \times Z/A$, where Z and A are respectively the atomic and mass number of lead. In p-Pb collisions, physics is generally described in the nucleon-nucleon center of mass reference system, whose energy is denoted by $\sqrt{s_{NN}}$.

Instantaneous luminosity express the number of collisions per unit of time and inelastic cross section. The amount of statistics acquired by experiments is therefore proportional to it and having a high luminosity is especially important when we are searching for a rare process. In the case of a collider, instantaneous luminosity can be expressed as

$$L = \frac{n\ N_1\ N_2\ f\ \gamma}{4\ \pi\ \epsilon\ \beta^*} F \tag{2.1}$$

Among quantities used in this expression, the most intuitive ones are the number of colliding bunches n, the number of particles per bunch in each of the two beams N_1 and N_2, beam revolution frequency f, beam Lorentz factor γ. The emittance ϵ is a measure of the average beam spread in the position-momentum phase space, whereas β^* is the value of the betatron function at the interaction point. The betatron function at a point represents the distance from this point to the next one at which the beam is twice as wide. ϵ and β^* are related to beam spatial spread, so that reducing them increases the luminosity, but, on the other side, increases the pile-up probability as well. This last quantity represents the probability to have more than a single proton-proton interaction per bunch crossing. Finally, F is the geometric luminosity reduction factor at the IP

$$F = \left[1 + \left(\frac{\theta_{cross}\sigma_z}{2\sigma}\right)\right]^{-1/2} \tag{2.2}$$

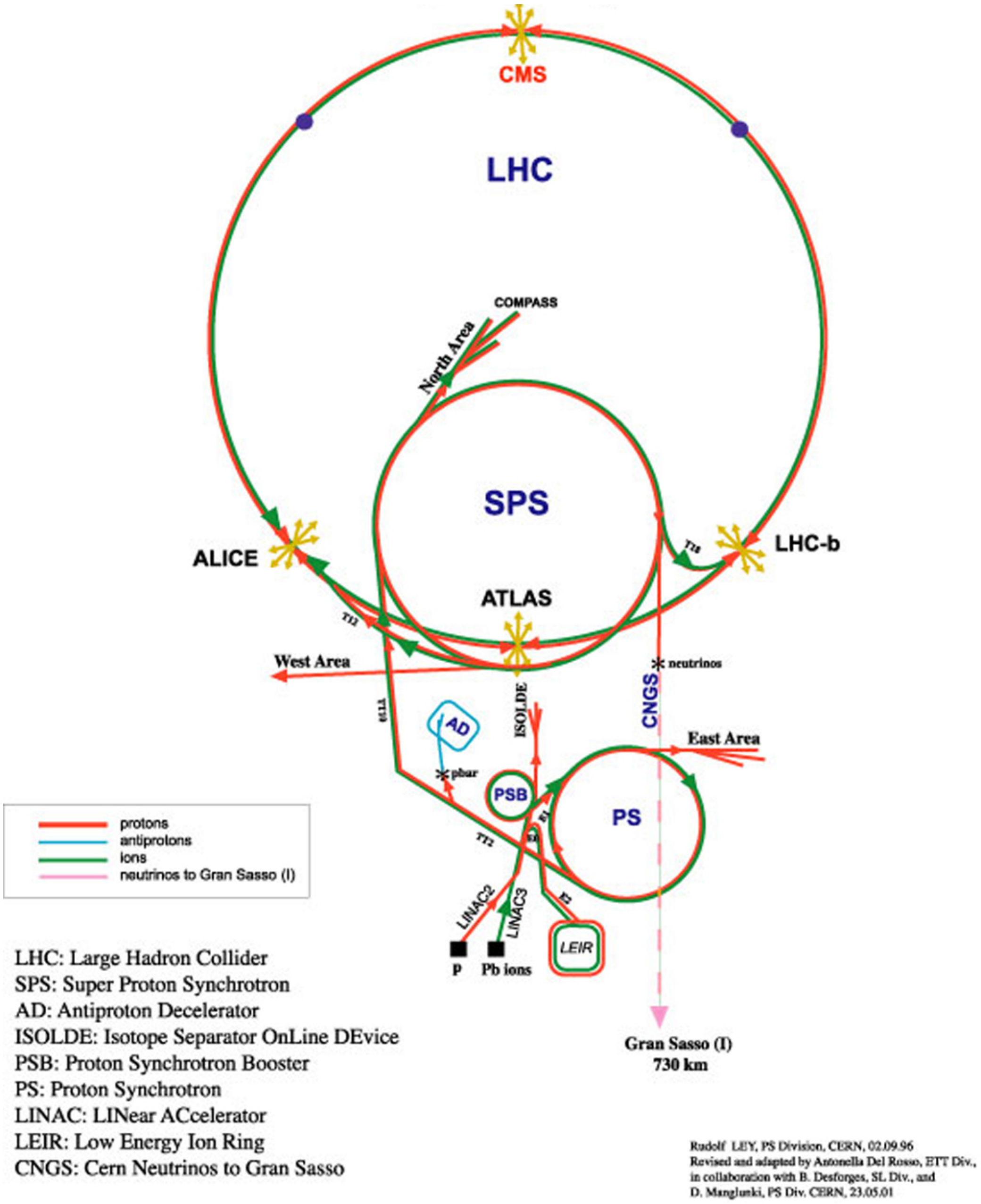

Rudolf LEY, PS Division, CERN, 02.09.96
Revised and adapted by Antonella Del Rosso, ETT Div.,
in collaboration with B. Desforges, SL Div., and
D. Manglunki, PS Div. CERN, 23.05.01

Figure 2.1: Schematic view of the CERN accelerators system from Linac2 (p) or Linac3 (Pb) to LHC. Only the four big LHC experiments are shown here.

E_{beam}	$7\ TeV$
γ	7461
L	$10^{34}\ cm^{-2}s^{-1}$
n	2808
$N_1,\ N_2$	1.15×10^{11}
f	$11.25\ kHz$
σ	$16.7\ \mu m$
σ_z	$7.55\ cm$
ϵ	$3.5 - 3.75\ \mu m\ rad$
β^*	$0.55 - 18\ m$

Table 2.1: LHC beam parameters taken from technical design report [41].

where θ_{cross} is the beam crossing angle, σ_z the bunch length and σ the transverse beam size at the interaction point. Beam crossing angle is introduced to avoid unwanted parasitic interactions away from IP, but as we can notice it has the effect of decreasing luminosity as well. All LHC design parameters are summarized in Tab.2.1.

The Large Hadron Collider has already successfully completed Run I (2009-2013), when the machine operated up to a maximum $\sqrt{s}$ = 7-8 TeV and $L = 6 \times 10^{33}\ cm^{-2}s^{-1}$. In Run II, started in 2015 and scheduled to end in 2018, the LHC will reach its designed parameters values with an energy of $13-14\ TeV$ and a luminosity of $1 \times 10^{34}\ cm^{-2}s^{-1}$. The integrated luminosity, *i.e.* the instantaneous luminosity integrated over data taking time, was about 25 fb^{-1} in Run I and it is scheduled to reach 75-100 fb^{-1} at the end of Run II. After that, several luminosity upgraded are foreseen, leading to a Run III (2020-2022) with $L = 2 \times 10^{34}\ cm^{-2}s^{-1}$ and a Run IV (after 2023, the so called High Luminosity-LHC) with $L = 5 \times 10^{34}\ cm^{-2}s^{-1}$. In the meanwhile, other projects have been proposed to study physics at energies above 14 TeV. Among them, there is the construction of a 100 km circumference collider able to reach 100 TeV, to be integrated in the CERN accelerators system (called Very Large Hadron Collider or Future Circular Collider).

2.2 Experiments at the LHC

Seven experiments are installed at the Large Hadron Collider. Each one of the four interaction points houses one of the four big experiments (ATLAS [42], ALICE [43], CMS [44], LHCb [45]). In addition, three of them share the IP with another small experiment (LHCf [46], TOTEM [47] and MoEDAL [48]). Their placement inside the LHC ring is the following: ATLAS and LHCf are installed at IP1, ALICE at IP2, CMS and TOTEM at IP5, LHCb and MoEDAL at IP8.

Physics motivations of LHC experiments cover very different research fields. ATLAS and CMS are general purpose detector that can provide essential information on various open questions in the standard model, mainly electroweak symmetry breaking, hierarchy problem, grand unification theories, supersymmetry, dark matter. ALICE and LHCb are dedicated to the study of quark-gluon plasma and CP-violation, respectively. Finally, the purpose of the three small LHC experiments are: the study of particle production spectra in the very forward region (LHCf), the measurement of elastic and inelastic cross section in high energy p-p collisions (TOTEM), the search of magnetic monopole and other highly ionizing massive particles (MoEDAL).

Experimental measurements at a hadron collider can be expressed in terms of different quantities. If we define the z axis as the one parallel to beam direction and the $x - y$ plane in such a way that it is normal to z, the properties of a particle produced in the collisions can be written in function of kinematic variables p_x, p_y and $\mathrm{p_Z}$. Another possible solution is to rewrite the three components of momentum in terms of transverse momentum $\mathrm{p_T} = \sqrt{p_x^2 + p_y^2}$, azimuthal angle $\phi = arctan(y/x)$ and scattering angle $\theta = arctan(\mathrm{p_T}/\mathrm{p_Z})$. Actually, the third variable is generally substituted with pseudorapidity η

$$\eta = \frac{1}{2} ln \left(\frac{p + p_Z}{p - p_Z} \right) = -ln \left[\left(tan \frac{\theta}{2} \right) \right] \tag{2.3}$$

where $p = \sqrt{p_T^2 + \mathrm{p_Z}^2}$. This quantity is a generalization of rapidity y

$$y = \frac{1}{2} ln \left(\frac{E + p_Z}{E - p_Z} \right) \tag{2.4}$$

to which η converges in the case $m \ll p$. The reason to prefer $\mathrm{p_T}$, y (or η), ϕ to the three component of momentum is mainly due to the fact that, under Lorentz transformations along z, $\mathrm{p_T}$ is invariant and y transforms simply . If we consider the Lorentz boost β needed to change from a reference system SR_a to another reference system SR_b, the rapidity of a particle in SR_b is linked to the one in SR_a by the simple relation $y_b = y_a + atanh(\beta)$.

2.3 Forward physics at the LHC

The LHC is the most suitable place where we can obtain important information relative to the key parameters in EASs development. This is because p-p collisions at $\sqrt{s} = 14\ TeV$ are equivalent to about $10^{17}\ eV$ in the reference frame in which one of the proton is at rest - an energy not so distant from the UHECRs typical values. Of course, no experiment can cover all parameters of interest for EASs physics alone, but combining the results obtained from different collaborations we can achieve a good understanding on air showers evolution. At the LHC, we can distinguish two main kinds of measurements useful for the calibration of hadronic interaction models: the first group is related to quantities that can be used directly in EASs simulations; the second category is relative to observables in a different phase space from the one of air showers. This distinction arises from the fact that the nature of a collider, on one side, allows to reach the highest energy we can get from an accelerator, on the other side, involves some serious limitations on the experimental apparatus in the forward region. Because of this reason, it is easier to obtain measurements in the central region, that are useful to put some constraints on models even if in a different phase space, but the price that we pay for it is exactly this, *i.e.* the fact that these observations can cover only a few percent of EASs physics, being the shower strongly focused along the original direction of the projectile. This is shown in Fig2.2, where we can see differential energy flow and multiplicity as a function of η, according to DPMJet 3-04 model. It is evident that if we want to measure production spectra of the secondary particles that contribute the most to the evolution of EASs we have to look at the pseudorapidity region above 6. Given the good performances both in energy and position resolution, LHCf is the best candidate for the measurements of secondaries production rates in the very forward region, even if three of the big experiment have zero degree calorimeters as well (ATLAS [50], ALICE [51], CMS [52]). Among other shower parameters discussed in §1.4, k can be derived from LHCf data, σ_{inel} can be measured by TOTEM, ATLAS and CMS roman pots, m is accessible in different pseudorapidity regions to the four big experiments and TOTEM. Using all this

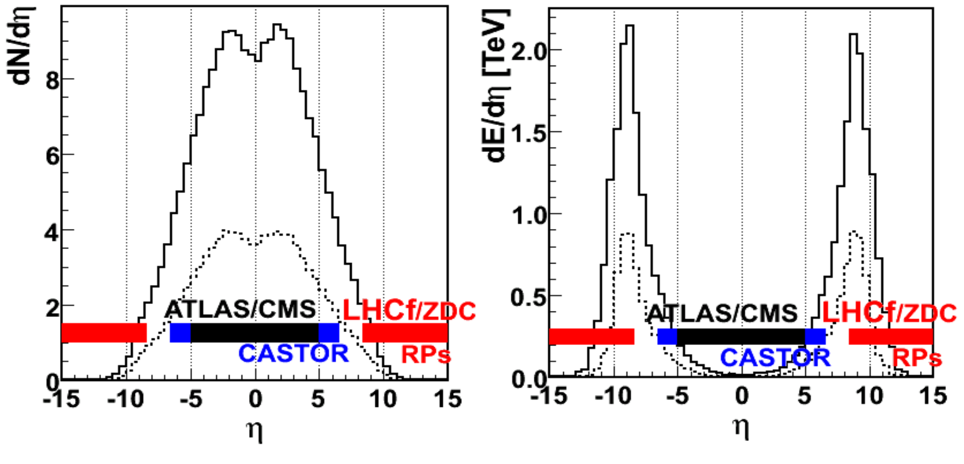

Figure 2.2: Multiplicity (left) and energy flow (right) of secondary particles produced by p-p collisions at $\sqrt{s} = 14\,TeV$ per unit of pseudorapidity as a function of η, obtained using DPMJet 3-0.4 simulations. Solid and dashed lines represent charge+neutral and neutral particles respectively. The η coverage of some LHC detectors is also shown.

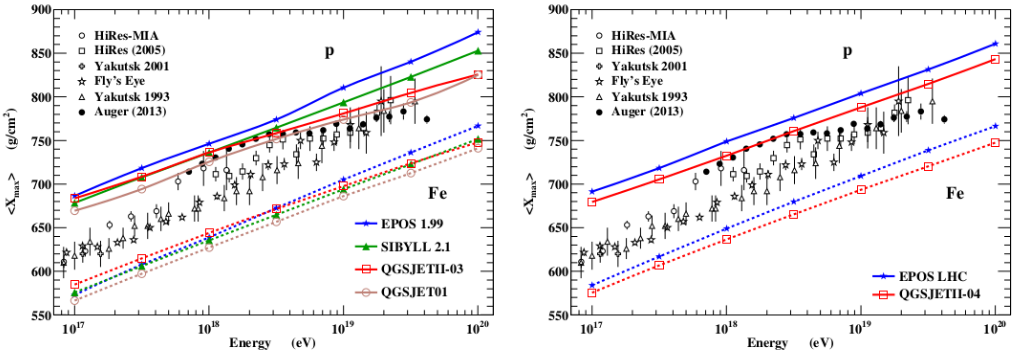

Figure 2.3: Comparison of experimental observations of $< X_{max} >$ with model predictions in the case of proton and iron primaries [49]. On the left the *pre-LHC* models (QGSJet II-03 and EPOS 1.99) and on the right the *post-LHC* models (QGSJet II-04 and EPOS-LHC).

information, model developers can tune generators in the high energy region to reproduce experimental results. The power of LHC measurements is shown in Fig.2.3, that represents the $< X_{max} >$ obtained by different ground-based cosmic rays experiments, compared to the models before (*pre-LHC*) and after (*post-LHC*) the tuning based on the LHC Run I results from the four big experiment and TOTEM. We can see a clear improvement in the agreement between EPOS-LHC and QGSJet II-04 respect to EPOS 1.99 and QGSJet II-03, that is especially evident in the region above 10^{19} eV in the hypothesis of proton primaries.

2.4 The LHC-forward experiment

In this section we describe the LHC-forward experiment (LHCf), dedicated to measurements in the very forward region that could be useful to test and tune hadronic interaction models used by ground-based cosmic rays experiments. The section is divided in four parts: in the first one we present LHCf detectors and their location in the LHC ring, in the second we illustrate the data acquisition system, in the third one we discuss about the importance of ATLAS-LHCf common operations and in the last one we describe data acquired so far and already published results.

2.4.1 The detector

The LHCf experiment [46] consists of two detectors, Arm1 and Arm2, placed on the opposite sides of IP1 in regions called TANs (Target Neutral Absorbers), at a distance of approximately ± 141.05 m (+ for Arm1, − for Arm2) from the interaction point. The schematic view of IP1 is shown in Fig.2.4 top, whereas bottom is a picture of a TAN, both taken from the outside (left) and from the inside (right). As we can see, in this region the beam vacuum chamber has a Y

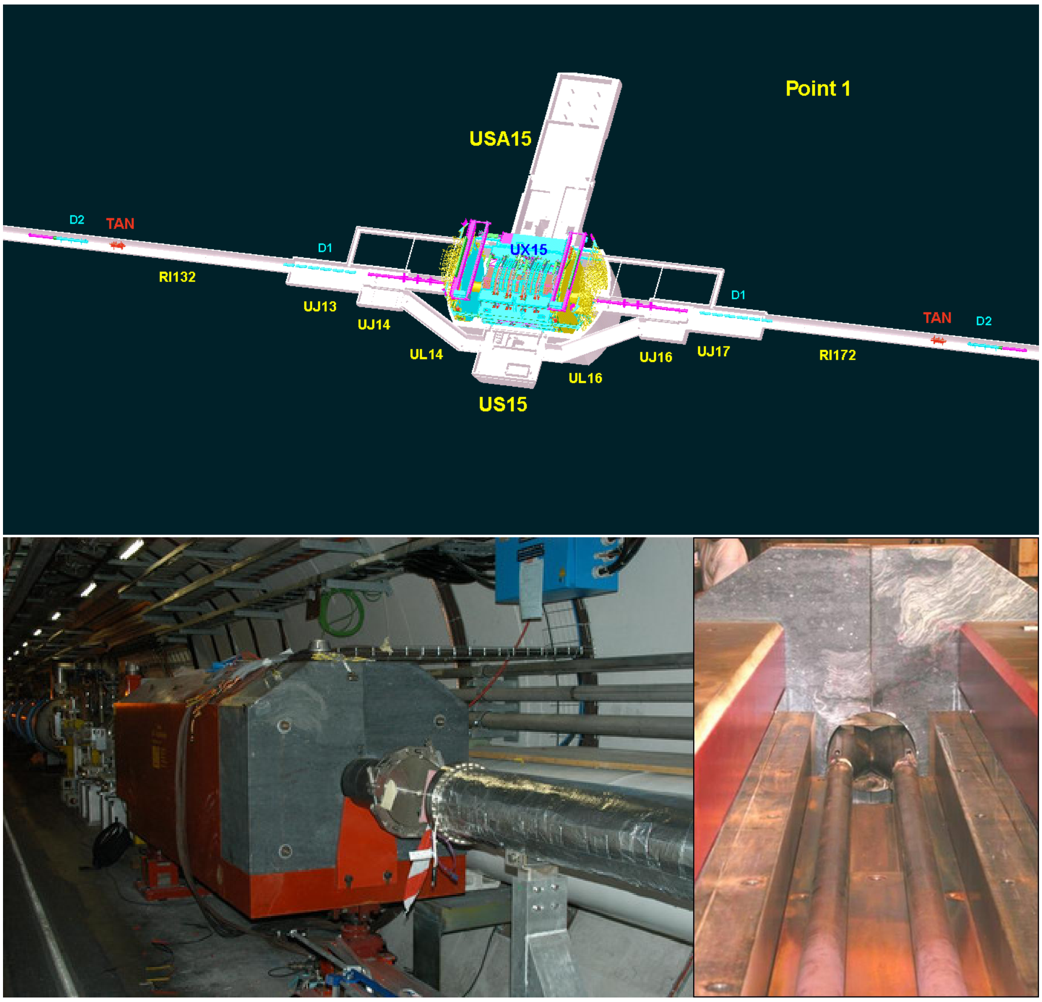

Figure 2.4: On the top schematic view of IP1 where we can see the two TAN region on the opposite side of it [46]. On the bottom a picture of the TAN region seen from the outside (left) and from the inside (right) [46]. Note the Y-shape piece where the beam pipe splits in two, in the middle of which LHCf detector is installed during operations.

shape because it changes from a single common beam tube facing the IP to two separate beam tubes joining to the arcs of LHC. In the middle of the two resulting beam pipes (one for each proton beam) the detector is placed. Because TAN is located 55 m after the dipole magnet D1 that separates the two proton beams, only neutral particles can reach LHCf. In addition, before being detected, particles have to cross the beam pipe region located at the TAN front wall, that has been carefully machined in order to have a uniform one radiation length thickness over a 100 $mm \times 100$ mm square centered on the zero degree crossing angle beamline. Detector acceptance is limited by the beam pipe shape at D1 and by the TAN slot internal walls, as shown in Fig.2.5a. Considering this, LHCf is able to cover a η range going from 8.4[1] to ∞.

Each Arm is formed by two calorimetric towers made up by 16 scintillators layers (1 mm thick) alternated to 22 W layers (7 mm thick) for a total length of about 21 cm, equivalent to 44 radiation length X_0 and 1.6 interaction length λ_I. The transverse size of the two towers, called *small tower* (ST) and *large tower* (LT), is respectively 20 $mm \times 20$ mm and 40 $mm \times 40$ mm for Arm1, 25 $mm \times 25$ mm and 32 $mm \times 32$ mm for Arm2. As we can see from Fig.2.5a not only towers dimensions, but even their positions inside detector box differ. The different geometry of the two Arms was studied in order to have independent measurements in some common η regions, but at the same time to cover the largest possible interval in η considering their different acceptance. In addition, the fact that detectors have two towers ensure a very good resolution in the indirect reconstruction of π^0 from its 2γ decay in the case each photon enters a different tower. This is important not only because π^0 is one of the most important physics item of LHCf, but also because the reconstruction of its invariant mass provides an essential information for the absolute calibration of the energy scale. Apart from energy, reconstructed using the deposit in the 16 scintillator layers, the two towers have the possibility to reconstruct transverse position as well, making use of 4 xy imaging layers placed at different depths in the calorimeter. These imaging layers are made up by 1 mm width scintillator bars in the case of Arm1 and by 0.16 mm read out pitch silicon microstrip detectors in the case of Arm2. In addition, each Arm is mounted on a manipulator, allowing us to move down the detector only in case of stable beams, otherwise keeping it in a safe region above the beam line, called *garage position*. A 3D and a schematic view of Arm2 geometry are shown in Fig.2.5b and c respectively.

We should remark here that the detector just now described has been used to acquire all data analyzed in this work, but it is not the same detector originally developed by the collaboration and employed until 2013 LHC operations. Several upgrades were necessary because in p-p collisions at $\sqrt{s} = 13$ TeV the expected energy flow was higher than in the past operations. Given the expected radiation dose of about 30 $Gray/nb^{-1}$ and the target integrated luminosity of 5 nb^{-1},

---

[1] This value refers to maximum detectable scattering angle if beam crossing angle θ_{cross} is -145 μrad, but in the case of 0 μrad the minimum detectable pseudorapidity is 8.7.

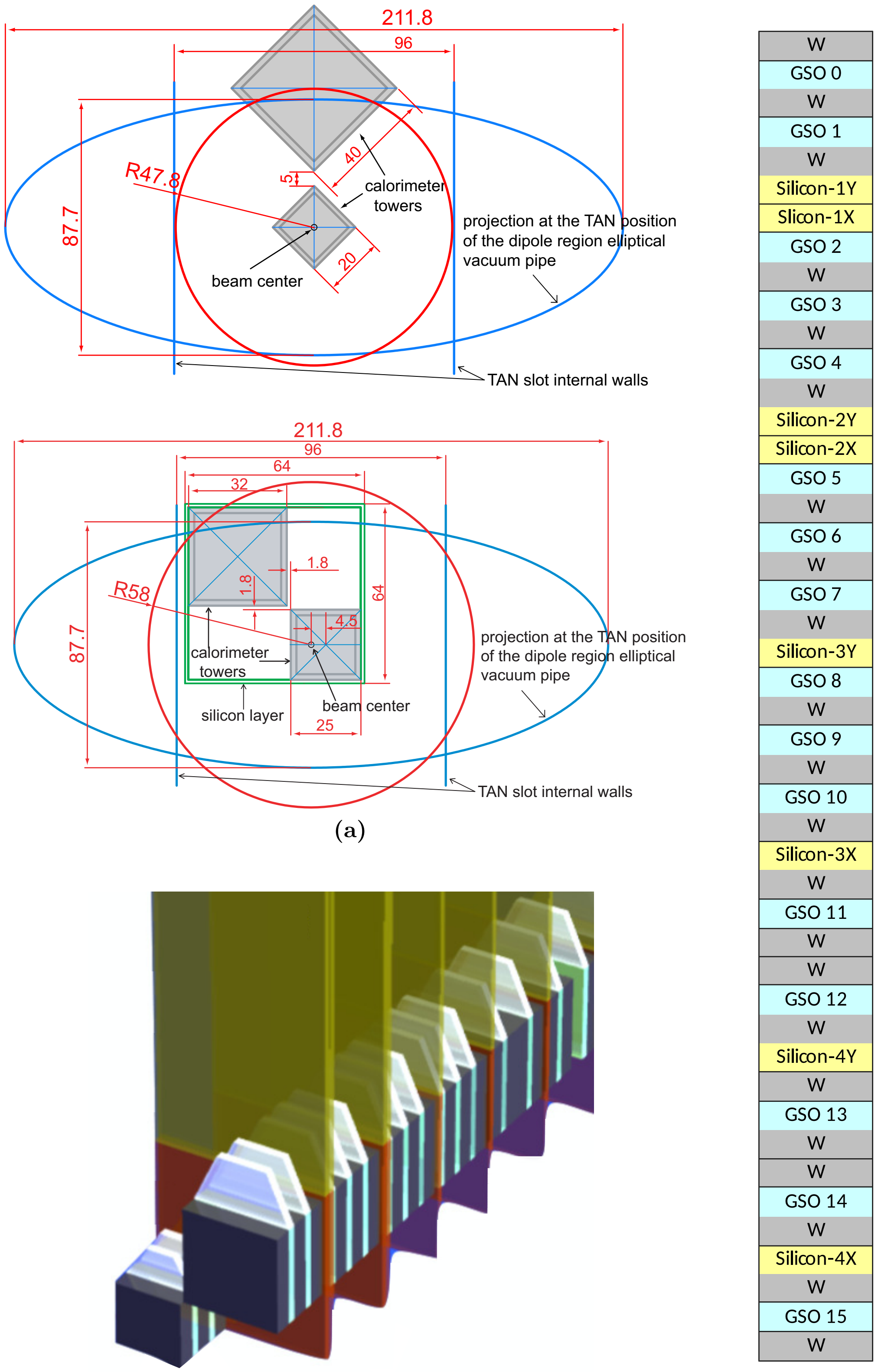

(a)

(b)

(c)

Figure 2.5: (a) Arm1 and Arm2 downstream position at TAN [46]. (b) 3D upstream view of the Arm2 detector. (c) Schematic longitudinal view of the Arm2 detector (not in scale). The geometry refers to the current detector, after the upgrade needed for 2015 LHC operations (see text).

	EJ-260	GSO
$\rho(g/cm^3)$	1.023	6.71
$\tau(ns)$	9.6	30-60
$I(NaI = 100)$	19.6	20
$\lambda(nm)$	490	430
$RH(Gray)$	100	10^6

Table 2.2: Comparison between the properties of EJ-260 and GSO scintillators. From the top to the bottom, quantities represent density, decay constant, relative light intensity, emission wavelength and radiation hardness.

scintillators should have been able to sustain a dose of 150 *Gray* without damage. As shown in Tab.2.2, the old EJ-260 plastic scintillators were clearly not able to fulfill this request, so they were replaced with Gd_2SiO_5 (GSO) scintillators that have a similar emission wavelength and light intensity, but a radiation hardness of 10^6 *Gray*. On the other side GSO has a decay constant slightly higher than EJ-260, but it is still enough fast for our purposes if all data acquisition conditions described in §2.4.2 are satisfied. Fig.2.6 top shows a picture of old and new scintillators. Another problem related to high energy deposit is the saturation of

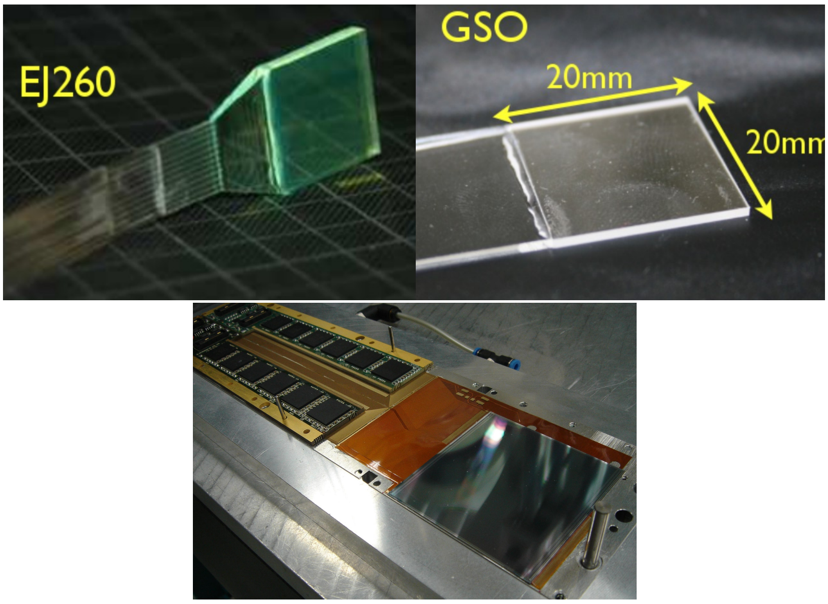

Figure 2.6: An active layer of the calorimeter obtained using the old EJ-260 and the new GSO scintillators (top) and a silicon hybrid made by a microstrip detector connected to the read-out electronics (bottom).

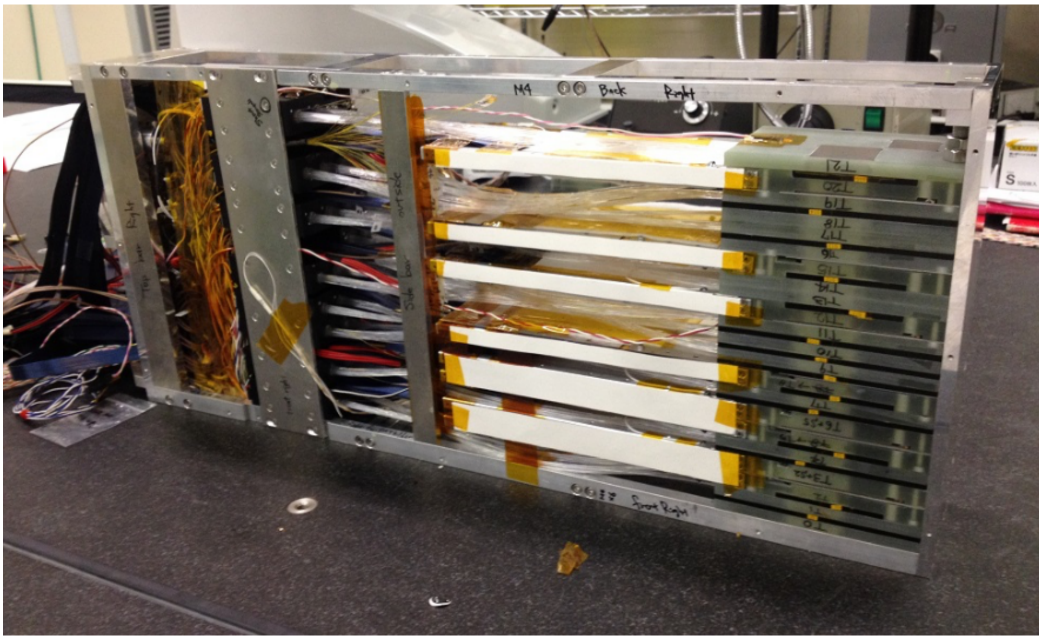

Figure 2.7: The upgraded Arm2 detector during the assembling process. We can see the green fiberglass frames where tungsten layers are glued and thin black frames supporting GSO planes. Lightguides coming out from scintillators are connected to the black PMTs shown on the left. Very thin silicon hybrids are located in the position corresponding to the white strips parallel to lightguides. Incoming particles enter the detector from the face at the bottom of the figure.

silicon read-out electronics. Each silicon layer, as the one shown in Fig.2.6 bottom, is made by a square of 768 microstrips, but only a strip every two is connected to the PACE3 chips [53] in order to reduce the necessary read-out electronics. In the old detector these unistrumented channels were left floating so that the charge produced by ionization in this region was collected by the nearby strips. In the upgraded detector these uninstrumented channels were instead connected to ground in order to reduce the amount of signal in the nearby strips, thus limiting saturation effects. The upgraded Arm2 detector during the assembling process is shown in Fig.2.7.

Apart from problems due to higher energy flow, other upgrades have been performed in order to improve energy resolution and to check response stability. First point is related to the new layout of imaging layers in Arm2, that has been carefully studied to optimize energy resolution for electromagnetic showers in silicon detectors. In this way it is possible to cross check the energy measured in scintillators using the energy deposited in silicon, therefore improving the precision on the final reconstructed energy. Second point is related to the LASER calibration system. Each GSO layer is connected to a light guide which brings the light signal to a photomultiplier tube (PMT) Hamamatsu R7400. Because PMT gain changes with temperature, in each device a dedicated light guide has been inserted, through which it is possible to inject signal from a LASER source. During data taking, special LASER runs have been performed to extract data useful for offline calibration. In addition, temperature has been monitored through several thermistors installed inside the detector.

In front of each Arm a sub-detector called Front Counter is installed. This is made by two 2 mm plastic scintillators separated by a 0.5 mm copper plate for a total depth of 0.06 X_0 and a sensitive area of 8 $cm \times 8$ cm. Through the detection of charged particles reaching LHCf, Front Counters can provide important information on the event rate and, if properly calibrated using Van Der Meer scan, measure the instantaneous luminosity.

2.4.2 The data acquisition system

LHCf data acquisition system (DAQ) has been designed in order to operate with less than 43 crossing bunches and less than 0.1 $\mu b^{-1} s^{-1}$ luminosity. If these limits are respected, the time interval between two consecutive crossing bunches is at least 2 μs and the expected trigger rate is about 1 kHz. In these conditions live time is about 50%. A schematic diagram of DAQ is shown in Fig.2.8. This can be divided in two parts: the one relative to scintillators and the one relative to silicon.

Scintillators signals are amplified before transmission through 200 m length cables making use of Technoland N-SE810 pre-amplifiers installed in the LHC tunnel. Amplified signals then reach USA15 (ATLAS Counting Room), where DAQ system is installed. Here Technoland N-SE820 fan-out modules split them into two parts. First output is sent to CAEN V965 that measures the charge signal trough a 12 bit ADC. Two dynamic ranges are available: Narrow Range ADC (NRADC), equivalent to 0.025 pC/ADC count, and Wide Range ADC (WRADC), equivalent to 0.2 pC/ADC count. Second output is sent to GNV-250 GPIO logic module after low pass filter (LHCF-LPF) and discriminator (V814B) in order to generate experimental trigger.

Silicon signals are amplified and digitalized by the electronics installed in the LHC tunnel. When a trigger is received, it is handled by the Trigger Sequencer Card (TSC [54]) and sent to the Front End Control Unit for embedded slow control (FEC [55]), both located in USA15. This last board controls silicon electronics installed in the tunnel through a 200 m optical fiber. Here the control ring drives four custom motherboards (MDAQs) that acquire analog signals from the PACE3 chips directly connected to the silicon microstrips layers inside the detector. After that, MDAQs perform analog to digital conversion and send data to the VME Receiver placed in USA15 making use of four optical fibers.

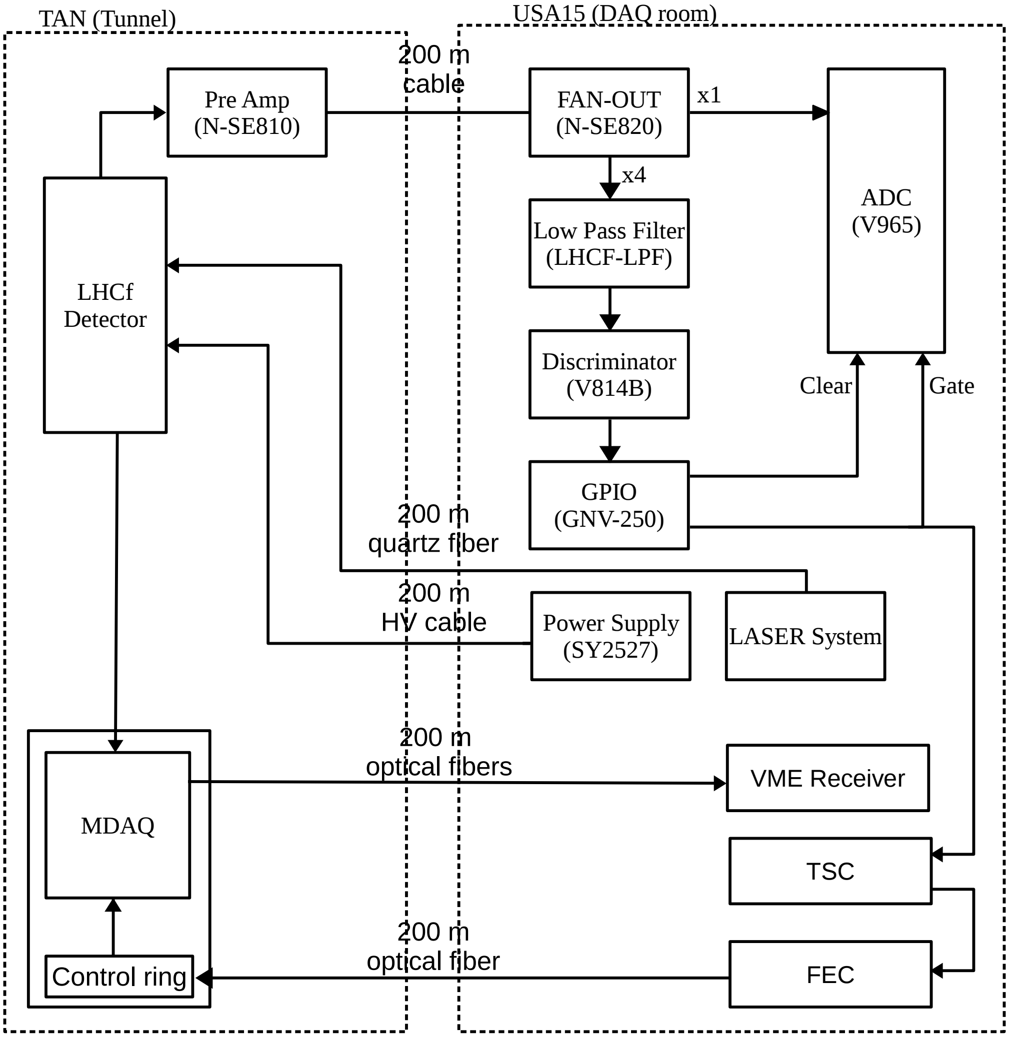

Figure 2.8: Schematic view of the LHCf Data Acquisition System: top and bottom parts are relative to scintillators and silicon respectively.

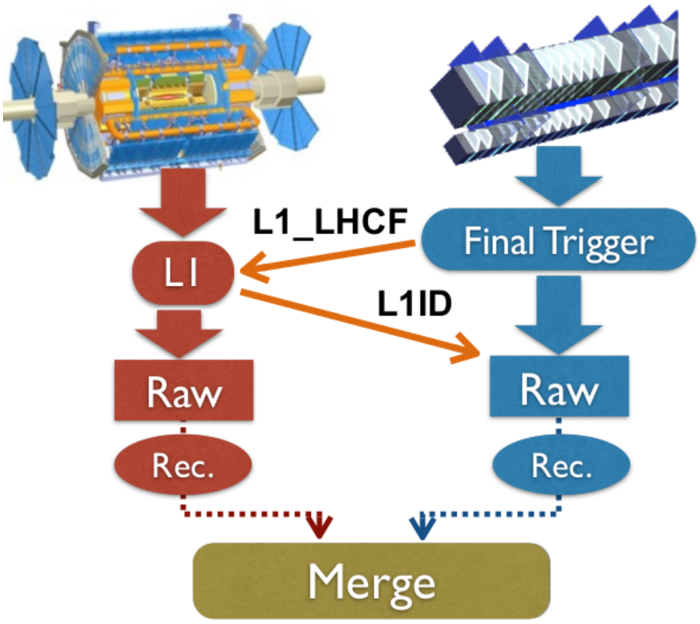

Figure 2.9: Schematic view of the principle of ATLAS-LHCf common operations. Left and right are ATLAS and LHCf experiments, respectively.

LHCf logic is based on three level triggers. First level trigger (L1T) is generated when beam reaches Beam Pick-Up Timing for Experiments (BPTX), placed at ±175 m from IP1. An enable signal is generated (L1T-ENABLE) if detector is ready to acquire a new event. Then, a second level trigger (L2T) is issued if three consecutive layers have a signal above a predefined threshold. For both Arms, discriminator thresholds have been chosen in order to have a detection efficiency higher than 99% for photons with energy above 200 GeV. Third level trigger (L3T) is finally generated combining all different kind of triggers (pedestal, LASER calibrations,...). When L3T is asserted the event is recorded.

2.4.3 ATLAS-LHCf common operations

A common data taking between LHCf and ATLAS experiments has been employed since 2015 operations. This solution, already tested for a very short period during 2013 operations, is illustrated in Fig.2.9. During operations LHCf sends its trigger to ATLAS that, after an appropriate prescaling, generates a common trigger. After that, data are acquired independently by the two experiments and events are later matched offline. The possibility of using information in the central region is very important for LHCf, because it helps to distinguish between diffractive and non-diffractive events. For example, we can identify an event in LHCf as diffractive if there are no charged particles in $|\eta| < 2.5$ having $\mathrm{p_T} > 100$ MeV/c, because in such kind of processes a large rapidity gap is expected between the products of the collision. The power of this common analysis can be understood if we consider that in hadronic interaction models these diffractive and non-diffractive interactions are treated separately. Thus, given a certain deviation observed by LHCf from a generator prediction, it would be very helpful for model developers to know which of the two events categories is responsible for it. In addition, ATLAS can also take advantage of this common operations, for example using neutron tag in LHCf to study pion exchange type of interactions at high energies. Because of all these reasons, LHCf-ATLAS common analysis has already started and we expect to focus more on it after that LHCf past studies will be extended to 2015 data.

2.4.4 Acquired data and published results

LHCf physics operations requires conditions that are quite different from the usual ones of LHC experiments. Because of this reason, since the first data taking in 2009, LHCf has always operated in dedicated runs of a few days and immediately removed after that. First requirement of these dedicated runs is that luminosity must be lower than about 0.1 $\mu b^{-1} s^{-1}$ because we want to keep pile-up below 1%: in this way we can assume that all detected particles come from a single p-p collision. Second condition is that β^* must be of the order of 20 m so that protons are mostly parallel at collision point: this is very important for proper reconstruction of scattering angle. Final optional requirement is to have a -145 μrad crossing angle in order to increase the pseudorapidity coverage from a minimum value of 8.7 to 8.4. Under these conditions, LHCf has collected data from p-p collisions at $\sqrt{s} = 0.9$, 2.76, 7 TeV and from p-Pb collisions at $\sqrt{s_{NN}} = 5.02$ TeV with the old detector, whereas new detector has been employed for p-p collisions at $\sqrt{s} = 13$ TeV and for p-Pb collisions at $\sqrt{s_{NN}} = 8.1$ TeV. LHCf detectors, or an improved version of them making use of silicon pad detectors, may be used in the future if proton-light ion collisions will be available at LHC.

The main analysis target of LHCf is the measurement of production rates relative to the three most abundant neutral particles detectable by the experiment: photons, π^0 and neutrons. This quantity is generally expressed as the inclusive production cross section in terms of energy E, for different pseudorapidities η, or in terms of transverse momentum p_{T}, for different rapidities y. In this way we can study absolute yield of secondary particles generated by the collision in a situation similar to the interaction of a cosmic ray with an atmospheric nucleus and, indirectly, obtain information on inelasticity (from E) and lateral distribution (from p_{T}). However, all these measurements are obtained in the case of p-p collisions, but actually EASs originate mainly from p-ion interactions. The second analysis target of LHCf is therefore to study the changes in the production spectra due to nuclear effects, exploiting the fact that at the LHC it is possible to have p-ion collisions as well. At present the only ion available for such purpose is lead, but in the future it will be possible to have oxygen as well, a situation much more similar to air showers, generally initiated by the interaction of a proton with an atmospheric light nucleus (mainly N and O). Making use of p-p and p-Pb collisions, LHCf is therefore able to give very important information regarding the properties of EASs, but if we want to extend it from 10^{17} eV up to 10^{20} eV a scaling law is needed. The validity of this hypothesis can be verified measuring secondaries production spectra at different center of mass energy. The third analysis target of LHCf is indeed to test the most popular scaling laws: $\mathrm{p_T}$ scaling [56], Feynman scaling [57] and limiting fragmentation hypothesis [58].

After having explained the analysis goals of LHCf, we would like to make a brief list of results published for each one of the three particles considered. Even if preliminaries studies on γ are needed for the reconstruction of π^0, photons are not so much interesting as themselves because in most cases they originate from neutral pions decay. The results published so far are single particle energy spectra relative to p-p collisions at $\sqrt{s} = 0.9$ TeV [59] and 7 TeV [60]. The same analysis at $\sqrt{s} = 13\ TeV$ is almost concluded. The possibility of reconstructing the properties of π^0 from the detection of the two γ originated from its decay is the main feature of LHCf detectors. This point allows us to carry on precise measurements on neutral pions, because energy resolution for electromagnetic showers is better than 2% above 100 GeV. For this reason, π^0 is the most powerful probe we have to study nuclear effects and test scaling laws. Even more important than these two points is the precise measurement of its production rates, because of the essential role it has in EASs evolution, where it transfers energy from the hadronic to the electromagnetic channel. It is possible to identify two kinds of π^0 events detectable by LHCf: Type-I, in which we have a single photon for each tower, and Type-II, in which a pair of photons hits the same tower. Type-I inclusive production cross section in terms of p_{T} was published for data relative to p-p collisions at $\sqrt{s} = 7\ TeV$ [61] and p-Pb collisions at $\sqrt{s_{NN}} = 5.02\ TeV$ [62]. These results were then extended to Type-II π^0s, including p-p collisions at $\sqrt{s} = 2.76$ TeV, and, in addition, the measured production spectra were used to study nuclear effects and test scaling laws [63]. Being the most abundant baryons reaching LHCf, neutrons have a particular importance for the calibration of hadronic interaction models, as discussed in §1.3. Unfortunately, this kind of analysis is complicated by the 40% energy resolution we have in the case of hadronic showers, as a consequence of the strong limitations on detector depth due to the available room in the TAN region. Because of this reason, neutron analysis started only recently and, for the moment, only energy spectra relative to $\sqrt{s} = 7\ TeV$ p-p collisions have been published [64].

Chapter 3

Detector calibration

LHCf detectors were upgraded before operations relative to $\sqrt{s} = 13\ TeV$ p-p collisions. In order to analyze data acquired at the LHC it was first necessary to calibrate Arm2 for the reconstruction of hadronic events. This was done using both experimental data taken at the CERN-SPS and Monte Carlo simulations generated using COSMOS and EPICS libraries. In this chapter we describe the calibration procedure and the estimated performances of the LHCf Arm2 detector. Data sets used for these purposes are discussed in §3.1. Calibration is divided in three main steps: determination of absolute and relative gain of scintillator layers using experimental data (§3.2); computation of energy conversion coefficients and position dependent corrections making use of MC simulations (§3.3.3, §3.3.4 and §3.3.5); comparison of data and MC after having applied all calibration factors previously estimated (§3.4). Performances, relative to trigger efficiency, energy resolution and transverse position resolution (§3.5), can be studied using both data and MC.

3.1 Calibration data sets

3.1.1 Experimental data sets

Experimental data have been acquired at the CERN-SPS in two different occasions: September-October 2014 and July-August 2015. The two beam tests were carried on before and after LHC data taking respectively. In this work we consider only the second data set because we expect to obtain a more accurate calibration for our analysis. This is because LHC runs analyzed in the next chapter correspond to the last physics fill acquired by LHCf, so that a possible change in detection response due to radiation damage is better reproduced by 2015 rather than 2014 SPS data.

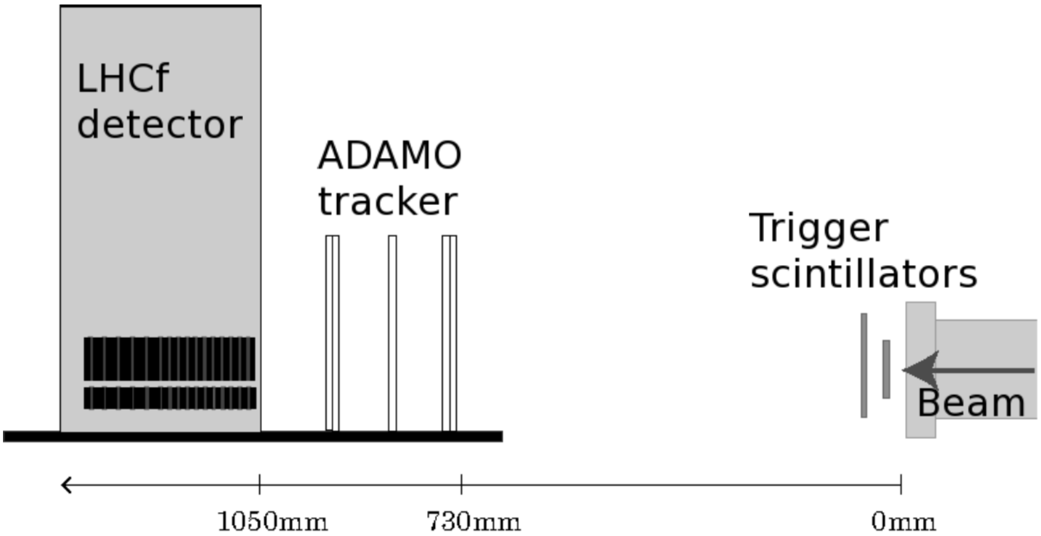

Figure 3.1: The setup of the SPS beam test. The trigger signal was generated using small scintillators just outside the beam extraction window. The detector was mounted on a movable table together with the ADAMO tracker to scan the sensitive area through the beams.

Both beam tests were carried on at the SPS-H4 beam line. The experimental setup is shown in Fig.3.1. Arm1 and Arm2 were installed in turn on the remotely movable table present in the experimental area, so that it was possible to perform position scanning over the whole sensitive area. Each detector was placed in an aluminium box which has a thin window on the front part in order to reduce the amount of material present between beam pipe and calorimeter itself. During data acquisition, temperature inside the box was kept stable ($< 0.1^\circ$ C per hour) by the use of a chiller. ADAMO tracker [65], composed by 5 xy silicon planes, was installed in front of LHCf detector in order to estimate position resolution of imaging layers. Trigger signal was generated using two small scintillators ($20\ mm \times 20\ mm$ and $40\ mm \times 40\ mm$) placed just outside the beam extraction window.

In order to perform hadron calibration, 300 GeV and 350 GeV protons beams have been used (p300GeV and p350GeV, hereafter). Data at the center of each tower were acquired making use of both energies, whereas p350GeV beam was selected to perform a complete scan of the whole sensitive area. Data sets used for calibration are summarized in Tab.3.1. For the determination of ADC/GeV conversion factors we employed p300GeV@center and p350GeV@center, whereas we made use of p350GeV and p350GeV@center for the comparison with MC at the end of calibration.

	ST		LT	
Beam	Run Number	Number of events	Run Number	Number of events
p300GeV @center	50690–50698	100 k	50699–50707	100 k
p350GeV @center	50679–50687	100 k	50667–50674	100 k
p350GeV	50730–50750 50772–50780	700 k	50709–50728 50751–50771 50781–50783	850 k

Table 3.1: Run table relative to Arm2 proton experimental data acquired at SPS.

3.1.2 MC data sets

Monte Carlo simulations have been generated using COSMOS (v7.645) and EPICS (v9.165) libraries [66] Two different geometrical configurations were implemented for detector simulation, one for SPS beam test and another one for LHC operation. SPS geometry was used to generate simulations needed to compare experimental data and MC at the end of calibration. On the other side, estimation of energy coefficients and position dependent correction factors were carried on using simulations relative to LHC geometry.

In the case of SPS configuration two different models were used to simulate proton-detector interaction. The first one is DPMJET 3.0-4 [36] (DPM, hereafter), whereas the second one makes use of DPMJET 3.0-4 and QGSJET II-04 [33] for energies below and above 90 GeV respectively (QGS, hereafter). The choice of these two models is the same that was taken for the calibration of the old detector [67]. The reason for this is that they were found to reproduce enough well the longitudinal profile of hadronic showers at energies where we can compare model predictions with beam test data. This is an important point because in case of small detector depth the energy deposit is strongly affected by longitudinal leakage. Therefore, not all models that reproduce well the energy release in case of full shower containment can also work in our case. For both DPM and QGS models, $\sim$ 800 k ($\sim$ 1600 k) events were generated for ST (LT) in the case of p300GeV and twice this statistics in the case of p350GeV. Protons were injected uniformly on towers area.

In the case of LHC configuration only DPM model was used. Energy coefficients were estimated using simulations in which single neutrons of different energies are injected at towers center : 100, 200, 300, 500 GeV and 1, 2, 3, 4, 5, 6 TeV. Number of events is $\sim$ 125 k for energies below 500 GeV and $\sim$ 50 k above 1 TeV. Determination of position dependent corrections requires MC in which neutrons are injected uniformly on towers area. These factors were estimated using 1 TeV neutrons, whereas 500 GeV and 4 TeV neutrons were employed to check their energy dependence. Number of events is $\sim$ 1512 k ($\sim$ 2400 k) for 1 TeV neutrons on the ST (LT) and a bit less than this statistics for the other two cases.

3.2 Determination of ADC/GeV conversion factors

Optical coupling between GSO and PMT strongly affects the amount of deposited energy that is finally detected, hence decreasing the accuracy in the energy measurement. In addition, this coupling is different for each layer so that relative gains changes as well, resulting in a worse detection resolution. It is therefore important to determine conversion factors between the true energy deposited in the scintillator (expressed in GeV) and the energy measured by the electronics (expressed in ADC) for every GSO layer.

Because of large uncertainties present in hadronic interaction models, these factors are usually estimated using particles whose interaction with matter is well-known, like muons or electrons. This was also done in the case of LHCf, but electromagnetic showers can not reach the deepest layers and muon data are affected by the uncertainty due to the change of PMT gain as a function of high voltage [1].

Estimation of conversion factors was carried on by the use of electrons beam for layers 0-11 and of protons beam for layers 12-15. The first study, described in [68], was realized through a minimization procedure involving experimental data and MC simulations. In the second case, this was not directly possible because no interaction model reproduces well the layer by layer energy deposit of a primary proton. Because of this reason we decided to perform a relative calibration in the assumption that the energy distribution in each layer is the same if we select the same shower starting point. We proceeded in the following way.

We define some event selection criteria common to all layers. Then we fill the energy distribution for layers 8-11 using ADC/GeV conversion factors determined by electrons beam. Each layer $j_{ref} \in [8, 11]$ is used as a *reference* layer for the determination of the conversion factor $f_{j_{cal}}[ADC/GeV]$ of each *to-be-calibrated* layer $j_{cal} \in [12, 15]$. This is done through a iterative minimization algorithm that makes use of the energy distributions $x_{j_{ref}}[GeV]$ and $x_{j_{cal}}[ADC]$[2] to minimize the difference between $x'_{j_{cal}}[GeV] = f_{j_{cal}} \cdot x_{j_{cal}}[ADC]$ and $x_{j_{ref}}[GeV]$. At each step, for each layer j_{cal}, through each layer j_{ref}:

---

[1] Data relative to electrons and protons beam have been acquired using a high voltage of 600 V, whereas 1 kV was needed to detect the small ionization energy deposit of muons. A comparison of ADC/GeV conversion factors obtained using electrons and muons shows different results in the two cases, without any clear layer by layer correlation [68]. Because of this reason, it is not possible to correct muons-estimated factors on last layers using a constant shift from electrons-estimated factors on first layers. Thus, we need an alternative way to estimate these factors for the deepest part of the calorimeter and protons beam data are the best candidate for this purpose.

[2] Here ADC means WRADC, so that final conversion factors are obtained in terms of WRADC/GeV. To get their values in terms of NRADC/GeV we estimated the relative gain between the two ADC ranges. This was done performing a linear fit on the WRADC-NRADC scatter plots relative to p300GeV@center data set. For all layers NRADC/WRADC is in the range [7.9, 8.0].

- we define a range for $f_{j_{cal}}$ centered on the value determined at the end of last iteration, reducing the size of the range at each iteration
- we fill hitmap distributions of j_{cal} and j_{ref}; for each bin k of this map we get the weight w_k that will be applied in the next point to take into account the difference in position distribution between the two layers
- we fill energy distributions of j_{cal} and j_{ref}; $x_{j_{ref}}[GeV]$ is fixed because we assume that $f_{j_{ref}}$ is exact, whereas $x'_{j_{cal}}[GeV]$ is computed again for each value of $f_{j_{cal}}$ in the defined range[3]
- given the considered value of $f_{j_{cal}}$, it is thus possible to compute the associated χ^2 using all bins i for which $x_{j_{ref},i} > 10$

$$\chi^2 = \sum_{i=0}^{N_{bin}} \frac{(x'_{j_{cal},i} - x_{j_{ref},i})^2}{\sigma'^2_{j_{cal},i} + \sigma^2_{j_{ref},i}} \tag{3.1}$$

  so that changing f_j in the selected range it is possible to plot the χ^2 function and perform a fit using a second order polynomial function
- $f^{best}_{j_{cal}}$, the best value for $f_{j_{cal}}$, is given by the function minimum obtained by the fit and its error $\sigma_{j_{cal}}$ by the distance from $f^{best}_{j_{cal}}$ for which χ^2 changes by 1, whereas agreement between $x_{j_{ref}}$ and $x'_{j_{cal}}$ is estimated computing the *p-value* relative to f^{best}_j

As starting value of minimization we use the value of $f_{j_{cal}}$ determined in [68], whereas at each successive step we make use of the one obtained through the reference layer that gives the lowest *p-value.* The initial range used for $f_{j_{cal}}$ is 1000 ADC/GeV and this is reduced of 100 ADC/GeV at each iteration. After three steps the minimization procedure converges and we have no gain in decreasing the range further. At this point, we consider all different estimations of $f_{j_{cal}}$ obtained using the four reference layers 8-11 and we properly combine this information to get the final value for the conversion factor of layer j_{cal}

$$f_i^{final} = \sum_{j=8}^{11} w_{i,j} \cdot f_{i,j} \tag{3.2}$$

$$\sigma_i^{final} = \sqrt{\sum_{j=8}^{11} w^2_{i,j} \cdot \sigma^2_{i,j}} \tag{3.3}$$

---

[3] Because the measured energy deposit depends on light collection efficiency, we weight each entry in both histogram for the relative correction factor in the selected layer, as described in §3.3.5

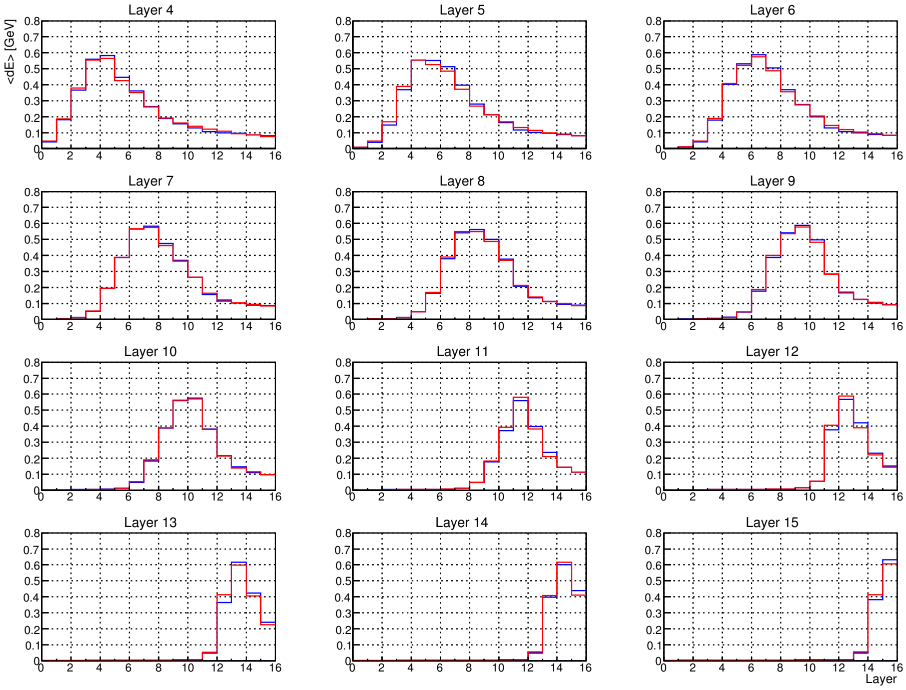

Figure 3.2: Average energy deposit for each scintillator when the software trigger condition is satisfied in the considered layer. Red is DPM simulations, blue is experimental data, obtained using the starting value of conversion factors. Data set refers to p300GeV@center on ST.

where

$$w_{i,j} = \frac{(1 - p_{i,j})}{\sum_{j=8}^{11}(1 - p_{i,j})} \tag{3.4}$$

and $f_{i,j}$, $\sigma_{i,j}$, $p_{i,j}$ refers respectively to the best value, its error and the relative p-value obtained for *to-be-calibrated* layer i using *reference* layer j.

Event selection criteria have been chosen in order to avoid possible non-uniformity of detector response, select pure single proton event and obtain the same shower starting point for each layer. The first point requires to consider only a 10 $mm \times 10$ mm area around towers center. The second point has two main implication: the identification of hadronic showers, performed looking at the longitudinal profile by the use of the simple cut $L_{90\%} > 20$ X_0[4]; the rejection of event in which more than one particle enters the detector (*multihit*, hereafter), that can be obtained both applying the ROOT TSpectrum class [69] to the transverse profile reconstructed by the imaging layers and requiring that *sumdE*, the total energy deposit in the calorimeter, is inside a interval of ±2.5 RMS from its mean[5]. Finally, the trigger

---

[4] For the definition of $L_{90\%}$ see §4.3.

[5] For the definition of *sumdE* see §3.3.3.

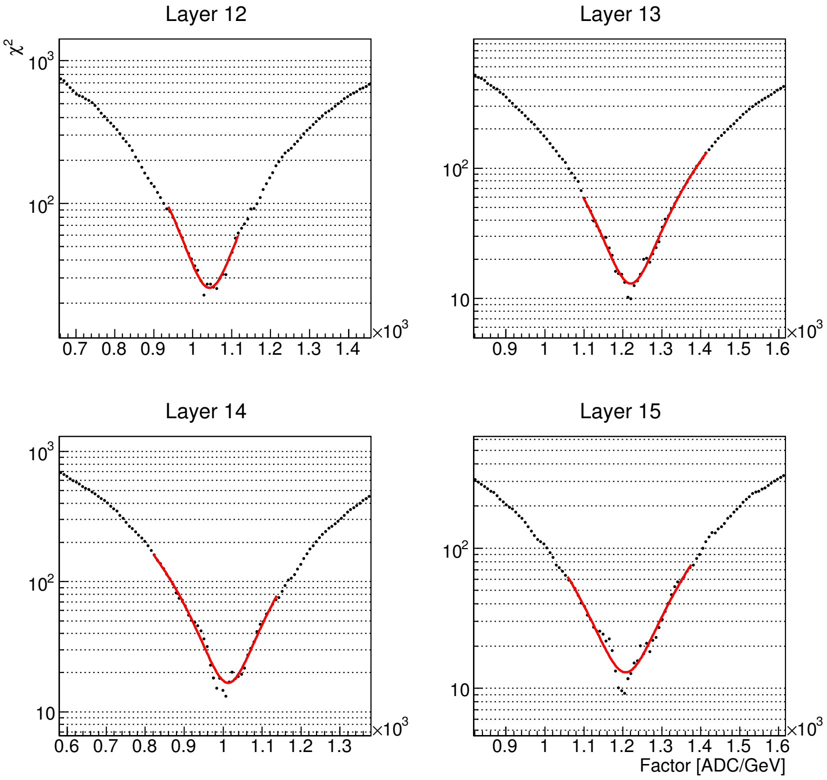

Figure 3.3: Results at the end of minimization for p300GeV@center on ST: χ^2 distribution and polynomial fit.

criteria was optimized in order to sample the maximum energy deposit in each layer. For each layer i at a given depth $t[X_0]$ we require $dE(t-4X_0) > 150\ MeV$ and $dE(t-8X_0), dE(t-12X_0), ... < 150\ MeV$. Because sampling step of layers 11-15 is twice the one of layers 0-10, when we express the previous condition in terms of i instead of t we get a different formulation for the two groups of layers. The effect of this software trigger is shown in Fig.3.2, where we can see the average energy deposit in scintillators when this condition is satisfied for the selected layer. The two curves refer to DPM simulation (red) and experimental data (blue) obtained applying conversion factors estimated using electrons beam for layers 0-11 and muons beam for layers 12-15. We can see that in this case the energy deposit on the layer itself is the maximum among all layers in the calorimeter. In addition, it is important to note that MC predictions do not agree with data everywhere: this is the main reason why we decided to not use them for the estimation of conversion factors.

χ^2 functions and energy distributions at the end of the minimization procedure are shown in Fig.3.3 and 3.4 in the case of p300GeV@center on ST. The *reference* layer used for this plot is the one that exhibits the best agreement with the *to-*

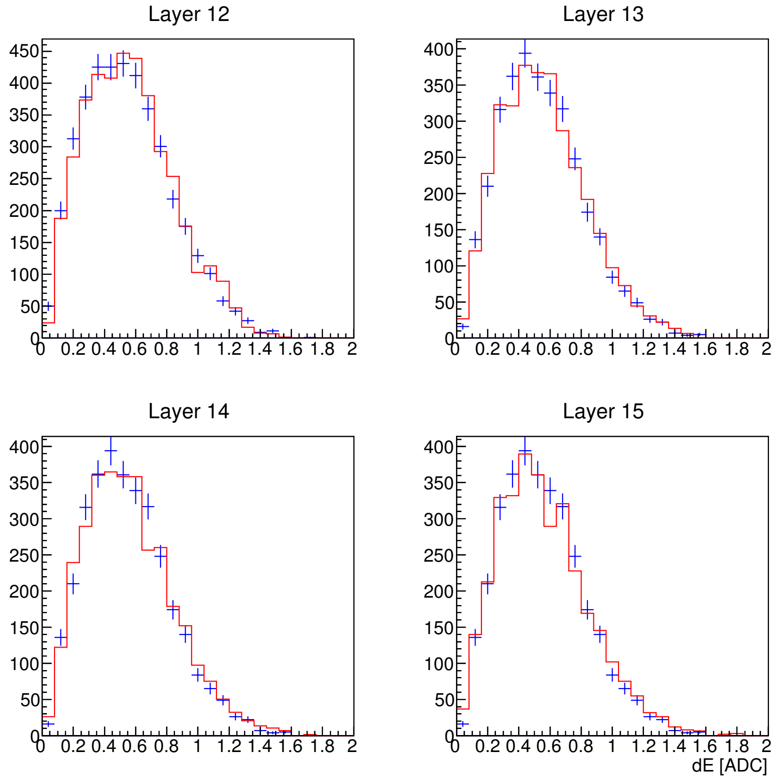

Figure 3.4: Results at the end of minimization for p300GeV@center on ST: energy distribution for the *to-be-calibrated* layer (red) and the *reference* layer having the best agreement (blue).

be-calibrated layer after the last iteration. Fig.3.5 shows the change of average energy deposits in layers 12-15 between muons and protons conversion factors, whereas the values on other layers are obtained using electrons results. We can clearly observe that mean values move towards the ones of layers 8-11 as a result of calibration.

On the other side, it is possible to observe that average energy deposits in layers 4-11 are not exactly constant. This fact can be due to several different reasons that are not so easy to investigate. For example, the discontinuity in layers 5 and 8, present in MC simulations as well, is explained by the presence of silicon planes before them. If, apart from this effect, there are some other reasons for a layer by layer difference in energy deposit, we can expect that layers 8-11 will be anyway more similar to the deepest ones compared to 0-7. In addition to this, we have to consider that the combination of selecting the starting point of the shower and rejecting non-proton event via $L_{90\%}$ cut has a strong impact on the distribution of the first layers. For this two different reasons we decided to restrict the number of *reference* layers to the interval 8-11.

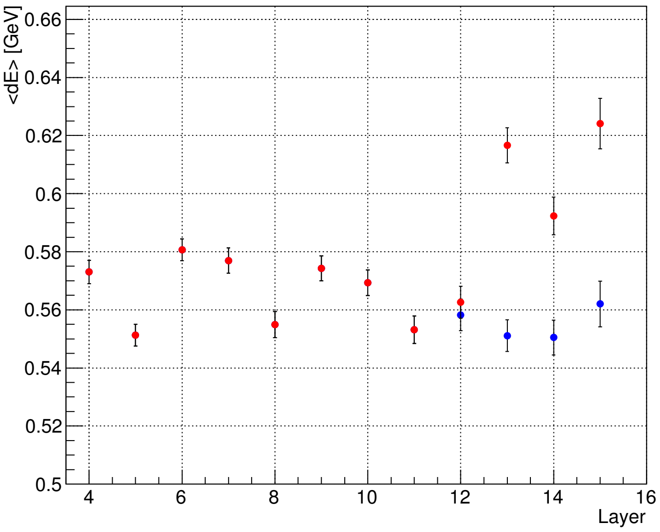

Figure 3.5: Average energy deposit before (red) and after (blue) determination of conversion factors using proton beam data. Data set refers to p300GeV@center on ST.

The comparison of conversion factors obtained using protons beams at towers center (p300GeV@center, p350GeV@center) with the ones estimated in [68] is shown in Fig.3.6 (absolute value) and 3.7 (ratio). For each protons data set, we can see the four measurements obtained with different *reference* layers (purple) and the final value obtained using Eq.3.2 and 3.3 (green). In order to check the performance of this minimization algorithm, the procedure was applied to layers 8-11 as well, in this case excluding the layer itself as a possible *reference*. Agreement between proton and electron results in layers 8-12 is better than 3%, while even 15% deviation is found between proton and muons in the last three layers. Comparing p300GeV@center and p350GeV@center results, we can conclude that they are consistent for ST, but there is at most 10% difference for LT. This can be due to the fact that 350 *GeV* data have been acquired in slightly different beam conditions for the two towers and, in particular, pile-up was higher for the LT than for the ST data set. Because of this reason we decided to build the final conversion factors table using electrons for layers 0-11 and p300GeV@center for layers 12-15. This is shown in Tab.3.2.

The last important point to be discussed here is the estimation of the uncertainty on conversion factors just obtained. There are three contributions to it: the first one is coming from the method we used and can be estimated by the ratio between the results obtained for layers 8-11 in the case of protons and electrons beams; the second one is due to the fact that for the *to-be-calibrated* layer

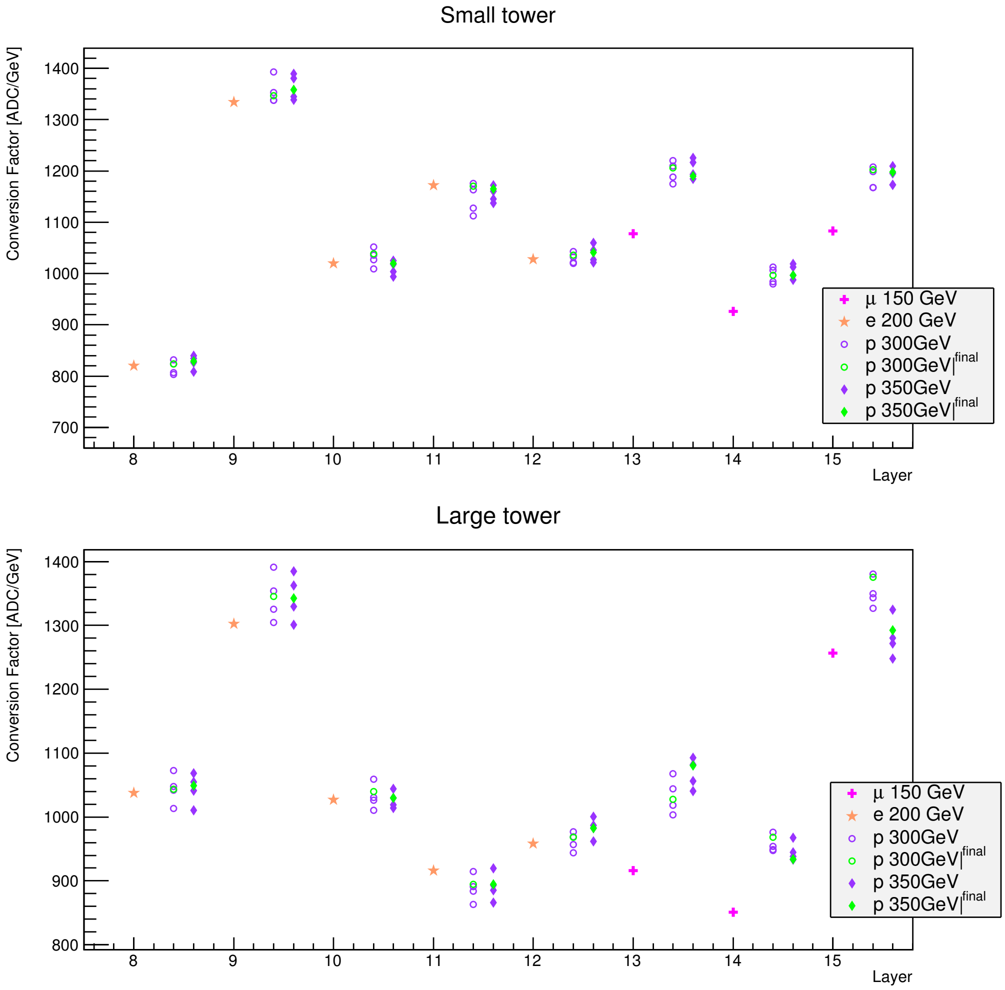

Figure 3.6: Absolute conversion factors determined for the two considered protons data sets. Purple markers refer to the estimation obtained using different reference layers, whereas green markers are relative to the final measurement given by the combination of all reference layers results. For comparison, conversion factors estimated though electrons (layers 8-12) and muons (layers 13-15) beams are also reported.

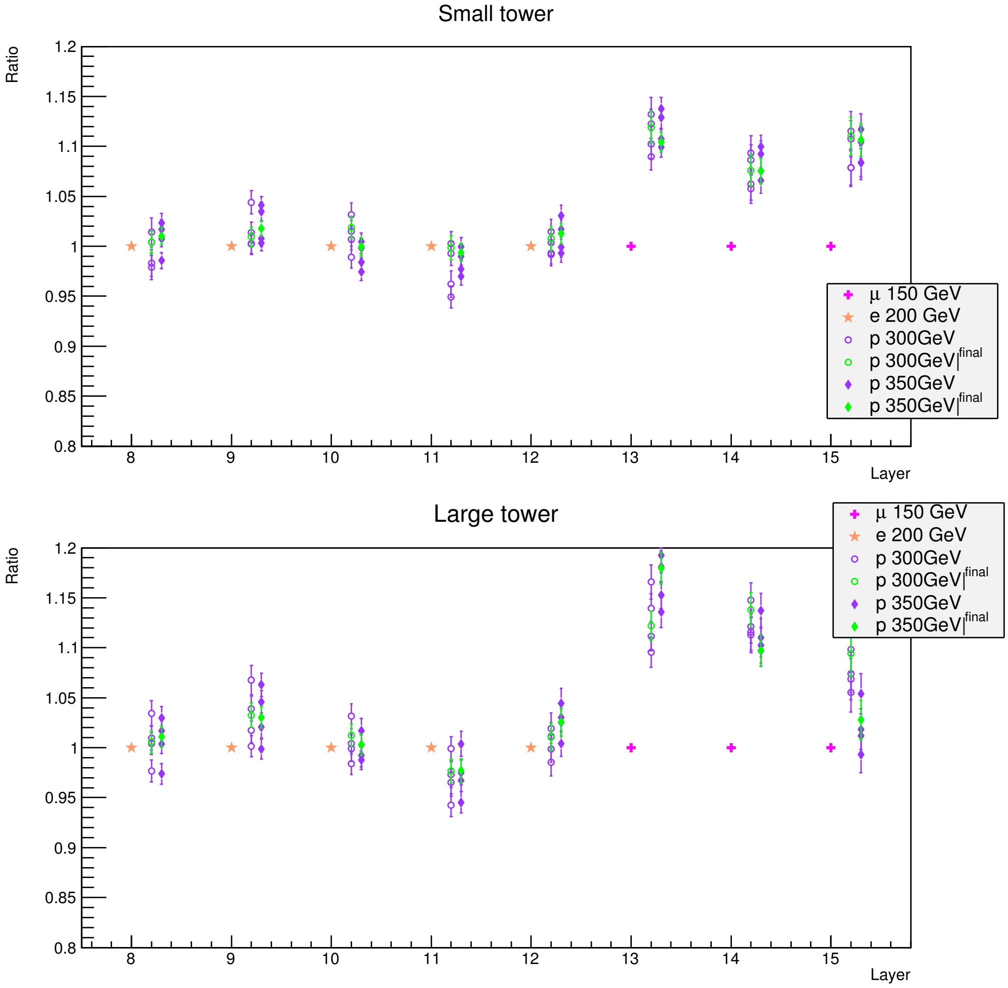

Figure 3.7: Ratio of conversion factors determined for the two considered protons data sets to the electrons and muons results. Purple markers refer to the estimation obtained using different reference layers, whereas green markers are relative to the final measurement given by the combination of all reference layers results. For comparison, conversion factors estimated though electrons (layers 8-12) and muons (layers 13-15) beams are also reported.

	Small Tower		Large Tower	
Layer	Factor (ADC/GeV)	Error (ADC/GeV)	Factor (ADC/GeV)	Error (ADC/GeV)
0	812	-	970	-
1	828	-	757	-
2	576	-	643	-
3	802	-	1118	-
4	743	-	723	-
5	381	-	555	-
6	780	-	963	-
7	730	-	581	-
8	820	-	1037	-
9	1334	-	1303	-
10	1020	-	1027	-
11	1172	-	916	-
12	1036	13	968	13
13	1206	17	1028	13
14	997	15	968	15
15	1202	21	1375	29

Table 3.2: Conversions factors and related errors expressed in ADC/GeV for all scintillators. For layers 0-11, the value is the one reported in [68] and the error is not considered here. For layers 12-15, values and errors are estimated from Eq.3.2 and 3.3 making use of p300GeV@center data set.

we combined four different measurements obtaining a final uncertainty given by Eq.3.3; the third one is related to the two independent measurements we have for each layer if we make use of both protons data sets and can be estimated by the ratio of the two results. These three terms are shown in Fig.3.8. Their contribution to the systematic uncertainty was estimated using the maximum relative uncertainty for the second term and the RMS for the other two. Summing up these three contributions in quadrature we obtained a systematic uncertainty for the conversion factors of last layers given by $\sigma_{gain\_last} = 1.9\%$ for ST and 5.3% for LT. Calibration of first layers obtained using electrons beam data resulted in a systematic uncertainty of $\sigma_{gain\_first} = 1\%$ for both towers. For simplicity, we decided to consider only one systematic contribution on the energy scale coming from the estimation of conversion factors. This was done weighting each one of the two uncertainties for the average fraction of energy deposit in that group of layers respect to the total signal. In order to have an estimation that can be valid for the analysis discussed in the next chapter we decided to consider the energy deposit by particles produced in p-p collisions at $\sqrt{s} = 13\ TeV$. For this purpose we employed the QGSJET II-04 toy MC that will be described in §4.1.2 and the

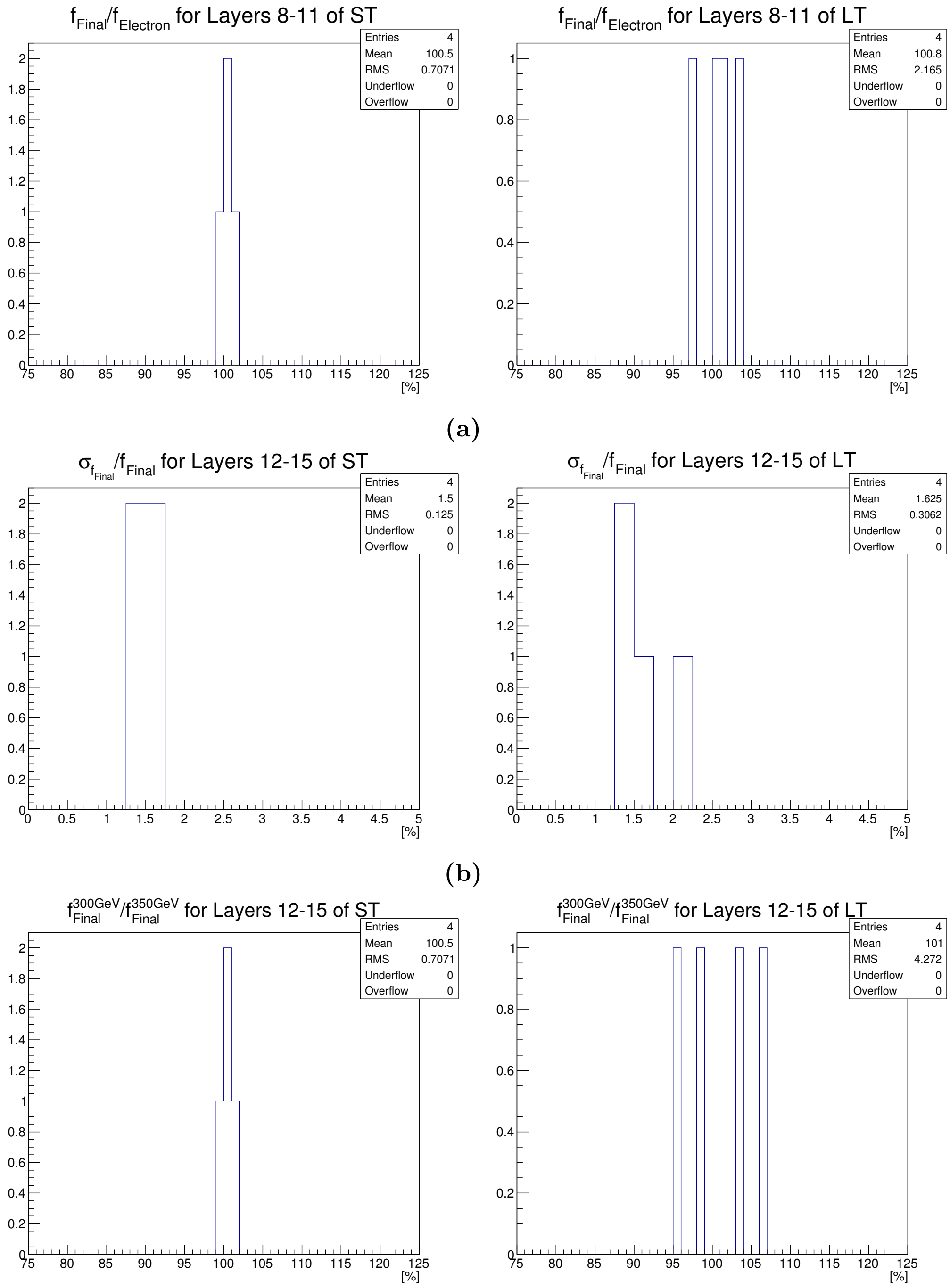

(a)

(b)

(c)

Figure 3.8: Estimation of the uncertainty on conversion factors obtained from p300GeV@center data set. Left figure is ST, right figure LT. (a) Distribution of the ratio of protons-estimated/electrons-estimated conversion factors for layers 8-11. (b) Distribution of relative uncertainty on the final measurements for layers 12-15. (c) Distribution of the ratio of p300GeV@center/p350GeV@center conversion factors for layers 12-15.

same event selection criteria that will be discussed in §4.3. Considering each layer i, having sampling step n_i and average energy deposit $< dE_i >$, the fraction of energy deposited in the first 12 layers is

$$f = \frac{\sum_{i=0}^{11} n_i < dE_i >}{\sum_{i=0}^{15} n_i < dE_i >} \tag{3.5}$$

and, conversely, $1 - f$ is the fraction of energy deposited in the last 4 layers. We obtained that these two fractions are respectively about 60% and 40%. Hence, we estimated the final uncertainty combining the two contributions

$$\sigma_{gain} = \ f \times \sigma_{gain\_first} + (1 - f) \times \sigma_{gain\_last} \tag{3.6}$$

In conclusion, we obtained that the contribution to the uncertainty on the energy scale coming from the calibration of GSO layers gains is $\sigma_{gain} = 1.4\%$ for ST and 2.7% for LT, for an average value of about 2%.

3.3 Determination of energy coefficients

3.3.1 Event selection

All three studies discussed in this paragraph were performed using the same event selection methods. The first criteria, that is actually implicit in the production of the simulations used for this analysis, is that we are considering events in which just one neutron at a time is injected in the detector. The second choice is the use of true particle position in order to separate the contribution to energy scale due to correction factors from the one related to position resolution. The last two conditions applied are particle identification (PID, hereafter) and software trigger. Both of them will be used for the analysis of neutron energy spectra produced by p-p collisions at $\sqrt{s} = 13\ TeV$. Because they affect energy distributions, it is important to consider them for the three studies discussed here if we want to estimate accurate calibration factors for the analysis of LHC data. Details about these two analysis cuts are given in §4.3.

3.3.2 Definition of reference systems

An important point to be discussed here is the definition of coordinates reference system (RS). In this work we adopted two different RSs: the *downstream* tower reference system and the *upstream* LHC reference system. In both RSs, z axis is parallel to beam direction and positive going from IP1 to Arm2, y is perpendicular to the ground and x is normal to the z-y plane, but positive sense of x is heading towards the center of the collider ring in the case of LHC RS and in the opposite direction in the case of tower RS. The origin in the x-y plane corresponds to the tower left bottom corner in the tower RS and to the projection of beam center

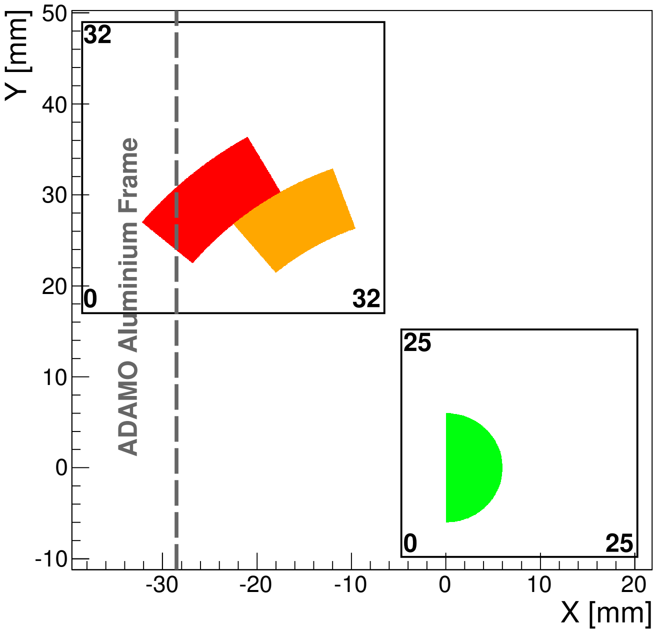

Figure 3.9: Illustration of *downstream* LHC reference system. Black squares corresponds to LT (left) and ST (right). Pseudorapidity regions described in §4.3 are: 0 (green), 1 (yellow) and 2 (red). Black numbers inside squares refer to the coordinates of towers edges measured in the downstream tower reference system. Note the region at the left of dashed gray line that was covered by the ADAMO aluminium frame during 2015 SPS beam test.

on the detector in the LHC RS. In tower RS, both coordinates range from 0 to 25 *mm* for ST and from 0 to 32 *mm* for LT, whereas in LHC RS x and y ranges are respectively [-21.83, 39.61] mm and [-11.19, 50.25] mm. We used the tower RS in this chapter and the LHC RS in next chapter.

Tower RS has been employed for lateral leakage and light collection efficiency correction factors and for the uncertainties involving position dependent response (all contributions estimated in §3.3 and 3.4 except the one related to energy conversion coefficients). Actually, for the estimation of calibration factors we employed the whole detector area, whereas the corresponding systematic uncertainties were computed using the same pseudorapidity regions that will be defined in §4.3. Because they are defined in the upstream LHC RS, but in this chapter we used the downstream tower RS, this can create some confusions. In order to avoid it, Fig.3.9 shows the position of tower and pseudorapidity regions in both the *downstream* LHC RS and the downstream tower RS. This figure must be directly compared with Fig.4.3 that is instead relative to upstream LHC RS.

	Small Tower	Large Tower
a $[GeV^{-1}]$	$1.84 \pm 0.08 \times 10^{-7}$	$1.43 \pm 0.08 \times 10^{-7}$
b	$1.096 \pm 0.004 \times 10^{-2}$	$1.184 \pm 0.004 \times 10^{-2}$
c $[GeV]$	1.96 ± 0.02	1.97 ± 0.02

Table 3.3: Energy conversion coefficients obtained by fit on the relation between *sumdE* and E making use of Eq.3.8.

As a last note we would like to remark here that during 2015 SPS beam test a region of LT was covered by the ADAMO aluminium frame, thus adding some material in front of it. As shown in the figure, this area corresponds to an interval on x going from 0 to 10 mm in the LT RS. Because this is partially including one of the two pseudorapidity regions in the LT, events hitting in this area have not been taken into account for the comparison of data with models, as described in §3.4.

3.3.3 Determination of energy conversion coefficients

Energy deposited in the calorimeter is defined through the quantity *sumdE*

$$sumdE = \sum_{i=2}^{15} n_i \times dE_i \tag{3.7}$$

where dE_i is the energy deposited in layer i and n_i is 1 for layers 2-10 and 2 for layers 11-15. This weight factor takes into account the fact that the sampling step of last layers is twice the one of first layers. We assume that the relationship between *sumdE* and primary energy E is polynomial

$$sumdE = aE^2 + bE + c \tag{3.8}$$

Neutron simulations at towers center provide the average value of *sumdE* for each considered true energy E. a, b, and c coefficients are determined using polynomial fit according to Eq.3.8. The results are shown in Tab.3.3 separately for the two towers. In the case of hadrons, non linearity is due mainly to software trigger condition that removes low energy tails for particles below 500 GeV. These points are therefore ignored in the fit shown in Fig.3.10 in order to assign a larger weight to energies above 500 GeV. As expected, residuals are very high below 250 GeV, but it is not a problem because these energies will not be considered in the analysis, being detection efficiency so small. Above 500 GeV residuals are quite reasonable and we can use the maximum deviation as a systematic uncertainty. In this way, we get that $\sigma_{ene\_conv} = 1.5\%$ is the contribution to the uncertainty on the energy scale related to the conversion between *sumdE* and E.

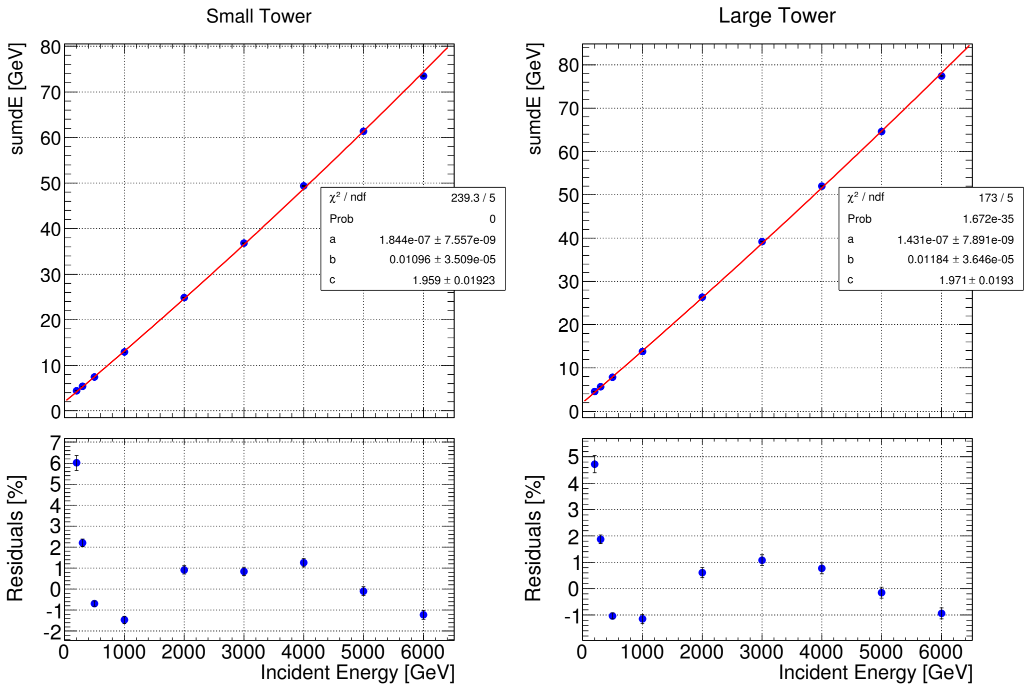

Figure 3.10: Top figure shows *sumdE* as a function of E with the fit superimposed to the plot, bottom figure displays residuals of the fit.

3.3.4 Lateral leakage correction factors

Coefficients in Eq.3.8 have been determined for the reconstruction of primary energy in the case that the incident particle is hitting towers center. Given the relatively small towers size and the wide lateral profile of hadronic showers, if the particle hits far away from towers center a certain amount of the energy developed in the calorimeter leaks out from it. In addition, because distance between ST and LT is only 1.8 mm along both x and y directions, it is possible that a fraction of the energy leaking out from a tower leaks in the adjacent tower. Because both effects worsen the energy reconstruction, we need to compute some correction factors for them.

As a starting point we define a bidimensional map for each kind of leakage

$$\mathrm{LeakOut}_T(x,y) = \frac{< sumdE^T(x,y) >}{< sumdE^T_{center} >} \tag{3.9}$$

$$\mathrm{LeakIn}_T(x,y) =< \frac{sumdE^{1-T}}{sumdE^T(x,y)} > \tag{3.10}$$

where $sumdE^T(x,y)$ is the energy deposited in tower T - 0 standing for ST and 1 for LT - when the particle is hitting tower T in position (x,y).

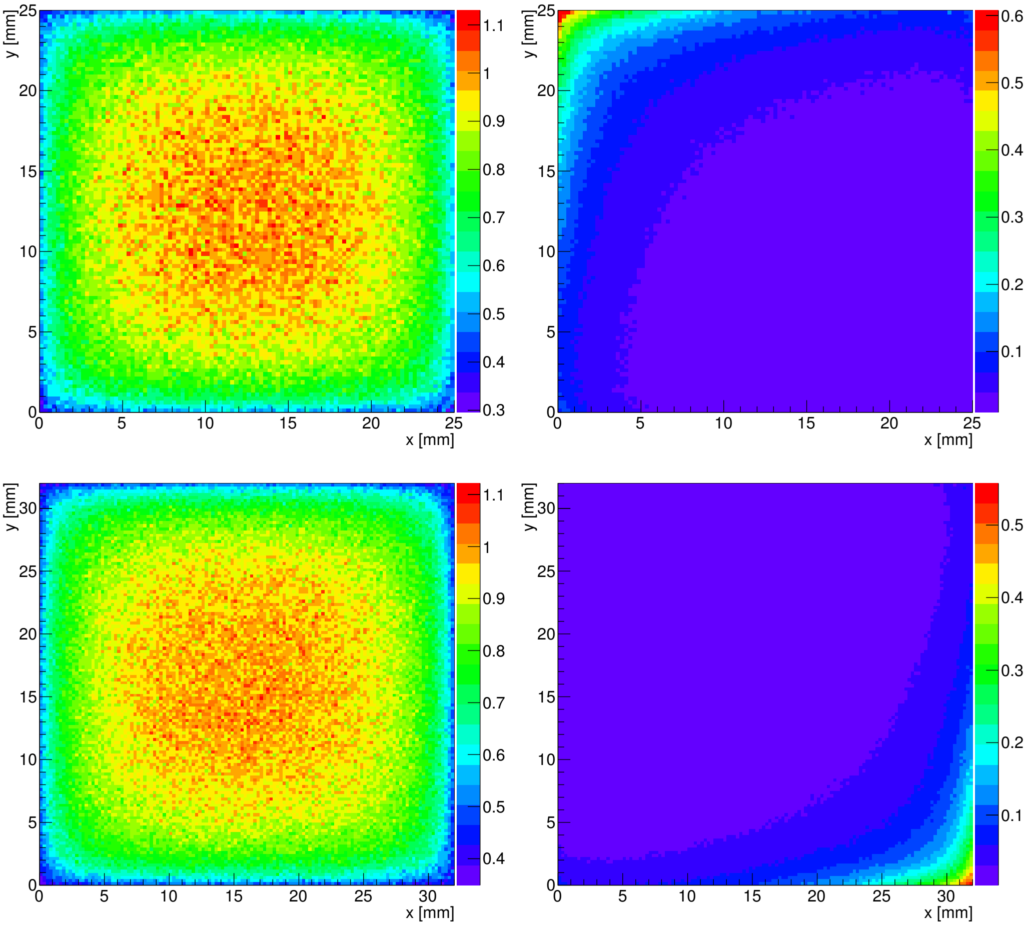

Figure 3.11: Leak-out (left) and leak-in (right) maps for 1 TeV neutrons. Top is ST, bottom is LT.

Fig.3.11 shows leakage maps obtained using 1 TeV neutrons for a bin size of 0.25 $mm \times 0.25$ mm. We can see that, being the section of the tower a square, leak-out maps are symmetric, but leak-in maps depend on the relative position of ST and LT inside the detector box. Having determined the impact point of incident particle making use of silicon sensors, leak-out correction factors are given by the content of leak-out map corresponding to the measured position through linear interpolation between adjacent bins, whereas it was shown in a previous study [67] that leak-in corrections factors depends on primary energy E as $Ae^{-BE}+C$. Because detector resolution for hadronic showers is almost 40%, it is very complicated to apply leak-in correction, therefore in this work we decided to neglect leak-in and correct only for leak-out.

In order to check the energy dependence of lateral leakage, we repeated the same procedure for 500 GeV and 4 TeV neutrons. Fig.3.12 and 3.13 show the ratio of leak-out and leak-in maps obtained at these energies to the one relative to 1 TeV neutrons.

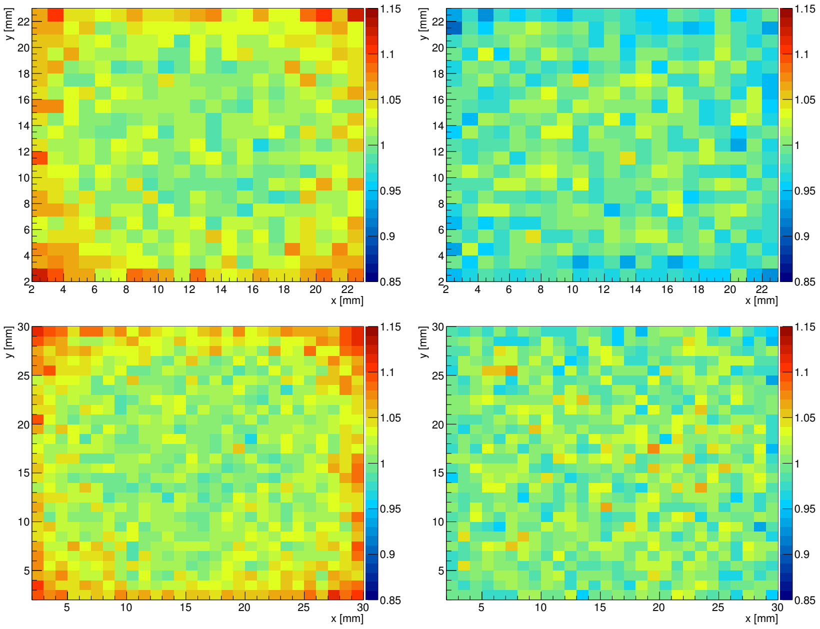

Figure 3.12: Leak-out maps ratio: on the left 500 $GeV/1\ TeV$, on the right 4 $TeV/1\ TeV$. Top is ST, bottom is LT.

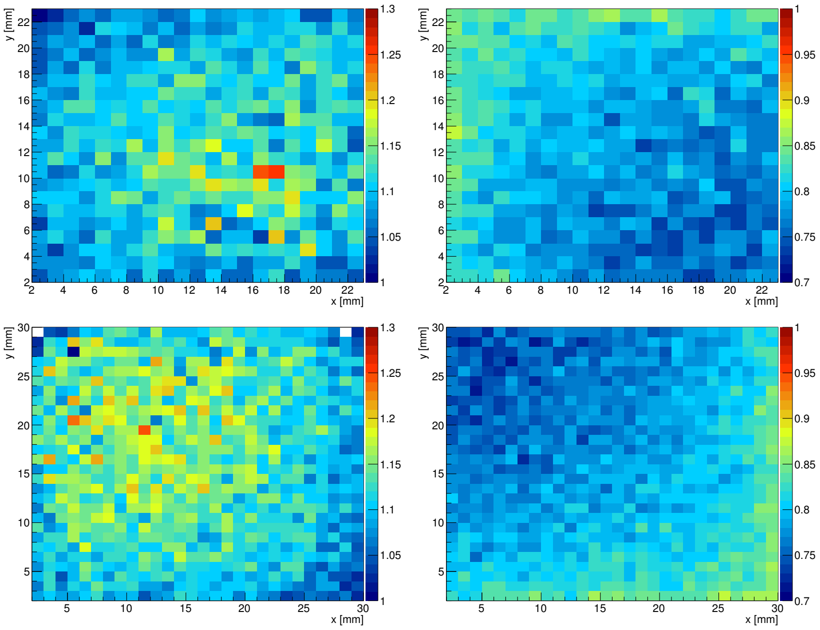

Figure 3.13: Leak-in maps ratio: on the left 500 $GeV/1\ TeV$, on the right 4 $TeV/1\ TeV$. Top is ST, bottom is LT.

Regarding leak-out, we can see that in most cases energy dependence is below 5%. The most problematic region is the one near towers edge where the software trigger condition strongly affects the average of *sumdE* distributions, especially at low energies. In addition, we can observe that leak-out maps lead to higher correction factors at 500 GeV than at 4 TeV, effect that can be related to a deposit more focused along the original direction of the particle at higher energies. Anyway, we can not see any significant trend near towers center, so we can believe that energy independent leak-out assumption holds well. In the next section we will consider the contribution to the uncertainty on the energy scale due to the hypothesis that position correction factors (leak-out and light collection efficiency) do not depend on the energy of the incident particle.

Regarding leak-in, we can observe the same energy trend that was observed for leak-out, with higher effect at 500 GeV than at 4 TeV. In this case we can observe a strong energy dependence up to 30%, but we must note that this happens in a region where leak-in effect is very small. If we consider the region in Fig.3.11 where *leak-in* is higher than 0.25, energy dependence is below 10%. Therefore one possible solution to apply the correction could be to treat leak-in effect exactly in the same case as leak-out effect, assuming that it is not depending on the energy of the incident particle and correcting for it through linear interpolation between adjacent bins. However, the performance of such kind of approach has not been investigated in the past, so we decided to ignore leak-in effect for the present analysis.

3.3.5 Light collection efficiency corrections

Lateral leakage is changing the amount of energy deposit as a function of position, but there is another effect that, even if energy deposit is the same, will lead to different measured amount of this quantity in different points: this is the non-uniformity in light collection efficiency, due to the optical coupling between scintillator layers and PMTs. Differently from leak-out, light collection efficiency is layer dependent, so we need to define an efficiency map for each layer i

$$\text{Efficiency}_i(x,y) = < \frac{dE_i^{real}(x,y)}{dE_i^{ideal}(x,y)} > \tag{3.11}$$

Efficiency maps were originally measured at the Heavy Ion Medical Accelerator in Chiba (HIMAC) using low energy ion beams. Fig.3.14 shows the results for each scintillator layer of the small tower. These maps are not directly applicable to the case of high energy particles, where some kind of smearing is unavoidable due to the large transverse size of showers. Because of this reason these maps were implemented in the MC geometry of the detector so that for each event we can have information on both dE_i^{real} and dE_i^{ideal}. In this way we obtained the efficiency maps shown in Fig.3.15 and 3.16 using 1 TeV neutrons. As in the leak-out case, light collection efficiency correction factors are given by the bin content of the map itself through linear interpolation between adjacent bins.

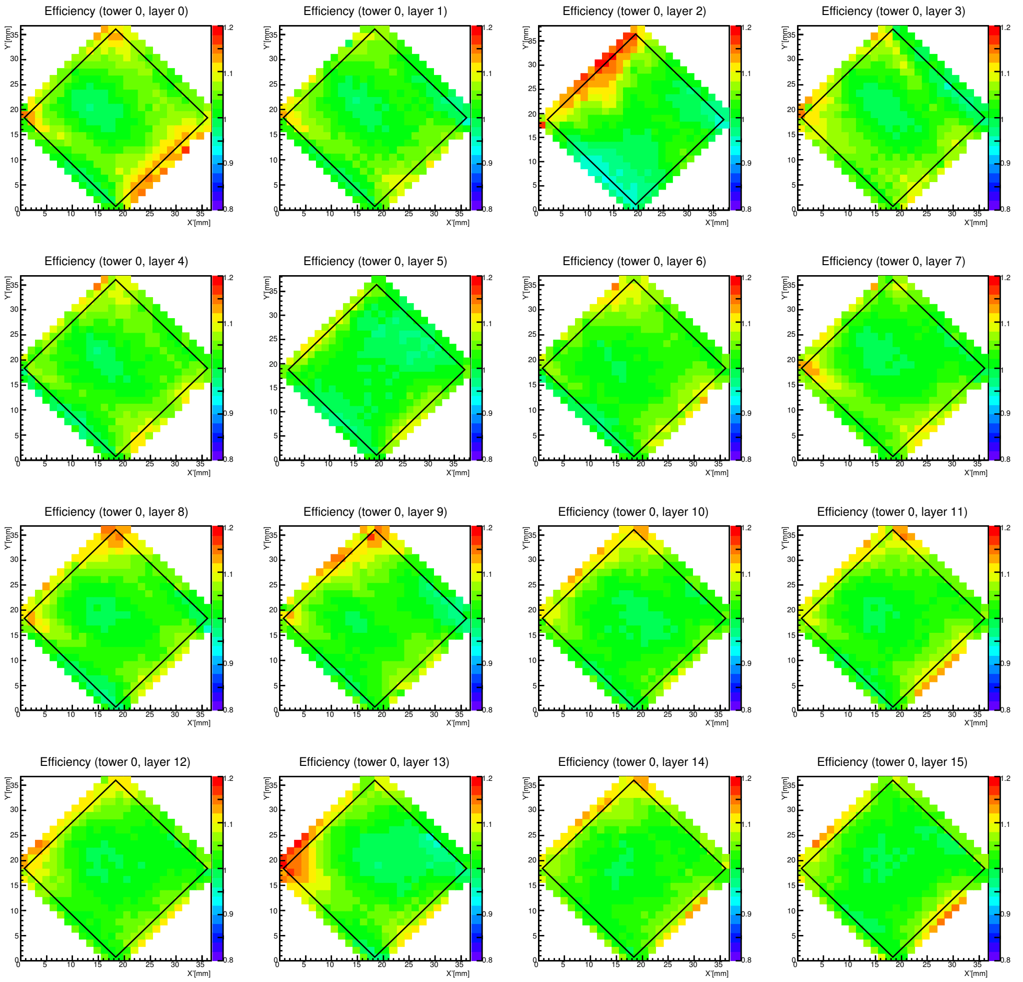

Figure 3.14: Efficiency maps for each layer of the small tower measured using HIMAC data [68]. Data were collected for every point according to a different reference system respect to the one used in this work. Respect to tower RS that we defined, x and y axis are rotated by 45° and x is directed in the opposite way.

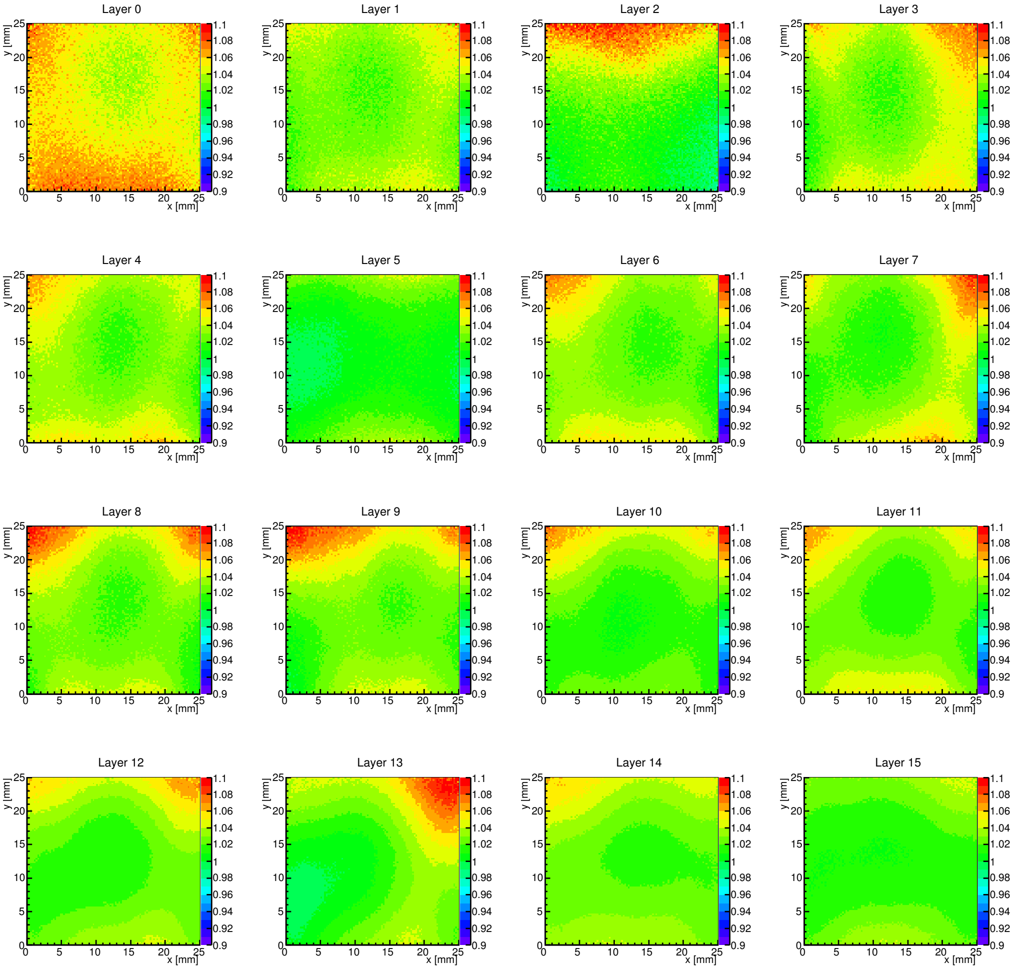

Figure 3.15: Efficiency maps for 1 TeV neutrons on ST.

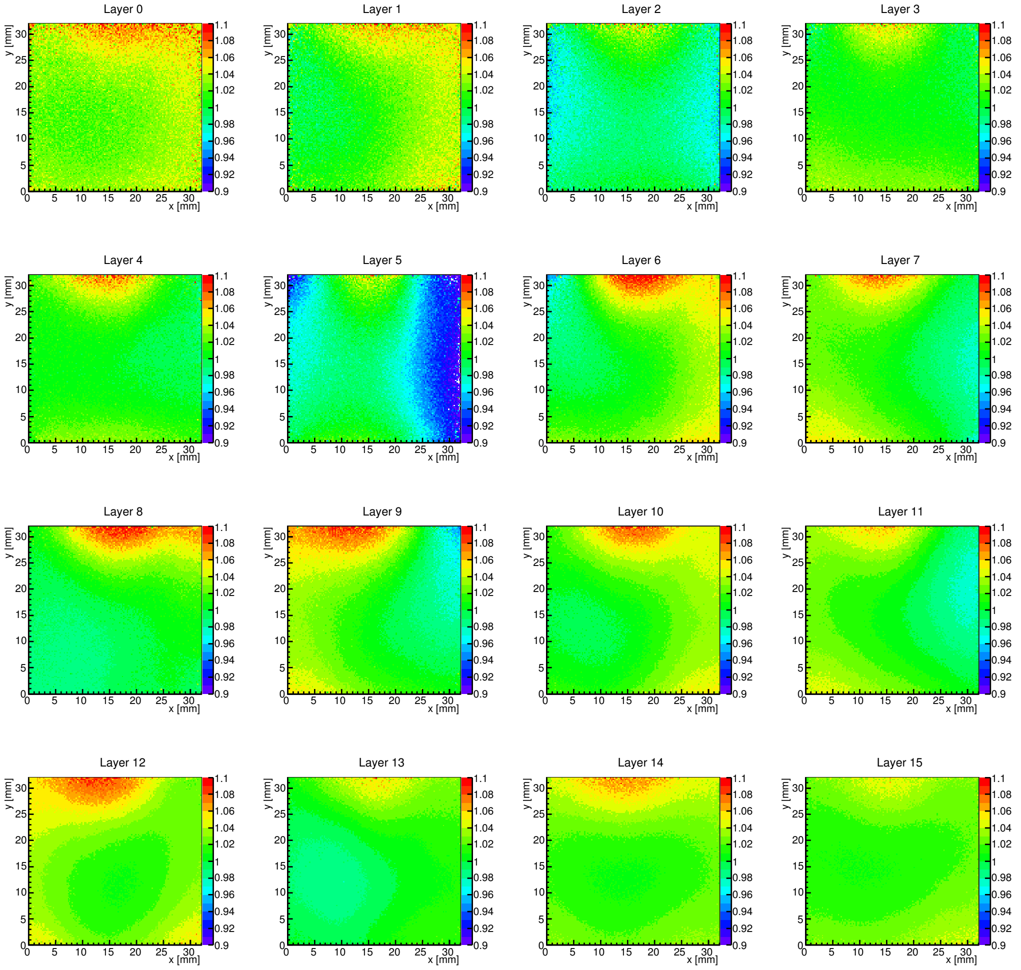

Figure 3.16: Efficiency maps for 1 TeV neutrons on LT.

Similarly to what we described in the previous chapter, we checked the energy dependence of efficiency, repeating the same procedure for 500 GeV and 4 TeV neutrons. Fig.3.17 and Fig.3.18 show the ratio of efficiency maps obtained at these energies to the one relative to 1 TeV neutrons. If we exclude very limited region near towers edge, energy dependence of efficiency is always less than 1%.

So far we estimated leak-out and efficiency correction factors for 1 TeV neutrons, assuming that they are energy independent. This means that applying these factors to correct the event by event position dependent energy deposit does not insert some bias in the result relative to 500 GeV and 4 TeV neutrons. As a consequence, at the end of reconstruction $< sumdE >$ distribution in each position bin must be consistent with $< sumdE_{center} >$, the average deposit at towers center in the ideal case in which light collection efficiency is 1. This last quantity

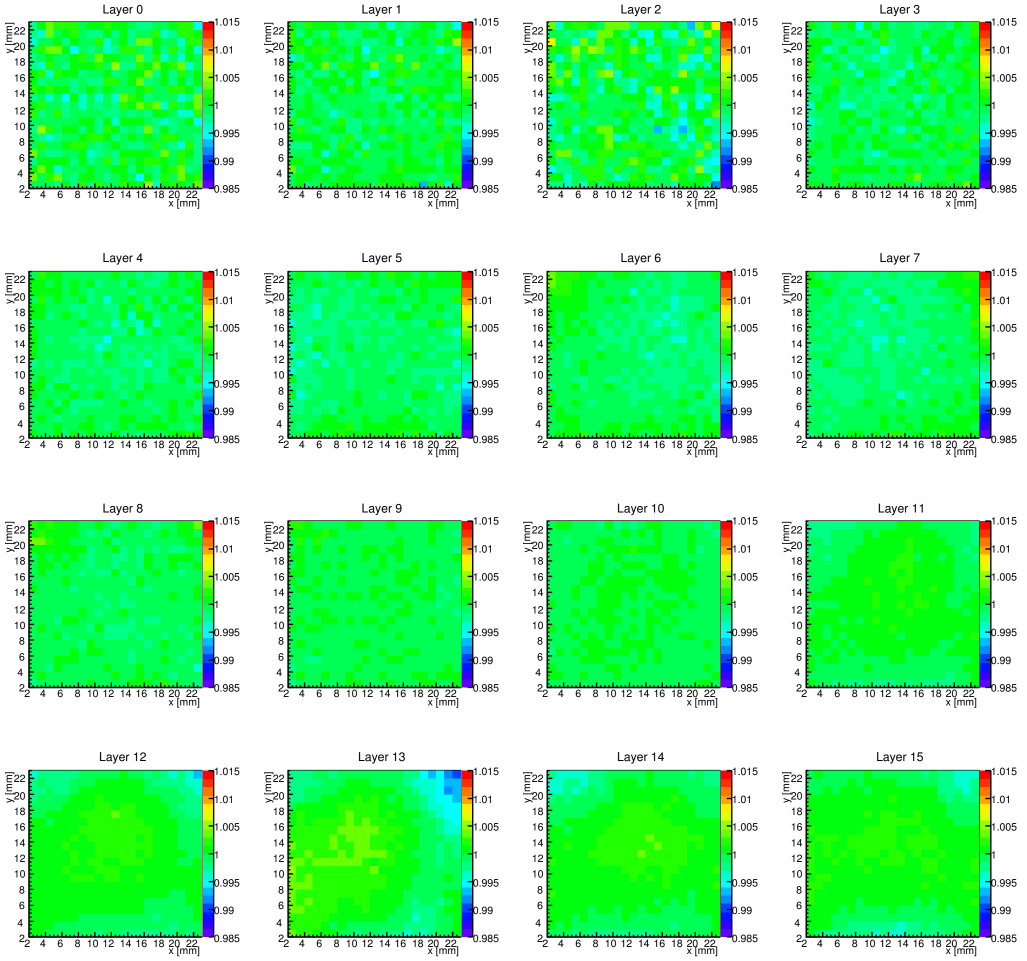

Figure 3.17: Efficiency maps ratio for ST: 500 GeV/1 TeV.

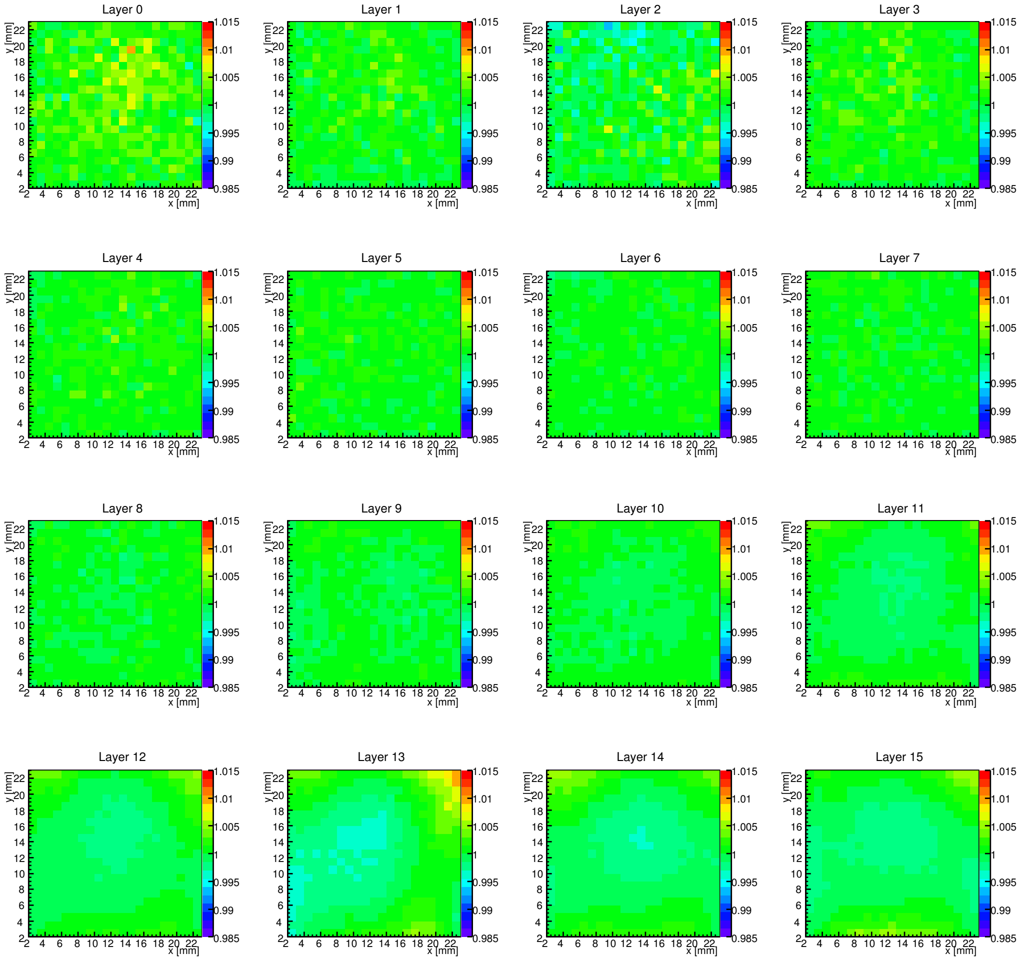

Figure 3.18: Efficiency maps ratio for ST: 4 $TeV/1\ TeV$.

can be estimated using MC simulations employed in §3.3.3. The distributions of the ratio $< sumdE > / < sumdE_{center} >$ using all bins inside the selected pseudorapidity regions are shown in Fig.3.19 for 500 GeV and 4 TeV neutrons. The observed maximum deviation of the mean from 1 is 1.2%, whereas the average value of the four shifts is about 0.6%. Thus we can conclude that the contribution to the systematic uncertainty on the energy scale coming from the energy dependence of leak-out and efficiency correction factors is $\sigma^{mc}_{pos\_dep} = 0.6\%$. Please note that this term does not take into account for fluctuations of the quantity $< sumdE > / < sumdE_{center} >$ around 1. The results in Fig.3.19 shows that this contribution is generally less than 2%, but, as discussed in §3.4, we decided to estimate this uncertainty directly from experimental data at the end of the reconstruction process.

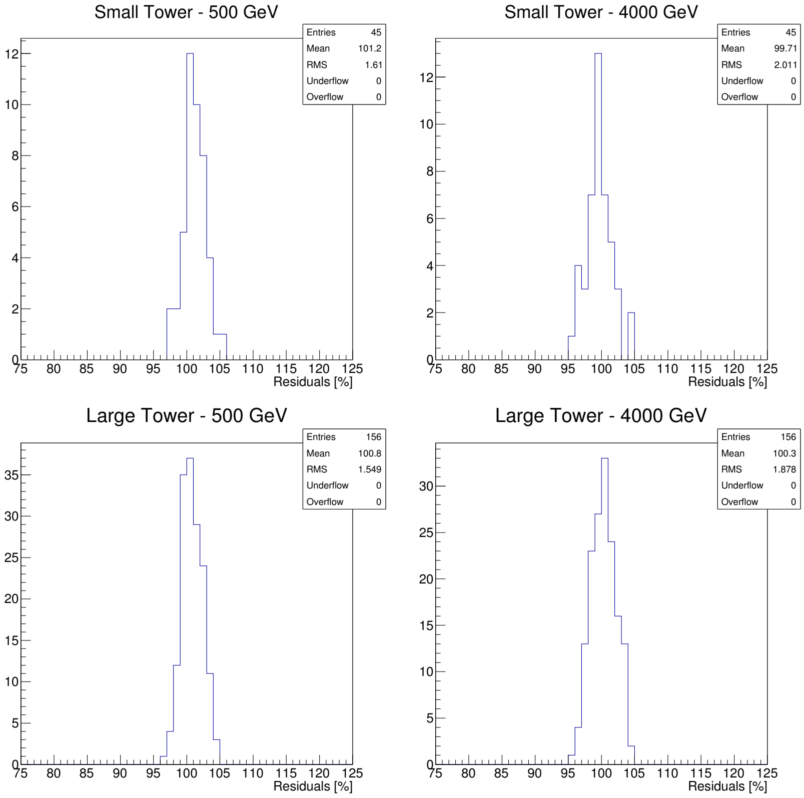

Figure 3.19: $< sumdE > / < sumdE_{center} >$ distributions as a function of position for 500 GeV (left) and 4 TeV (right) neutrons. Top is ST, bottom is LT.

3.4 Comparison of data and MC

The last point of the calibration consists in the reconstruction of both experimental data and MC simulations using all factors determined in §3.2 and §3.3. This is necessary to estimate the two remaining contributions to the uncertainty on the energy scale coming from the calibration process. The first one is related to the fluctuations we have in the reconstruction of the deposited energy in different regions of the tower after the application of position dependent correction factors. The second one is due to the possible presence of some systematic effects in the hadronic interaction model used to estimate the calibration coefficients so that MC simulations do not correctly reproduce experimental data. For these purposes we decided to use the p350GeV and p350GeV@center data set. There are two main reasons for preferring protons at 350 GeV than at 300 GeV: the first one is that the purity of the beam is higher; the second one is that statistics is higher and distributed on the whole towers area.

Event selection criteria applied to experimental data and MC simulations was the same. At first, we selected for both towers only events hitting in the pseudorapidity regions defined for LHC data analysis[6]. Contamination was removed using the condition $L_{2D} > L_{2D}^{thr}$ with threshold values determined in §4.3. Weakly developed shower events were removed applying software trigger condition. For this purpose the threshold was changed from the 600 MeV value defined in §4.3 to 50 MeV for ST and 100 MeV for LT. The choice was motivated by the fact that, as it will be discussed in §3.5, software trigger condition selects only about 8% of events at 350 GeV. This means that we are considering only the high energy tail of the signal in the calorimeter, possibly hiding some discrepancies between data and models in the remaining region, where the energy deposit of most 350 GeV interacting protons is located. Because we can test the agreement between data and models only at low energy, it is important that at 350 GeV all components contributing to the spectra at high energy are considered. Assuming that the shape of the energy deposit scales linearly with the incident energy, if we do not find any strong discrepancy at 350 GeV including all significant contributions to the spectra, we can be more confident on the reliability of models at high energy. Modified software trigger thresholds (50 MeV for ST, 100 MeV for LT) were simply computed scaling the nominal one (600 MeV) by the ratio of the proton energy at SPS (350 GeV) to the average energy of particles produced in p-p collisions at $\sqrt{s} = 13$ TeV (4 TeV for ST, 2 TeV for LT). These last two values were estimated making use of QGSJET II-04 toy MC described in §4.1.2. The last selection is regarding the contamination from multihit events, that, as anticipated in §3.2, was quite strong in the case of the LT. As described in that paragraph, we removed these events making use of both the shower transverse profile in silicon

---

[6] As discussed in §3.3.2, in addition to this selection, it was necessary to remove 10 mm from the left edge of the LT because the ADAMO aluminium frame was covering that region, thus adding some material in front of the Arm2 detector.

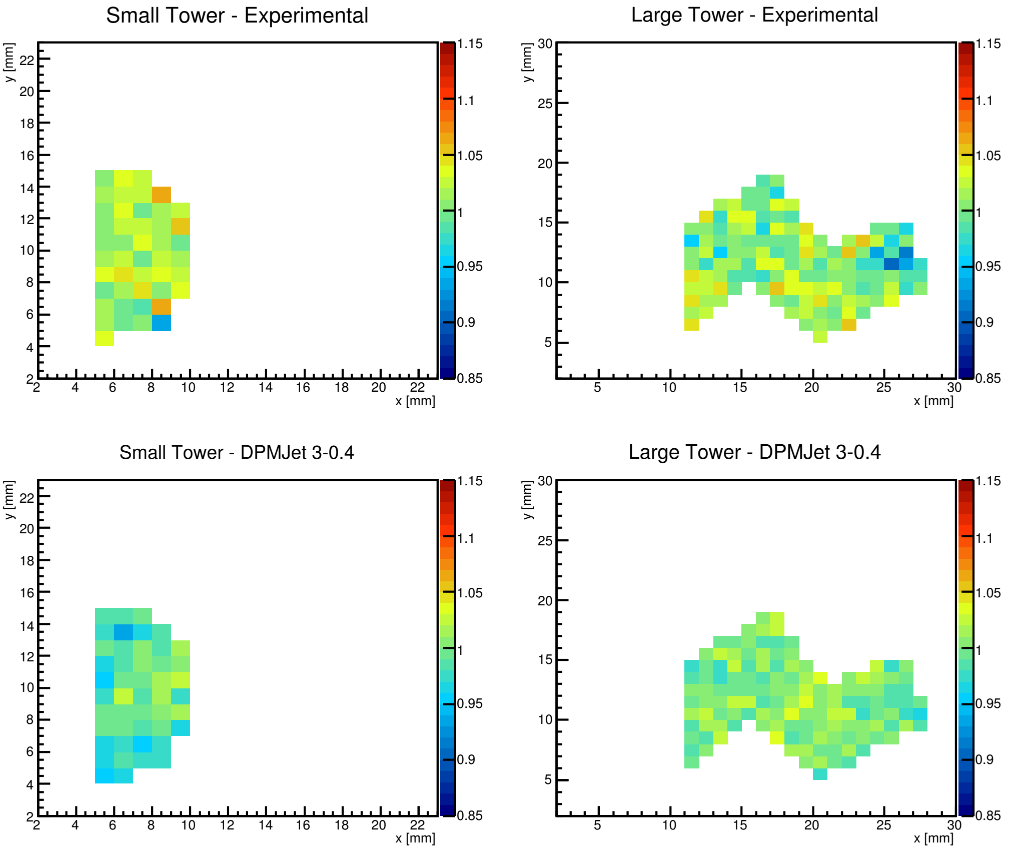
Small Tower - Experimental

Large Tower - Experimental

Small Tower - DPMJet 3-0.4

Large Tower - DPMJet 3-0.4

Figure 3.20: $< sumdE >$ / $< sumdE_{center} >$ for 350 GeV protons as a function of position for ST (left) and LT (right). Top is experimental data, bottom is DPM simulations.

and the total energy deposit in the calorimeter[7]. Because this selection was not enough, we decided to use the ADAMO tracker for this purpose. As we can see from Fig.3.1 ADAMO is placed before LHCf, therefore the energy deposit in it is the typical one of minimum ionizing particles (MIPs). Because of this reason, it is more easy to identify pile-up events searching for peaks in ADAMO than looking at the shower transverse profile in Arm2. All dead and noisy strips in ADAMO were masked, then we considered the central layer to identify multihit events. Definition of multihit event is when there are at least two peaks distant more than 10 strips and having an energy deposit above 50 ADC in the x or in the y view of the central layer.

---

[7] Here we extended the condition on *sumdE* from ±2.5 RMS to ±4 RMS from its average in order to be sensitive to a possible discrepancy between experimental data and MC simulations in the high energy tail of the distribution.

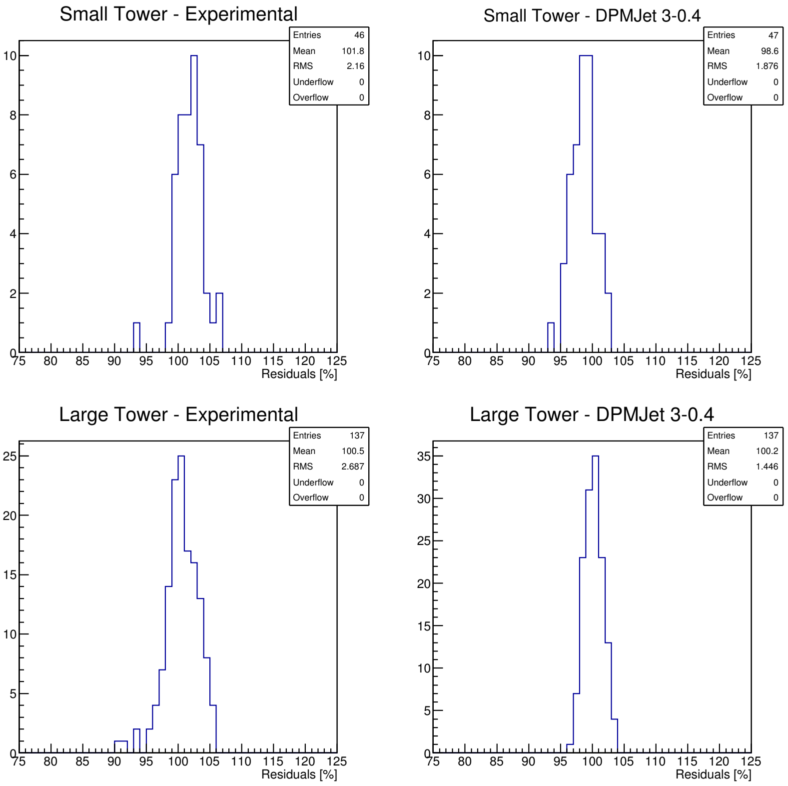

Figure 3.21: Residuals obtained from Fig.3.20 for ST (top) and LT (bottom). Left is experimental data, right is DPM simulations.

In Fig.3.20, it is shown the quantity $< sumdE > / < sumdE_{center} >$ for each position in the three pseudorapidity regions using $1\ mm \times 1\ mm$ bins[8]. We can see that, after applying position dependent correction factors, the distribution is mostly uniform in the regions considered in this analysis. This is true especially for DPM simulations, whereas experimental data exhibit larger fluctuations. In order to take into account this effect, we filled the content of each bin in a histogram and we estimated residuals at the end of reconstruction. This is shown in Fig.3.21, where we can see that again performances for DPM simulations are better than for experimental data. Even if the mean and the RMS of these distributions are mostly consistent with the values observed in Fig.3.19, we can observe that the RMS for 350 GeV protons data is slightly higher not only respect to the MC in the same experimental configuration, but also to the simulations relative to 500 GeV and 4 TeV neutrons. Because of this reason we decided to estimate fluctuations of the quantity $< sumdE > / < sumdE_{center} >$ around 1 using the towers averaged

---

[8] $< sumdE_{center} >$ was computed using a small area around center: $1\ mm \times 1\ mm$ for ST and $2\ mm \times 2\ mm$ for LT.

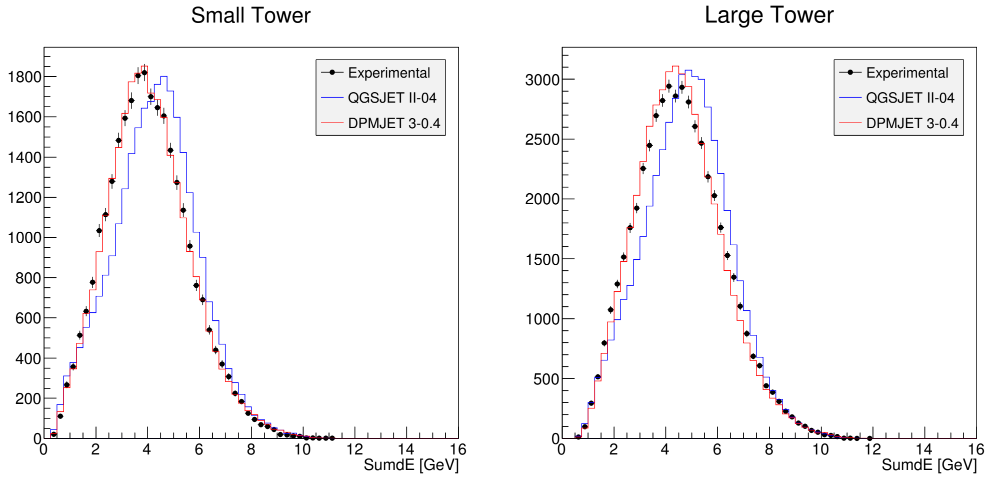

Figure 3.22: *sumdE* distributions relative to 350 *GeV* protons for experimental data and MC simulations. Left is ST, right is LT.

RMS observed in the experimental data set. In this way, the contribution to the systematic uncertainty on the energy scale coming from the position dependence of $< sumdE >$ after applying correction factors is $\sigma^{data}_{pos\_dep} = 2.4\%$.

Observed *sumdE* distributions for experimental data and MC simulations are shown in Fig.3.22. In order to reproduce in the best way the configuration present at SPS, electric noise was added to MC simulations using pedestal events directly taken from experimental data. We can see that DPM model agrees very well with data, whereas QGS model is slightly different. One possible reason for that, aside from differences present in models themselves, is that estimation of position dependent correction factors was carried on using DPM. To quantify the level of agreement we simply made use of the ratio between the mean in MC and the mean in data. This is shown in Tab.3.4, where we can see that the mean of the DPM distribution differs of about 0.6% from the one observed experimentally. Even considering the whole area of the tower removing only 2 *mm* from the edges, this difference is at most 1.2%, well below the 2% uncertainty on conversion factors estimated in §3.2. Thus we can conclude that DPM model is reproducing well the total energy deposit in the calorimeter and there is no need to add a σ_{model} contribution to the uncertainty on the energy scale.

At this point, we estimated all systematic contributions to the energy scale related to the calibration of the detector. Additional terms will be added in §4.7.1.1 to take into account for some effects relative to LHC operation conditions, like radiation damage on scintillators, temperature effects on PMTs, stability of high voltages, ... For the moment we can say that the uncertainty relative to the calibration of the energy scale for the reconstruction of hadronic events is

$$\sigma^{cal}_{E} = \sqrt{(\sigma_{gain})^2 + (\sigma_{ene\_conv})^2 + (\sigma^{mc}_{pos\_dep})^2 + (\sigma^{data}_{pos\_dep})^2} \simeq 3.5\% \qquad (3.12)$$

		Mean [GeV]	σ/Mean [%]	Ratio
Small tower	Experiment	4.041	39.283	-
	QGS	4.310	38.174	1.067
	DPM	4.065	39.430	1.006
Large Tower	Experiment	4.571	36.899	-
	QGS	4.820	34.594	1.055
	DPM	4.542	36.253	0.994

Table 3.4: Mean, energy resolution and mean ratio for distributions shown in Fig.3.22.

3.5 Detector performances

Hadron detector performances have been investigated making use of the same MC set employed in §3.3. It is important to note that monoenergetic neutron simulations at towers center correspond to the best possible condition, so we can expect that we will have slightly worse results when considering the real case. Performances studied here are detection efficiency, energy resolution and transverse position resolution. In order to reproduce the event selection used for the analysis of LHC data, we applied similar selection to the ones defined in §4.3.

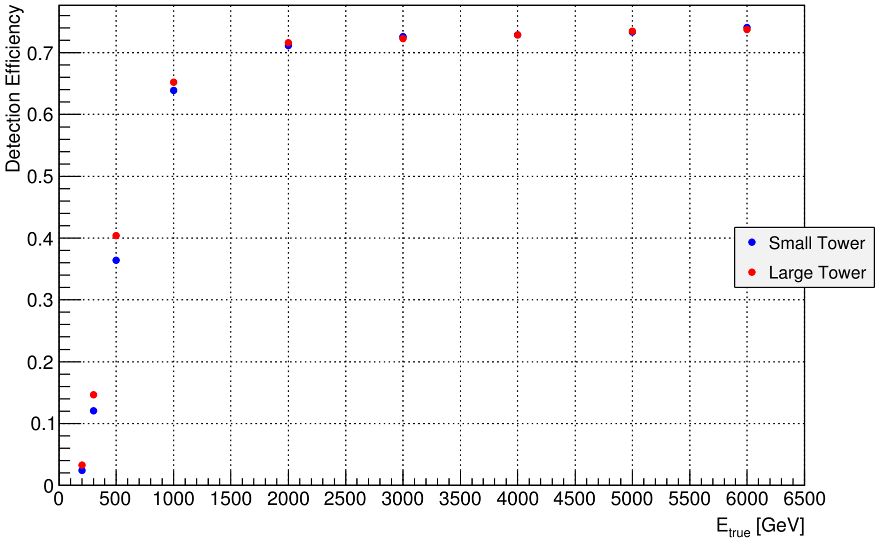

Figure 3.23: Neutrons detection efficiency as a function of energy.

Detection efficiency at a given energy is defined as the fraction of events that pass the software trigger selection respect to the total. This is shown in Fig.3.23, where we can see that it exhibits basically the same trend for both towers: starting from very small efficiency at low energies. it increases up to an approximately constant value of 70% above 2 TeV. This observed behavior reflects the energy dependence of the release in each layer, on which software trigger condition acts, and not of inelastic cross section, that changes less than 5% in the range going from 100 GeV to 6.5 TeV. Because detection efficiency is very small below 500 GeV, we will not consider them in the final results relative to the analysis of LHC data.

Energy resolution, shown in Fig.3.24, was computed using $\mathrm{RMS}_{sumdE}/sumdE$ as a function of the energy among events that pass software trigger and PID selections. The dominant factor is the longitudinal leakage leading to a resolution of about 40% at high energy. On the other side, software trigger has a large impact on the energy dependence of this parameter. This is due to the fact that trigger condition removes poorly developed showers at low energy, therefore decreasing fluctuations. For this reason, energy resolution rapidly worsens from 20% at low energy to 35% around 2 TeV. Above it, software trigger contribution is mostly constant up to 6 TeV, so that resolution increases only slightly, reaching 39% at the highest energy. We can compare the values obtained from simulations to the one shown in Tab.3.4 for the case of 350 GeV protons. It is important to note that event selection is slightly different in the two case: in particular in Fig.3.22 we changed the trigger condition in order to scale 350 GeV to the typical energy for p-p collisions at $\sqrt{s} = 13\ TeV$. Considering this point, the energy resolution observed experimentally (39% for ST and 36% for LT) should match the one shown in Fig.3.24 at the corresponding scaled energies (4 TeV for ST and 2 TeV for LT). As we can see the two different measurements are mostly consistent.

Transverse position resolution, shown in Fig.3.25, was computed using the Full Width Half Maximum (FWHM) of the distribution $d_{reco} - d_{true}$ among events that pass software trigger and PID selections. Here d_{true} and d_{reco} are the coordinates (x or y) obtained from the MC true information and reconstructed position in silicon, respectively. The FWHM was obtained through a fit based on the following parametrization of the Lorentzian function

$$f_{Lorentzian}(x) = \frac{A}{2\pi} \frac{1}{\frac{(x-x_0)^2}{FWHM} + \frac{FWHM}{4}} + B \tag{3.13}$$

We can observe that transverse position resolution improves as energy increases, as a consequence of the higher average deposit in imaging layers. Again it is possible to compare the values obtained from simulations to the ones observed in the case of 350 GeV protons. In order to do this we applied the same procedure described before, using ADAMO for the determination of the true position in the

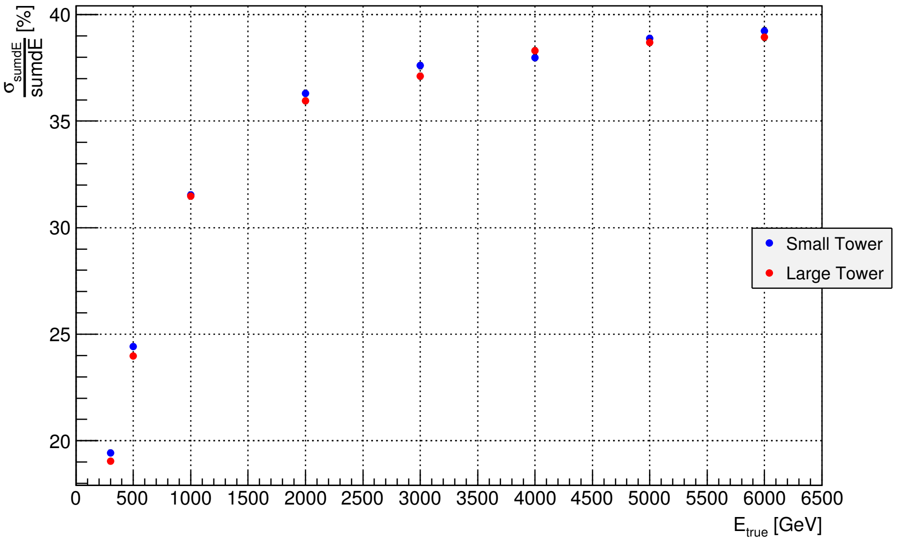

Figure 3.24: Neutrons energy resolution as a function of energy.

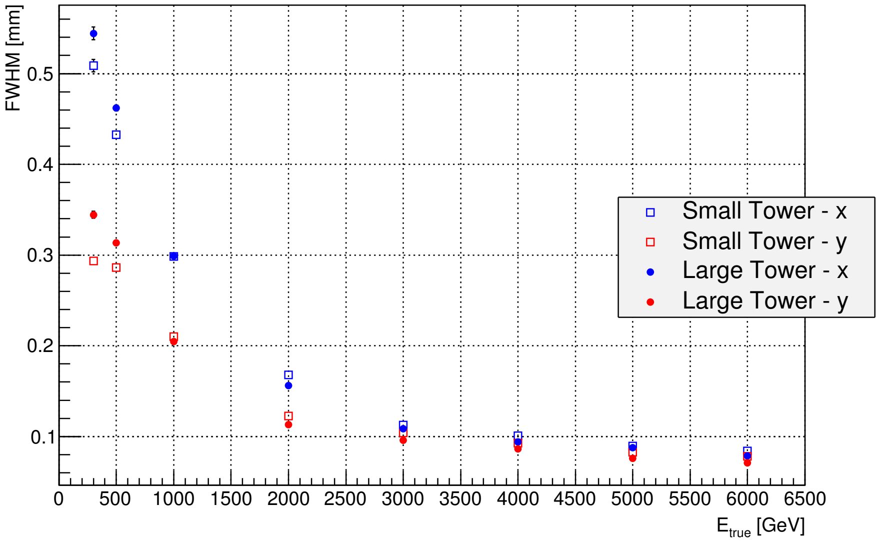

Figure 3.25: Neutrons transverse position resolution as a function of energy.

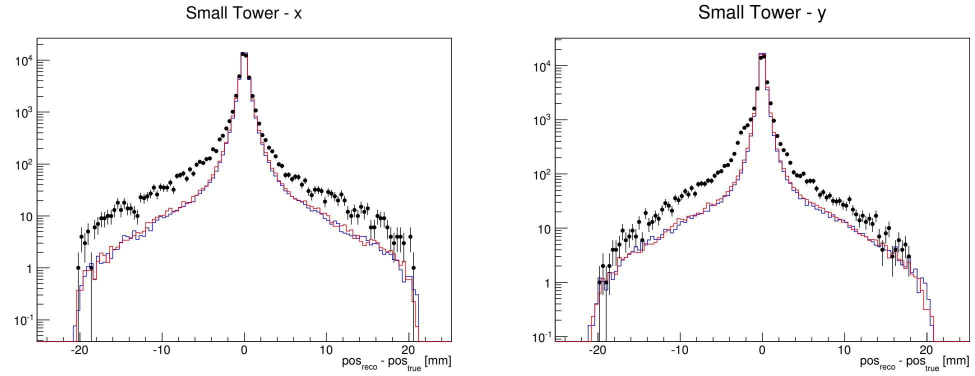

Figure 3.26: Distribution of the difference between the transverse position reconstructed in Arm2 and the one obtained from ADAMO (experimental data) or from the true information (MC simulations) for 350 GeV protons on the ST. The meaning of the colors is the same used in Fig.3.22. Left is x view, right is y view.

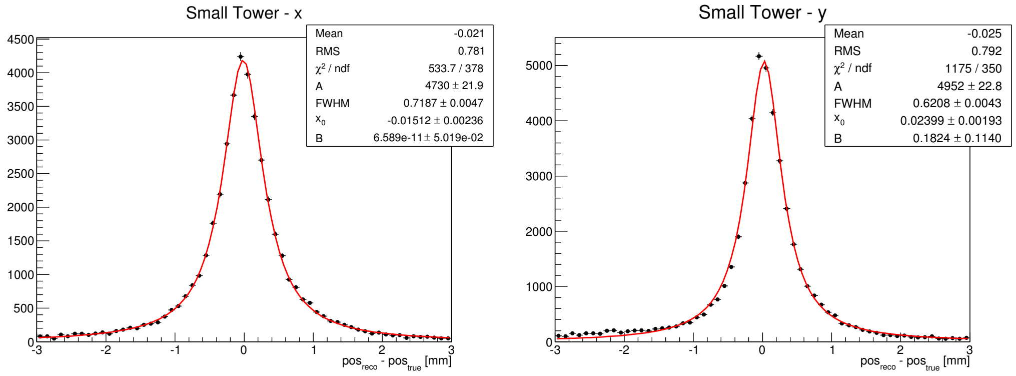

Figure 3.27: Lorentzian fit superimposed to the distribution of the difference between the transverse position reconstructed in Arm2 and the one obtained from ADAMO for 350 GeV protons on the ST. Left is x view, right is y view.

		FWHM-x (μm)	FWHM-y (μm)
Small tower	Experiment	719	621
	QGS	497	372
	DPM	549	419
Large Tower	Experiment	714	586
	QGS	511	367
	DPM	564	415

Table 3.5: FWHM obtained using Lorentzian fit on experimental data and MC simulations for 350 GeV protons.

case of experimental data. For this study we did not select the pseudorapidity regions defined in §4.3, but we used the whole towers area removing only 2 mm from the edges. The distributions obtained in this way are shown in Fig.3.26, whereas Fig.3.27 is relative to the Lorentzian fit for experimental data only. Transverse position resolutions for 350 GeV protons are summarized in Tab.3.5. We can see that FWHM is between 600 and 800 μm with no strong difference between the two towers. Simulations predict better resolution, probably because electric noise was not artificially added in silicon layers. In addition, it is important to note that in MC not only FWHM is smaller, but the impact of tails is reduced as well. If we compare the results obtained from MC for 350 GeV protons with the ones shown in Fig.3.25, we observe that in the first case we get a bit worse performance. This can be due to different particles position distributions and/or different event selection criteria.

Another interesting point is that y resolution is better than x resolution. This is due to the new configuration of the Arm2 upgraded detector shown in Fig.2.5c: the first four silicon layers are coupled in two x-y planes, whereas the x and y views of the last four ones are placed at different depths. Because we reconstruct the position making use of the x-y layers with the highest energy deposit, in the case of hadronic showers we are using the last silicon planes most of the times. The reason of different resolutions between x and y has not been investigated in detail, but it is probably due to the shape of the longitudinal profile, shown in Fig.3.28 for different incident neutrons energies. Even if it is not so easy to conclude something from the energy deposit in scintillators, we can see that in general the release increases up to a maximum value, located between layer 8 and 10, and decreases after that. All last four silicon layers are placed after layer 7, but the y view is always located before the x view. This fact can partially explain the different resolution as a consequence of the fact that determination of impact point is more accurate where energy release is higher. Anyway, a more accurate study of this difference is needed.

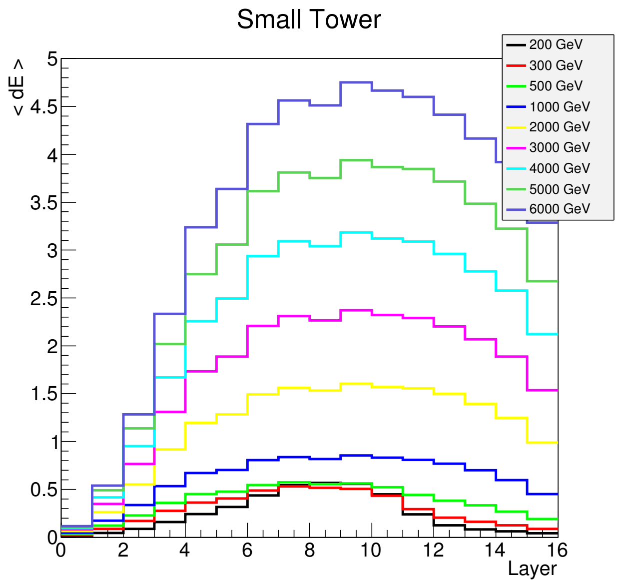

Figure 3.28: Average layer by layer energy deposit in the 16 scintillator layers. Simulations refer monoenergetic neutrons hitting the center of the ST.

3.6 Summary

In this chapter we discussed detector calibration for the reconstruction of the energy of the incident hadron, involving: determination of gains for each scintillator layer of the calorimeter, estimation of conversion coefficients from deposited energy to incident energy, computation of position dependent correction factors. The final systematic uncertainty on the energy scale due to the calibration resulted to be $\sigma_E^{cal} \sim 3.5\%$, adding in quadrature the uncertainty relative to the scintillator gains ($\sigma_{gain} \sim 1.5\%$), conversion coefficients ($\sigma_{ene\_conv} \sim 2\%$), energy dependence and measured efficacy of position dependent correction factors ($\sigma_{pos\_dep}^{mc} \sim 0.6\%$ and $\sigma_{pos\_dep}^{data} \sim 2.4\%$ respectively). Differently from what observed in the past, DPM-Jet 3-0.4 resulted to be in good agreement with experimental data for 350 GeV protons, hence no systematic uncertainty for this effect was introduced. Detector performances, mainly studied making use of monoenergetic neutrons simulation, showed that detection efficiency is about 70% above 2 TeV, energy and position resolution above 350 GeV respectively better than 40% and 1 mm, even if in data we found long tails in position distribution that are not present in MC.

Chapter 4

Data analysis

In this chapter we present the analysis procedure for the measurement of neutrons energy spectra relative to p-p collisions at $\sqrt{s} = 13\ TeV$. For the moment, only Arm2 spectra are available, because Arm1 calibration for the reconstruction of hadronic events is not finished yet. Due to this reason, every time that in the following we refer to LHCf we are implicitly meaning Arm2 only.

The chapter is divided as following. Data sets acquired during operations at LHC and simulations relative to the same experimental configuration are described in §4.1.1 and 4.1.2, then in §4.2 and §4.3 event reconstruction method and analysis selection criteria are discussed. In order to have an idea of what LHCf can observe, a study on generators is presented in §4.4. Finally, determination of correction factors, unfolding and estimation of systematic uncertainties are presented in §4.5, §4.6 and §4.7 respectively.

4.1 Analysis data sets

4.1.1 Experimental data sets

LHCf data relative to p-p collisions at $\sqrt{s} = 13\ TeV$ were acquired at the LHC during a special run between 10 and 13 June 2015. The data set analyzed in this work was taken from 22:32 of 12 June to 1:30 of 13 June, corresponding to LHC Fill n° 3855 and to LHCf Run n° 44299-44472. During this time the beam conditions were the following:

- number of bunches $n_b = 35$ (Beam 1), 31 (Beam 2)
- number of colliding bunches $n_b^{coll} = 29$
- beam crossing angle $\theta_{cross} = -145\ \mu rad$
- $\beta^* = 19.11\ m$

- instantaneous luminosity $L = 0.04 - 0.06\ \mu b^{-1} s^{-1}$

Given the DAQ average live time $\epsilon_{DAQ} = 50\%$ obtained using $\mathrm{N_{L1T\_ENABLE}}/\mathrm{N_{L1T}}$, the total operation time $\Delta t = 9945.67$ s and the instantaneous luminosity L derived from ATLAS measurements, the Arm2 integrated luminosity L_{int} relative to the runs selected for the analysis was estimated to be 0.190531 nb^{-1} [70]. The systematic uncertainty on L_{int} is related to the one on instantaneous luminosity provided by ATLAS, that at the moment is 5% [70], but it may be improved in the future.

Regarding inelastic cross section, ATLAS preliminary measurement leaded to $\sigma_{inel} = 73.1 \pm 0.9(exp.) \pm 6.6(lum.) \pm 3.8(extr.)\ mb$ for p-p collisions at $\sqrt{s} = 13\ TeV$ [71]. Because this result is slightly lower than model predictions at $\sqrt{s} = 13\ TeV$ and it is still a measurement, we decided to estimate the inelastic cross section extrapolating TOTEM results relative to 8 TeV [72], obtaining $\sigma_{inel} = 78.53\ mb$ [70]. The uncertainty on σ_{inel} was not considered in this analysis, because this is just an extrapolation and we expect to update its value using more precise measurements by LHC experiments soon.

In this way we estimated the number of inelastic collisions used for this analysis as $N_{inel} = L_{int} \times \sigma_{inel} = 1.497 \times 10^7$ with 5% systematic uncertainty.

Beam background is discussed in §4.5.1, whereas beam pile-up effect is negligible. This has been estimated considering the average number of collisions per bunch crossing $\mu = (L\ \sigma_{ine})/(f_{rev}\ n_b^{coll}) \sim 0.015$. Assuming Poissonian probability distribution $P(n, \mu)$, pile-up probability is given by $P(n > 2, \mu)/P(n > 1, \mu)$, leading to a value of 0.0072. Taking into account the fact that LHCf acceptance for an inelastic event is about 0.03, we get that less than 0.02% of events involves two or more particles produced in different collisions.

4.1.2 MC data sets

Simulations relative to the same experimental configuration present at the LHC are necessary for four different purposes: estimation of correction factors, validation of the whole analysis procedure, energy spectra unfolding and comparison of model predictions with the final experimental result. We can separate MC in three different categories:

a) simulations requiring full detector simulation, *i.e.* to generate collisions, to propagate products from IP1 to LHCf taking into account the effect of magnetic field and the interaction with the beam pipe and finally to inject them in the detector

b) simulations that require only generation of collisions

c) simulations that require only interaction with the detector.

In the following we will give a description of each MC category.

Among MC samples belonging to category a we can distinguish between three different groups depending on their purpose:

α) estimation of most correction factors and related uncertainties

β) as α but dedicated to multihit, fake and missed events corrections only

γ) validation of the whole analysis procedure

In the following, we will call *toy* MC the ones belonging to groups α and β and *reference* MC the ones belonging to group γ. All these three sets of simulations have been generated making use of COSMOS (v7.645) and EPICS (v9.165) libraries [66]. The Gencol interface is used to simulate single p-p collisions exploiting one of the generators employed in cosmic rays physics. Products of collisions having $\mathrm{p_Z}/p > 0.999999$ are then transported through the beam pipe from IP1 to the TAN region making use of the DoubleArm interface. Interaction of particles during transport can be considered or not: in the first case the DPMJet 3-0.4 model is used to simulate this process. True MC information of incoming particles is saved when particles cross the vertical plane relative to the starting point of the TAN region, located 1.25 m before LHCf detectors. Finally, the End2End interface injects them in LHCf performing a full detector simulation by the use of the DPMJet 3-0.4 model.

Simulations belonging to group α and γ are simulated exactly in the same way and separated in different samples only after that. Three different models have been used to generate collisions: QGSJet II-04, EPOS-LHC and DPMJet 3-0.4. A sample of 10^7 collisions generated using QGSJet II-04 was propagated through the beam line taking into account possible interactions with the beam pipe. In all other samples this possibility was not considered and if a particle interacts with the beam pipe it is simply removed from the output. Using this configuration we simulated 10^8, 5×10^7 and 2×10^7 events for QGSJet II-04, EPOS-LHC and DPMJet 3-0.4 respectively. For each model, about 2×10^7 of them were used as reference sample (γ), whereas the remaining fraction was used as toy sample (α)[1].

Simulations belonging to category γ are dedicated to the estimation of correction factors and relative uncertainties due to multihit, fake and missed events. As it will be described in §4.5.3 and 4.5.4, they require dedicated MC simulations

---

[1] Note that in this way we have toy sample relative to QGSJet II-04 and EPOS-LHC, but not to DPMJet 3-0.4. Being statistics not enough to estimate correction factors, the latter model can be used only as reference MC: anyway, it would be not recommendable to use it as toy MC because, as shown in the neutrons analysis relative to p-p collisions at $\sqrt{s} = 7\ TeV$ [64] and also in the folded spectra presented in the next chapter, it exhibits large deviation not only from other models but from experimental data itself.

using both QGSJet II-04 and EPOS-LHC generators. For this purpose, we chose about 4×10^7 collisions from the group α for which we have full detector simulations. Then we selected only multihit events, we separated the two particles entering the detector considering them as two different events and we simulated again the interaction with the detector, this time one particle at a time. More details about this procedure are given in §4.5.3.

Simulations belonging to group b require only generation of collisions and are dedicated to the comparison of the final experimental result with model predictions, making use of true information taken in the TAN region. These MC data sets were obtained using the Cosmic Ray Monte Carlo package (CRMC) v1.5.6 [73], a very useful interface to generate collisions exploiting one of the models employed in cosmic rays physics. The reason for preferring CRMC to Gencol is that, as discussed in App.A, we found that their results are slightly different and, being CRMC widely used in cosmic rays physics, the comparison of data with its output can be more useful for model developers. Using CRMC we therefore simulated 10^8 events for each one of the following models: QGSJet II-04, EPOS-LHC, DPMJet 3.06 and SIBYLL 2.1. Additionally, 10^8 collisions were generated using PYTHIA 8.212, this time using a standalone software because CRMC does not support PYTHIA 8. Anyway unfolded spectra can not directly be compared to the products of the collisions, because this approach does not take into account the bending effect of dipole magnet and the decay of particles during transport to TAN. Thus, CRMC output was converted to the Gencol format and propagation though the beam pipe was performed using DoubleArm. True information in the TAN region is then used to obtain the energy distributions of particles entering the LHCf detector.

Simulations belonging to category c require only interaction with the detector and are dedicated to spectra unfolding. In order to build the response matrix, single neutrons simulations in the energy range between 0 and 6.5 TeV are needed. For this purpose we decided to get free from model predictions simulating a flat energy spectra uniformly distributed on the whole area of the detector. In the following we call to this simulation set, composed by about 10^7 for each tower, *flat* MC.

As last note, we would like to mention that in case of p-p collisions at $\sqrt{s} = 13\,TeV$, QGSJet II-04 predicts a large number of neutrons having exactly $\mathrm{p_T} = 0\ GeV/c$. According to author's suggestion, in the analysis these events were removed from all simulation data sets relative to this model. More details are found in App.B.

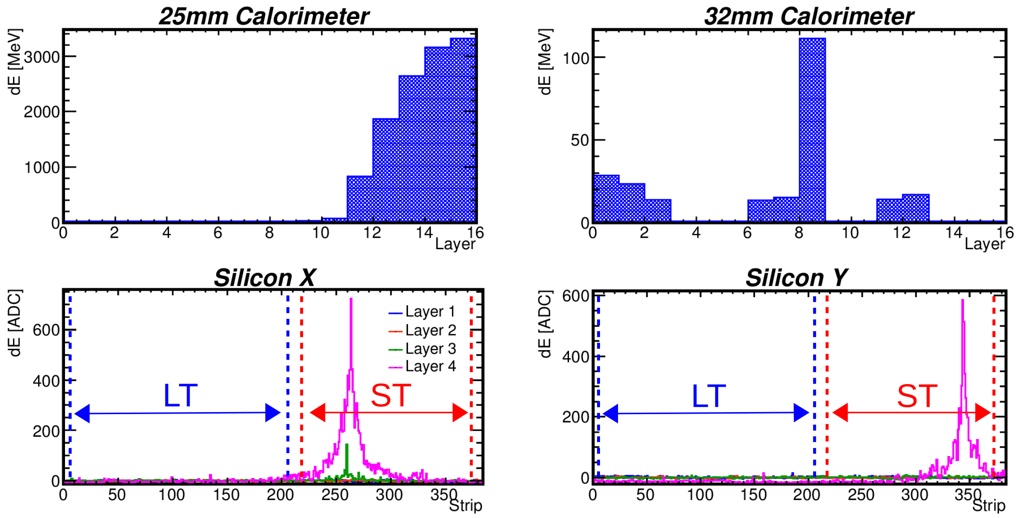

Figure 4.1: Illustration of the interaction of a hadron with the Arm2 ST using an event acquired during p-p collisions at $\sqrt{s} = 13\ TeV$. Top shows the layer by layer energy deposit (in MeV) in scintillators, from which we can measure energy and perform particle identification. Bottom shows the energy deposit (in ADC) in silicon sensors, from which we can measure the transverse impact position. The strips intervals corresponding to the edges of both towers are also indicated.

4.2 Event reconstruction

The reconstruction process of a hadronic event, starting from the DAQ flag up to the PID identification, can be summarized in the following way. Thanks to the L2T_SHOWER flag it is possible to identify events in which at least one of the two Arm detected a shower, removing all other kind of events (pedestals, LASER calibration, ...). After this hardware trigger, we apply a software trigger, defined in §4.3, in order to reject low energy background events from the analysis. At this point, for each triggered event we reconstruct three important quantities: impact point on the detector, energy and identity of the incident particle. For this purpose we exploit the two basic information that we have: the energy deposit in scintillators for incident energy and longitudinal profile; the energy release in silicon sensors for transverse profile and impact position. This is illustrated in Fig.4.1 that is relative to the interaction of a hadron with the Arm2 ST using an event acquired during p-p collisions at $\sqrt{s} = 13\ TeV$. At first, we reconstruct the transverse position employing the x-y couple of the imaging layers on which the energy deposit is maximum. As anticipated in §3.2, we make use of the ROOT TSpectrum class [69] in order to identify the number and the position of the peaks present in the transverse profile. These results are then used as a starting value for a fit based on the superimposition of Lorentzian functions as proposed in [74]. It is important to note here that this fit is performed always assuming a singlehit event because, as discussed later, we decided not to reject multihit due to difficulties to set an efficient algorithm for hadronic showers. All particles whose position is less then 2 *mm* away from towers edge are removed from the analysis because reconstruction performances are very poor. The transverse position obtained by the fit is then used to compute the position dependent factors described in §3.3.4 and 3.3.5 in order to correct the energy deposit in each scintillator layer. At this point it is possible to compute the total energy deposited in the calorimeter *sumdE* and to convert it to the reconstructed energy E making use of coefficients determined in §3.3.3. The quantity measured in such a way is the *hadron equivalent energy*, *i.e.* the energy reconstructed making use of all calibration factors determined for hadron analysis[2]. Finally, the energy measured in scintillator layers give us the opportunity to reconstruct the shower longitudinal profile, thus providing a very simple way to distinguish electromagnetic from hadronic showers. This is performed making use of the cut $L_{2D} > L_{2D}^{thr}$ as described in §4.3.

Because of the present inability of reconstructing multihit events, all events are regarded as singlehit, *i.e.* we associate the energy deposited in the calorimeter to only one particle, we obtain its relative position looking for the maximum peak in the silicon layers and we perform particle identification based on the only value of the L_{2D} parameter that we are able to reconstruct. In order to treat simulations consistently, in multihit events we associated the variables reconstructed in the way just described to the true MC information of the most energetic particle entering the tower. This is not a perfect procedure because, being hadron detection efficiency of about 70%, it is not guaranteed that in a multihit event in which the most energetic particle is a hadron it will actually interact with the detector, leading to an incorrect match between the true and reconstructed information if the second most energetic particle generated the shower. As described in §4.5.3, this difficulty is overcome applying multihit correction factors to data, so that, from this point to the end of the analysis procedure, each particle hitting the detector corresponds to an entry in the energy spectrum, independently from the fact that it was entering the tower as a singlehit or a multihit. Conversely, this means that in all steps before this point - *i.e.* reconstruction of MC simulations, background subtraction and computation of PID correction factors - when we mention the true code of the particle we always refer to the one of the most energetic particle entering the tower.

---

[2] Note that the energy deposit of a photon is about three times larger than the one of a hadron with the same incident energy. Because calibration factors were determined for hadron energy reconstruction, they convert a certain energy release in the detector to the energy of the incident hadron. If we reconstruct the energy of a photon in terms of the hadron equivalent energy we will therefore get a value that is about three times larger than its true incident energy.

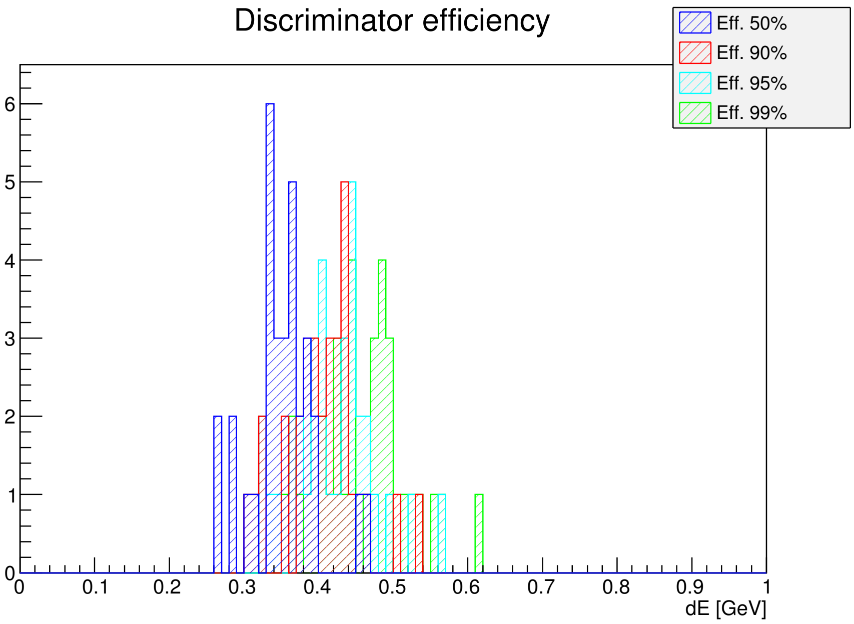

Figure 4.2: Energy distribution corresponding to different discriminator efficiency values for all layers. This figure is realized using the parametric functions for the efficiency curves determined in [70].

4.3 Event selection

Event selection is based on four simple conditions: software trigger, energy threshold, pseudorapidity regions and particle identification.

4.3.1 Software trigger

As it will be discussed in §4.4, interaction of particles with the beam pipe generates a background in the low energy region up to about 250 GeV. The LHCf trigger has been therefore chosen in order to select only high energy particles produced by collisions. As described in §2.4.2, this hardware trigger is equivalent to an energy deposit on at least three consecutive layers greater than some discriminator-dependent threshold values. Definition of software trigger is the same as hardware one, but in this case we want to fix the same threshold value for all layers in order to get free from differences in discriminator efficiency curves. Fig.4.2 shows the energy distribution corresponding to different efficiency values for all layers, obtained making use of parametrization determined for each discriminator in [70]. We can see that all discriminator reach 99% efficiency for an energy deposit less than 600 MeV with the only exception of layer 8 of LT. In any case deviation from

1 is less than 5% so that it is reasonable to define *software trigger condition* as an *energy deposit greater than* 600 MeV *in at least 3 consecutive layers.*

4.3.2 Energy threshold

Software trigger condition just described imposes a minimum energy deposit detectable by LHCf. In addition, it is not recommendable to include the very low energy region in the analysis because of background. Thus, in order to keep detection efficiency enough high and background contamination enough low, we decided to set the starting point of the final energy spectra to 500 GeV. As we can see from Fig.3.23 and it will be shown in Fig.4.11, this condition ensures a detection efficiency above 30% and a background contamination below 5% considering the whole energy range. As discussed in 4.5.1, events originated by the interaction of particles with the beam pipe that survive to this selection will be later removed. Even if we set the starting point of the unfolded energy spectra to 500 GeV, we found that considering an additional bin ($250 - 500$ GeV) below this energy improves unfolding performances. Because of this reason the energy threshold was fixed to 250 GeV throughout the analysis and this bin will be removed only in the final spectra after unfolding[3].

4.3.3 Pseudorapidity regions

Pseudorapidity regions selected for neutron analysis in p-p collisions at $\sqrt{s} =$ 13 TeV are the same used in the case of 7 TeV [64]. These intervals are chosen taking into account the different acceptance of Arm1 and Arm2, in order that it will be possible to combine the two different measurements in the final result. Conventionally each region is called with a progressive number starting from 0 to 2, in order of decreasing η. Pseudorapidity region 0 corresponds to $\eta > 10.76$ and $\Delta\phi = 180°$, pseudorapidity region 1 to $8.99 < \eta < 9.22$ and $\Delta\phi = 20°$, pseudorapidity region 2 to $8.81 < \eta < 8.99$ and $\Delta\phi = 20°$. Fig.4.3 shows these three pseudorapidity regions seen in the upstream LHC reference system, where the real beam center position observed in the runs selected for the analysis was already taken into account. In the case of pseudorapidity region 0, the $\Delta\phi$ coverage is half the one used in the analysis at 7 TeV, because beam center resulted to be too much close to the right edge of small tower.

4.3.4 Particle Identification

Two different kinds of particles reach LHCf: photons and hadrons (mainly neutrons, Λ^0 and K^0). Because there is no significant difference between the showers

---

[3] The reason for not including even a bin below 250 GeV is that in this region we have small detection efficiency, high background contamination and large photon/hadron ratio, so that correction factors would be incredibly huge here.

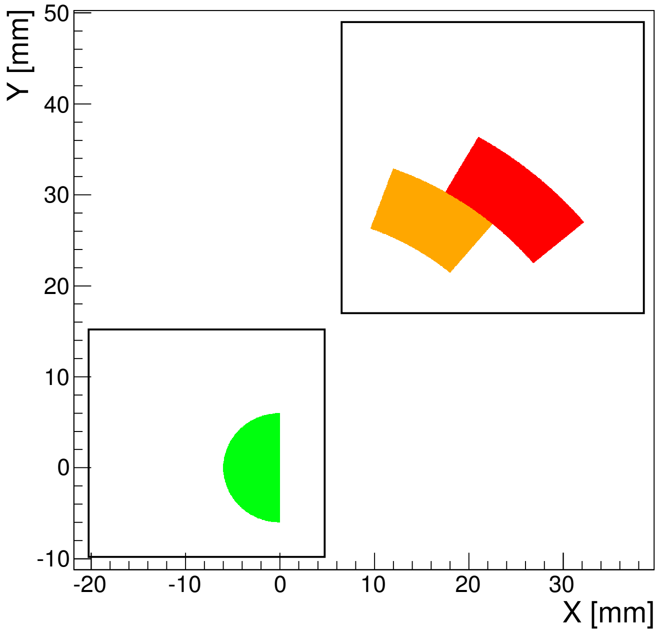

Figure 4.3: Illustration of the three pseudorapidity regions seen in the upstream LHC reference system: 0 (green), 1 (yellow) and 2 (red). Black squares show the edges of small tower and large tower. The origin corresponds to the observed beam center position relative to the runs selected for the analysis. For a detailed description of the LHC reference system see §3.3.2.

of different hadrons, the results relative to hadrons analysis will unavoidably include all of them. Exploiting the different features of electromagnetic and hadronic showers, it is instead possible to separate photons from hadrons events. The most powerful mean to perform particle identification in LHCf is the shower longitudinal profile. The reason for this is that hadronic showers develop much more slowly than electromagnetic ones. This is shown in Fig.4.4a for incident photons (red) and hadrons (blue) in the case of pseudorapidity region 0. The quantity reported here is the layer by layer average deposit obtained using a QGSJet II-04 sample, even if the choice of the generator has a weak impact on this discussion. Note that, as in the case of $sumdE$ reconstruction, the average energy release $< dE_i >$ in each layer i is multiplied for its relative sampling step n_i. We can clearly see the difference between the two kinds of showers, with the electromagnetic one reaching the maximum energy deposit in layer 4 and the hadronic one being much wider and releasing most of its energy around layer 10. This difference is even more clear, if we consider the average transition curve, *i.e.* the fraction of energy deposited from layer 0 to the given layer respect to the total energy release. As shown in Fig.4.4b, this curve increases rapidly in the photon case, reaching the value of 90%

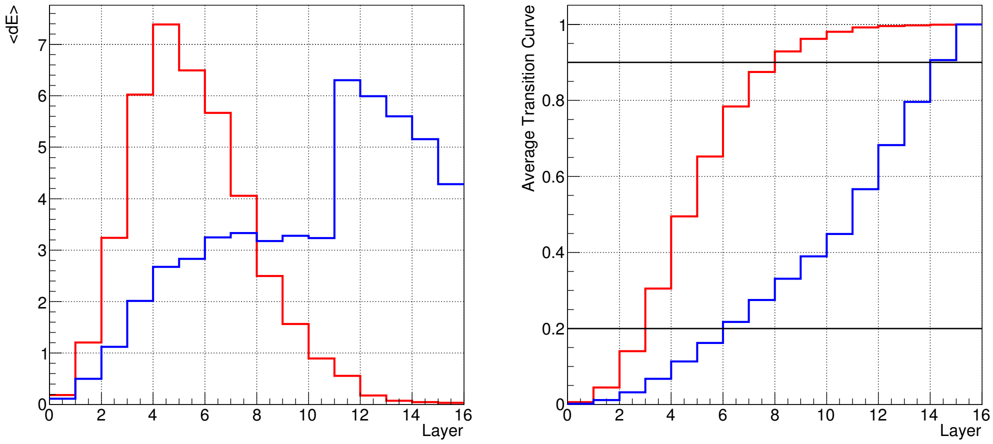

(a) **(b)**

Figure 4.4: Average layer by layer energy deposit (a) and average transition curve (b) for photons (red) and hadrons (blue) hitting the pseudorapidity region 0. Both quantities were obtained using a QGSJet II-04 sample. The two black solid line in (b) represent the 20% and 90% values of the transition curve.

before layer 8, thing that happens only after layer 14 in the hadron case. On this basis, we can define the variable $L_{X\%}$, expressed in units of radiation length ($r.l.$), that represents the depth at which transition curve reaches the $X\%$ value, *i.e.* the distance from the beginning of the calorimeter defined in such a way that the energy deposit up to it is equal to the $X\%$ of the total amount. Two quantities are particularly interesting, $L_{20\%}$ and $L_{90\%}$, corresponding to the 20% and 90% of the energy release. It has been shown in a previous study [67] that the best discrimination power of hadronic from electromagnetic showers can be obtained using the following variable

$$L_{2D} = L_{90\%} - 0.25 \cdot L_{20\%} \tag{4.1}$$

Fig.4.5 shows the scatter plot of $L_{90\%}$ versus $L_{20\%}$, with the same meaning of colors as in Fig.4.4. We can see that the two categories of events are well separated by the black line that corresponds to L_{2D}^{thr}, a fixed threshold value of L_{2D}. Thus, in this work particle identification is performed tagging all particles with $L_{2D} > L_{2D}^{thr}$ as hadrons and the remaining ones as photons. For each pseudorapidity region, the threshold value L_{2D}^{thr} was chosen in order to maximize the product efficiency × purity. If we define N_a^b as the number of type a particles identified by the condition on L_{2D} as type b particles, efficiency ϵ and purity P are defined as follows

$$\begin{aligned} \epsilon &= \frac{N_h^h}{N_h^h + N_h^\gamma} \\ P &= \frac{N_h^h}{N_h^h + N_\gamma^h} \end{aligned} \tag{4.2}$$

where γ stands for photons and h for hadrons.

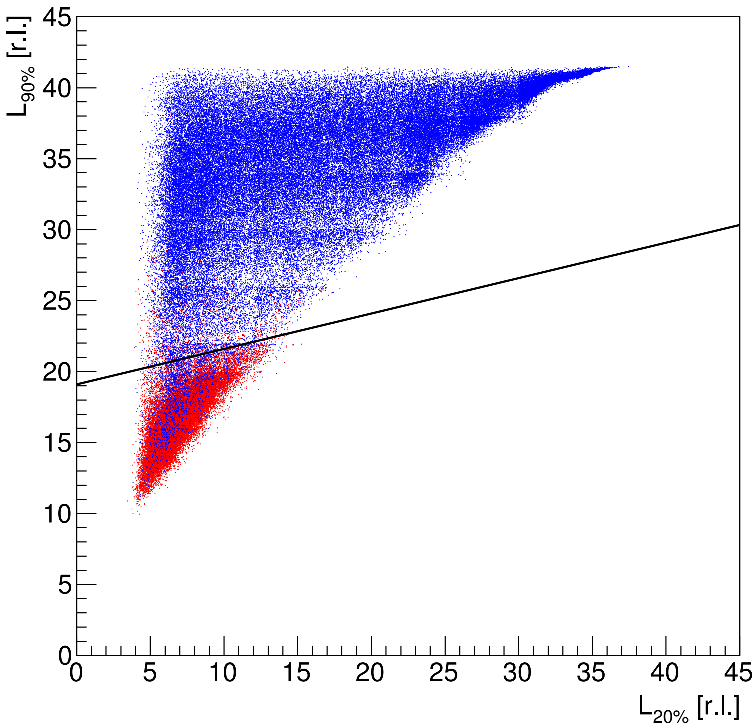

Figure 4.5: Scatter plot of $L_{90\%}$ versus $L_{20\%}$ for photons (red) and hadrons (blue) hitting the pseudorapidity region 0. Both quantities were obtained using a QGSJet II-04 sample. The two black solid line refers to L_{2D}^{thr}, a fixed threshold value of L_{2D}.

L_{2D}^{thr} threshold values were computed separately for each pseudorapidity region using toy MC, proceeding in the following way. After applying the first three selection criteria discussed above, we separately filled L_{2D} distributions relative to hadrons and photons. Then we uniformly scanned the interval going from 0 to 45 X_0 with a sampling step of 0.001 X_0, computing ϵ and P corresponding to each tested L_{2D}^{thr}. At the end, we choose the final threshold value as the one that maximizes $\epsilon \times P$. This is shown in Fig.4.6 for pseudorapidity region 0 in the case of QGSJet II-04 toy MC. No strong model dependence was found comparing results from QGSJet II-04 and EPOS-LHC. This is because L_{2D}^{thr} is mostly sensitive to the model used for the interaction with the detector and only weakly to the different abundances of hadrons and photons in the generator used to simulate collisions. Energy dependence of this parameter was also investigated, repeating the previous procedure for each energy bin in the spectra. Results for pseudorapidity region 0 are shown in Fig.4.7, where we can see that in the low energy region L_{2D}^{thr} values depend more strongly on relative abundances than in the global case. Because identifying a clear energy trend in this threshold is not so easy, we decided to use a energy independent value of L_{2D}^{thr} for each pseudorapidity region. Anyway, this is not a critical point because, as discussed in 4.5.2, we will later apply corrections to take into account limited purity and efficiency of this selection. The final L_{2D}^{thr} computed using QGSJet II-04 toy MC are 19.088, 20.935, 21.014 X_0 for pseudorapidity region 0, 1, 2 respectively.

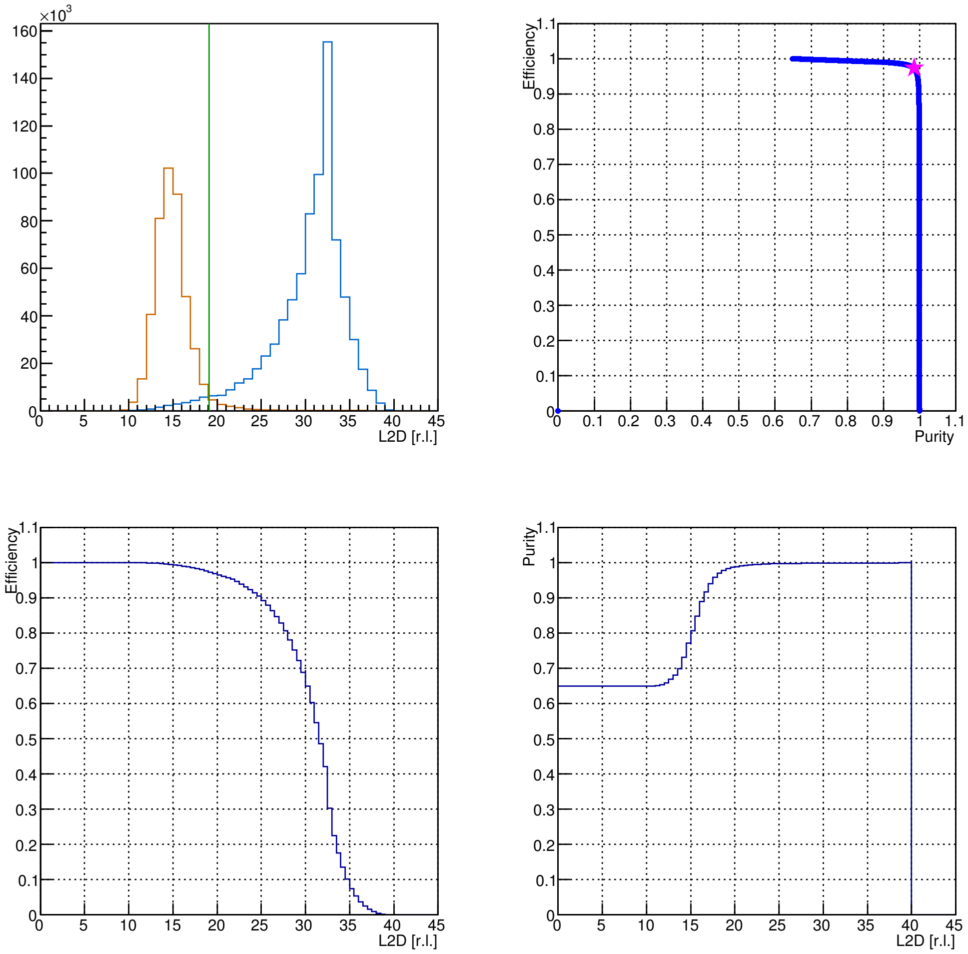

Figure 4.6: Results of energy independent L_{2D}^{thr} study on pseudorapidity region 0 based on QGSJet II-04 toy model. For each region, top left pad is relative to L_{2D} distributions for photons (orange) and hadrons (blue), whereas the remaining three pads show ϵ versus P (top right), ϵ (bottom left) and P (bottom right) as a function of L_{2D}. Green vertical line in first pad indicates the final value of L_{2D}^{thr} and magenta marker in second pad shows the corresponding ϵ and P.

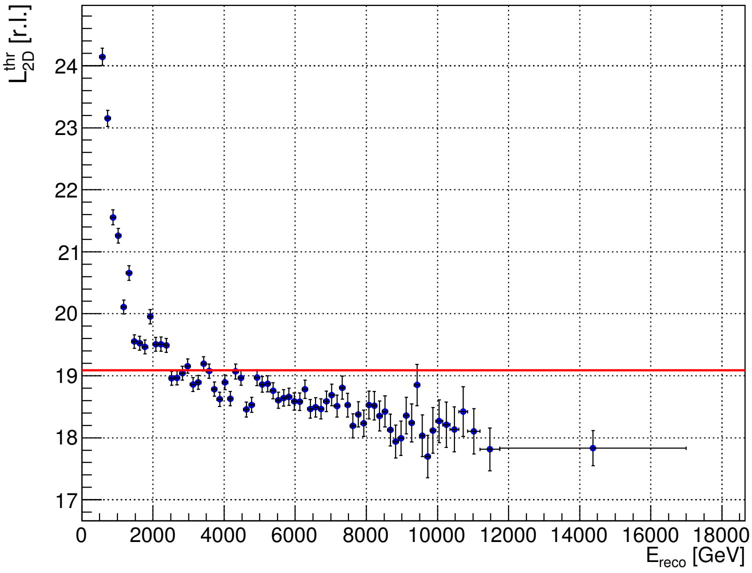

Figure 4.7: Results of energy dependent L_{2D}^{thr} study on pseudorapidity region 0 based on QGSJet II-04 toy model. Each point represents the L_{2D}^{thr} value that maximize the product $\epsilon \times P$ for the corresponding energy interval, whereas red line shows the L_{2D}^{thr} value obtained from energy independent study.

4.3.5 Summary on event selection criteria

Event selection based on reconstructed information involves the following requirements:

- TRG : Software trigger flag on
- E_{reco}^{thr} : $E_{reco} > 250\ GeV$
- FV_{reco} : $(x, y)_{reco}$ inside on of the three pseudorapidity regions
- PID_{reco} : $L_{2D} > L_{2D}^{thr}$

Similarly, event selection based on true MC information requires the following conditions:

- E_{true}^{thr} : $E_{true} > 250\ GeV$
- FV_{true} : $(x, y)_{true}$ inside on of the three pseudorapidity regions
- PID_{true} : Code in range [4, 30][4]

---

[4] This code in EPICS includes all neutral and charged hadrons.

4.4 Preliminary study on generators

In order to have a general idea of what we can expect from measurements and which are the main limitations in our analysis, a preliminary study based on reference MC was carried on. For this purpose, we decided to use the QGSJet II-04 sample that includes interaction of particles with the beam pipe, hence all spectra shown here are relative to 10^7 simulated collisions. Three different points are discussed in this section: the energy distributions of particles generated in the collisions or in the decay of secondaries during transport from IP1 to LHCf; the impact of background due to the interaction of particles produced in the collisions with the beam pipe; the features of multihit events, in which more than one particle produced in the collisions enters the tower at the same time. In all the three cases we considered only particles reaching the LHCf detector and hitting it in one of the three pseudorapidity regions defined. Energy, position and particle identification are directly the ones of true MC information taken at TAN.

True energy distributions for each kind of particle produced in the collision or in the decay of secondaries during transport from IP1 to LHCf are shown in Fig.4.8. We can see that photons spectra is quite soft, being very abundant at low energy and rapidly decreasing after that, while neutrons spectra has a similar behavior in the two regions on LT and exactly the opposite behavior in the one on ST. In addition, due to the strongly focused distribution along beam direction, neutrons abundance in pseudorapidity region 0 is higher than the photons one. Another important point that we must note here is that neutrons are not the only hadrons reaching LHCf, but other neutral and charged hadrons enter the detector. Some of them are directly produced in collisions, like Λ^0 or K^0, other ones are mainly coming from the decay of other particles, like p and π^- resulting from Λ^0 decay after D1[5]. Additionally, some charged particles can be not properly bent or even deviated inside LHCf acceptance by the combination of quadrupole and dipole magnets: this is for example the case of π^- around 3 TeV in LT. The relative percent abundances of all particles above 500 GeV are summarized in Tab.4.1. We can see that in pseudorapidity region 0 about 76% of particles are hadrons, but only 83% of them are neutrons, whereas these two numbers reduce to a bit less than 50% and a bit more than 65% respectively when we consider the other two regions. Because the interaction of hadrons at high energy is basically independent from the type of particle, we have no possibility to separate neutrons from the other hadrons using for example longitudinal profile. It is also difficult to identify charged particles using Front Counter placed before LHCf detectors due to the large low energy background present in that area and, anyway, this would be not so much useful because most abundant hadrons next to neutrons are neutral (Λ^0 and K^0). Therefore, our final measurement will include all detectable hadrons, not only neutrons, but for simplicity *in the following we will use the term "neutron" to refer to "all hadrons reaching LHCf detector"*.

---

[5] Λ^0 has mean life $\tau = 2.6 \times 10^{-10}$ s, corresponding to $c\tau$ of 7.89 cm, therefore only very energetic particles can reach the detector. For example, given the mass m of 1116 MeV, a 1 TeV Λ^0 has Lorentz factor $\gamma \sim 896$, corresponding to $\gamma c\tau \sim 71m$.

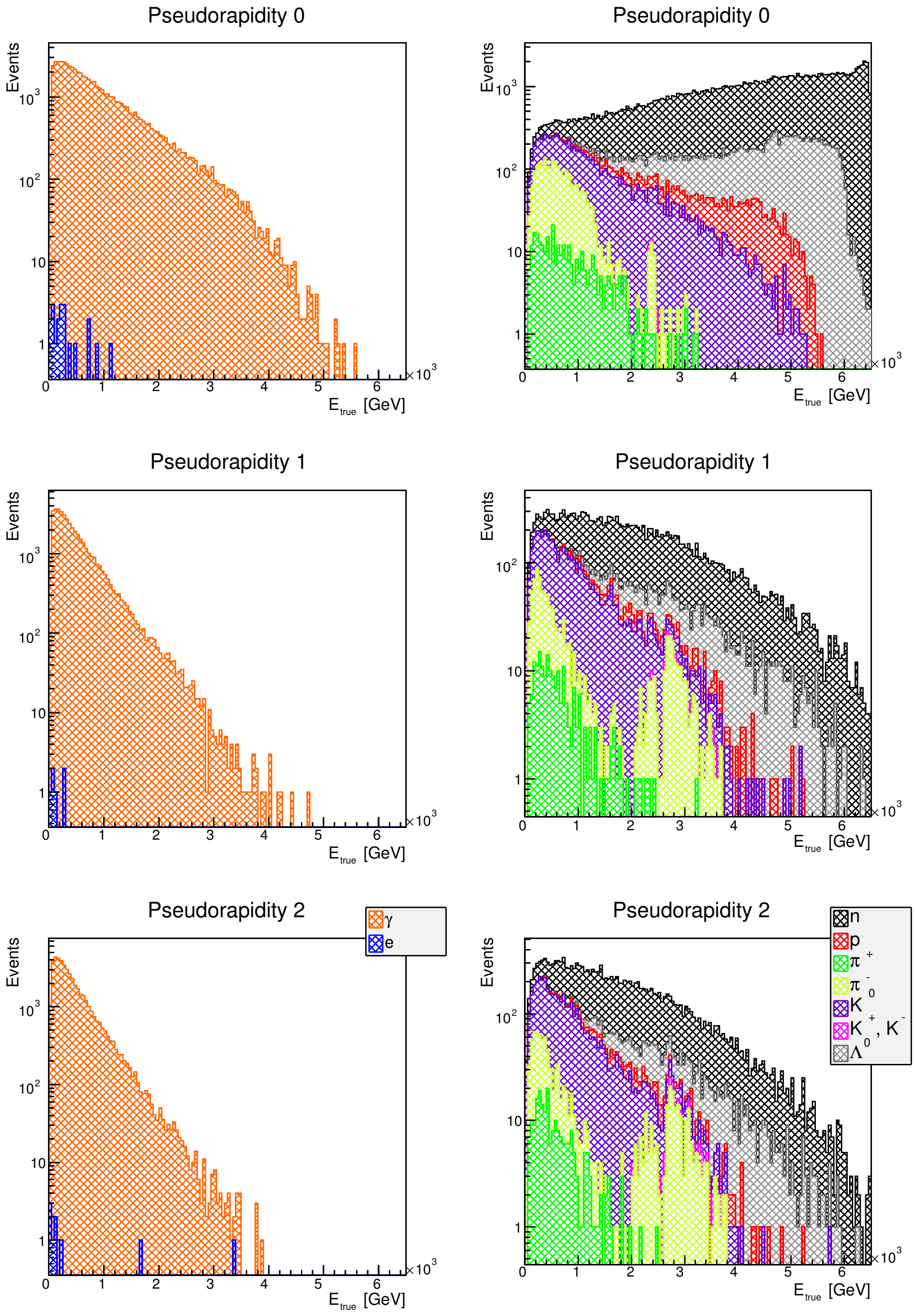

Figure 4.8: QGSJet II-04 true energy distributions relative to collisions products: (a) and (b) refers to particles producing electromagnetic and hadronic showers respectively. Note that histograms are stacked and vertical scale is logarithmic.

	Pseudorapidity 0	Pseudorapidity 1	Pseudorapidity 2
γ	23.883	50.752	52.252
e^-	0.003	0.000	0.007
n	62.925	33.447	31.277
Λ^0	8.057	5.411	5.014
p	1.323	1.293	1.326
π^-	0.766	1.222	1.381
π^+	0.141	0.320	0.362
K^0	2.869	7.353	8.141
K^-, K^+	0.003	0.052	0.095
others	0.007	0.010	0.033
$h/(h+\gamma)$	76.084	49.097	47.595
n/h	82.704	68.124	65.715

Table 4.1: Relative percent abundances of each kind of particle reaching the LHCf detector normalized to the total number of them. The last two lines refers to the fractions of hadrons with respect to all particles and to the fraction of neutrons with respect to all hadrons. All numbers refer to particles above 500 GeV.

Background due to the interaction of particles produced in the collisions with the beam pipe affects the low energy region of secondaries spectra. True energy distributions of such background events in each pseudorapidity region are shown in Fig.4.9, where we can see that this contribution extends up to about 250 GeV. After applying software trigger and energy threshold conditions, this background is strongly reduced. As described in §4.5.3, the fraction of it surviving to event selection is later removed making use of specific correction factors.

Multihit events have a not negligible effect on our analysis, because their identification in the hadron case is very complicated. As anticipated, we decided to reconstruct all events as singlehit and later correct for this effect making use of generators. The validity of this approach depends on how much large are these corrections, therefore a study relative to multihit distributions is necessary. We call multihit an event in which there are more than two hits in the same tower, where a hit is defined as whatever particle having more than 10 GeV reaching the detector. Note that at this level "reaching the detector" does not mean that there is an interaction, as discussed in §4.2. It is possible to distinguish between three different types of multihit events: photon-photon ($\gamma - \gamma$), hadron-photon ($h - \gamma$) and hadron-hadron ($h - h$). The corresponding energy distributions are shown in Fig.4.10. $\gamma - \gamma$ events, originated mainly from Type-II π^0, are not a serious problem in the case of hadron analysis because their longitudinal profile

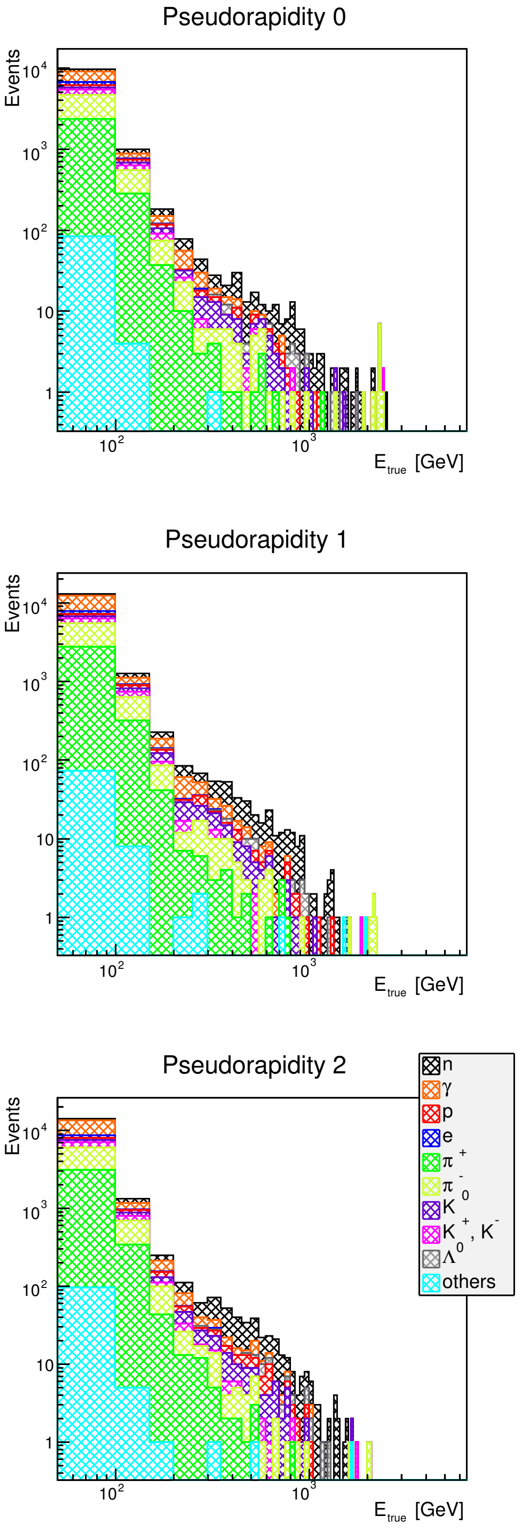

Figure 4.9: QGSJet II-04 true energy distributions relative to the background coming from the interaction of particles produced in the collisions with the beam pipe. Note that histograms are stacked and both scales are logarithmic.

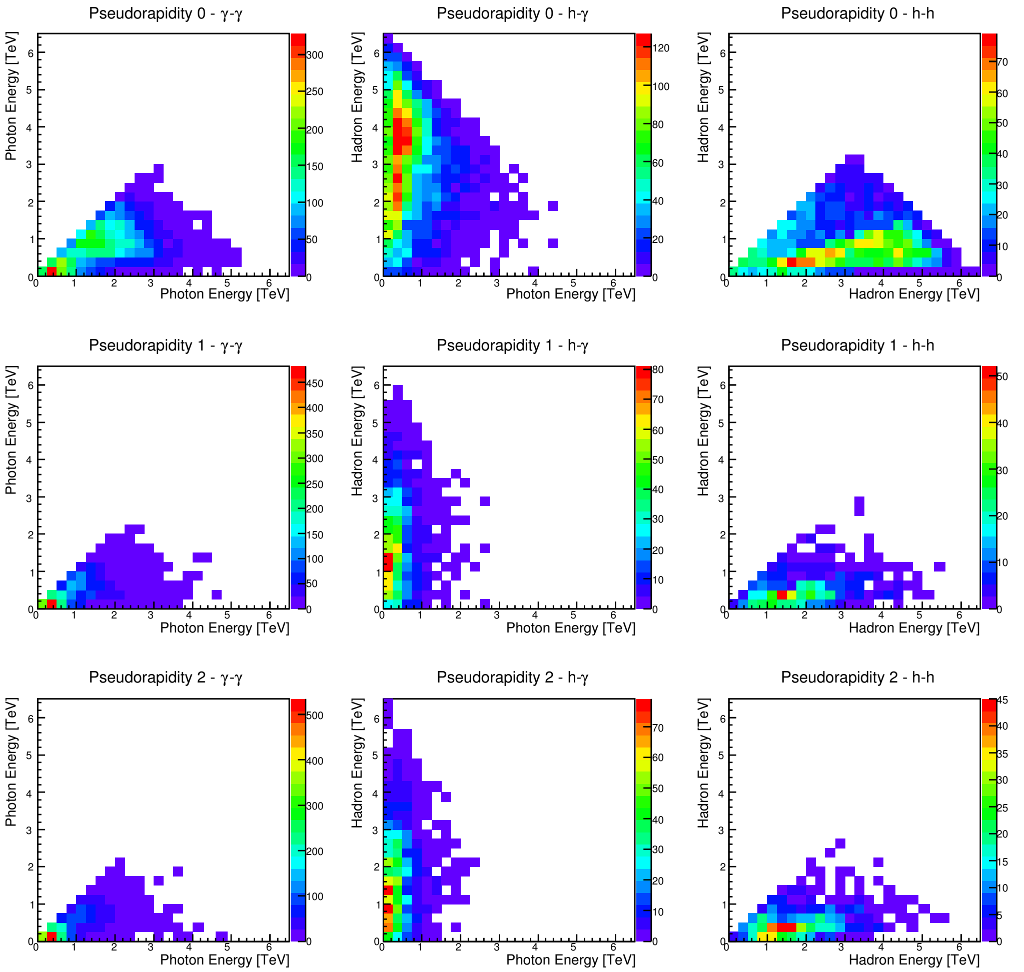

Figure 4.10: QGSJet II-04 true energy distributions for multihit events in the cases of photon-photon (left), photon-hadron (middle) and hadron-hadron (right).

	Pseudorapidity 0	Pseudorapidity 1	Pseudorapidity 2
N_t	10.7	9.3	9.0
$h-h\ /\ N_t$	2.3	1.3	1.3
$\gamma-h\ /\ N_t$	4.4	2.9	2.7
$\gamma-\gamma\ /\ N_t$	4.0	5.1	5.1
N_h	10.0	14.3	15.4
$h-h\ /\ N_h$	3.5	4.4	4.9
$\gamma-h\ /\ N_h$	6.6	10.0	10.4

Table 4.2: Percent fraction of multihit events entering the Arm2 detector in one of the three pseudorapidity regions. They are divided in the following three categories: $\gamma-\gamma$, $\gamma-h$, $h-h$. The denominator is expressed both in terms of N_t (top), the number of photons and hadrons events, and of N_h (bottom), the number of hadrons events only.

is similar to a single γ interaction and, therefore, they are removed by the PID selection. The other two categories show a common feature: either the lowest energy particle is a photon or a hadron, the highest energy particle is generally much more energetic than it. This is an important point, because it means that if both particles interact and we reconstruct the event as a singlehit we do not have a large error on the energy measurement of the most energetic hadron. To be more precise we must observe that, being the energy deposit of a photon about three times larger than the one of a hadron of the same energy, in some cases the energy measurement can be strongly affected even by a low energy photon. This is only partially true, because if the photon energy deposit starts to be significant the PID selection will likely remove the event. Anyway, even if distortion in the spectra due to multihit effect is not so strong, we will need a kind of correction to take into account hadron events whose energy is improperly reconstructed or that are removed from distributions.

The fraction of multihit events is shown in Tab.4.2. This quantity takes into account only events in which there is at least a particle in the given pseudorapidity region, *i.e.* the numerator is the number of multihit events in which one of the two most energetic particles passes FV_{true} selection and the denominator include all singlehit and multihit events satisfying the FV_{true} condition. Multihit represent a fraction going from 9 to 10% of the total number of events, depending on the pseudorapidity region. The dominant contribution in the LT is $\gamma-\gamma$ (5%), probably because hadrons flux is not so high as in the ST, where $\gamma-\gamma$ and $h-\gamma$ have almost the same impact (4%). $h-h$ multihit are below 3% in all the three cases. In order to have a better idea of the impact that multihit can have on the hadron energy spectra, in Tab.4.2, fraction is expressed not only with respect to all events, but also with respect to hadrons events only. In this last case, the fraction of multihit is basically the same in ST (10%), but it increases up to 14-15% in the case of LT. About the type of hadron involved in multihit events, it is approximately distributed according to the same abundances of singlehit events (in decreasing order neutrons, Λ^0 and K^0) in the case of $h - \gamma$. In the case of $h - h$, 53-60% of events come from Λ^0 decay in $p + \pi^-$ very near to the detector, depending on the pseudorapidity region. This number is quite large if we consider that the second most abundant $h - h$ multihit ($n + n$ in pseudorapidity region 0 and $\pi^+ + \pi^-$ in pseudorapidity region 1 and 2) is less than 15%.

4.5 Correction factors

Neutron analysis requires the estimation of several correction factors in order to cope with different effects. We can divide them in two categories depending on if they are applied before or after unfolding. To the first group belong background, PID, multihit and fake events corrections, whereas to the second group belong missed events corrections only. The order in which these factors are applied to data is exactly the same in which they were mentioned. All these corrections were estimated making use of toy MC relative to QGSJET II-04 and EPOS-LHC models. The choice of these two generators is due to the fact that they resulted to be the most reliable ones in the very forward region, as confirmed by previous measurements from LHCf and from other LHC experiments.

4.5.1 Background corrections

Background in reconstructed spectra is due to two different interactions that can take part during transport from IP1 to LHCf: particles produced in the collisions with beam-pipe and protons constituting the beam with gas in vacuum. The second contribution can be estimated using events triggered by non-colliding bunches: this study was not carried on so far for neutron analysis, but results for photon analysis showed that this background is below 1% [70], hence we decided to neglect this effect. The first contribution can be estimated making use of the only toy MC where this effect was simulated: background correction factor for the energy bin i is

$$C_i^{BG} = \frac{E_i^s}{E_i^s + E_i^{bg}} \tag{4.3}$$

where E_i^s and E_i^{bg} represent the number of entries in the energy bin i associated to signal (p-p collisions) and background (beam pipe interactions) respectively. Corrections factors are shown in Fig.4.11, where we can see that they range from about 5% around 500 GeV to less than 1 % above 1 TeV.

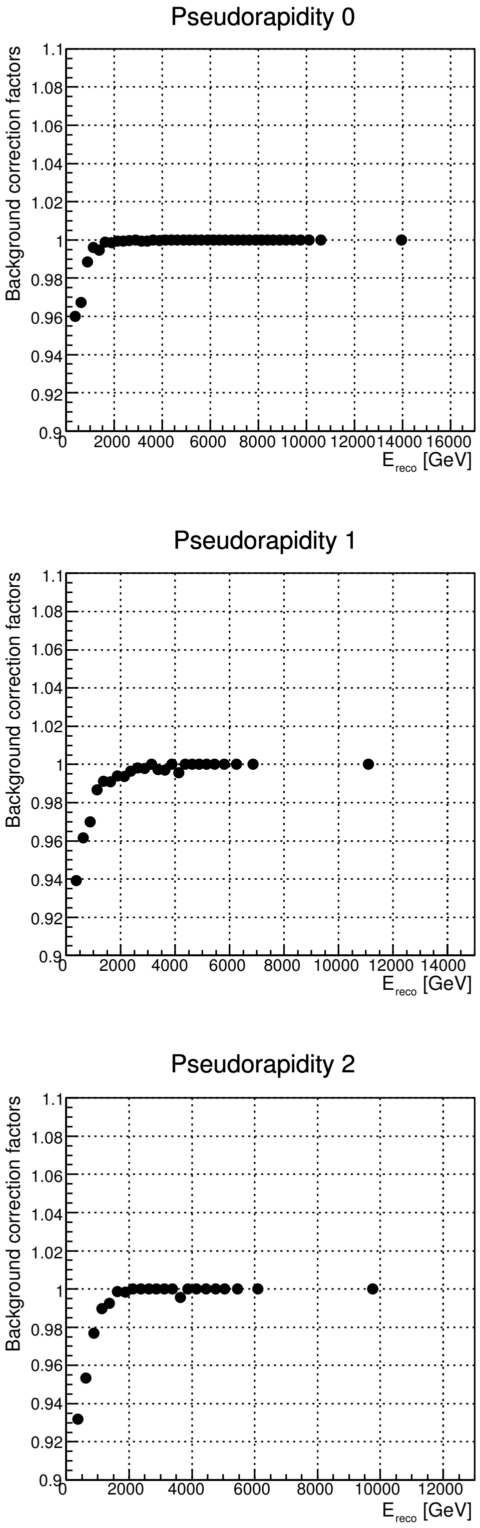

Figure 4.11: Background correction factors for the three pseudorapidity regions.

4.5.2 PID corrections

As described in §4.3, the threshold value L_{2D}^{thr} on L_{2D} parameter used for particle identification was chosen in order to maximize $P \times \epsilon$. Limited efficiency and purity in each energy bin i are taken into account making use of the PID correction factor

$$C_i^{PID} = \frac{P_i}{\epsilon_i} \tag{4.4}$$

These correction factors can not be directly estimated using simulations because the photon/hadron ratio predicted by a given generator can be different by the one observed in data. Therefore, for each energy bin i it is necessary to compute normalization factors between data and MC, α_i for photons and β_i for hadrons. In order to do this we need the L_{2D} distribution measured in data (without L_{2D}^{thr} cut), and the same quantity obtained from simulations, but making use of the true information to distinguish between photons and hadrons. Given the energy bin i, in the bin j of L_{2D} distribution relative to this energy we will have N_{ij}^{Data}, N_{ij}^{γ} and N_{ij}^{h} events for data, MC photons and MC hadrons respectively. Normalization factors α_i and β_i are the ones for which MC L_{2D} distributions have the best fit with the experimental one. Note that this procedure is different from a common fit, in which we assume that data are distributed according to a given function and we change function parameters in order to have the best fit with experimental measurements. In our case, we do not know an analytic expression, but we look for a global scale factor that gives the best fit of the distribution observed in a sample (MC) to the one observed in another sample (data) that we call "template". This procedure is known as *template fit*. The best value of α_i and β_i are therefore given by the minimization of χ^2

$$\chi^2 = \sum_{j=0}^{N_{bin}^{L_{2D}}} \frac{(N_{ij}^{Data} - \alpha_i \cdot N_{ij}^{\gamma} - \beta_i \cdot N_{ij}^{h})^2}{N_{ij}^{Data} + \alpha_i^2 N_{ij}^{\gamma} + \beta_i^2 N_{ij}^{h}} \tag{4.5}$$

Some examples of template fit for three different energy bins in pseudorapidity region 0 are shown in Fig.4.12. Taking into account α_i and β_i, it is then possible to estimate ϵ_i and P_i simply correcting Eq.4.2 as[6,7]

$$\begin{aligned} \epsilon &= \frac{\beta N_h^h}{\beta N_h^h + \beta N_h^{\gamma}} \\ P &= \frac{\beta N_h^h}{\beta N_h^h + \alpha N_{\gamma}^h} \end{aligned} \tag{4.6}$$

---

[6] Note that, according to their definition, purity is affected by different photon/hadron ratio between data and MC, but efficiency does not change.

[7] In the following we will ignore the subscript $_i$, always assuming that quantities are relative to the energy bin i.

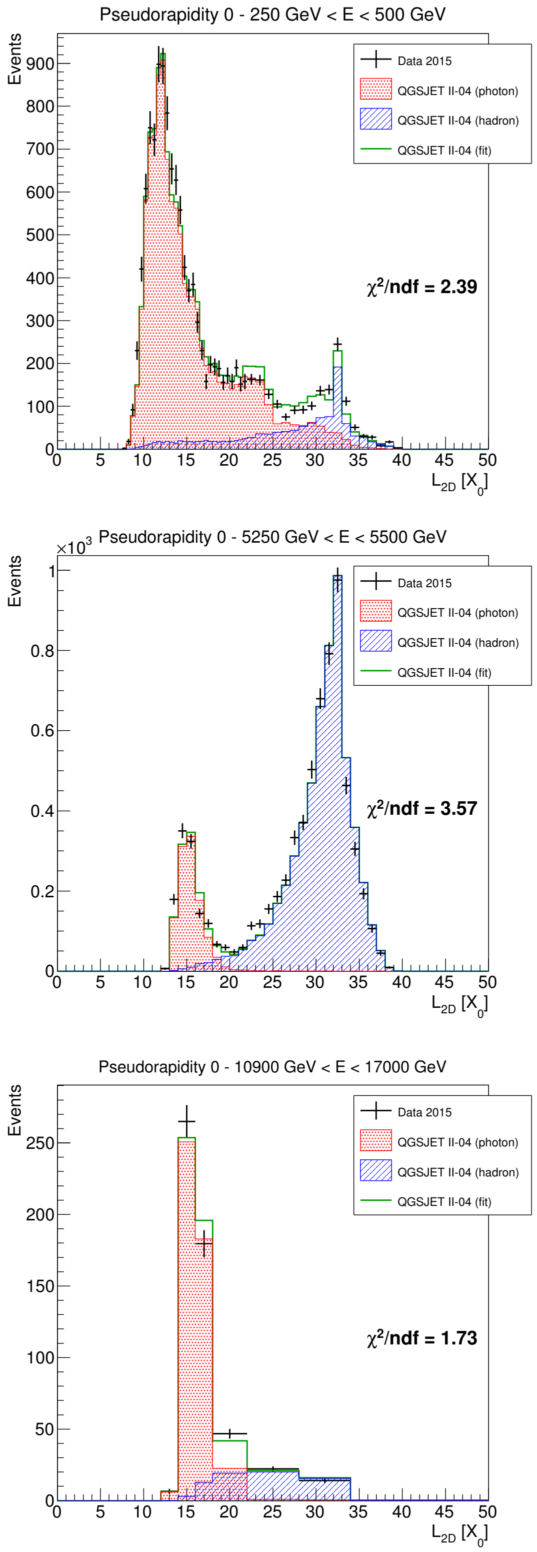

Figure 4.12: Template fits relative to three energy bins on pseudorapidity region 0: from the top to the bottom, the first one, a medium one and the last one. The binning of the L_{2D} scale was defined according to the expected statistics in each energy bin. QGSJET II-04 hadrons (blue) and photons (red) distributions were fitted to experimental data (black). The result of the fit is shown in green.

After that, the best value of correction factor, together with its statistical error, is estimated through a log-likelihood fit, under the following assumptions: βN_h^h is the variable of a Binomial distribution where $\beta N_h^h + \beta N_h^\gamma$ $(\beta N_h^h + \alpha N_\gamma^h)$ is the number of trials and ϵ (P) the probability of success; $N_{obs} = N_{exp} \times \epsilon/P$ is the variable of a Poisson distribution, where N_{exp} and N_{obs} are respectively the number of expected and observed events in the energy bin i. The function to be minimized is

$$\chi^2 = \ -2\ ln(\frac{L}{L_0}) \tag{4.7}$$

where

$$\begin{aligned} L = {} & P_{Poisson}(N_{obs}, N_{exp} \times \epsilon/P) \times \\ & \times P_{Binomial}(\beta N_h^h, \beta N_h^h + \beta N_h^\gamma, \epsilon) \times \\ & \times P_{Binomial}(\beta N_h^h, \beta N_h^h + \alpha N_\gamma^h, P) \end{aligned} \tag{4.8}$$

and L_0 is the maximum likelihood, *i.e.* the one corresponding to $\epsilon = \epsilon_0$, $P = P_0$ and $N_{exp} \times \epsilon_0/P_0 = N_{obs}$, with ϵ_0 and P_0 given by Eq.4.6. The free parameters are ϵ, P and N_{exp}, for each one of them the fit gives us best value and statistical error. In particular, the final value of correction factor is

$$C^{PID} = \frac{N_{exp}}{N_{obs}} \tag{4.9}$$

PID correction factors, together with their relative statistical error, are shown in Fig.4.13 in the case template fit is performed using QGSJET II-04 or EPOS-LHC model. As expected, no evident model dependence was found because template fit takes into account the different fractions of photons and hadrons predicted by the generator, adjusting them to the ones observed experimentally. In addition, longitudinal distributions corresponding to a defined energy bin i must have the same shape in all models due to the fact that we simulated the interaction with the detector using DPMJet 3-0.4 in both cases. Anyway, even if the largest deviation found between the models is still consistent inside the statistical error, we decided to conservatively add a systematic uncertainty for this discrepancy using half the distance between the two results. On the other side, the change that we have on these factors, if we make use of L_{2D}^{thr} values estimated using EPOS-LHC instead of QGSJet II-04, resulted to be negligible.

In order to obtain the final results for corrections, we considered the average on the two models as the best estimation of the correction factors and the quadrature sum of statistical and systematic error (from model dependence) as their relative uncertainties. This is shown in Fig.4.14, where we can see that corrections are mostly below 10%, apart from at low energy in pseudorapidity region 0, while uncertainty, dominated by the statistical contribution, is mainly below 5%. The different trend of correction factors as a function of the energy in the three pseudorapidity regions reflects the different behavior of photons and hadrons distributions present in experimental data.

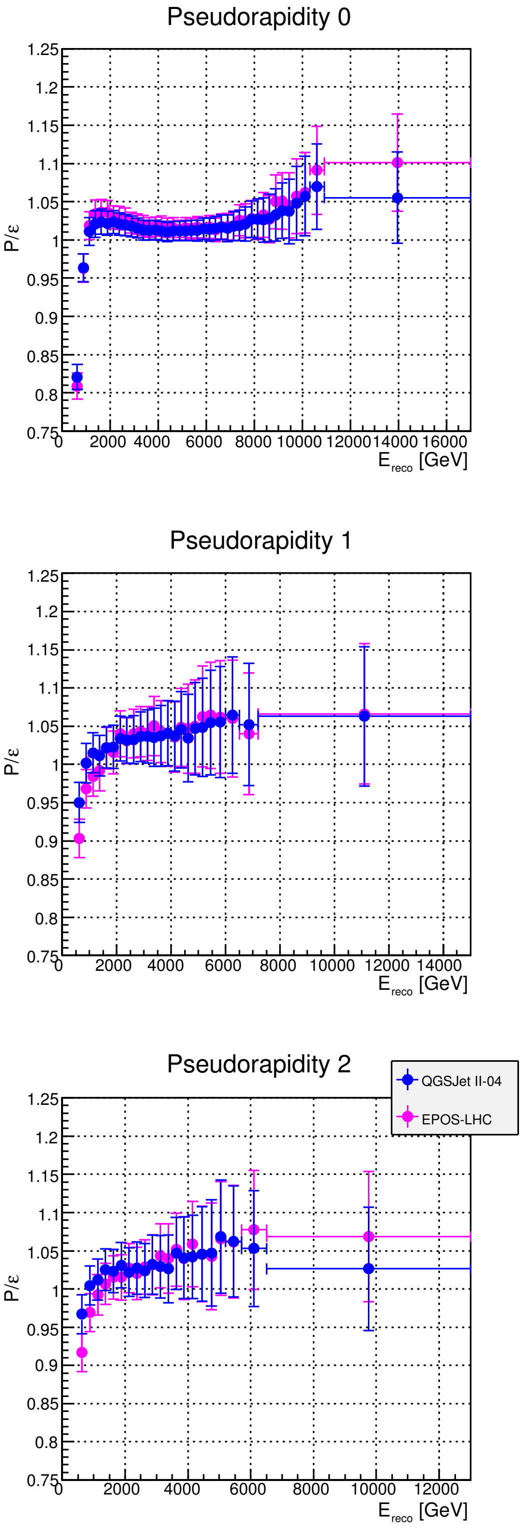

Figure 4.13: PID correction factors, together with relative statistical errors, obtained using QGSJET II-04 and EPOS-LHC.

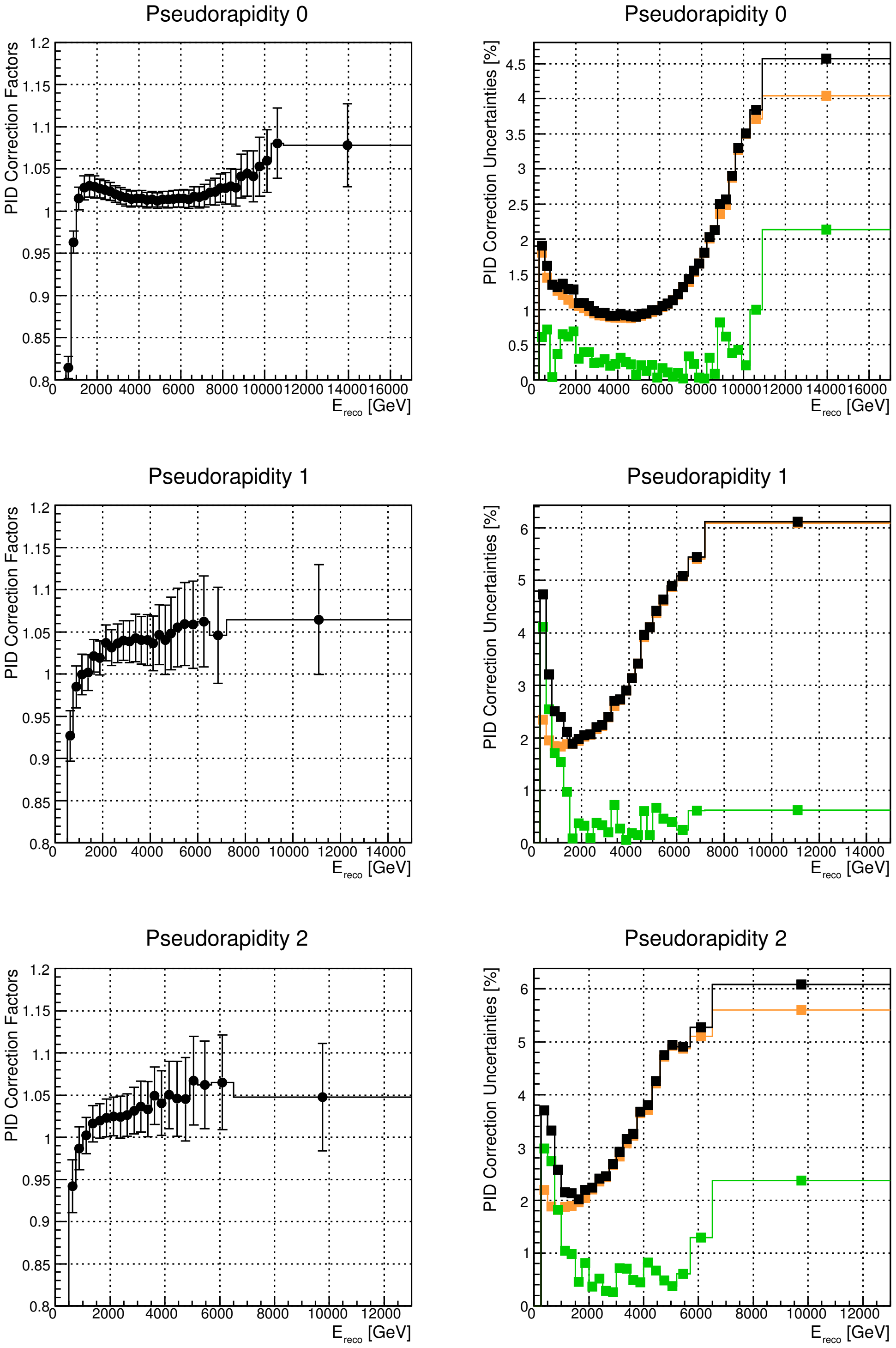

Figure 4.14: Final values (left) and uncertainties (right) for PID correction factors. Colors in right figure refers to statistical uncertainties (yellow), systematic uncertainties (green) and the quadrature sum of them (black).

4.5.3 Multihit corrections

As described in §4.2, impact position was reconstructed using a singlehit fit on the transverse shower profile measured in silicon layers. Even if an algorithm for the reconstruction of multihit in the hadron case was proposed, some discrepancies between data and MC were found relative to the performances in the low energy region. The origin of this problem is still not well understood, but can be related to the silicon baseline shift already observed in the past [75]. Because of this reason, in the present analysis we decided to reconstruct all events as singlehit and later apply correction factors to recover the energy spectra that we could observe if we were able to separate the two particles of a mulihit event.

Multihit correction factor for the energy bin i is

$$C_i^{MH} = \frac{SH_i + MH_i^{observed}}{SH_i + MH_i^{ideal}} \tag{4.10}$$

where SH refers to the energy spectrum coming from events in which only one particle hits the tower and MH to the one related to events in which more than one particle hits the tower. $MH_i^{observed}$ corresponds to what we observe in the detector reconstructing the event as a singlehit, whereas MH_i^{ideal} corresponds to the ideal case in which the two particles are reconstructed as if they are two different events. This means that two hadrons entering the same tower corresponds to a different number of entries in the spectrum: one in $MH_i^{observed}$ and two in MH_i^{ideal}.

SH spectrum can be derived from main toy MC, whereas we needed a dedicated set of toy MC to estimate the two remaining spectra. For this purpose we considered all multihit events present in the main MC set and we simulated again the interaction with the detector, this time injecting only one of the two particle at the same time[8]. Then we analyzed this second MC set in two different ways: in the first case we simply reconstructed all events in order to obtain the MH^{ideal} spectrum; in the second case the $MH^{observed}$ spectrum was obtained piling-up each couple of particles before reconstruction in order to restore the original multihit nature of the event[9]. Because the generation of this second MC set takes additional computing time, we decided to estimate multihit correction factors only using about 4×10^7 collisions for each model.

Event selection applied to SH, $MH^{observed}$ and MH^{ideal} is the same described in §4.3, with the only exception of particle identification for which we used directly the true MC information, being multihit correction applied to data after PID correction. This means that each one of the two hits in MH^{ideal} is filled in its relative spectrum only if it has a hadron-like code, whereas the multihit in $MH^{observed}$ is filled in its relative spectrum if the most energetic particle has a hadron-like code.

---

[8] If more than two particles enter the tower, we choose only the two most energetic ones.

[9] In principle we could have used the multihit reconstructed in the first MC set to derive the $MH^{observed}$ spectrum, but this was not possible because for simplicity we used a different seed in the second MC set.

Fig.4.15 shows (left) the fraction of multihit expected from the two models as a function of true energy (and true event selection) and (right) the multihit correction factors obtained using the method just described as a function of reconstructed energy (and reconstructed event selection apart from PID). From Fig.4.15 left we can see that the two models predicts a different number of multihit events in pseudorapidity region 0, whereas no strong difference was found in the two other cases. In general, if both particles interact in the detector, the energy reconstructed in $MH^{observed}$ will be higher than the one corresponding to the most energetic particle in MH^{ideal}, whereas the one corresponding to the least energetic particle will be present only in MH^{ideal}. This means that, if a model predicts a larger multihit fraction at some energy, the correction factor at that energy will be also higher and, in particular, it will account for the migration of a certain number of entries from this bin i ($C_i^{MH} < 1$) to a lower bin j ($C_j^{MH} > 1$). If we take into account this fact we can understand how Fig.4.15 left reflects in Fig.4.15 right. From Fig.4.15 right we can derive the final values of multihit correction factors, using the average of the two models as the best estimation and the quadrature sum of statistical error and systematic error (estimated by half the difference between the two results) as their relative uncertainties. Final values and uncertainties are shown in Fig.4.16, where we can see that correction factors are mostly below 10% and uncertainty mainly below 4%.

4.5.4 Fake and missed events correction factors

Fake and missed events correction factors take into account any remaining limitation respectively in the purity and efficiency of the selected sample. Because they are applied after PID and multihit corrections factors, toy MC used for their computation is made by $SH + MH^{ideal}$, where only particles having a hadron-like true code are considered. Roughly speaking, fake events are the ones that pass event selection on reconstructed variables and not on true variables, whereas missed events are exactly the opposite. Because fake events are a kind of background, *i.e.* they are not present in the true spectra, they must be removed before unfolding. This means that fake events correction factors must be computed for each bin i in the E_{reco} spectra. On the other side, missed events must be added after unfolding, because they are not present in the reconstructed spectra. For this reason, missed events correction factors were estimated for each bin j in the E_{true} spectra.

For a more precise explanation of what is a fake event and what is a missed event let us refer to the event selection criteria described in §4.3 and define an event as *fake* if it satisfies

$$PID_{true} \wedge (TRG \wedge E_{reco}^{thr} \wedge FV_{reco} \wedge (\neg(E_{true}^{thr} \wedge FV_{true})))$$

and as *missed* if it satisfies

$$PID_{true} \wedge (E_{true}^{thr} \wedge FV_{true} \wedge (\neg(TRG \wedge E_{reco}^{thr} \wedge FV_{reco})))$$

where $\wedge$ and $\neg$ are respectively logical AND and NOT operators.

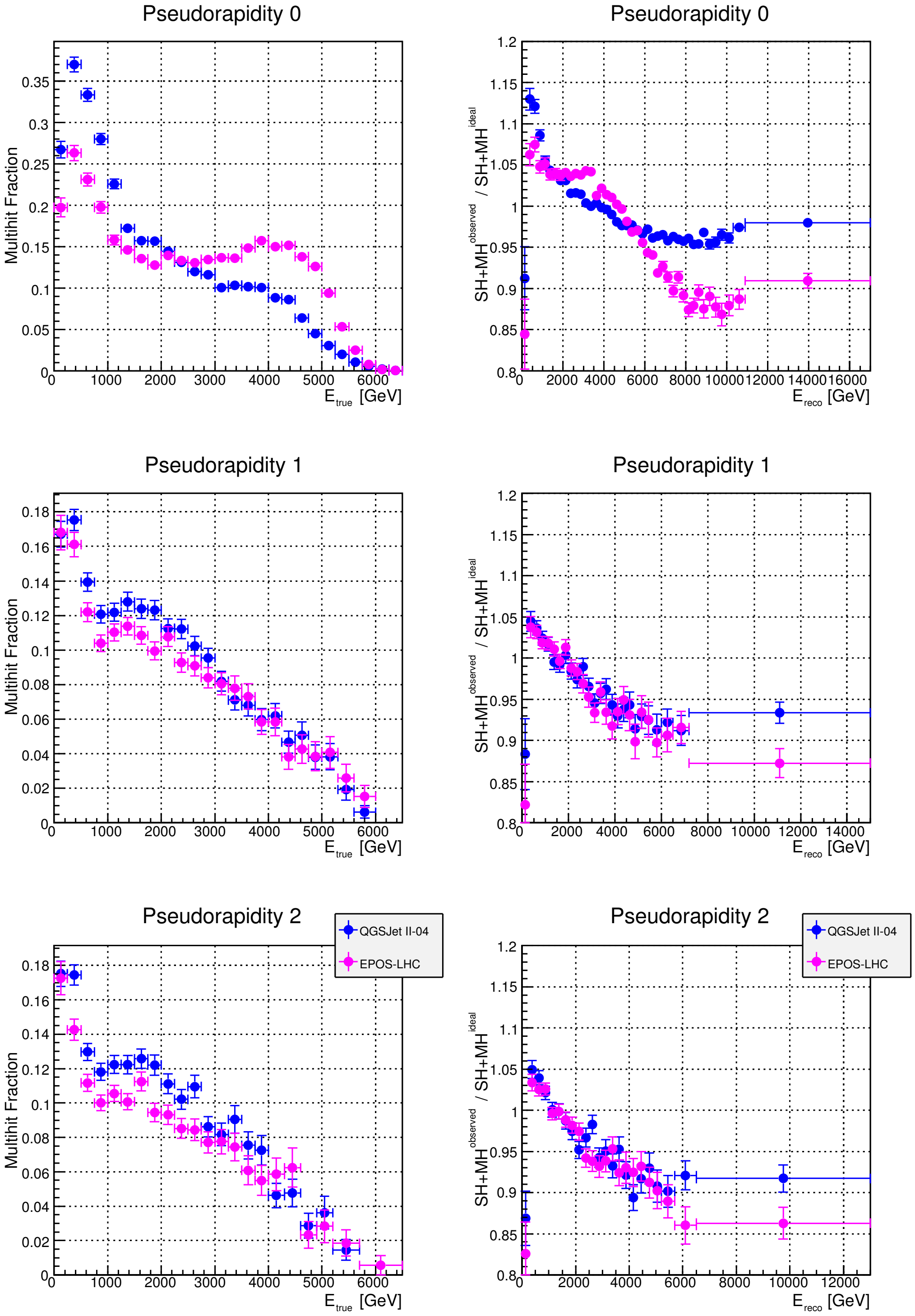

Figure 4.15: Multihit fraction using MC true information (left) and multihit correction factors (right) obtained using QGSJET II-04 and EPOS-LHC toy MC.

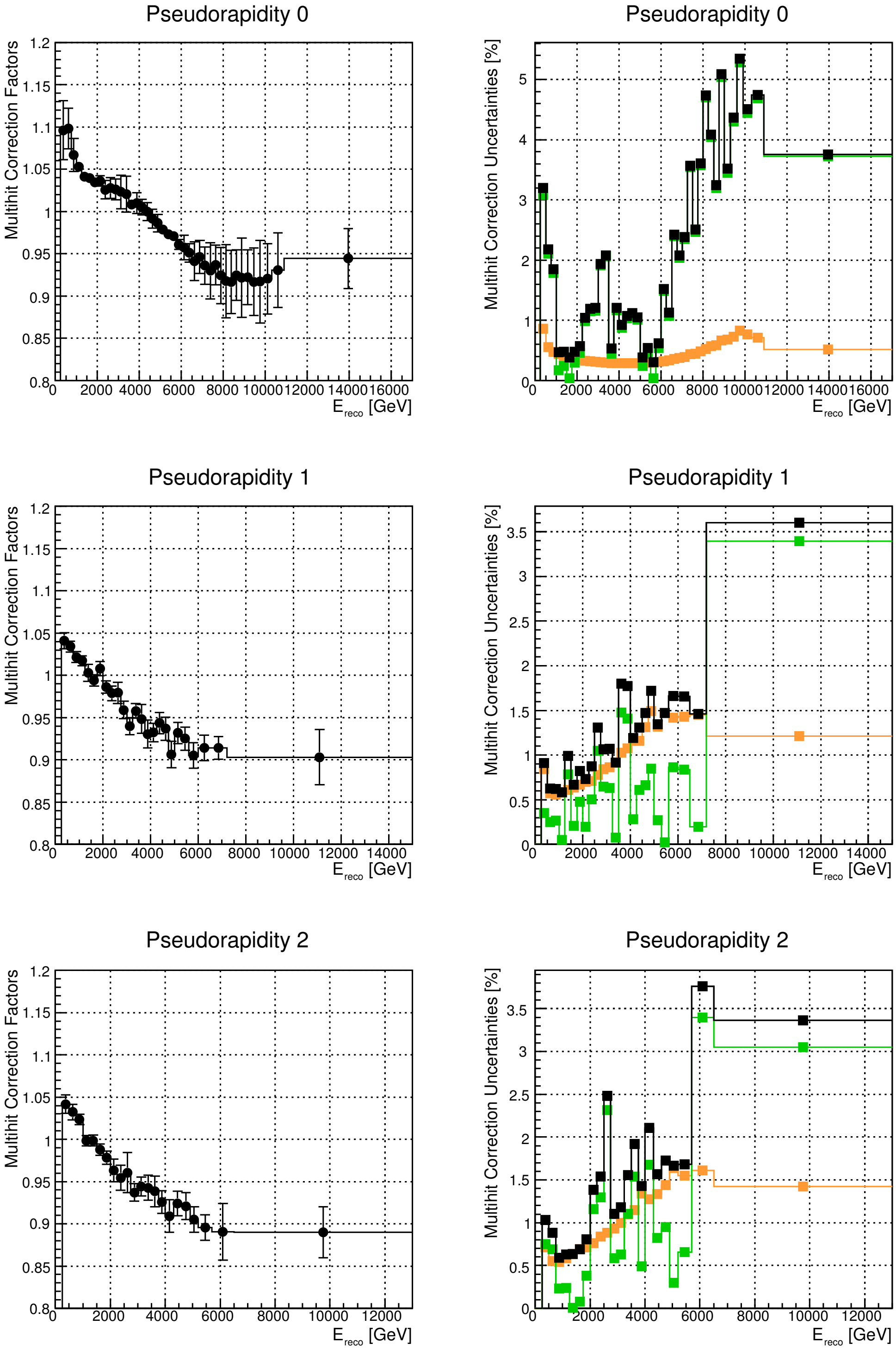

Figure 4.16: Final values (left) and uncertainties (right) for multihit correction factors. Colors in right figure refers to statistical uncertainties (yellow), systematic uncertainties (green) and the quadrature sum of them (black)

The fraction of fake and missed events with respect to the total number of events selected are shown in Fig.4.17 left and right respectively. In both case the fraction is strongly decreasing going from low to high energies. This is due to the fact that the E_{thr} cutoff is contributing mostly in the region just above 250 GeV and that, as shown in Fig.3.25, position resolution improves with energy reducing the impact of FV selection. Limited trigger efficiency is acting only on the missed fraction, generating a loss of events of about 70% at 500 GeV and 30% above 2 TeV, consistently with what observed in Fig.3.23. If we call the fraction of fake and missed events f_i^{Fake} and f_j^{Missed} respectively, the corresponding correction factors for reconstructed energy bin i and true energy bin i are

$$\begin{aligned} C_i^{Fake} &= 1 - f_i^{Fake} \\ C_j^{Missed} &= \frac{1}{1 - f_j^{Missed}} \end{aligned} \tag{4.11}$$

The final values for f_i^{Fake} and f_j^{Missed} were computed using the average on the two models as the best estimation and the quadrature sum of statistical error and systematic error (estimated by half the difference between the two results) as their relative uncertainties. Thanks to them it is then possible to calculate C_i^{Fake} and C_j^{Miss} with proper error propagation. The results are shown in Fig.4.18 and 4.19, where we can see that uncertainty is mostly 1% in both cases. Being very small compared to all other systematic contributions, we decided to neglect this source of uncertainty on the final spectra.

Even if model dependence of fake and missed correction factors is negligible, so far we did not consider the uncertainty due to the hadronic inelastic cross section. Due to the limited depth of LHCf detector, we expect that only 70% of hadrons will interact with it and, as said, this effect represents the largest contribution in the determination of the number of missed events. In order to estimate how the corresponding correction factors depends on interaction cross section[10] σ_{int}, we compared detection efficiency estimated using EPICS to the one obtained from GEANT4 simulation toolkit [76]. For simplicity, instead of repeating simulations, we decided to directly extract σ_{int} from the two frameworks. This was made considering the interaction cross section of a proton with a W nucleus in the energy range between 100 GeV and 10 TeV, as shown in Fig.4.20. EPICS tables provide cross section for atomic mass number A=180 (yellow) and 190 (green), interpolating which we obtained the one relative to A=183.67, the isotopes abundances weighted atomic mass number of W (black). This black line must be compared to the results of GEANT4 for p-W (red) and n-W (blue) interaction, from where we can see that at such high energies protons and neutrons behave basically in the same way. The maximum deviation between EPICS and GEANT4 results below 6.5 TeV is 6%, that was take into account as a systematic uncertainty. To distinguish this contribution from the negligible one due to model dependence, in the following we will refer to it as σ_{int} uncertainty, even if it is still acting on missed events correction factors.

---

[10] In order to distinguish between hadronic inelastic cross section due to the interaction of a hadron with the detector and the one due to p-p collisions at $\sqrt{s} = 13\ TeV$, in the following we will label the former as σ_{int} and the latter as σ_{inel}.

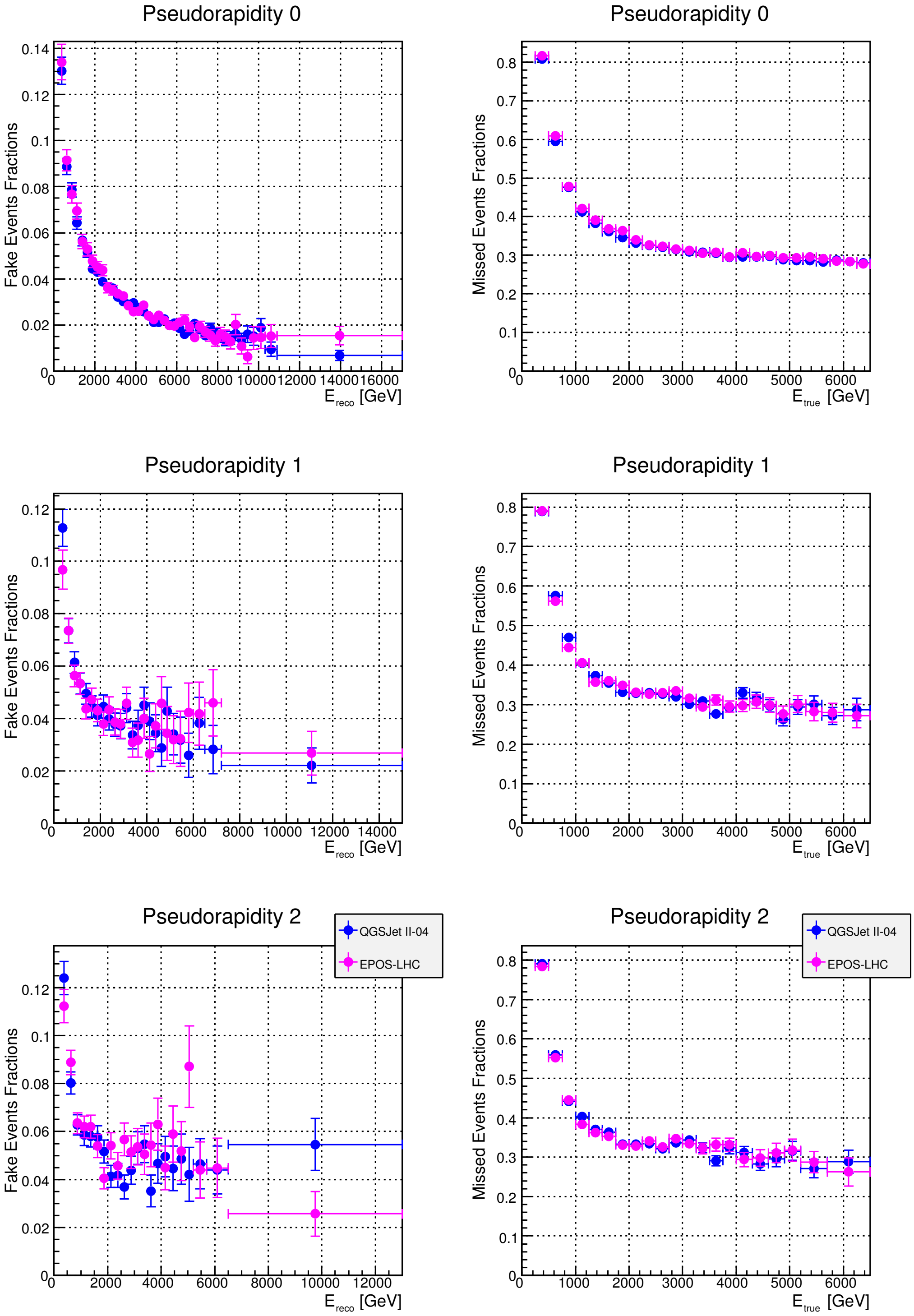

Figure 4.17: Fraction of fake events (left) and missed events (right) estimated using QGSJET II-04 and EPOS-LHC toy MC.

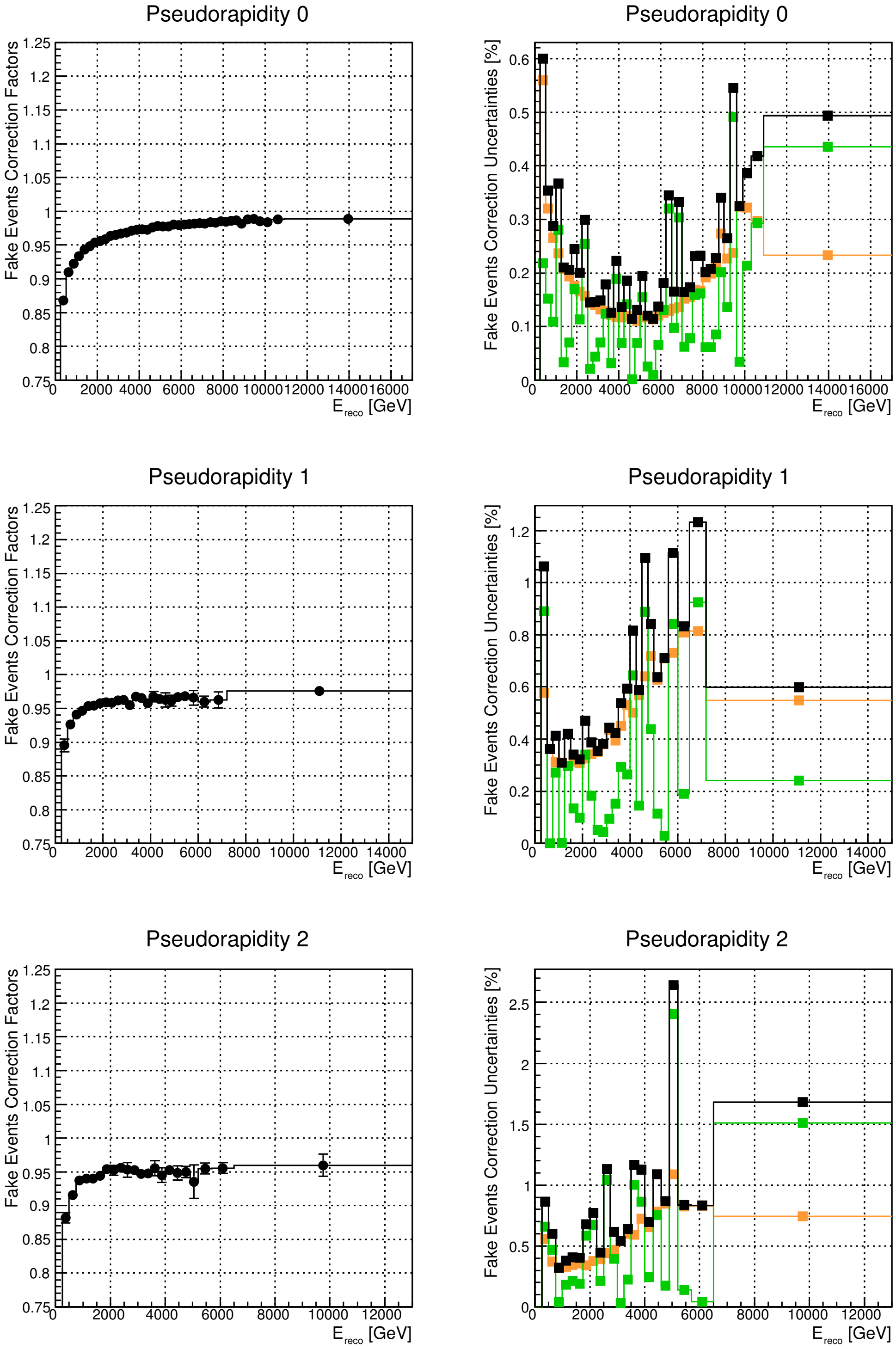

Figure 4.18: Final values (left) and uncertainties (right) for fake events correction factors. Colors in right figure refers to statistical uncertainties (yellow), systematic uncertainties (green) and the quadrature sum of them (black).

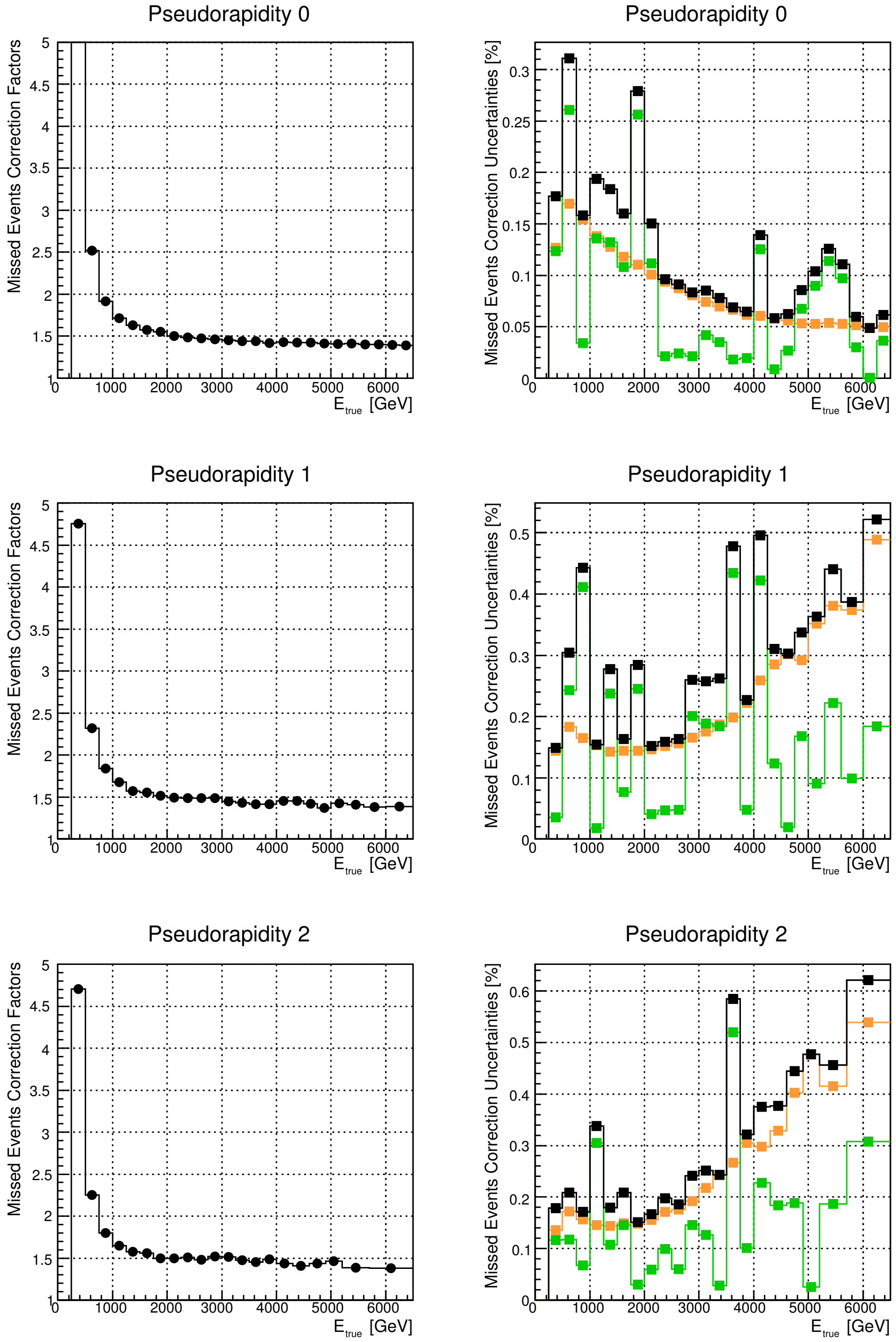

Figure 4.19: Final values (left) and uncertainties (right) for missed events correction factors. Colors in right figure refers to statistical uncertainties (yellow), systematic uncertainties (green) and the quadrature sum of them (black).

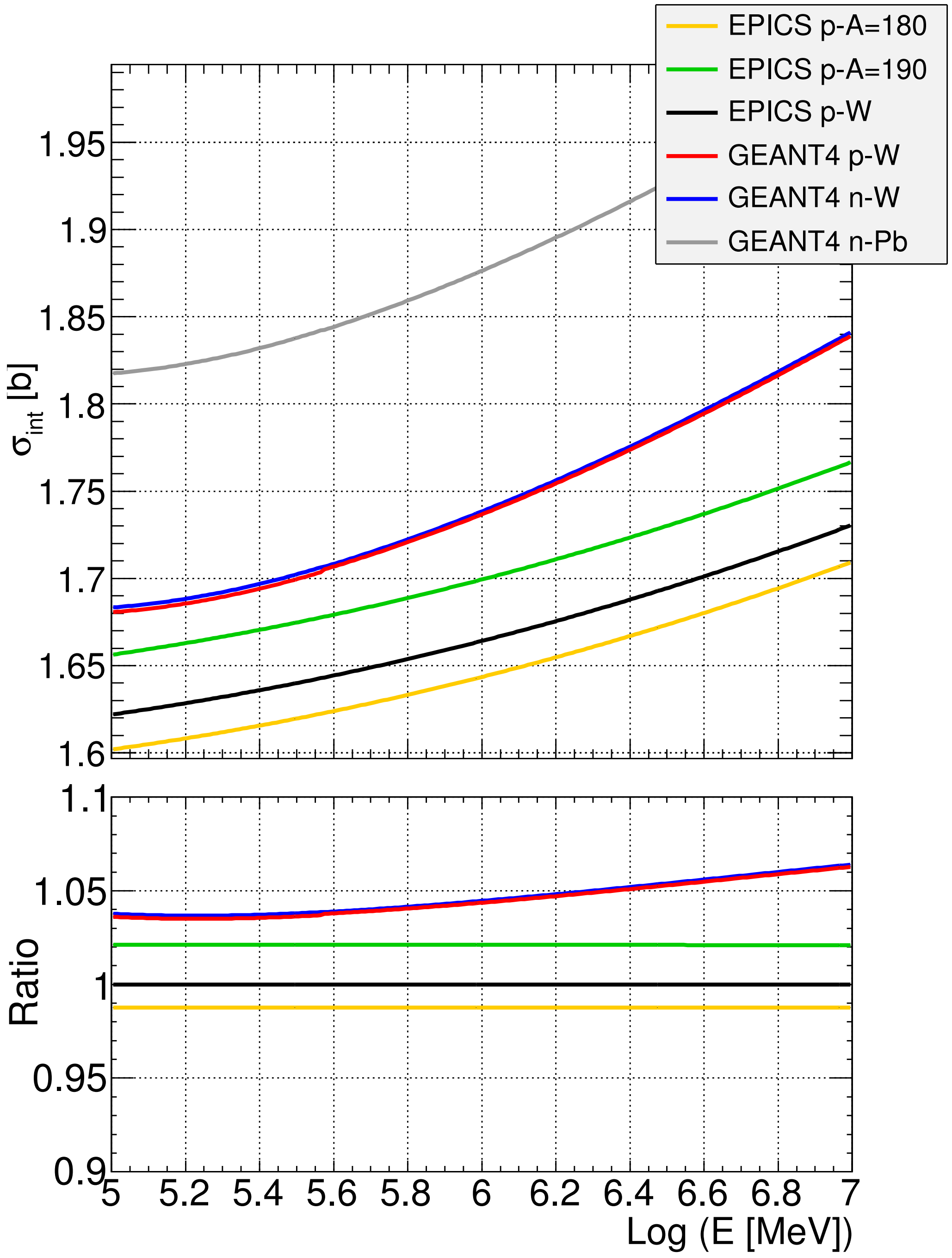

Figure 4.20: Hadronic inelastic cross section for p-W interaction obtained from EPICS (black) and GEANT4 (red). For comparison the following cross section are also shown: p-A=180 (yellow) and p-A=190 (green) from EPICS, n-W (blue) and n-Pb (gray) from GEANT4. For each cross section the ratio to the value relative to p-W interaction in EPICS is also shown.

4.5.5 Summary on correction factors

Fig.4.21 shows relative correction factors applied to data before (left) and after (right) unfolding. As we can see, the term due to missed events generates large corrections because of the limited detection efficiency, whereas the contribution of all other effects is mostly below 10%.

4.6 Spectra Unfolding

The simple measurement of energy spectra is enough to test generators if we fold their output according to detector response, but it is not very useful for their tuning because, due to limited resolution, it can not clearly indicate which are the experimental observations that models developers should follow. In order to overcome this problem, a common procedure nowadays applied in high energy physics is unfolding. In this way, instead of making use of response matrix to convolute model predictions, we use it to deconvolute experimental results. Unfolded distributions are therefore the best estimation that we can obtain from our data using measured spectra and knowing detector response. Unfortunately, unfolding is an ill-posed problem, *i.e.* a small change in the folded spectrum can change a large variation in the unfolded one. For this reason, results are also very sensitive to the algorithm used for the deconvolution and choosing the proper method can help in reducing the ill-posedness of the problem. Among all proposed approaches, we decided to use iterative bayesian unfolding [77], nowadays widely used thanks to its ability to properly tackle the problem from a statistical point of view. In addition, it is very simple to implement, just requiring the usage of bayesian probability and a small number of iterations to converge. Exploiting the Bayes theorem, the *posterior*, *i.e.* the probability of a true spectrum given the one measured by our detector, can be computed knowing the response matrix and assuming an initial true distribution, that is called *prior*. Making use of the bayesian posterior and the measured spectrum it is possible to obtain the unfolded distribution. However, just acting in this way we would introduce a large bias on our result due to the choice of the prior. In order to overcome this problem, iterative bayesian unfolding makes use of a certain number of iterations, at each one using as prior the unfolded spectrum estimated at the previous iteration and stopping the procedure when the difference between input and output distribution is “enough small”. More details about this unfolding method are given in App.C.

In the case of present analysis, unfolding is based on RooUnfold libraries v1.1.1 [78]. The correct approach should involve three dimensional unfolding, *i.e.* energy-η-ϕ unfolding over the whole sensitive area, because detector is affected by limited resolution not only in energy but in position as well. Nevertheless, this solution is quite difficult to implement, because it would require to extend all the analysis to a three dimensional space, thus complicating the choice of binning, the estimation of correction factors and the spectra unfolding. We therefore decided to perform

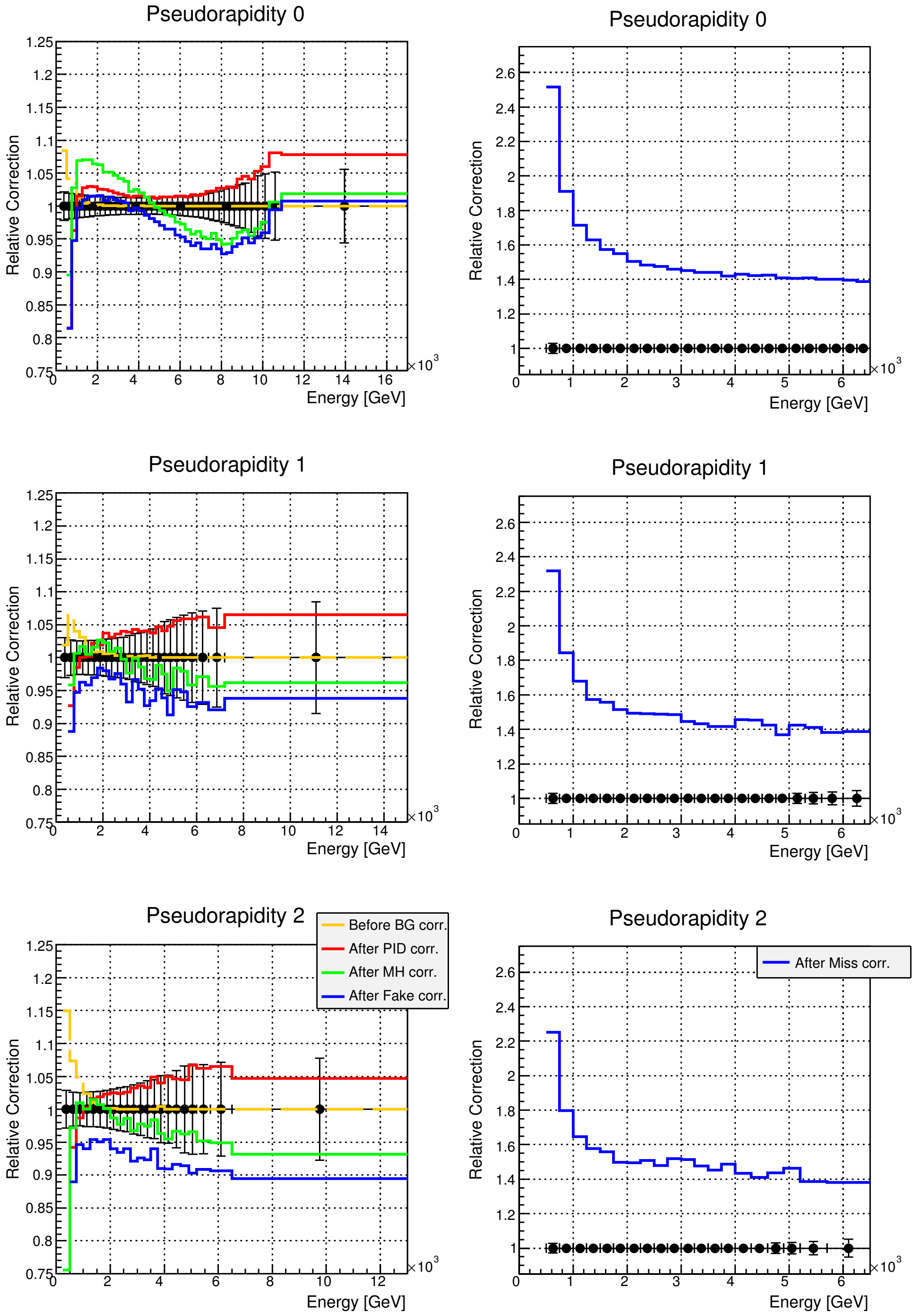

Figure 4.21: Summary of relative correction factors before (left) and after (right) unfolding. Black markers show the statistical error present on the folded spectra after background correction (left) and on the unfolded spectra before missed events correction (right). Data points shown here belong to folded and unfolded spectra described in §5.2 and 5.3, respectively.

one dimensional unfolding, *i.e.* energy unfolding over one pseudorapidity region at a time, considering that energy resolution is the main limitation of LHCf detector. As discussed in §3.5, position resolution is better than 1 mm above 350 GeV, even if long tails in the corresponding distributions were found. This means that migration inside a pseudorapidity region of particles hitting outside it (and vice versa) can happen, but we do not expect this phenomenon to be very large. Because of this reason, we ignored position reconstruction effects in unfolding and simply estimated some correction factors for them, as described in §4.5.4. Anyway, in order to be more conservative, we added a systematic uncertainty relative to the change we have in the final spectra if we use true MC information for position instead of reconstructed one, as discussed in §4.7.1.3.

An important difference between our analysis and the standard approach of iterative bayesian unfolding is the treatment of background contamination and detection inefficiencies in the measured spectra, that, making use of RooUnfold terminology, we called fake and missed events, respectively. According to author's suggestion, these effects should be considered in the iterative procedure itself and this is what is done by default in RooUnfold, where it is possible to fill *Fake* and *Miss* histograms while building response matrix. Anyway, as described in §4.5.4, we decided to not exploit this possibility, independently compute these correction factors and apply them outside unfolding (fake corrections before it and missed corrections after it). The reason for this choice is that, as explained later, response matrix was built using flat MC, but, because fake and missed events depends on energy/position distributions of particles produced in collisions, we expected to estimate them more carefully making use of toy MC relative to generators rather than an unphysical flat simulation. Once computed them, we decided to apply corrections outside unfolding instead of including them in the iterative procedure simply to have more control on our analysis.

In iterative bayesian unfolding three points are very important in the determination of the final result: building of detector response matrix, choice of input prior[11] and number of iterations of the algorithm. In order to get the unfolded spectra we chose the flat MC as training sample to build the response matrix and a generic flat energy distribution as input prior. This solution was adopted in order to prevent any loss of generality on the final result caused by possible generators bias.

Response matrix built using flat MC is shown in Fig.4.22 for pseudorapidity region 0 after normalization. Here *normalization* means that the content of each (E_{reco}, E_{true}) bin has been divided for the integral over all E_{reco} bins corresponding to the given E_{true} bin. As we expected, due to the limited energy resolution, migration effects are significant, therefore complicating spectra unfolding. The

---

[11] *Input prior* indicates the prior used for the first iteration (because after that the prior is simply the unfolded spectrum estimated at the previous iteration). If not differently specified, in the following we will refer to the prior used for the first iteration simply as *prior*.

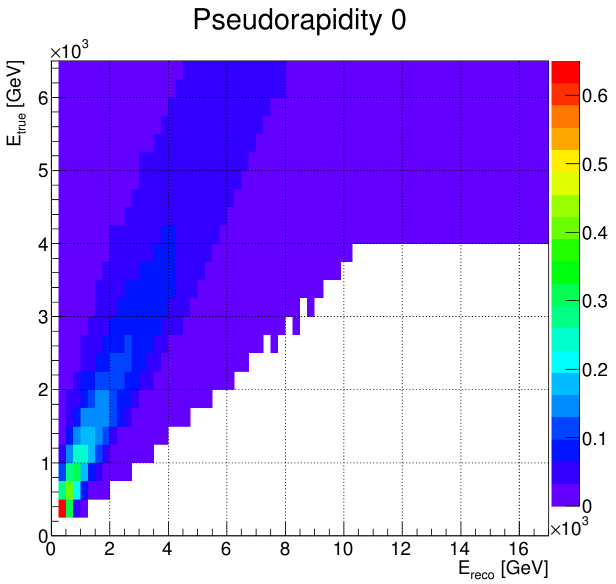

Figure 4.22: Normalized response matrix for pseudorapidity region 0 obtained making use of flat MC.

shape of the true distribution used to build the response matrix has no strong effect on the unfolded spectrum if all the energy range is covered with enough statistics. As said, in our case we used a flat true distribution, but we confirmed that the final result is comparable if we build response matrix using the true distribution of a generator. This is not surprising, because response matrix depends strongly on the model used to simulate the interaction with the detector and only weakly on the true distribution employed to generate it. What we have just said is shown in Fig.4.23 for pseudorapidity region 0, in which we can see the ratio between unfolded and true spectrum for QGSJet II-04 test sample. Black markers are relative to the true distribution and unfolded histograms to three different approaches: red histogram is obtained using flat MC for response matrix and an independent QGSJet II-04 sample for prior; green histogram is equivalent to red one but independent QGSJet II-04 sample was employed for response matrix as well; blue histogram is the same as green one except that fake and missed events corrections are computed and applied inside RooUnfold. If we neglect for the moment the choice of the prior[12], the method chosen in our analysis is the red one, whereas the standard approach is the blue one. Apart from the very first bin in pseudorapidity region 0, consistency between the two unfolding philosophies and their agreement with true model distribution is almost always better than 5%. In addition, this study confirmed that in our case building response matrix with

---

[12] Note that in all the three cases we used the same prior, in order to separate the discussion on the response matrix from the one on the prior.

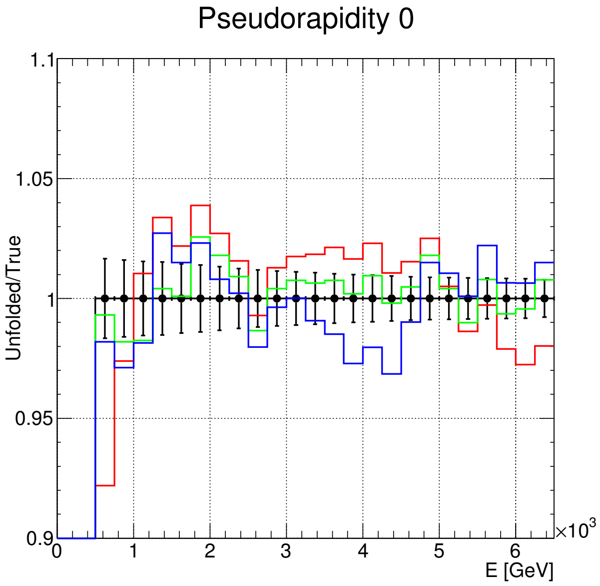

Figure 4.23: Test of the unfolding procedure making use of different response matrix. For details about meaning of different distributions see the text.

a different model from the one chosen as prior does not significantly affect the result. Generally, it is recommended to use the same sample for both purposes, because the particular shape of true distribution in a given energy bin can affect events migration towards nearby bins. Anyway, in our case this effect is not so strong because energy resolution is very limited and binning is finer than it, hence migration involves a large number of bins.

The prior used for the final unfolded result is a flat energy distribution. The choice of the prior is a crucial point in our analysis because unfolded spectra resulted to be quite sensitive to it, being the energy resolution very limited. In addition, the variation among hadronic interaction models is very strong in the forward region, therefore generators that are very different from our measurements at the folded spectra level must not be taken into account in the analysis. The input prior is obtained from the true distribution simply normalizing its area to 1. This is shown in Fig.4.24a for different possible priors: flat (green), QGSJet II-04 (blue), EPOS-LHC (magenta) and DPMJet 3-0.4 (red). Note that, being a probability, prior does not depend on the absolute yield, *i.e.* the total number of neutrons produced per unit of N_{ine}, that is actually quite different among the three generators considered. Fig.4.24b shows the dependence of the unfolded spectrum in pseudorapidity region 0 from the choice of the prior for the same QGSJet II-04 test sample used in Fig.4.23. Here it is shown the ratio between unfolded and true spectrum, this time fixing the response matrix to the one relative to

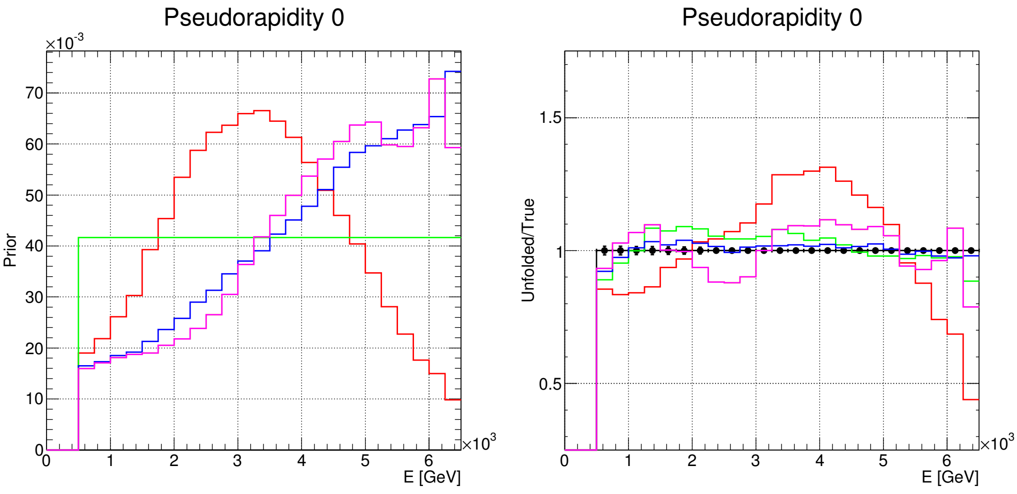

(a) **(b)**

Figure 4.24: Prior probabilities (a) and test of the unfolding procedure making use of different distributions as prior (b). For details about meaning of different distributions see the text.

flat MC and changing the prior among the four different ones shown in Fig.4.24a. Black markers are relative to true distributions and unfolded histograms to different priors with the same meaning of colors of Fig.4.24a. As we can see, the unfolded spectrum obtained using as prior the same model that was employed to generate the test sample (QGSJet II-04) has the smallest discrepancy from the true spectrum. If we take this unfolded spectrum as reference and we compare the differences between it and unfolded distributions obtained making use of different priors, large deviations are found: about 10% in the flat case, 20% for EPOS-LHC and up to 50% with DPMJet 3-0.4. This is due to the fact that this last model predicts a true distribution completely different from the one present in the test sample. As described in §4.7.2, in order to take into account for the dependence of our result from the choice of the prior we estimated a systematic contribution from the maximum shift observed in case we replace flat prior with the ones taken from generators. For this purpose, we made use of QGSJet II-04 and EPOS-LHC models, but we excluded DPMJet 3-0.4, because, as shown in §5.2, it exhibits a large discrepancy from data already at the folded spectra level and considering it would only dramatically increase the final uncertainty.

The number of iterations to be used in the algorithm is generally recommended to be below 10, in order to avoid crazy spectra due to the excess of regularization. Author's suggestion is to stop the iterative procedure when $\Delta\chi^2$, the χ^2 between input and output spectra of the given iteration is "enough small". The rapidity with whom the algorithm converges towards this arbitrary small value depends of course on the agreement between the starting prior and the true distribution

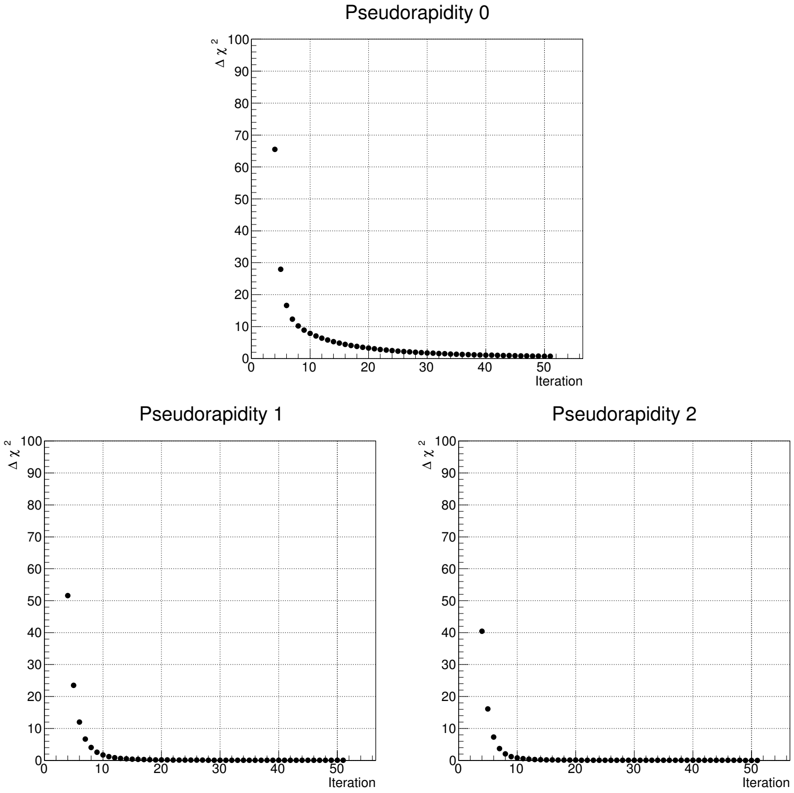

Figure 4.25: Behavior of $\Delta\chi^2$ as a function of the number of iterations of the algorithm. The figure refers to unfolding of experimental distribution making use of flat energy distribution as input prior.

present in nature. Anyway, we did not observed a very strong dependence of this parameter from the choice of the prior, instead the spread between different models in the number of iterations needed to reach for example $\Delta\chi^2 < 10$ resulted to be about 2 or 3. Fig.4.25 shows $\Delta\chi^2$ as a function of the number of iterations in the case of flat energy distribution as input prior. The ideal stopping point of the algorithm should be not too early (in order to avoid large prior bias), not too late (in order to avoid statistical fluctuations enhancement). In our case, convergence of unfolding is much slower in pseudorapidity region 0 than in the 1 and 2, so that we can not set an absolute stopping value of $\Delta\chi^2$ common to the three regions. For example, the condition $\Delta\chi^2 < 10$ leads to a number of iterations of about 4 for the two regions on the LT, but very near to 10 for the one on ST, a value large enough to start observing strange behaviors in the unfolded spectra. Being not possible to uniquely define an absolute stopping value of $\Delta\chi^2$ valid for all three pseudorapidity regions, we simply decided to follow RooUnfold default value of this parameter, stopping the iterative procedure after 4 iterations.

4.7 Systematic uncertainties

In this section the estimation of each systematic uncertainty is discussed. We can divide these contributions in two main categories: the ones related to the reconstruction of measured distributions and the ones coming from the unfolding process itself.

4.7.1 Systematics related to reconstruction

Systematic effect related to the reconstruction process belongs to two different groups. The first one consists of uncertainties on the measurements of a physical quantity: energy, beam center position, transverse position and number of inelastic collisions. The second one is composed by the already discussed uncertainties on correction factors previously described (PID, multihit, fake events and missed events).

4.7.1.1 Energy

The uncertainty on the energy scale is given by four main contributions. The first one is the uncertainty on the ADC/GeV conversion factors $\sigma_1 = \sigma_{gain} \sim 2\%$, derived in §3.2, acting on data but not on MC. The second one is the quadrature sum of different systematic effects related to the reconstruction of the primary energy starting from the energy deposited in each layer of the calorimeter. As described in §3.3 and §3.4, the total amount of this second contribution, acting both on data and on MC, is $\sigma_2 = \sigma_{ene\_conv} \oplus \sigma^{mc}_{pos\_dep} \oplus \sigma^{data}_{pos\_dep} \sim 2.9\%$. The third one is due to the quadrature sum of different systematic effects related to hardware issues: ADC linearity, cables attenuation length, relationship between high voltages and PMT gains and stability of high voltages. The contribution of all these factors to the uncertainty on the energy scale is $\sigma_3 = 2\%$ [70]. The fourth one is related to a possible energy shift σ_{energy_shift} between data and simulations that can be due to two different effects: an hardware effect, *i.e.* a change in collected signal due to temperature effects on PMTs and/or radiation damage on GSO scintillators; a theoretical effect, *i.e.* the inability of DPMJet 3-0.4 to correctly simulate the interaction with the detector at energies that are well above the ones on which the model was directly calibrated. Because presently we can not separate these two terms, this contribution acts both on data and on MC.

In the following we will discuss how to estimate the fourth term of the uncertainty on the energy scale. In photon analysis [68], Type-I π^0 invariant mass (the one reconstructed from a π^0 decay in two γ, one hitting the ST and the other one hitting the LT) provides a very powerful method to check the absolute energy scale of the detector in the case of electromagnetic showers. As shown in Fig.4.26, performing a Gaussian fit on this distribution it is possible to estimate the mean value and, by comparison, to derive the relative energy shift between MC and data. For the runs considered in this work, this method lead to a deviation of

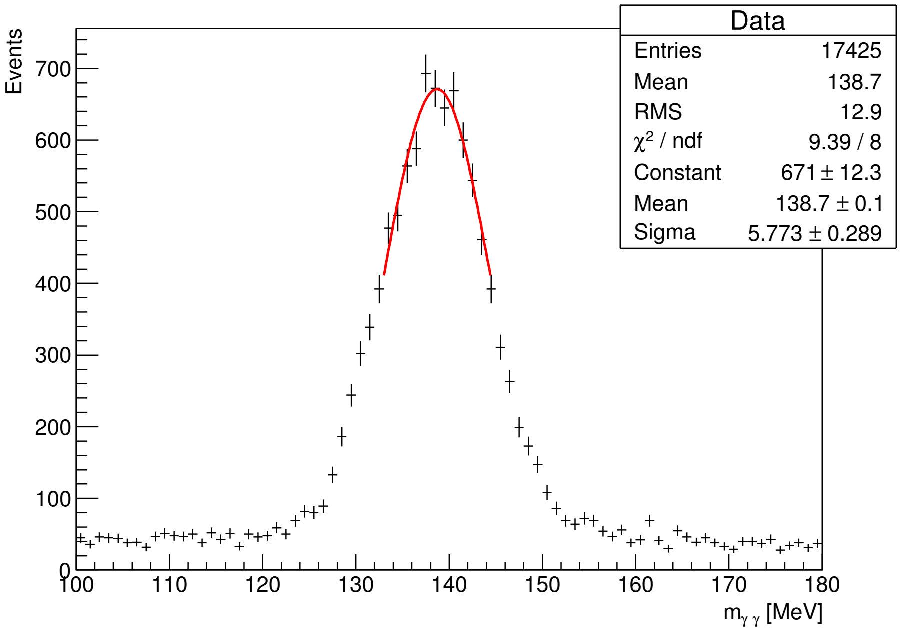

Figure 4.26: $\gamma - \gamma$ invariant mass in which each photon enters a different tower. The superimposed red line represents the result of the fit on the π^0 peak [68].

2.15%. In a simple extension of it to hadron analysis, we can to think to find a hadron decaying in two hadrons from which reconstructing the invariant mass in order to give an estimation of the absolute energy scale in the case of hadronic showers. The best candidate is very energetic Λ^0 ($E \gtrsim 1.5\ TeV \Rightarrow \gamma \gtrsim 1000$) that, having a $c\tau$ of 7.89 cm [1], can decay in $p + \pi^-$ after D1 so that both daughters can reach the detector. In this case the event is more frequently Type-II than Type-I (*i.e.* the two particles hit the same tower) and we see a broad distribution instead of a Gaussian because the decay can happen at different distances from the detector. The main problem of this method is that it has a large dependence from the model used to generate collisions, because different generators predicts a different number of Λ^0 in the very high energy region.

Due to the difficulties in finding a model-independent estimator for the absolute calibration of the energy scale, in this analysis we finally decided to use the π^0 mass shift as an indication of the remaining possible systematic effects not included in the first three uncertainties already discussed. However, we must be careful that, even if at present this is the best that we can do, using $\sigma_4 = +2.15\%$ from π^0 mass shift is not a so proper way of estimating this uncertainty. This is because of two reasons. The first one is that electromagnetic showers generate signal in the first 12 layers, so that this shift is not sensitive to what happens in the last 4 layers, where hadronic showers deposit most of their energy. The second one is that we expect that at high energy the reliability of the model used to simulate the interaction with the detector is much better for an electromagnetic shower than for a hadronic shower. In the future we expect to have at least an independent estimation of this uncertainty in the case of hadron analysis, directly making use of neutrons produced by Ultra Peripheral Collisions (UPC) [79] in p-Pb operations.

The final uncertainty on the energy scale is given by the quadrature sum of all previous four contributions discussed for a total of $\sigma_{energyscale} = 4.5\%$. In order to estimate the systematic effect on the energy spectra, we artificially shifted the reconstructed energy of ±4.5% and we computed the ratio of these two distributions to the one obtained using the nominal value, *i.e.* no shift. The uncertainty of each bin was finally estimated using the deviation observed in the two artificial samples, one corresponding to positive direction and the other one to negative direction. This is shown in Fig.4.27, where we can see that this contribution is generally below 10% at low energy, but strongly increases at high energy, reaching a maximum value of about 30-90% depending on the pseudorapidity region. This is therefore the dominant term in the systematic uncertainty at high energy. Note that this is the only systematic effect for which we did not use symmetric errors derived from the maximum deviation observed, because in this case bin-by-bin correlation is quite strong and we expect to have a better estimation of the final uncertainty in this way.

4.7.1.2 Beam Center

In order to reconstruct the pseudorapidity η of the incoming particle we need to know the scattering angle θ that, being the distance between IP1 and LHCf very large (141.05 m), can be approximated as

$$\theta = \frac{d}{iptolhcf} \tag{4.12}$$

where $d = \sqrt{(x - x_0)^2 + (y - y_0)^2}$ and $iptolhcf$ is the IP1-LHCf distance along the z axis. As described in §3.3.2, upstream LHC reference system is defined in such a way that the z axis is aligned with the beam direction and positive going from IP1 to Arm2, the y axis is normal to the ground and the x axis is perpendicular to the y-z plane and positive going from Arm2 towards the center of LHC ring. The point (x_0, y_0) represents the projection of beam center on the LHCf detector taking into account the beam crossing angle θ_{cross}[13]. The estimation of this point is of course mandatory for the reconstruction of θ and can be performed in two different ways: the first one is making use of Beam Position Monitors (BPMSW) installed at ±21 m from IP1; the second one is exploiting the fact that neutrons

---

[13] Note that, differently from the standard LHC reference system, in this paragraph the origin is the expected position of the beam center on the tower (8 mm from right edge for x, 12.5 mm from bottom edge for y), not the experimental one (x_0, y_0), that is what we want to measure.

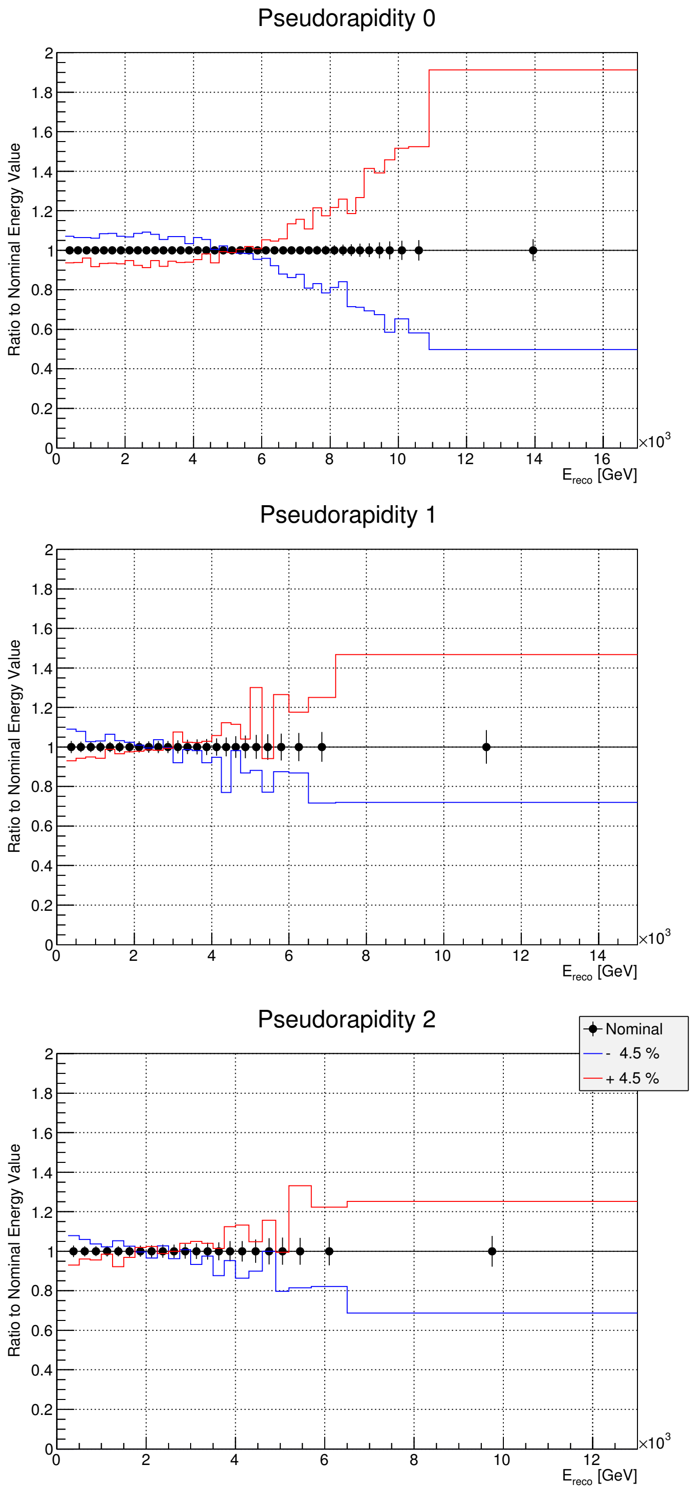

Figure 4.27: Ratios of the energy distribution obtained artificially shifting reconstructed energy to the same distribution relative to the nominal energy value. Statistical uncertainty due to data sample size is also shown.

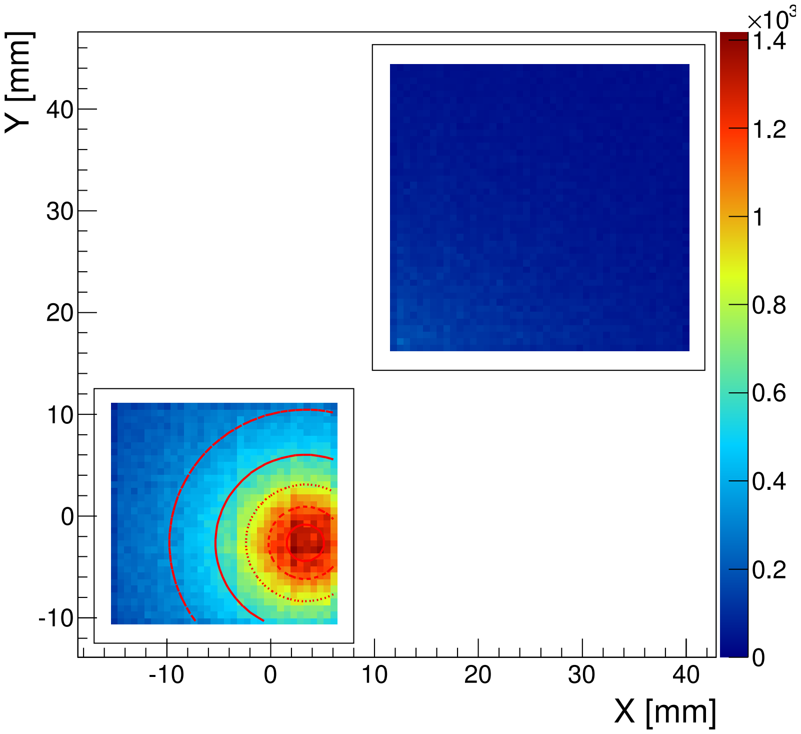

Figure 4.28: Arm2 hadron position distribution seen in the LHC reference frame for the runs used in the analysis. The origin is the expected position of the beam center on the tower (8 mm from right edge for x, 12.5 mm from bottom edge for y). The superimposed red line represents the result of the fit.

position distribution is strongly focused along beam axis. Because in past analyses the second method showed a higher accuracy compared to the first one, in this work we did not consider the BPMSW data and estimated the beam projection on the detector performing a fit on the bidimensional neutron position distribution. The fit function used is the one that was found to have the best agreement with simulations among different hadronic interaction models

$$f(x, y) = Ae^{-B\sqrt{(x-x_0)^2+(y-y_0)^2}} \tag{4.13}$$

where A, B, x_0, y_0 are *fit* parameters. The best value for the point (x_0, y_0) was obtained using hadrons whose reconstructed energy is above 1 TeV, whereas the uncertainty was estimated comparing this result to the one that we obtain selecting higher energy hadrons (5 and 9 TeV). Fig.4.28 shows the position distribution seen from upstream together with the fitted function. Respect to the expected beam center value, the experimental one obtained from the bidimensional fit is $x_0 = 3.3 \pm 0.3\ mm$ and $y_0 = -2.7 \pm 0.3\ mm$.

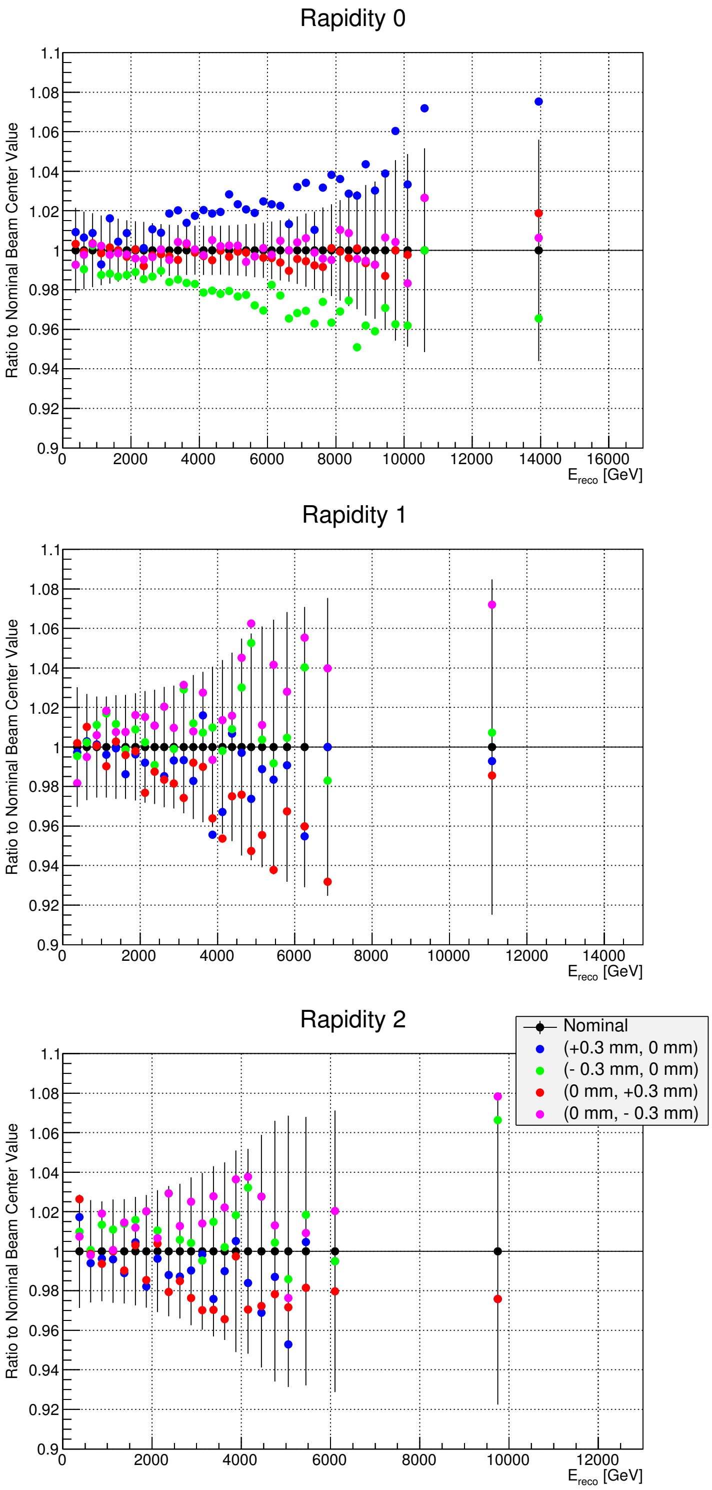

Figure 4.29: Ratios of the energy distribution obtained artificially shifting beam center position to the same distribution relative to the measured beam center value. Statistical uncertainty due to data sample size is also shown.

In order to estimate the impact of the beam center uncertainty on the final energy spectra, we artificially shifted the point (x_0, y_0) by $\pm 0.3\ mm$. We produced four different data sample relative to a shift of $(+0.3, 0.)$, $(-0.3, 0.)$, $(0., +0.3)$ and $(0., -0.3)\ mm$. For each sample we computed the ratio of the relative energy spectra to the one obtained using beam center nominal value. This is shown in Fig.4.29, where we can see that distributions obtained using the shifted value are mostly consistent with the nominal one considering statistical uncertainties. This is especially true for the two regions on LT, whereas for the one on ST it is not always the case. The final beam center systematic uncertainty was estimated for each energy bin using the maximum deviation from 1 among the four sample. This effect ranges from about 1% at low energy to about 8% at high energy, independently from the pseudorapidity region.

It is interesting to note that on pseudorapidity region 0 the dominant contribution to this systematic uncertainty comes from beam position on x axis. This is natural if we consider that beam center lies on the x edge of this region and that neutrons distribution is strongly focused along beam direction: therefore a small change in x_0 turns into a large difference in the number of selected hadrons events. An additional reason for this strong dependence could be that, being the beam center very near to the edge of the tower, a small change in x_0 selects a region of the detector for which performances of position dependent correction factors are worse than at center.

4.7.1.3 Position resolution

As described in §3.5, if we consider the reconstructed position of hadrons above 350 GeV, the FWHM is better than 1 mm, but long tails were found. In order to take into account this effect we decided to be conservative introducing an additional systematic uncertainty. This can be estimated from simulations making use of two energy distributions: the one obtained reconstructing position by Lorentzian fit and the one obtained using true position provided by MC. Fig.4.30 shows the ratio between the second distribution and the first one obtained using QGSJet II-04 and EPOS-LHC toy MC. As we can see, due to limited statistics, curves are not so smooth and there are large fluctuations between adjacent bins. Anyway, there is no strong model dependence and a general trend can be found: from a reduction of about 10% at low energy to an enhancement of about 5% at high energy. The absolute value of this effect is reasonable considering that position resolution improves as incident energy increases. The final systematic uncertainty due to position resolution was estimated for each energy bin using the maximum deviation from 1 among the two models.

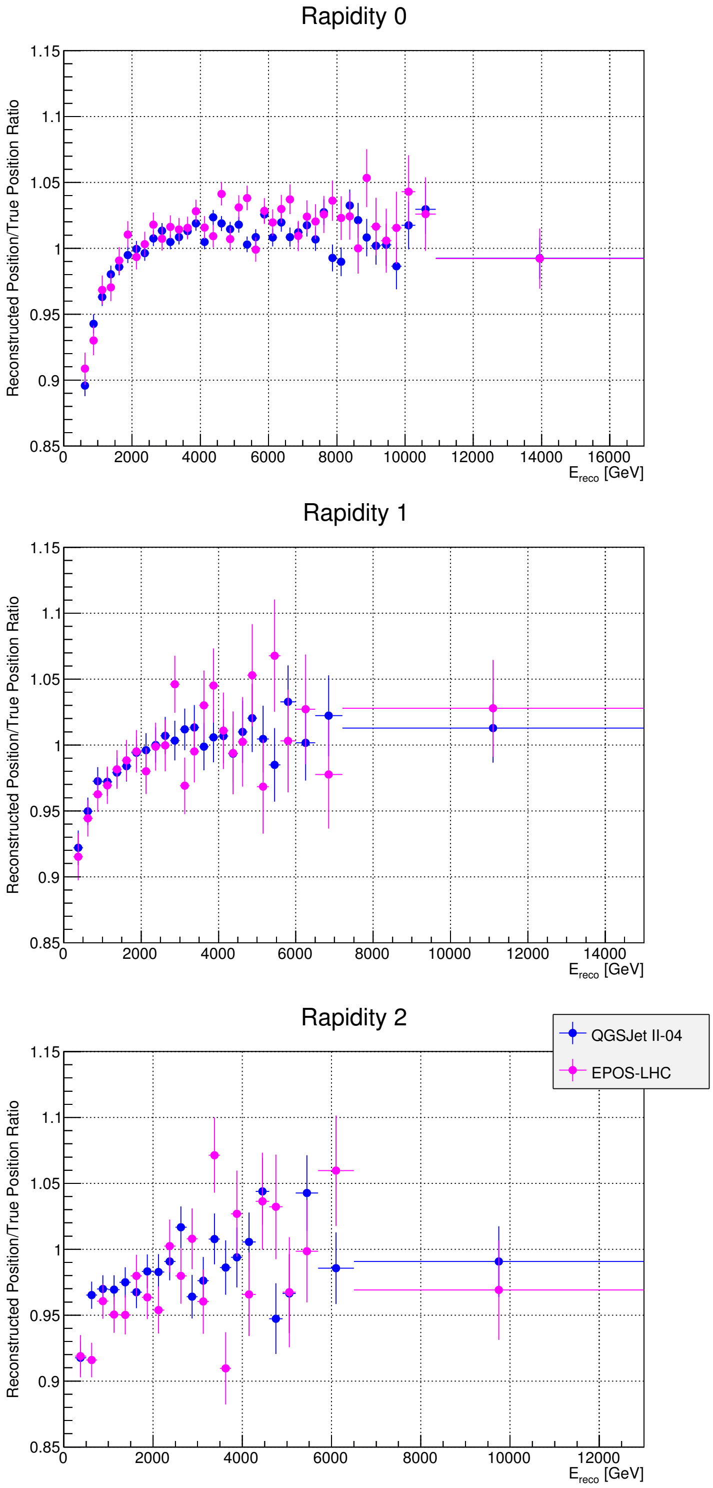

Figure 4.30: Ratios of the energy distribution obtained using true position provided by MC to the ones obtained reconstructing position by Lorentzian fit relative to QGSJet II-04 and EPOS-LHC toy MC.

4.7.1.4 Impact on unfolded spectra

All uncertainties related to the reconstruction process have been estimated for each bin of folded distributions. In order to consider their effect on unfolded spectra they must be taken into account inside unfolding algorithm. Being a statistical method, iterative bayesian unfolding is able to take into account statistical but not systematic uncertainties. Because of this reason we decided to proceed in the following way. We considered each contribution independently and we artificially shifted the folded spectra by its estimated relative uncertainty[14]. Once we built the two distributions corresponding to the two extremes of the error bars, we separately unfolded them. At this point we could easily estimate the contribution to the relative uncertainty on final spectra by the ratio of the unfolded distribution corresponding to the error bar edges to the nominal one obtained from unfolding. This procedure was repeated for all systematic sources. In the end, the final uncertainty was estimated using the quadrature sum of terms computed in this way, again independently for the two edges of the error. Fig.4.31 shows relative systematic uncertainties of each contribution on folded (left) and unfolded (right) spectra, once we applied the procedure just described. We can see that energy trend of each term is comparable before and after unfolding, even if regularization introduced by the algorithm increases the smoothness of results in the second case. It is interesting to note that energy uncertainty does not contributes in unfolded spectra as strongly as in folded ones. This is probably due to the fact that bins affected by such a high error have small statistics as well. Anyway, we can see that the dominant uncertainty is coming from energy contribution at high energy (about 30%) and position resolution (20%) at low energy, whereas all remaining terms are mostly below 10%.

4.7.2 Systematics related to unfolding

Iterative bayesian unfolding introduces three main systematic uncertainties, due to prior dependence, interaction model dependence and unfolding algorithm reliability. In the following we call them *model*, *interaction* and *method* uncertainty respectively.

Model uncertainty is related to the dependence of the unfolded spectra from the choice of the prior used as input of the first iteration. As described in §4.6, unfolding was performed using flat energy distribution as prior, whereas the associated systematic effect was estimated repeating the unfolding with a different prior. For this purpose we used toy MC relative to the two generators that resulted to have the best agreement with data at the folded spectra level: QGSJet II-04 and EPOS-LHC. For each bin, the uncertainty was estimated as the maximum deviation from 1 of the ratio between unfolded spectra using flat prior and unfolded spectra using generator prior.

---

[14] Remember that error bars are symmetric for all terms apart from energy contribution for which we decided to use directly the spectra relative to the two artificial shifts applied.

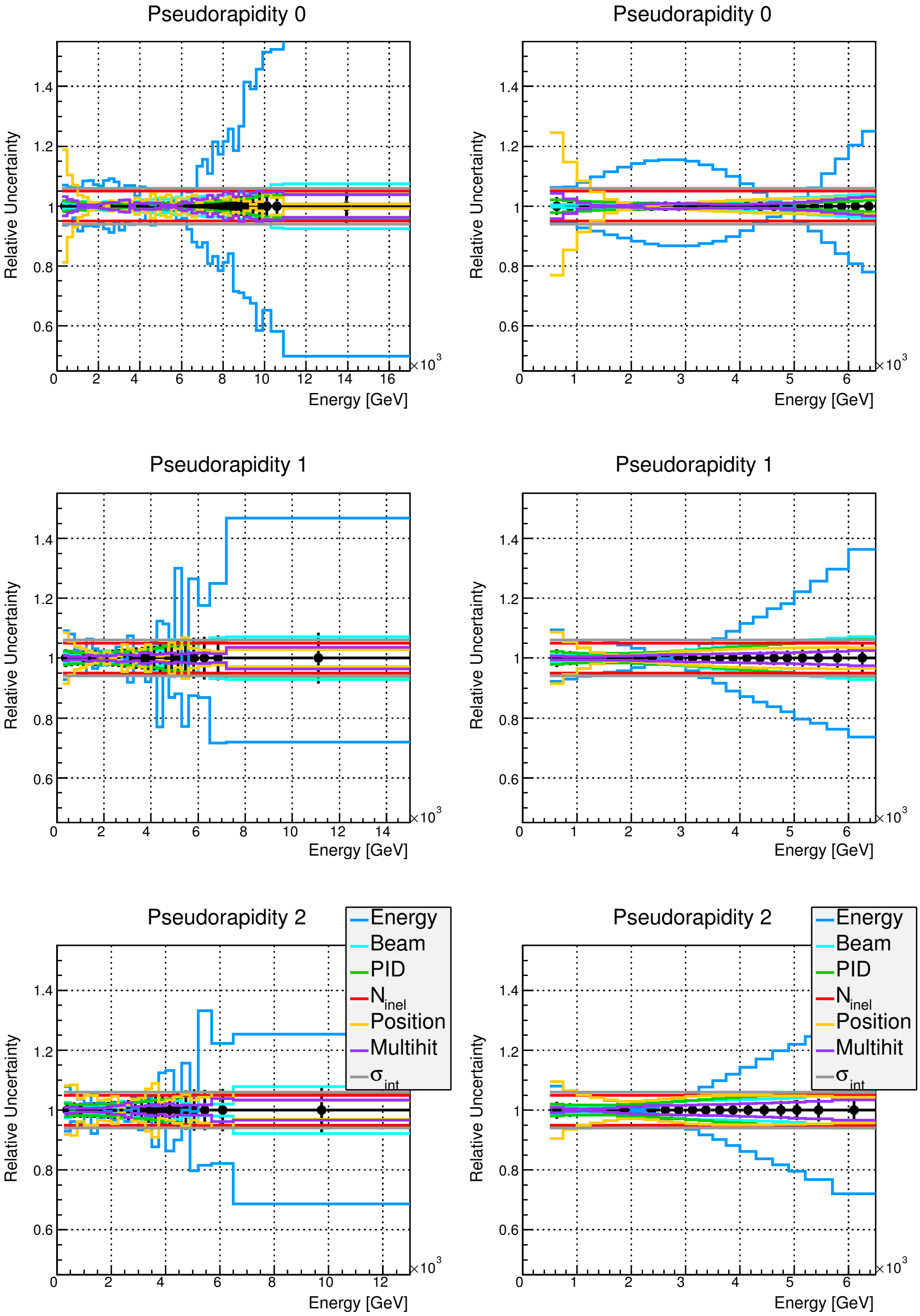

Figure 4.31: Summary of relative systematic uncertainties related to the reconstruction process before (left) and after (right) unfolding. Black data show the statistical error present on the folded spectra (left) and on the unfolded spectra (right) after corrections, discussed in §5.2 and 5.3 respectively.

Interaction uncertainty is related to the interaction model that was used to build response matrix. As described in §3.1.2, two models are currently considered for this purpose: we labeled them DPM and QGS. Flat MC was simulated making use of the DPM interaction model and now we want to estimate how the final result changes if we employ the QGS model instead. In order to save computation time, we generated an artificial QGS sample starting from the DPM sample and applying to each event some shift and smearing factors, determined on the basis of the different detector response in the two interaction models. For each bin, the uncertainty was estimated as the deviation from 1 of the ratio between the unfolded spectra using QGS for response matrix and the unfolded spectra using DPM for response matrix.

Method uncertainty is related to the ability of the unfolding algorithm to give a result very near to the true spectra associated to the folded distribution. For this purpose we used again toy MC relative to the two generators that resulted to have the best agreement with data at the folded spectra level: QGSJet II-04 and EPOS-LHC. For each bin, the uncertainty was estimated as the maximum deviation from 1 of the ratio between unfolded spectra and true model distributions.

The three terms just discussed are shown in Fig.4.32. As we can see, the largest contribution in the pseudorapidity region on ST comes from interaction uncertainty at very low energy (up to 55%) and in the two regions on LT from model uncertainty at very high energy (up to 70%). This fact can be due to different possible reasons. In general, unfolding is very critical in the first and last bins of the spectrum because of the discontinuity constituted by the boundaries. In addition, if at these edges statistics is small compared to other energies, the content of the unfolded spectra at the boundary bins can be very sensitive to the input prior and/or response matrix, as a consequence of limited resolution of the detector. Apart from these critical points, model uncertainty contributes in general for less than 20%, method uncertainty is mostly below 10% and interaction uncertainty is basically negligible.

4.8 Summary

In this chapter we presented the analysis procedure defined for the reconstruction of energy spectra relative to neutrons produced in p-p collisions at $\sqrt{s} = 13\ TeV$. In particular we discussed about correction factors, spectra unfolding and systematic uncertainties. All corrections are summarized in Tab.4.3, where we can see that missed events factors are by far the dominant one, due to limited detection efficiency. Other terms are below 20% for pseudorapidity region 0 and below 10% for pseudorapidity region 1 and 2. All systematic uncertainties are summarized in Tab.4.4, where we can see that, being always above 30%, among ones not due to unfolding, the dominant factor is coming from the uncertainty on the energy scale, generally below 10% except at high energies where it can reach about 30%, whereas other contributions are generally less than 10%. Unfolding strongly con-

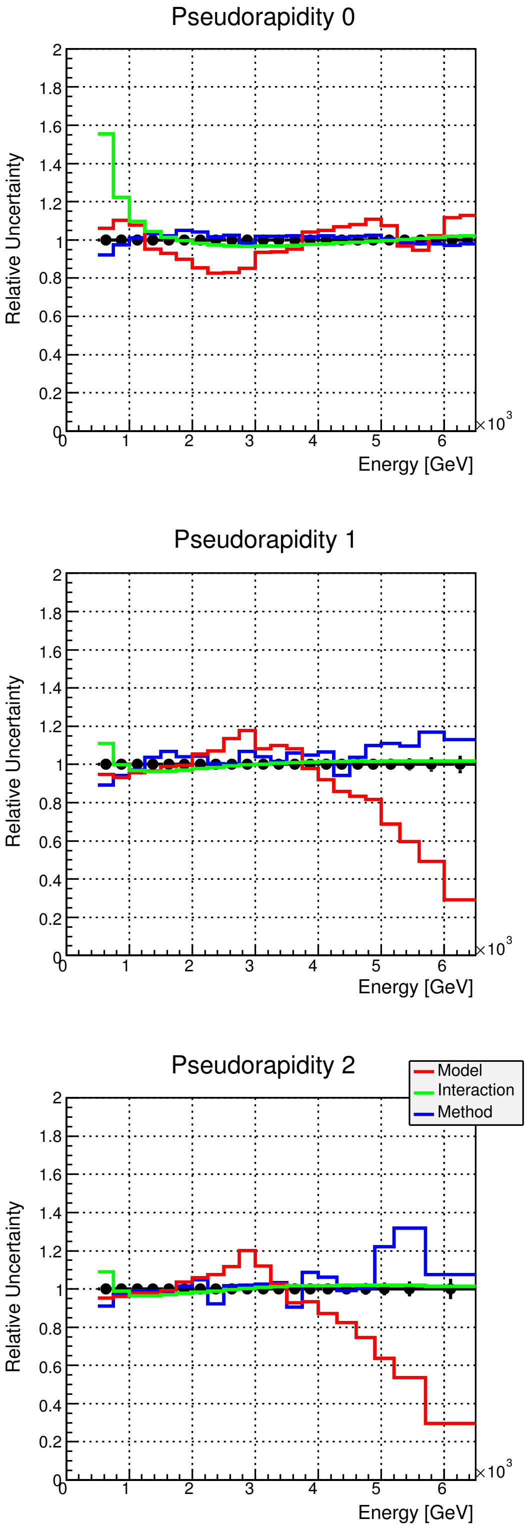

Figure 4.32: Summary of relative systematic uncertainties related to the unfolding process. Black data show the statistical error present on the unfolded spectra after corrections discussed in 5.3. Note that this shows only ratios of different contributions to the nominal unfolded value. The final symmetric error bars are estimated using the maximum deviation from 1.

	η_0	η_1	η_2
Background	0–4 %	0–6 %	0–7 %
PID	1–19 %	0–7 %	0–7 %
Multihit	0–11 %	0–5 %	0–7 %
Fake Events	0–19 %	2–11 %	5–11 %
Missed Events	39–152 %	37–132 %	38–125 %

Table 4.3: Minimum–maximum correction factors for each contribution in the three pseudorapidity regions selected for the analysis.

	η_0	η_1	η_2
Energy	1–25 %	0–36 %	0–29 %
Beam Center	0–4 %	1–7 %	1–6 %
PID	1–2 %	2–6 %	2–6 %
$\mathrm{N}_{\mathrm{inel}}$	5–5 %	5–5 %	5–5 %
Position Resolution	0–25 %	1–9 %	3–10 %
Multihit	0–4 %	0–3 %	0–3 %
σ_{int}	6–6 %	6–6 %	6–6 %
Unfolding Method	1–8 %	0–17 %	0–32 %
Unfolding Model	2–17 %	0–71 %	1–71 %
Unfolding Interaction	0–55 %	0–11 %	0–9 %

Table 4.4: Minimum–maximum systematic uncertainties for each contribution in the three pseudorapidity regions selected for the analysis. Numbers refer to the final unfolded spectra.

tribute to the final uncertainty due mainly to the large prior dependence found, that turned out in very different results once we considered different models for it, leading to a systematic error below 20% in the most forward pseudorapidity region, but that can reach about 70% in the other two regions. Some deviation between unfolded and true spectra due to the unfolding method was also found, especially on the two regions on LT. Finally, the dependence of the result from the interaction model used to build response matrix generates a strong uncertainty only below 1 TeV in pseudorapidity region 0, otherwise it has a negligible effect.

Chapter 5

Analysis results

In this chapter we present the analysis results relative to the energy spectra of very forward neutrons produced in p-p collisions at $\sqrt{s} = 13\ TeV$. In §5.1 the main differences between the present and the past neutrons analysis are described. Folded and unfolded energy spectra are then presented in §5.2 and §5.3, respectively. In both cases, they refer to measurements relative to the LHCf Arm2 detector only. Analysis results, regarding in particular their impact on cosmic rays physics, are discussed in §5.4. Finally, in §5.5 a test of Feynman scaling making use of neutrons distributions relative to p-p collisions at $\sqrt{s} = 7$ and $13\ TeV$ is presented.

5.1 Differences from past analysis

The analysis of neutrons energy spectra produced in p-p collisions at $\sqrt{s} = 13\ TeV$ is mostly similar to the $7\ TeV$ case [64]. Main differences concern the treatment of some of the topics described in the previous chapter: multihit, unfolding procedure and unfolding uncertainties.

Multihit problem was tackled in a different way in the two analysis. In both of them, all events were reconstructed as singlehit, but in the present case we decided to separately estimate corrections for this point and add a systematic uncertainty due to model dependence of these factors, whereas in the past case the change in the spectra due to this effect was considered only as a source of the systematic uncertainty. This was estimated artificially splitting the energy deposit in the calorimeter according to the fraction of true incident energies of the two particles entering the tower. This approach involves a certain number of approximations, including for example that both hadrons interact with the detector, and is still valid if multihit fraction is quite small. Because this fraction increases with energy, in our case this approximated estimation of uncertainty would have lead to large errors in the low energy region, hence we decided to run dedicated toy simulation for multihit and estimate corrections and uncertainties as described in §4.5.3.

Unfolding procedure is based on iterative bayesian unfolding implemented inside RooUnfold. In both analyses, an energy flat MC sample was used to build response matrix. Anyway, in the 7 TeV case the standard unfolding approach was followed, computing fake and missed events corrections while building response matrix, *i.e.* using the flat MC sample, and correcting for this effect in the iterative procedure, whereas in the 13 TeV case we decided to estimate these factors making use of generators and apply corrections outside unfolding.

Unfolding uncertainties are the most different point in the two analysis, because the treatment of unfolding results was carried on using opposite philosophies. In this analysis we estimated three sources of uncertainties, accounting for the dependence on the generator used to set the input prior of the iteration procedure, the dependence on the model used to simulate the interaction with the detector and the dependence on the algorithm used to unfold energy spectra. In particular, the first contribution was estimated making use of a different prior from the flat one, chosen from the models whose agreement with data is enough good at the folded spectra level, QGSJet II-04 and EPOS-LHC. This strong prior dependence was also found in the past analysis, but it was tackled from a different point of view. Instead of considering how the choice of the prior affects the final result, it was estimated the deviation of unfolded/true ratio from 1 making use of all available models. Then, these differences were employed to compute correction factors (using average) and systematic uncertainties (using maximum deviation) on the final experimental unfolded spectra. This is an hybrid approach in which the first and the third contribution considered in the 13 TeV case are mixed up, whereas the second one was not considered at that time. The reason for choosing a different approach from the 7 TeV case is that from a theoretical point of view it is not recommendable to apply unfolding corrections after unfolding, even if deviations between their estimation making use of different models are quite small. An additional motivation is that, even if they can not clearly show the shape of the spectra, folded distributions are enough to exclude models having a poor agreement with experimental results if our knowledge of detector response is reliable, therefore there is no need to take them into account in the estimation of unfolding uncertainties.

In the following, we will sometimes discuss about similarities between the results at 7 and 13 TeV, especially focusing on models deviation from them. Anyway, we must pay attention that the version of generators used in the two analysis is different, hence we can not expect to observe the same difference between data and models. This is particularly true for QGSJET II and EPOS generators, for which in the present analysis we used versions released by authors after their tuning based on LHC Run I results, whereas in the past analysis such versions were clearly not available. Actually, there is a more important and physical reason preventing us from a direct comparison of the two analysis, *i.e.* the fact that the phase space in the two cases is different. According to several scaling laws, *e.g.* Feynman scaling, we can expect a similar behavior[1] of inclusive production cross section at different

---

[1] Feynman scaling is formulated expressing production cross sections as a function of the variable $x_F = 2p_Z/\sqrt{s}$. Simply computing them in terms of energy of the incident particle leads to different energy ranges and different normalization factors between the 7 TeV and 13 TeV results. Hence, here "similar behavior" means generically similar shape of the distributions.

	η_0		η_1		η_2	
η	∞	10.76	9.22	8.99	8.99	8.81
θ (μrad)	0	42	198	249	249	298
r (mm)	0	6	28	35	35	42
${p_T}^{\sqrt{s}=7\ TeV}$ $[GeV/c]$	0	0.149	0.693	0.873	0.873	1.045
${p_T}^{\sqrt{s}=13\ TeV}$ $[GeV/c]$	0	0.276	1.288	1.620	1.620	1.940

Table 5.1: Phase space of the three pseudorapidity regions. We considered interval on pseudorapidity η, scattering angle θ, radius r in the $x-y$ plane at detector position, maximum detectable p_T for a given $\sqrt{s}$.

$\sqrt{s}$ in the very forward region, but this is true only if p_T coverage is the same. In our case, this condition is not verified because we chose the same η coverage for the two analysis, but beam energy is of course different. Tab.5.1 shows p_T coverage for a incident particle having momentum equal to beam energy, computed using the simple approximation $p_T = \sqrt{s}/2 \times \theta$, where θ is the crossing angle at the given η. We can clearly see the difference between the 7 TeV and 13 TeV case, hence, even assuming Feynman scaling is valid, we can not expect data to have a very similar behavior in the two analysis.

5.2 Folded energy spectra

Fig.5.1 shows the folded neutrons energy spectra for p-p collisions at $\sqrt{s} = 13\ TeV$ measured by the LHCf Arm2 detector, compared with QGSJet II-04, EPOS-LHC and DPMJet 3-0.4 generators. The quantity chosen to study neutrons production is the number of events normalized to the number of inelastic collisions and bin size of reconstructed energy. Event selection is the same described in §4.3 for reconstructed information, apart from the fact that in the case of generators we performed particle identification using MC true code instead of reconstructed L_{2D}. Background and PID corrections were applied to data, whereas we decided to not consider other corrections here, *i.e.* multihit and fake events[2]. The reason for this choice is that one of the motivation for studying folded spectra is to understand which models have a poor agreement with data in order to exclude them from the following steps of analysis (multihit, fake events and missed events corrections and uncertainties, unfolding uncertainty). Therefore we did not apply the two last corrections mentioned, because they were estimated exclusively using generators to which we want to compare our experimental results, possibly introducing a bias in our judgment. Consequently, we considered systematic uncertainties due to energy scale, beam center, PID correction, number of inelastic collisions and position resolution, but not due to multihit correction. Statistical uncertainties

---

[2] Remember that missed events corrections can be applied only after spectra unfolding.

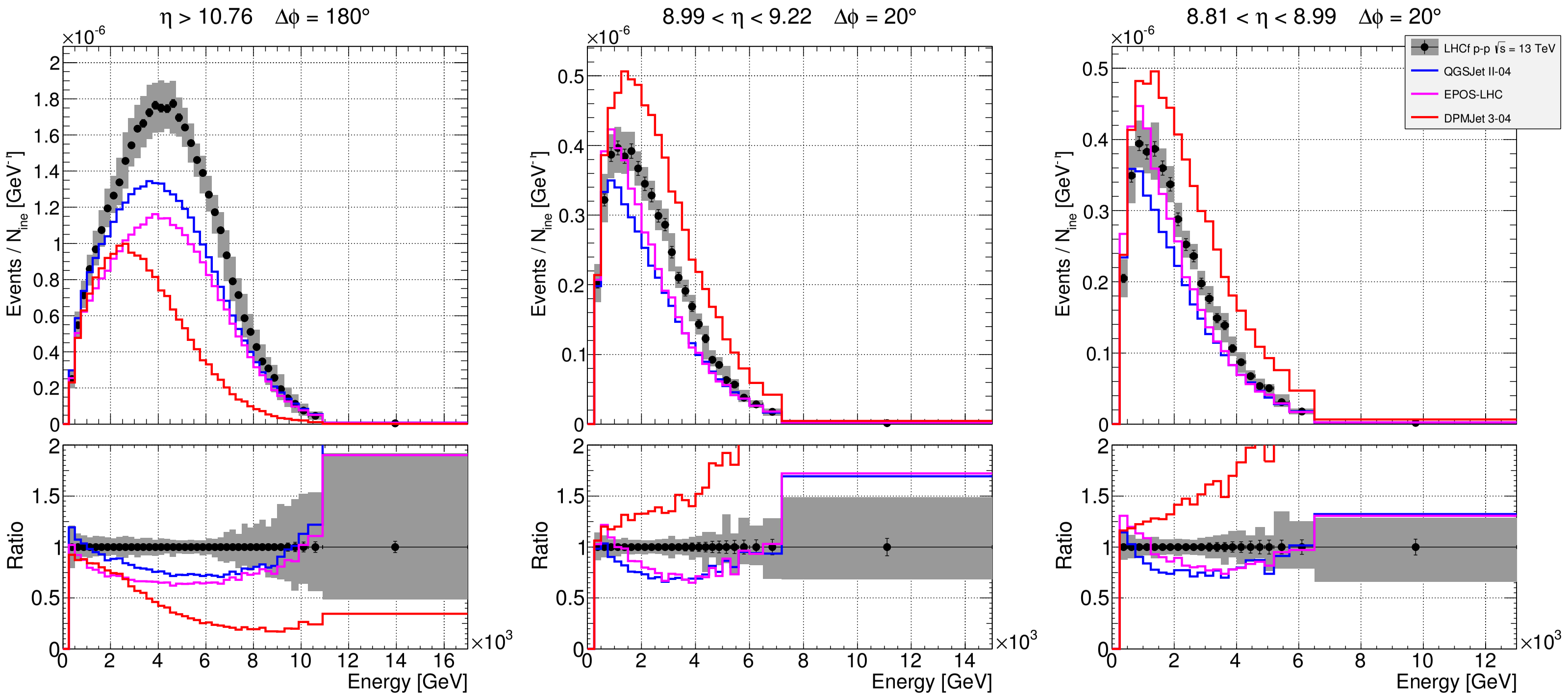

Figure 5.1: Folded neutrons energy spectra for p-p collisions at $\sqrt{s} = 13\ TeV$ measured by the LHCf Arm2 detector. Black markers are experimental data with statistical uncertainty, whereas gray bands represent the quadratic sum of statistical and systematic uncertainty. Histograms refer to generators folded spectra simulated using COSMOS-EPICS according to Arm2 detector response given by DPMJet 3-0.4 model. Top are energy distributions expressed as number of events normalized to the number of inelastic collisions and bin size of reconstructed energy and bottom are the ratios of these distributions to experimental data.

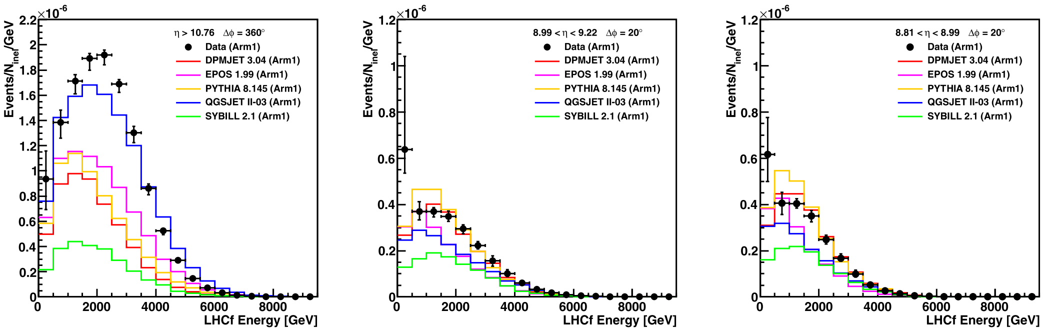

Figure 5.2: Folded neutrons energy spectra for p-p collisions at $\sqrt{s} = 7\ TeV$ [64] measured by the LHCf Arm1 detector. Black markers are experimental data with error bars given by the quadrature sum of statistical and systematic uncertainties (excluding energy scale and luminosity contributions). Histograms refer to generators folded spectra simulated using COSMOS-EPICS according to Arm1 detector response given by DPMJet 3-0.4 model. Note that, in pseudorapidity region 0, $\Delta\phi$ in the case of 7 TeV is twice the one of 13 TeV.

were always below 10%, because in each pseudorapidity region binning was defined in order to have at least 100 entries in each bin. All sources of error, including statistical ones, were assumed to be independent and summed in quadrature.

Pseudorapidity region 0 shows the largest discrepancy between experimental data and hadronic interaction models. All three generators considered strongly underestimate the number of neutrons produced in this pseudorapidity interval. In the case of QGSJet II-04 and EPOS-LHC, we can observe this tendency in the entire energy range except from the two extremes of the histogram, but this effect is particularly serious around 4 TeV. Because the maximum of the distribution is located in this region, where we can also note that deviation between models and data is largest, this fact can turn out in a large systematic effect on generators. However, it is interesting to note that, apart from DPMJet 3-0.4, all other models predicts a shape of the energy spectra not so different from the one observed in data, even if limited detector resolution can mask possible differences. If we compute the number of neutrons produced per units of N_{ine} over the whole energy range, we get that QGSJet II-04 underestimates this number of about 20%, EPOS-LHC by 31% and DPMJet 3-0.4 by 54%. Considering all these points, we can conclude that QGSJet II-04 is the best model in pseudorapidity region 0 and its agreement with data is mostly comparable to the one of QGSJet II-03 in the analysis relative to p-p collisions at $\sqrt{s} = 7\ TeV$, shown in Fig.5.2. Among other models, EPOS-LHC appears to be improved respect to EPOS 1.99, even if it is still worse than QGSJet II-04, whereas no evident difference was found in the case of DPMJet 3-0.4, for which we used the same version in both analysis.

Pseudorapidity region 1 and 2 exhibit a similar behavior but the agreement between experimental data and hadronic interaction models is better. If we exclude

DPMJet 3-0.4, that in this case overestimates neutrons production, QGSJet II-04 and EPOS-LHC generally underestimate this number. Looking at the region around 1 TeV, where the maximum of the distribution is located, we can see that their deviation from data is quite small, sometimes negative, sometimes positive. Computing the number of neutrons produced per units of N_{ine} over the whole energy range, we get that QGSJet II-04 underestimates this number of about 20% and 17% for pseudorapidity region 1 and 2 respectively, EPOS-LHC of 13% and 5%, whereas DPMJet 3-0.4 overestimates this number of about 39% and 44%. Considering all these points, we can conclude that EPOS-LHC is the best model in pseudorapidity region 1 and 2, even if QGSJet II-04 is only slightly worse. If we compare these results to the ones relative to p-p collisions at $\sqrt{s} = 7\ TeV$, we can see quite different results. In the past analysis DPMJet 3-0.4 was the model in best agreement with data, whereas it resulted to be the worst among the ones considered in the present analysis. Because the version is the same in both cases, this fact must be due to different $\mathrm{p_T}$ coverage. Looking at Tab.5.1 we can think that a possible interpretation is that the number of neutrons produced is underestimated at small $\mathrm{p_T}$ (in order to have an idea we can say $\mathrm{p_T} < 0.5\ GeV/c$) and gradually increases with $\mathrm{p_T}$, leading at first to a good agreement with data ($0.5\ GeV/c < \mathrm{p_T} < 1.0\ GeV/c$) and then to an overestimation of this quantity ($1.0\ GeV/c < \mathrm{p_T} < 2.0\ GeV/c$). Regarding EPOS and QGSJet II, we can see that they predicts very similar distributions in the two analysis, but their agreement with data resulted to be better in the present case.

In conclusion, we can say that QGSJet II-04 and EPOS-LHC resulted to be the hadronic interaction models in best agreement with data, with clear but not dramatic differences found between them in the three pseudorapidity regions. On the opposite side, the deviation between experimental measurements and DPMJet 3-0.4 is very large, regarding not only the absolute number of neutrons produced in collisions, but also the shape of the energy distribution. Because of these reasons, all the following steps of analysis that require toy MC were carried on making use of QGSJet II-04 and EPOS-LHC generators only.

5.3 Unfolded energy spectra

Fig.5.3 shows the unfolded neutrons energy spectra for p-p collisions at $\sqrt{s} = 13\ TeV$ measured by the LHCf Arm2 detector, compared with QGSJet II-04, EPOS-LHC, DPMJet 3.06[3], PYTHIA 8.212 and SIBYLL 2.1 generators. The quantity chosen to study neutrons production is the differential neutrons production cross section

$$\frac{d\sigma_n}{dE} = \frac{1}{L}\frac{2\pi}{\Delta\phi}\frac{\Delta N}{\Delta E} \tag{5.1}$$

---

[3] DPMJet version is different in folded and unfodled spectra. This is because the version present in COSMOS v.7.645 is DPMJet 3-0.4, whereas the version present in CRMC v1.5.6 is DPMJet 3.06.

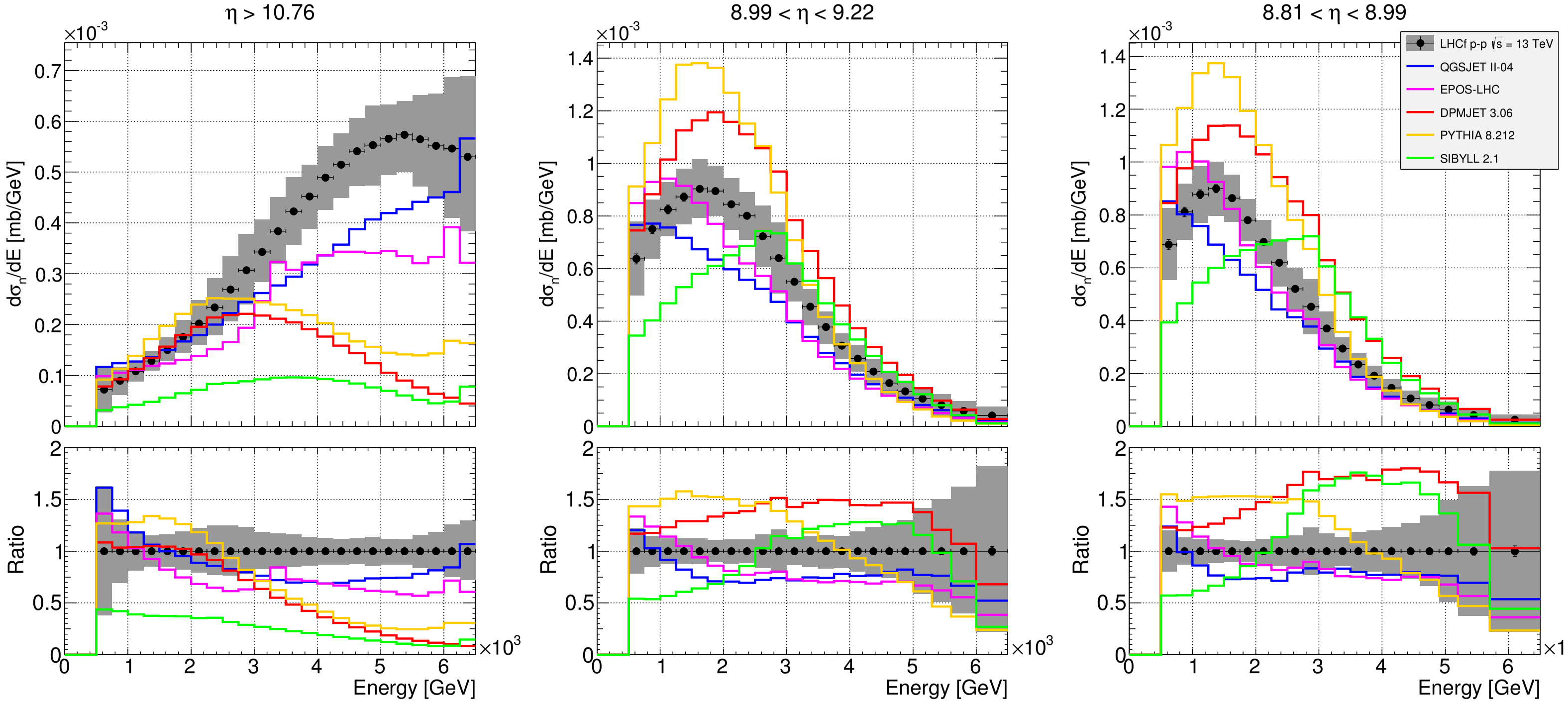

Figure 5.3: Unfolded neutrons energy spectra for p-p collisions at $\sqrt{s} = 13\,TeV$ measured by the LHCf Arm2 detector. Black markers are experimental data with statistical uncertainty, whereas gray bands represent the quadrature sum of statistical and systematic uncertainty. Histograms refer to generators spectra simulated using CRMC. Top are energy distributions expressed as $\mathrm{d}\sigma_\mathrm{n}/\mathrm{dE}$ and bottom are the ratios of these distributions to the experimental data.

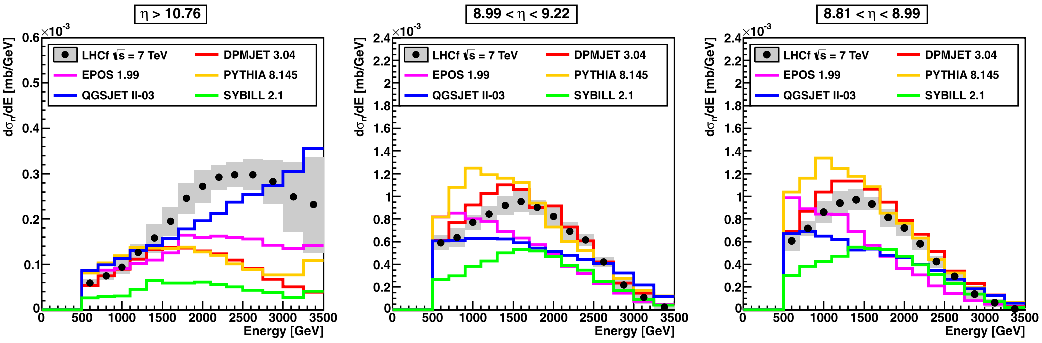

Figure 5.4: Unfolded neutrons energy spectra for p-p collisions at $\sqrt{s} = 7\ TeV$ [64] measured by the combination of Arm1 and Arm2 results. Black markers are experimental data with statistical uncertainty, whereas gray bands represent the quadrature sum of statistical and systematic uncertainty. Histograms refer to generators spectra simulated using COSMOS.

where L is the integrated luminosity corresponding to the data set and $\Delta N = \Delta N(\Delta\eta, \Delta E)$ is the number of neutrons observed for every pseudorapidity interval $\Delta\eta$ in each energy bin of width ΔE. Every correction factor was applied to spectra and every systematic uncertainty was considered. All sources of error, including statistical ones, were assumed to be independent and summed in quadrature.

Pseudorapidity region 0 is the most interesting region because only QGSJet II-04 and, in part, EPOS-LHC qualitatively reproduce the increasing number of neutrons in the high energy region. All other models predict the opposite behavior, leading to a clear underestimation of differential cross section that can reach up to a factor 80% near the upper edge of the spectrum. On the other side, in the low energy region some models slightly overestimate experimental results: this is true especially for PYTHIA 8.212, whereas QGSJet II-04 and EPOS-LHC are mostly consistent with our measurements considering the error bars. DPMJet 3.06 appears to be in very good agreement with data below 2 TeV, result that, even if the version of the model is different, is very similar to the one relative to p-p collisions at $\sqrt{s} = 7\ TeV$, shown in Fig.5.4. Considering the entire energy range, QGSJet II-04 is the model having the best overall agreement with data, predicting a maximum deviation of about 25% above 1 TeV. After that we should mention EPOS-LHC that, as noted in the previous paragraph, constitutes probably the most significant difference from the results of the past analysis, exhibiting an improvement respect to EPOS 1.99.

Pseudorapidity region 1 and 2 are characterized by a good overall agreement of EPOS-LHC and QGSJet II-04 with data. In particular the former is better than the latter in the region around 1.5 TeV, where data indicates that differential production cross section reaches the highest value. The deviation of EPOS-LHC from experimental measurements is mostly below 25%, apart from at high energy where anyway the model prediction is consistent with the measured value given the large error bars. In pseudorapidity region 1, even SIBYLL 2.1 agreement with data is not so bad above 2.5 TeV, while it differs significantly below this energy. PYTHIA 8.212 and DPMJet 3.06 lead to a general overestimation of the number of neutrons produced that can be even larger than 50% in the worst case. These results are quite different from the ones relative to p-p collisions at $\sqrt{s} = 7\ TeV$, where DPMJet 3.06 resulted to be the model in best agreement with data in these two pseudorapidity regions. This fact is probably due to the different $\mathrm{p_T}$ coverage between the two analysis, as discussed in §5.1 and 5.2.

5.4 Discussion

From the $d\sigma_n/dE$ spectra shown in Fig.5.3 three important quantities can be derived for each pseudorapidity region: inelasticity k, neutrons production cross section σ_n and neutrons energy flow E_n[4]. They are respectively defined as: the average fraction of beam energy not carried out by the forward leading baryon, the neutrons differential production cross section integrated over the energy range and the energy-weighted neutrons distribution normalized to the number of inelastic collisions. These quantities can be computed using the following relations

$$\begin{aligned} k &= \frac{1}{\sigma_n} \int \frac{d\sigma_n}{dE} \left(1 - \frac{E}{\sqrt{s}/2}\right) dE \\ \sigma_n &= \int \frac{d\sigma_n}{dE} dE \\ E_n &= \frac{1}{\sigma_{ine}} \int \frac{d\sigma_n}{dE} E dE \end{aligned} \tag{5.2}$$

where integrals are computed over all bins in the energy range going from 500 to 6500 GeV, while E and dE represent the center and the width of each energy bin of the spectrum, respectively. For each measurement the uncertainty has been calculated using the same relation but replacing the value of $d\sigma_n/dE$ with its relative lower/upper band error for each bin. Note that, being derived from the energy spectra, these three quantities do not refer only to neutrons, but also to a fraction of other types of hadrons (mainly Λ^0 and K^0), as discussed in §4.4.

Inelasticity k is shown in Fig.5.5. Note that this quantity is computed assuming that all neutrons are forward leading baryon because at present it is not possible to identify if a particle is the forward leading baryon. Despite this limitation, we can clearly see that most models overestimate this value in the most forward region. This point is quite interesting in cosmic rays physics, because larger value of k means a faster development of EASs. Thus, all models lead to showers that are less penetrating than what our measurements indicate when the forward leading

---

[4] Generally, "energy flow" indicates not the absolute value (E_n), but the differential value expressed as a function of η ($dE_n/d\eta$). Because here we considered both quantities, for simplicity we call the former *energy flow* and the latter *differential energy flow*.

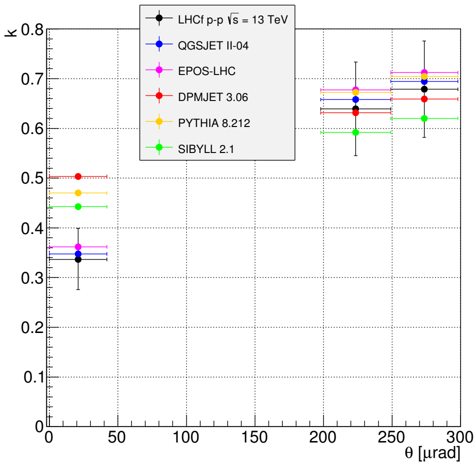

Figure 5.5: Inelasticity k for different scattering angle θ, each interval corresponding to one of the three pseudorapidity regions. Measurements are obtained considering only neutrons above 500 GeV. Black markers are LHCf data relative to p-p collisions at $\sqrt{s} = 13\ TeV$, whereas other markers refer to models simulated using CRMC.

baryon has pseudorapidity $\eta > 10.76$. This different value of k is a consequence of the large deviation between data and models at high energy, a problem already highlighted in the analysis relative to p-p collisions at $\sqrt{s} = 7\ TeV$. On the other side, we must observe that no strong discrepancy was found in the other two regions, where all models lay inside the experimental uncertainty. This is an important point because, as we will discuss in a moment, the contribution of these two regions to the evolution of the shower is higher.

Neutron production cross section σ_n and neutron energy flow E_n are reported in Tab.5.2 and 5.3. Fig.5.6a and b show the same quantities expressed in terms of differential value as a function of η[5], *i.e.* $d\sigma_n/d\eta$ and $dE_n/d\eta$. If in the most forward pseudorapidity region all models underestimate these two quantities, in the other two regions a different behavior is found. In particular, it is interesting to note that, despite its limited agreement with data when considering the $d\sigma_n/dE$ spectra, SIBYLL 2.1 predicts values of σ_n and E_n very similar to the ones observed experimentally. This is an important feature of a model because, being the energy flow very high in these two pseudorapidity regions, their contribution to the evolution of EASs is significant. Apart from SIBYLL 2.1, EPOS-LHC is also well consistent with data, whereas QGSJet II-04 leads to slightly smaller values.

---

[5] In the case of the most forward region we used $\eta = 13$ as upper limit to avoid problems with ∞ : from MC we checked that the area $\eta \in [10.76, 13]$ includes more than 95% of events belonging to the original interval $\eta \in [10.76, \infty]$ of pseudorapidity region 0.

	σ_n (mb)			σ_n/σ_n^{Data}		
	η_0	η_1	η_2	η_0	η_1	η_2
LHCf Data	2.19	2.69	2.23	-	-	-
QGSJet II-04	1.77	2.15	1.85	0.81	0.80	0.83
EPOS-LHC	1.49	2.40	2.17	0.68	0.89	0.97
DPMJet 3.06	0.87	3.61	3.20	0.40	1.35	1.43
PYTHIA 8.212	1.12	3.63	3.16	0.51	1.35	1.42
SIBYLL 2.1	0.42	2.27	2.22	0.19	0.85	0.99

Table 5.2: Neutrons production cross sections relative to p-p collisions at $\sqrt{s} = 13\ TeV$ in each of the three pseudorapidity regions. Measurements are obtained considering only neutrons above 500 GeV. LHCf data, model predictions and model/data ratio are reported.

	E_n (GeV)			E_n/E_n^{Data}		
	η_0	η_1	η_2	η_0	η_1	η_2
LHCf Data	120.38	80.21	59.43	-	-	-
QGSJet II-04	95.52	60.83	46.72	0.79	0.76	0.79
EPOS-LHC	78.56	64.21	51.68	0.65	0.80	0.87
DPMJet 3.06	35.67	110.25	90.42	0.30	1.37	1.52
PYTHIA 8.212	48.98	98.46	77.35	0.41	1.23	1.30
SIBYLL 2.1	19.47	76.69	69.66	0.16	0.96	1.17

Table 5.3: Neutrons energy flow relative to p-p collisions at $\sqrt{s} = 13\ TeV$ in each of the three pseudorapidity regions. Measurements are obtained considering only neutrons above 500 GeV. LHCf data, model predictions and model/data ratio are reported.

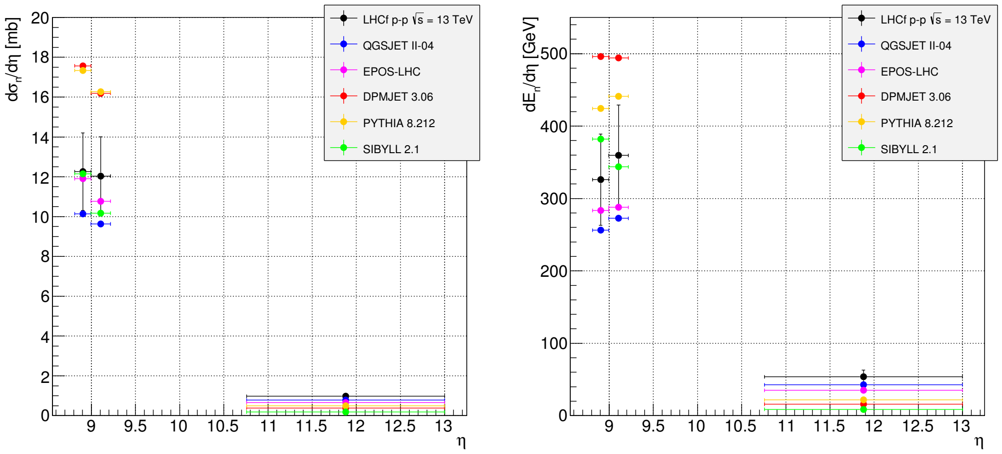

(a) **(b)**

Figure 5.6: Neutrons differential production cross section (a) and energy flow (b) expressed as a function of η. Measurements are obtained considering only neutrons above 500 GeV. Black markers are LHCf data relative to p-p collisions at $\sqrt{s} = 13\ TeV$, whereas other markers refer to models simulated using CRMC.

5.5 Feynman scaling

Feynman scaling hypothesis [57] asserts that, in the very forward region, secondary particles production cross sections expressed as a function of the $\mathrm{x_F} = 2\mathrm{p_Z}/\sqrt{s}$ variable should be independent on $\sqrt{s}$ if we consider the same $\mathrm{p_T}$ interval. Therefore it is possible to test it in the case of neutrons comparing LHCf results relative to p-p collisions at $\sqrt{s}$ =7 and 13 TeV. Because we do not have $\mathrm{p_T}$ but energy spectra, in both cases we have to perform two approximations. The first one is that the longitudinal momentum $\mathrm{p_Z}$ is basically the same as the incident energy E, an hypothesis very well verified in the forward region: anyway in the following we will redefine the x_F variable as $x_E = 2E/\sqrt{s}$ to make this assumption clearer. The second one is that $\mathrm{p_T}$ coverage is defined making use of scattering angle and maximum available energy in the beam, *i.e.* $\mathrm{p_T} = \theta\sqrt{s}/2$: referring to Tab.5.1, we considered the interval $\mathrm{p_T} < 0.15\ GeV/c$ obtained in the 7 TeV analysis for a radius $r < 6\ mm$ and we redefined the most forward pseudorapidity region in the 13 TeV analysis to a radius $r < 3.23\ mm$ in order to have the same $\mathrm{p_T}$ coverage. Fig.5.7 shows the unfolded spectra obtained for $r < 3.23\ mm$, corresponding to $\eta > 11.38$, after having repeated the entire analysis procedure for this new pseudorapidity region. The conclusions that we can obtain from it are mostly the same that we discussed in §5.3. Production cross sections of $\mathrm{p_T} < 0.15\ GeV/c$ neutrons produced in p-p collisions at $\sqrt{s} = 7$ and 13 TeV expressed as a function of x_E are shown in Fig.5.8. Even if the two curves are everywhere consistent inside the error bars, we can see that their agreement is quite good in the range $0.2 < x_E < 0.75$, whereas above these values it is limited to the boundary region of the uncertainty. The general agreement between the 7 and 13 results, more than telling us something about Feynman scaling, is a good indication of the validity of our analysis, that therefore will be extended to Arm1 in the future.

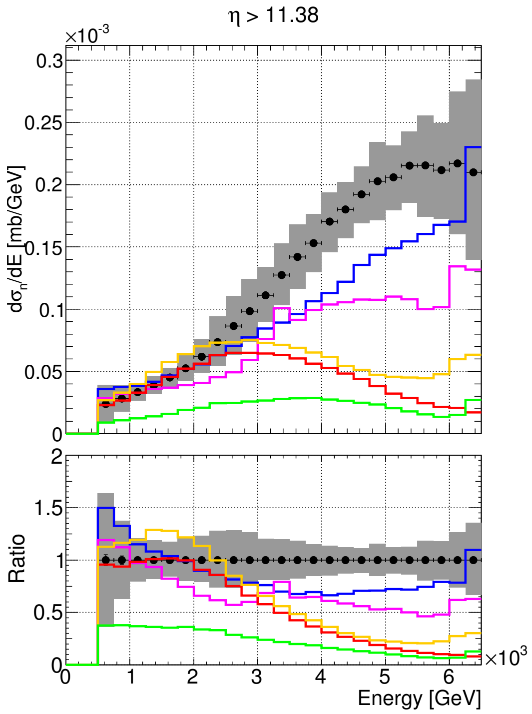

Figure 5.7: Unfolded energy spectra relative to $\eta > 11.38$ neutrons produced in p-p collisions at $\sqrt{s} = 13\ TeV$ measured by the LHCf Arm2 detector. Meaning of markers and colors is the same as in Fig.5.3.

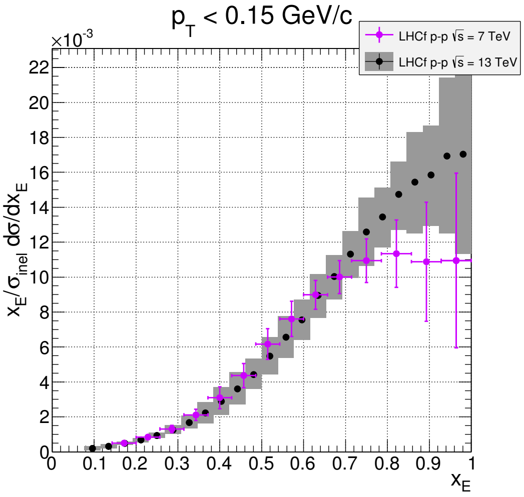

Figure 5.8: Neutrons production cross section expressed as a function of $x_E = 2E/\sqrt{s}$ for p-p collisions at $\sqrt{s} = 7$ and $13\ TeV$: $7\ TeV$ data refer to the combination of Arm1 and Arm2 results, whereas $13\ TeV$ data are relative to Arm2 results only.

Chapter 6

Conclusions

In order to have a better understanding of the processes responsible for acceleration and propagation of cosmic rays in the universe, it is necessary to perform measurements of flux and composition up to the GZK cutoff region. Because the flux of ultra high energy cosmic rays - *i.e.* cosmic rays having energies above 10^{18} eV - is less than 1 particle per km^2 per year, it is possible to study them only using large area detector arrays at the ground level. In this case their properties are obtained indirectly from the reconstruction of the extensive air showers they form when interacting with the atmosphere. EASs physics is described by soft (non perturbative) QCD, based on some phenomenological models involving the exchange of one or more Pomerons. Due to the lack of experimental calibration data at high energies, among these models very different predictions are found, therefore inducing large systematic uncertainties on UHECRs measurements.

The main aim of the LHC-*forward* (LHCf) experiment is to provide high energy calibration data that can be useful to test and tune models used in the very forward region. Thanks to two small sampling calorimeters, Arm1 and Arm2, installed at ± 140 m from LHC IP1, LHCf can detect neutral particles produced in the very forward region ($\eta > 8.4$) by proton-proton and proton-ion high energy collisions (proton-proton interaction at $\sqrt{s} = 14$ TeV is equivalent to the collision of a 10^{17} eV proton with a proton at rest, hence it is possible to perform measurements at an energy close to the typical one of UHECRs). Detectors are optimized for the reconstruction of π^0 from its 2γ decay, but they offer the possibility to study other secondary hadrons as well, despite with more limited performances. Neutrons, the most abundant hadrons reaching LHCf, have particular interest from the point of view of cosmic rays physics. This is because it has been noted that a small change in the number of baryons produced very near to the first interaction point of a cosmic ray with the atmosphere can explain the *muon excess problem*, observed by Pierre Auger Observatory and Telescope Array.

Calibration of LHCf Arm2 upgraded detector for the reconstruction of hadronic showers was performed making use of both beam test data and MC simulations. This involved the estimation of scintillators absolute gains, position dependent correction factors and deposited energy to primary energy conversion coefficients. The final systematic uncertainty on the energy scale due to calibration process resulted to be 3.5%, that is comparable with the value obtained in the case of the old detector. However, whereas in the past case a 6.5% discrepancy was found between experimental data and simulations relative to 350 GeV protons, in the present case we found that DPMJet 3-0.4 model deviations from our measurements are much below the uncertainty due to the calibration of scintillators absolute gains. Because energy and position resolutions were also comparable, we decided to rely on DPMJet 3-0.4 for the calibration of the detector up to the LHC energy. Performances of Arm2 as a function of energy were also studied through MC simulations based on this model, obtaining that above 2 TeV detection efficiency is about 70%, energy resolution 40% and position resolution 1 mm.

Analysis of data relative to p-p collisions at $\sqrt{s} = 13\ TeV$ with the Arm2 detector was divided in three different pseudorapidity regions: $8.81 < \eta < 8.99$, $8.99 < \eta < 9.22$, $\eta > 10.76$. Some preliminary studies on MC simulations were necessary to set event selection criteria, mainly software trigger condition and particle identification. Five different corrections factors were applied to data to take into account background and inefficiencies. Among systematic uncertainties due to the reconstruction process, the largest contribution on spectra is coming from the energy scale, resulting from the quadrature sum of uncertainties due to calibration (3.5%), hardware effect during operations (2%) and π^0 mass shift (2.15%) for a total of 4.5%. Even if not small, this is still a good improvement with respect to the past analysis where data-model deviation relative to 350 GeV protons (6.5%) and a higher π^0 mass shift (3.8%) lead to larger uncertainty. The effect of the energy scale on unfolded distributions is generally below 10% except at high energies where it can reach about 30%. A large dependence on the choice of prior used in iterative bayesian unfolding was also found, resulting in an uncertainty below 20% in the most forward pseudorapidity region, but that can reach about 70% at high energy in the other two regions.

After unfolding, energy spectra were compared to the most common generators employed in cosmic rays physics. Similarly to what observed in the past, our analysis proved that no model perfectly reproduces experimental data. In the most forward region a very large discrepancy has been found, qualitatively explained only by QGSJet II-04, leading to a general overestimation of inelasticity at this pseudorapidities by all models. In the other two regions the agreement is generally better, especially in the case of EPOS-LHC. As predicted by all models, the energy flow $dE/d\eta$ resulted to be higher for $8.81 < \eta < 9.22$ than for $\eta > 10.76$ and, in particular, the experimental value in the two lowest pseudorapidity regions is in good agreement with SIBYLL 2.1 and EPOS-LHC. Finally, a test of Feynman scaling using Arm2 results relative to p-p collisions at $\sqrt{s} = 13\ TeV$ and Arm1-Arm2 combined ones in the case of $\sqrt{s} = 7\ TeV$ confirmed that production cross sections are compatible inside the error bars. Considering this as a prove of the validity of our analysis, in the future we plan to extend it to Arm1 in order to combine the two measurement in a final result.

Bibliography

[1] K. A. Olive et al. Review of Particle Physics. *Chin. Phys.*, C38:090001, 2014.

[2] T Antoni, WD Apel, AF Badea, K Bekk, A Bercuci, J Blümer, H Bozdog, IM Brancus, A Chilingarian, K Daumiller, et al. KASCADE measurements of energy spectra for elemental groups of cosmic rays: Results and open problems. *Astroparticle physics*, 24(1):1–25, 2005.

[3] T.K. Gaisser. *Introduction to Ultrahigh Energy Cosmic Ray Physics.* Cambridge University Press, 1992.

[4] R. U. Abbasi *et al.* A Study of the Composition of Ultra-High-Energy Cosmic Rays Using the High-Resolution Fly's Eye . *Astrophys. J.*, 622:910, 2005.

[5] J. Abraham *et al.* Studies of Cosmic Ray Composition and Air Shower Structure with the Pierre Auger Observatory. *arXiv preprint arXiv:0906.2319*, 2009.

[6] Michael Unger et al. Study of the cosmic ray composition above 0.4 EeV using the longitudinal profiles of showers observed at the Pierre Auger Observatory. *arXiv preprint arXiv:0706.1495*, 2007.

[7] R. U. Abbasi *et al.* First Observation of the Greisen-Zatsepin-Kuzmin Suppression. *Phys. Rev. Lett.*, 100:101101, 2008.

[8] J. Abraham *et al.* Observation of the Suppression of the Flux of Cosmic Rays above 4×10^{19} eV. *Phys. Rev. Lett.*, 101:061101, 2008.

[9] T Abu-Zayyad, R Aida, M Allen, R Anderson, R Azuma, E Barcikowski, JW Belz, DR Bergman, SA Blake, R Cady, et al. The cosmic-ray energy spectrum observed with the surface detector of the telescope array experiment. *The Astrophysical Journal Letters*, 768(1):L1, 2013.

[10] T.G. Guzik *et al.* The ATIC long duration balloon project. *Advances in Space Research*, 33(10):1763–1770, 2004.

[11] E.S. Seo *et al.* Cosmic-ray energetics and mass (CREAM) balloon project. *Advances in Space Research*, 33(10):1777–1785, 2004.

[12] P. Picozza *et al.* PAMELA–A payload for antimatter matter exploration and light-nuclei astrophysics. *Astroparticle physics*, 27(4):296–315, 2007.

[13] J. Casaus. The AMS-02 experiment on the ISS. In *Journal of Physics: Conference Series*, volume 171, page 012045. IOP Publishing, 2009.

[14] Torii *et al.* The CALET, CALorimetric Electron Telescope, mission for the International Space Station. *Nuclear Physics B-Proceedings Supplements*, 113(1):103–110, 2002.

[15] DAMPE web page.

[16] M Bongi, O Adriani, S Albergo, L Auditore, MG Bagliesi, E Berti, G Bigongiari, M Boezio, L Bonechi, S Bonechi, et al. CALOCUBE: an approach to high-granularity and homogenous calorimetry for space based detectors. In *Journal of Physics: Conference Series*, volume 587, page 012029. IOP Publishing, 2015.

[17] S.N. Zhang et al. The High Energy cosmic-Radiation Detection (HERD) Facility onboard China's Future Space Station. *arXiv preprint arXiv:1407.4866*, 2014.

[18] Tanguy Pierog and Klaus Werner. Muon production in extended air shower simulations. *Physical review letters*, 101(17):171101, 2008.

[19] J. Abraham *et al.* Properties and performance of the prototype instrument for the Pierre Auger Observatory. *Nuclear Instruments and Methods in Physics Research Section A: Accelerators, Spectrometers, Detectors and Associated Equipment*, 523(1):50–95, 2004.

[20] H Kawai, S Yoshida, H Yoshii, K Tanaka, F Cohen, M Fukushima, N Hayashida, K Hiyama, D Ikeda, E Kido, et al. Telescope array experiment. *Nuclear Physics B-Proceedings Supplements*, 175:221–226, 2008.

[21] Valerio Verzi. The energy scale of the Pierre Auger Observatory. *Proceedings of the 33rd ICRC, Rio de Janeiro, Brasil*, 2013.

[22] Alexander Schulz. The measurement of the energy spectrum of cosmic rays above 3×10^{17} eV with the Pierre Auger Observatory. *Proceedings of the 33rd ICRC, Rio de Janeiro, Brasil*, 2013.

[23] Antoine Letessier-Selvon, A Aab, P Abreu, M Aglietta, M Ahlers, EJ Ahn, IFM Albuquerque, I Allekotte, J Allen, P Allison, et al. Highlights from the Pierre Auger Observatory. *arXiv preprint arXiv:1310.4620*, 2013.

[24] Diego Garcia-Gamez. Observations of the longitudinal development of extensive air showers with the surface detectors of the Pierre Auger Observatory. *33rd ICRC (Rio de Janeiro, 2013).*

[25] Jeff Allen. Interpretation of the signals produced by showers from cosmic rays of 10^{19} eV observed in the surface detectors of the Pierre Auger Observatory. *Energy*, 30:2, 2011.

[26] Ralf Ulrich, Ralph Engel, and Michael Unger. Hadronic multiparticle production at ultrahigh energies and extensive air showers. *Physical Review D*, 83(5):054026, 2011.

[27] V.N. Gribov. A reggeon diagram technique. *Sov. Phys. JETP*, 26(414-422):27, 1968.

[28] T Regge. Nuovo Cimento 14 951 Regge T 1960. *Nuovo Cimento*, 18:947, 1959.

[29] Hans Joachim Drescher, M Hladik, S Ostapchenko, T Pierog, and Klaus Werner. Parton-based Gribov–Regge theory. *Physics Reports*, 350(2):93–289, 2001.

[30] Klaus Werner, Fu-Ming Liu, and Tanguy Pierog. Parton ladder splitting and the rapidity dependence of transverse momentum spectra in deuteron-gold collisions at the BNL Relativistic Heavy Ion Collider. *Physical Review C*, 74(4):044902, 2006.

[31] T Pierog, Iu Karpenko, JM Katzy, E Yatsenko, and K Werner. EPOS LHC: Test of collective hadronization with data measured at the CERN Large Hadron Collider. *Physical Review C*, 92(3):034906, 2015.

[32] S Ostapchenko. QGSJET-II: towards reliable description of very high energy hadronic interactions. *Nuclear Physics B-Proceedings Supplements*, 151(1):143–146, 2006.

[33] Sergey Ostapchenko. Monte Carlo treatment of hadronic interactions in enhanced Pomeron scheme: QGSJET-II model. *Physical Review D*, 83(1):014018, 2011.

[34] Eun-Joo Ahn, Ralph Engel, Thomas K Gaisser, Paolo Lipari, and Todor Stanev. Cosmic ray interaction event generator SIBYLL 2.1. *Physical Review D*, 80(9):094003, 2009.

[35] Fritz W Bopp, J Ranft, R Engel, and S Roesler. Antiparticle to particle production ratios in hadron-hadron and d-Au collisions in the DPMJET-III Monte Carlo model. *Physical Review C*, 77(1):014904, 2008.

[36] Stefan Roesler, Ralph Engel, and Johannes Ranft. The Monte Carlo event generator DPMJet-III. In *Advanced Monte Carlo for Radiation Physics, Particle Transport Simulation and Applications*, pages 1033–1038. Springer, 2001.

[37] Torbjörn Sjöstrand, Stephen Mrenna, and Peter Skands. PYTHIA 6.4 physics and manual. *Journal of High Energy Physics*, 2006(05):026, 2006.

[38] Torbjörn Sjöstrand, Stefan Ask, Jesper R Christiansen, Richard Corke, Nishita Desai, Philip Ilten, Stephen Mrenna, Stefan Prestel, Christine O Rasmussen, and Peter Z Skands. An introduction to PYTHIA 8.2. *Computer physics communications*, 191:159–177, 2015.

[39] Lyndon Evans. The large hadron collider. *New Journal of Physics*, 9(9):335, 2007.

[40] S Myers and Emilio Picasso. The design, construction and commissioning of the cern large electron–positron collider. *Contemporary Physics*, 31(6):387–403, 1990.

[41] Oliver Brüning, Paul Collier, Paul Lebrun, Stephen Myers, Ranko Ostojic, John Poole, and Paul Proudlock. LHC design report Volume I. *Reports-CERN*, 2004.

[42] Georges Aad, E Abat, J Abdallah, AA Abdelalim, A Abdesselam, O Abdinov, BA Abi, M Abolins, H Abramowicz, E Acerbi, et al. The ATLAS experiment at the CERN large hadron collider. *Journal of Instrumentation*, 3(8), 2008.

[43] Kenneth Aamodt, A Abrahantes Quintana, R Achenbach, S Acounis, C Adler, M Aggarwal, F Agnese, G Aglieri Rinella, Z Ahammed, A Ahmad, et al. The ALICE experiment at the CERN LHC. *Journal of Instrumentation*, 3(08):S08002, 2008.

[44] CMS Collaboration, R Adolphi, et al. The CMS experiment at the CERN LHC. *Jinst*, 3(08):S08004, 2008.

[45] A Augusto Alves Jr, LM Andrade Filho, AF Barbosa, I Bediaga, G Cernicchiaro, G Guerrer, HP Lima Jr, AA Machado, J Magnin, F Marujo, et al. The LHCb detector at the LHC. *Journal of instrumentation*, 3(08):S08005, 2008.

[46] Oscar Adriani, L Bonechi, M Bongi, G Castellini, R D'Alessandro, DA Faus, K Fukui, M Grandi, M Haguenauer, Y Itow, et al. The LHCf detector at the CERN large hadron collider. *Journal of Instrumentation*, 3(08):S08006, 2008.

[47] Giovanni Anelli, G Antchev, P Aspell, V Avati, MG Bagliesi, V Berardi, M Berretti, V Boccone, U Bottigli, M Bozzo, et al. The TOTEM experiment at the CERN large hadron collider. *Journal of Instrumentation*, 3(08):S08007, 2008.

[48] James Pinfold, K Kinoshita, R Soluk, J Jakubek, Y Yao, D Felea, DH Lacarrère, L Patrizii, S Cecchini, T Hott, et al. Technical design report of the moedal experiment. Technical report, 2009.

[49] C Royon et al. LHC Forward Physics. 2015.

[50] S. White. The ATLAS zero degree calorimeter. *Nuclear Instruments and Methods in Physics Research Section A: Accelerators, Spectrometers, Detectors and Associated Equipment*, 617(1):126–128, 2010.

[51] N De Marco and G Puddu. ALICE Zero Degree Calorimeter. Technical report, 2013.

[52] A.S. Ayan, P Debbins, D d'Enterria, E Garcia, OA Grachov, L Jones, M Murray, E Norbeck, M Lehnherr, Y Onel, et al. CMS Zero Degree Calorimeter Technical Design Report, 2006.

[53] P Aspell, David Barney, D Moraes, J Crooks, M Dupanloup, Apollo Go, K Kloukinas, Wojciech Bialas, QR Morrissey, and S Reynaud. Pace3: a large dynamic range analog memory asic assembly designed for the readout of silicon sensors in the lhc cms preshower. 2004.

[54] M Ageron. Trigger sequencer card user manual. *IPNL Lyon*, 2001.

[55] C. Ljuslin C. Paillard. Front end control unit for embedded slow control, 2003.

[56] Daniele Amati, A Stanghellini, and S Fubini. Theory of high-energy scattering and multiple production. *Il Nuovo Cimento (1955-1965)*, 26(5):896–954, 1962.

[57] Richard P Feynman. Very high-energy collisions of hadrons. *Physical Review Letters*, 23(24):1415, 1969.

[58] J Benecke, TT Chou, Chen-Ning Yang, and Ed Yen. Hypothesis of limiting fragmentation in high-energy collisions. *Physical Review*, 188(5):2159, 1969.

[59] O Adriani, L Bonechi, M Bongi, G Castellini, R D'Alessandro, K Fukatsu, M Haguenauer, T Iso, Y Itow, K Kasahara, et al. Measurement of zero degree inclusive photon energy spectra for proton–proton collisions at LHC. *Physics Letters B*, 715(4):298–303, 2012.

[60] Oscar Adriani, L Bonechi, M Bongi, G Castellini, R D'Alessandro, A Faus, K Fukatsu, M Haguenauer, Y Itow, K Kasahara, et al. Measurement of zero degree single photon energy spectra for proton–proton collisions at LHC. *Physics Letters B*, 703(2):128–134, 2011.

[61] O Adriani, L Bonechi, M Bongi, G Castellini, R D'Alessandro, K Fukatsu, M Haguenauer, T Iso, Y Itow, K Kasahara, et al. Measurement of forward neutral pion transverse momentum spectra for s= 7 TeV proton-proton collisions at the LHC. *Physical Review D*, 86(9):092001, 2012.

[62] O Adriani, E Berti, L Bonechi, M Bongi, G Castellini, R D'Alessandro, M Del Prete, M Haguenauer, Y Itow, K Kasahara, et al. Transverse-momentum distribution and nuclear modification factor for neutral pions in the forward-rapidity region in proton-lead collisions at s N N= 5.02 TeV. *Physical Review C*, 89(6):065209, 2014.

[63] O Adriani, E Berti, L Bonechi, M Bongi, R D'Alessandro, M Del Prete, M Haguenauer, Y Itow, K Kasahara, K Kawade, et al. Measurements of longitudinal and transverse momentum distributions for neutral pions in the forward-rapidity region with the LHCf detector. *Physical Review D*, 94(3):032007, 2016.

[64] O Adriani, E Berti, L Bonechi, M Bongi, G Castellini, R D'Alessandro, M Del Prete, M Haguenauer, Y Itow, K Kasahara, et al. Measurement of very forward neutron energy spectra for 7 TeV proton–proton collisions at the Large Hadron Collider. *Physics Letters B*, 750:360–366, 2015.

[65] L Bonechi, M Bongi, D Fedele, M Grandi, S Ricciarini, and E Vannuccini. Development of the ADAMO detector: test with cosmic rays at different zenith angles. In *International Cosmic Ray Conference*, volume 9, page 283, 2005.

[66] K. Kasahara. EPICS web page. `http://cosmos.n.kanagawa-u.ac.jp/`.

[67] K Kawade, O Adriani, L Bonechi, M Bongi, G Castellini, R D'Alessandro, M Del Prete, M Haguenauer, Y Itow, K Kasahara, et al. The performance of the LHCf detector for hadronic showers. *Journal of Instrumentation*, 9(03):P03016, 2014.

[68] A. Tiberio. Study of the very forward electromagnetic component produced in proton-proton collisions at 13 TeV with the LHCf experiment, 2016.

[69] Miroslav Morháč, Ján Kliman, Vladislav Matoušek, Martin Veselskỳ, and Ivan Turzo. Identification of peaks in multidimensional coincidence γ-ray spectra. *Nuclear Instruments and Methods in Physics Research Section A: Accelerators, Spectrometers, Detectors and Associated Equipment*, 443(1):108–125, 2000.

[70] The LHCf collaboration. Internal note for the analysis of photons spectra produced in p-p collisions at $\sqrt{s} = 13$ TeV, 2016.

[71] The ATLAS collaboration. Measurement of the Inelastic Proton-Proton Cross Section at $\sqrt{s} = 13$ TeV with the ATLAS Detector at the LHC. In *Journal of Physics: Conference Serie.*

[72] G Antchev, P Aspell, I Atanassov, V Avati, J Baechler, V Berardi, M Berretti, E Bossini, U Bottigli, M Bozzo, et al. Luminosity-Independent Measurement

of the Proton-Proton Total Cross Section at s= 8 TeV. *Physical review letters*, 111(1):012001, 2013.

[73] C. Baus, T. Pierog, and R. Ulrich. CRMC web page. `https://web.ikp.kit.edu/rulrich/crmc.html`.

[74] AA Lednev. Electron shower transverse profile measurement. *Nuclear Instruments and Methods in Physics Research Section A: Accelerators, Spectrometers, Detectors and Associated Equipment*, 366(2):292–297, 1995.

[75] K Noda, O Adriani, L Bonechi, M Bongi, G Castellini, R D'ALESSANDRO, K Fukatsu, M Haguenauer, Y Itow, K Kasahara, et al. Data analysis of the LHCf Si microstrip sensors. *Small*, 1500:2500, 2000.

[76] Agostinelli, Sea and Allison, John and Amako, K al and Apostolakis, J and Araujo, H and Arce, P and Asai, M and Axen, D and Banerjee, S and Barrand, G and others. GEANT4—a simulation toolkit. *Nuclear instruments and methods in physics research section A: Accelerators, Spectrometers, Detectors and Associated Equipment*, 506(3):250–303, 2003.

[77] Giulio D'Agostini. A multidimensional unfolding method based on Bayes' theorem. *Nuclear Instruments and Methods in Physics Research Section A: Accelerators, Spectrometers, Detectors and Associated Equipment*, 362(2):487–498, 1995.

[78] Tim Adye. Unfolding algorithms and tests using RooUnfold. *arXiv preprint arXiv:1105.1160*, 2011.

[79] Carlos A Bertulani, Spencer R Klein, and Joakim Nystrand. Physics of ultra-peripheral nuclear collisions. *arXiv preprint nucl-ex/0502005*, 2005.

[80] Giulio D'Agostini. Improved iterative Bayesian unfolding. *arXiv preprint arXiv:1010.0632*, 2010.

[81] Georgios Choudalakis. Fully bayesian unfolding. *arXiv preprint arXiv:1201.4612*, 2012.

Appendix A

About COSMOS / CRMC discrepancy

Simulations presented in this work were generated using hadronic interaction models commonly employed in cosmic rays physics. In order to produce them we exploited two different interfaces, COSMOS [66] and CRMC [73]. The latter was used for the final comparison with data, whereas the former for the reconstruction process. However, when looking at energy distributions of hadrons reaching the LHCf detector we found some discrepancies between the two packages. This is shown in Fig.A.1 for the two generators for which we have simulations in both cases: QGSJet II-04 and EPOS-LHC. In the former case deviations are below 10%, but in the latter one they can be as large as 40%. Note that in the case of COSMOS, collisions were generated taking into account the $\theta_{cross} = 145\ \mu rad$ beam crossing angle present in experimental data, whereas this was not done in the case of CRMC. In order to take into account for possible effect due to this fact during transport from IP1 to LHCf, particles products were rotated immediately after collisions. Anyway, even simulating a COSMOS sample with $\theta_{cross} = 0^\circ$ and comparing it to CRMC results we obtained approximately the same deviation. In addition, this problem was also found in the photon analysis [68], even without simulating transport through the beam pipe. Another point that was checked is the different level of precision in floating point operations: single precision for CRMC v1.5.6 and double precision for COSMOS v7.645. After repeating simulations using CRMC v1.6.0, that makes use of double precision, the agreement with COSMOS improved, but still some differences were found. Because at the moment the reason of this discrepancy is still not clear and massive production of simulations have already been done using COSMOS v7.645 and CRMC v1.5.6, in this work we decided simply to separately use COSMOS simulations for all analysis steps, and to perform the final comparison with data employing CRMC simulations.

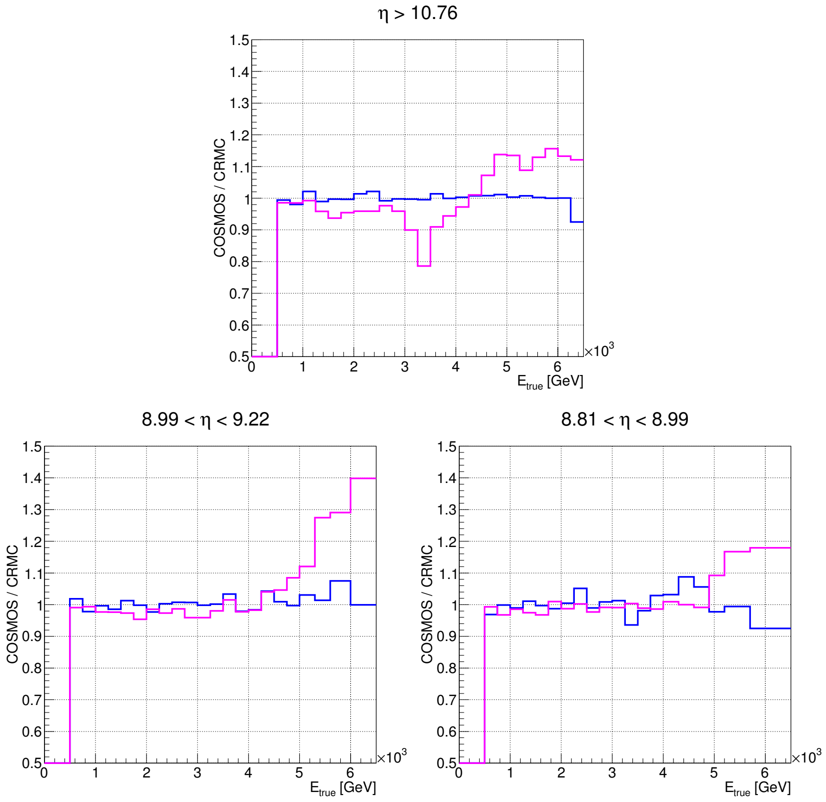

Figure A.1: COSMOS / CRMC ratio of neutrons energy spectra predicted in each pseudorapidity region for QGSJet II-04 (blue) and EPOS-LHC (magenta).

Appendix B

About forward neutrons in QGSJet II-04

QGSJet II-04 model exhibits a strange behavior when simulating p-p collisions at $\sqrt{s} = 13\ TeV$. If we look at neutrons position distribution in the x-y plane we can see a large amount of events perfectly collinear with beam original direction, *i.e.* having $\theta = 0°$ and $\eta = \infty$. This is shown in Fig.B.1, where we can see the hitmap in the LHCf reference system relative to $\eta > 10.76$ neutrons reaching the LHCf detector. To this particular narrow peak observed in position distribution does not corresponds an equivalent one in the energy spectrum, where these events appear to be distributed over the entire energy range, as shown in Fig.B.2. However, particle position has of course a large impact if we rely on this model to estimate corrections or systematics and, in any case, if we want to compare it with the final result. This is particularly true is we consider that these events constitute about 12% of all $\eta > 10.76$ neutrons reaching the LHCf detector. According to author's explanation, $\mathrm{p_T} = 0\ GeV/c$ neutrons are generated when a valence quark from the projectile of the target proton is involved in the collision. These neutrons should have very small $\mathrm{p_T}$ but it was approximated to $0\ GeV/c$ for simplicity. Because at present there is no simple way to correct for this effect, for example applying artificial smearing to position distribution, author's suggestion is to neglect them. Hence, those events have been removed from all COSMOS and CRMC simulations used for the analysis discussed in this work.

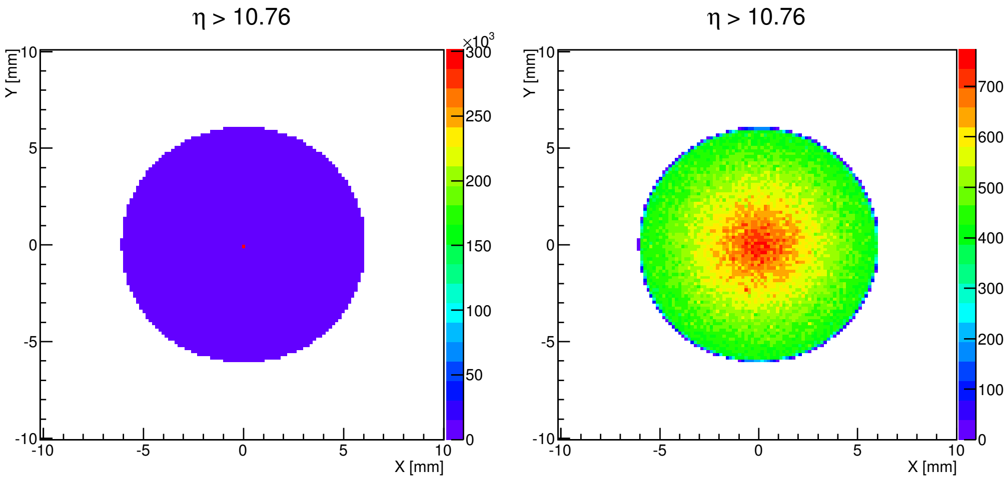

Figure B.1: $\eta > 10.76$ neutrons position distribution, seen in the LHC reference system, in case we consider all events (left) and in case we remove $\mathrm{p_T} = 0\ GeV/c$ particles (right). Simulations were generated making use of CRMC.

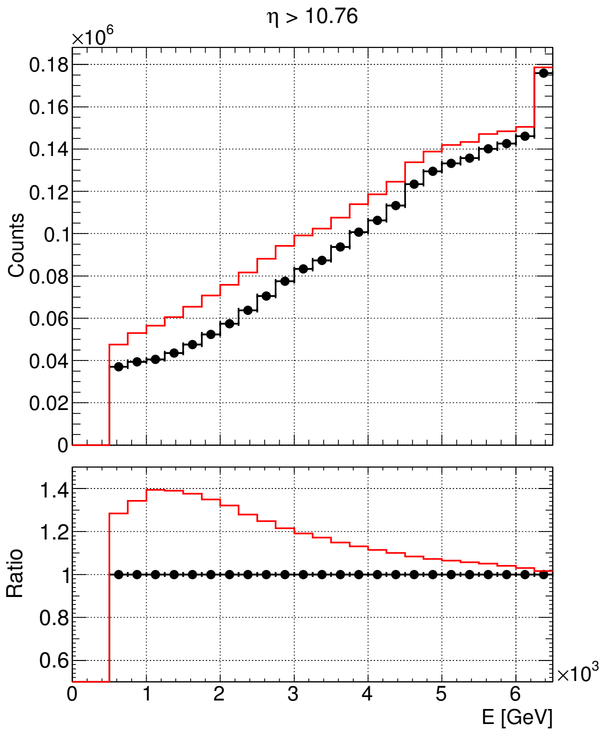

Figure B.2: $\eta > 10.76$ neutrons energy distribution in case in case we consider all events (red) and in case we remove $\mathrm{p_T} = 0\ GeV/c$ particles (black). Simulations were generated making use of CRMC.

Appendix C

Iterative bayesian unfolding

Given the limited resolution of a detector, the measured distribution D of any variable x is not directly the true distribution T, but the convolution (or folding) of T with the detector response Λ. In order to have a better understanding on how smearing is affecting our measurements and how we can correct for this effect, it is better to use the notation of linear algebra. Consider the vectors $\vec{x_T} \equiv \{x_{T_1}, ..., x_{T_i}, ..., x_{T_{N_T}}\}$ and $\vec{x_D} \equiv \{x_{D_1}, ..., x_{D_j}, ..., x_{D_{N_D}}\}$ defined in such a way that x_{T_i} (x_{D_j}) represents the number of entries in the bin i (j) of T (D). It is therefore possible to construct the *response matrix* Λ whose elements λ_{ji} is the probability that an entry in the bin i of T will be reconstructed in the bin j of D in such a way that

$$\vec{x_D} = \Lambda \vec{x_T} \tag{C.1}$$

The purpose of unfolding is to obtain the best estimation of $\vec{x_T}$ making use of all information we can extract from our detector, *i.e.* making use of measured value $\vec{x_D}$ and of response matrix Λ known from simulations. We should remark here that unfolding is a non parametric inference procedure and therefore should be used only if the goal of the analysis is the reconstruction of spectrum itself. In the case the goal is to estimate a parameter or to test an hypothesis it is much simpler to use directly folded spectrum.

The main issue related to unfolding is that the number of entries in each bin of D is affected by statistical fluctuations. Thus, solving the problem using a simple inversion of Λ is not correct from a probabilistic point of view and in general leads to several issues related to the instability of the results due to large statistical fluctuations. This is especially true in case data sample size is limited or detector resolution is poor. Among several different algorithms that have been suggested to cope with this critical point, in this work we decided to use the *Iterative Bayesian Unfolding* method proposed by D'Agostini [77,80] and implemented in the RooUnfold libraries [78].

The starting point of bayesian Unfolding is the question:

Which is the most probable true distribution T
we can infer from the measured distribution D?

The answer is found in Bayes theorem

$$\theta_{ij} = \frac{\lambda_{ji} P(T_i)}{\sum_{i=1}^{N_T} \lambda_{ji} P(T_i)} \tag{C.2}$$

where

$\theta_{ij} \equiv P(T_i|D_j)$ is the *a posteriori* (or posterior) probability that an event reconstructed in D_j was generated by an event in T_i

$\lambda_{ji} \equiv P(D_j|T_i)$ is the probability that an event in T_i is reconstructed in D_j

$P(T_i)$ is the *a priori* probability (or prior) to have an event in T_i

It is important to note that, if we take into account background sources, each entry in D is generated from an entry in T, but the opposite is not true because of reconstruction inefficiencies. We can summarize what we have just said writing the following two conditions

$$\sum_{i=1}^{N_T} \theta_{ij} = 1 \tag{C.3}$$

$$0 < \epsilon_i \equiv \sum_{j=1}^{N_D} \lambda_{ji} < 1 \tag{C.4}$$

Having estimated λ_{ji} using simulations, we can now get the number of entries in bin T_i if we know the prior $\vec{P}(T) \equiv \{P(T_1), ..., P(T_i), ..., P(T_{N_T})\}$

$$x_{T_i} = \frac{1}{\epsilon_i} \sum_{j=1}^{N_D} \theta_{ij} x_{D_j} \tag{C.5}$$

The problem is that in general we do not know the prior $\vec{P}(T)$, knowing that is exactly the purpose of unfolding, and an iterative process is needed:

1. we assume a starting value of $\vec{P_0}(T)$ for the prior $\vec{P}(T)^1$ and compute $\vec{x_0} = N_{obs}\vec{P_0}(T)$ where $N_{obs} = \sum_{j=1}^{N_D} x_{D_j}$
2. we estimate $\vec{x_T}$ using Eq.C.5

---

[1] In the case of complete ignorance the best choice is a flat prior, *i.e.*, in the case each bin i of T has the same width, $P_0(T_i) = 1/N_T$.

3. we perform a χ^2 test between $\vec{x_T}$ and $\vec{x_0}$
4. if χ^2 is small enough we stop the iterative process, otherwise we replace $\vec{x_0}$ with $\vec{x_T}$ and $\vec{P_0}(T)$ with $\vec{P}(T) = \vec{x_T}/N_{true}$ where $N_{true} = \sum_{i=1}^{N_T} x_{T_i}$
5. we smooth $\vec{x_0}$ (and $\vec{P_0}(T)$) distributions[2] and go back to second point

The key point of unfolding is to define the strength of regularization that fix how many components of folded spectra are really essential, removing the ones due to statistical fluctuations in unfolded spectra. In iterative bayesian unfolding, this is done choosing the proper number of iterations. This parameter should be enough high to avoid bias coming from the truth distribution used as the starting value of the prior, but enough low to prevent the enhancement of statistical fluctuations.

At each iteration, it is possible to estimate the covariance matrix making use of Eq.C.5. There are three different contributions to the final uncertainty:

$P(T_i)$ beside possible systematic effects due to the reliability of the model, this statistical term (not present in [77]) is due to the dependence of $P(T_i)$ from x_{T_i} and therefore from $\vec{x_D}$ because of Eq.C.5 [78]

x_{D_j} beside possible systematic effects related to the experiment, this statistical term is just due to the limited size of data sample

λ_{ji} beside possible systematic effects due to model reliability, this statistical term is just due to the limited size of simulation sample used to estimate λ_{ji}

In conclusion, the main advantages of iterative bayesian unfolding are:

- problems are resolvable even in the multidimensional case
- number of bins in true and measured spectra can be different
- statistical uncertainties are propagated throughout the iterative process
- model dependence is minimum in case that smearing is not too large

On the opposite side, this method has been criticized to not be truly bayesian and a so called *Full Bayesian Unfolding* method has been proposed [81].

---

[2] The reason why we can not directly use $\vec{x_0}$ (and $\vec{P_0}(T)$) as input of next iteration is that the iterative procedure leads to a positive feedback of statistical fluctuations. In order to recover the smoothness of the spectrum is therefore necessary to request continuity between adjacent bins, generally imposing some conditions on derivatives. However, the effect of smoothing is not always significant and it is automatically disabled in RooUnfold.

Acknowledgments

I would like to thank O. Adriani, L. Bonechi and R. D'Alessandro for having given me the possibility to work in LHCf and for their encouragement year after year. I also can not forget the continuous help and suggestion I received along my PhD from H. Menjo, G. Mitsuka and T. Sako, to whom I would like to express all my gratitude. Furthermore, I am grateful to all other members of the collaboration with whom I discussed less frequently, but that gave me a non-negligible help to the result of this work.

A particular thank goes to all PhD and Master Thesis student I met as a member of the LHCf collaboration: Y. Makino, E. Matsubayashi, Q. D. Zhou, S. Calì, T. Iwata, Y. Okuno, M. Shinoda and M. Ueno. Working together, discussing on the most different topics and knowing each other better and better as time was going on were definitely the best part of these three years.

My most intense and sincere gratitude goes to L. Viliani and A. Tiberio. Our friendship has been a continuous point of reference for me as a Master and then PhD student. I would not have arrived so far without them and I really hope the best for their future.

Finally, I think this is not the best place to thank people that are important for me in my daily life. A subset of them is already included in the previous acknowledgments. I hope each of the remaining ones knows the place he has in my heart.